SECURITY MARKING

The classified or limited status of this report applies to each page, unless otherwise marked.
Separate page printouts MUST be marked accordingly.

THIS DOCUMENT CONTAINS INFORMATION AFFECTING THE NATIONAL DEFENSE OF THE UNITED STATES WITHIN THE MEANING OF THE ESPIONAGE LAWS, TITLE 18, U.S.C., SECTIONS 793 AND 794. THE TRANSMISSION OR THE REVELATION OF ITS CONTENTS IN ANY MANNER TO AN UNAUTHORIZED PERSON IS PROHIBITED BY LAW.

NOTICE: When government or other drawings, specifications or other data are used for any purpose other than in connection with a definitely related government procurement operation, the U. S. Government thereby incurs no responsibility, nor any obligation whatsoever; and the fact that the Government may have formulated, furnished, or in any way supplied the said drawings, specifications, or other data is not to be regarded by implication or otherwise as in any manner licensing the holder or any other person or corporation, or conveying any rights or permission to manufacture, use or sell any patented invention that may in any way be related thereto.

AERODYNAMIC DEPLOYABLE DECELERATOR PERFORMANCE-EVALUATION PROGRAM

AUTHOR: F. R. NEBIKER

TECHNICAL REPORT AFFDL-TR-65-27

AUGUST 1965

AIR FORCE FLIGHT DYNAMICS LABORATORY
RESEARCH AND TECHNOLOGY DIVISION
AIR FORCE SYSTEMS COMMAND
WRIGHT-PATTERSON AIR FORCE BASE, OHIO

Prepared under Contract No. AF 33(657)-10955 by
Goodyear Aerospace Corporation, Akron, Ohio

NOTICES

When Government drawings, specifications, or other data are used for any purpose other than in connection with a definitely related Government procurement operation, the United States Government thereby incurs no responsibility nor any obligation whatsoever; and the fact that the Government may have formulated, furnished, or in any way supplied the said drawings, specifications, or other data, is not to be regarded by implication or otherwise as in any manner licensing the holder or any other person or corporation, or conveying any rights or permission to manufacture, use, or sell any patented invention that may in any way be related thereto.

Qualified users may obtain copies of this report from the Defense Documentation Center.

Foreign announcement and dissemination of this report are not authorized.

The distribution of this report is limited because the report contains technology identifiable with items on the strategic embargo lists excluded from export or re-export under U. S. Export Control Act of 1949 (63 Stat. 7) as amended (40 U. S. C. app 2020. 2031) as implemented by AFR 400-10.

Copies of this report should not be returned to the Research and Technology Division unless return is required by security considerations, contractual obligations, or notice on a specified document.

400 - October 1965 - 773-9-197

FOREWORD

The work described in this report was performed by Goodyear Aerospace Corporation (GAC), Akron, Ohio, under the authority of Projects 6065 and 8151, Tasks 606505, 606506, and 815101, entitled "Aerodynamic Deployable Decelerator Performance Evaluation Program" and Air Force Contract No. AF33(657)-10955.

Mr. S. McFarland, Flight Dynamics Laboratory, Research and Technology Division, served as contract monitor.

The authors and contributing personnel of Goodyear Aerospace Corporation were F. R. Nebiker, project engineer; A. C. Aebischer, field-testing; J. J. Dean, missile development; F. Bloetscher, decelerator evaluation; W. W. Sowa, thermal analysis; I. M. Jaremenko, aerodynamic analysis; J. Schlemmer, trajectory analysis; W. A. Barr, decelerator design; N. E. Houtz, decelerator structural analysis; and R. G. Slaymann, materials.

GAC wishes to acknowledge the support and technical information supplied by the following Recovery and Crew Station personnel on past and inhouse programs supporting decelerator research:

Mr. S. R. Metres
Capt. A. W. Gerzina
Mr. J. E. Schmalhofer, Jr.

This contractor's number for this report is GER-11672.

Manuscript released by authors October 1964 for publication as an RTD technical report.

PREVIOUS PAGE WAS BLANK, THEREFORE NOT FILMED.

ABSTRACT

The objective of this program is to advance the state of the art by using analytical and engineering techniques for designing aerodynamic deployable decelerators. Three classes of decelerators - small supersonic parachutes, ram-air-inflated BALLUTEs, and large high-dynamic-pressure parachutes were investigated. Free-flight tests using a newly developed GAC missile system and wind-tunnel tests in the full-scale propulsion wind-tunnel facility at Arnold Research Center were conducted. The results indicated that the engineering techniques that were developed led to improved decelerators and that an improved free-flight test capability was established.

PUBLICATION REVIEW

This report has been reviewed and approved.
For the Commander:

GEORGE A. SOLT, JR.
Chief, Recovery & Crew Station Branch
Vehicle Equipment Division
AF Flight Dynamics Laboratory

TABLE OF CONTENTS

LIST OF ILLUSTRATIONS

LIST OF TABLES

LIST OF SYMBOLS

1. AERODYNAMIC

A_e = area at exit (square feet)

A_i = area at inlet (square feet)

A^* = area at sonic condition (square feet)

C_{D_o} = drag coefficient based on construction diameter

C_ℓ = section-lift coefficient

C_p = pressure coefficient (external, internal, base)

c = velocity of sound (feet per second)

D_c = constructed diameter (feet)

D_o = normal diameter of canopy (feet)

D_r = reefing diameter (feet)

d = payload aft-body diameter (feet or inches)

F_o = peak load

g = gravitational constant

K = similarity parameter

M = Mach number (V/c)

M_e = Mach number at exit

M_i = Mach number at inlet

M_{loc} = Mach number local

M_1 or M_∞ = Mach number in free stream

M_2 = Mach number behind main shock

p = static pressure (pounds per square foot)

p_1 or p_∞ = static pressure, free stream

p_2 = static pressure behind main shock

p_t or p_o = stagnation (total) pressure (pounds per square foot)

q = dynamic pressure (pounds per square foot)

RN or R_e = Reynolds number

s = entropy

T = temperature (degrees Rankin)

u, v = velocity components in rectangular coordinates (feet per second)

V = air velocity (feet per second)

X = shock factor

x = axial distance between payload and vertex or decelerator (feet or inches)

β = Mach parameter

γ or K = ratio of specific heats

Δ = shock-detachment distance (inches)

δ = boundary-layer thickness (inches)

θ = body-surface inclination angle

λ = geometric porosity

ν = kinematic viscosity (square feet per second)

ρ = density (pounds or slugs per cubic foot)

σ = error value

ψ = stream function

2. STRESS

a = major axis of ellipse (inches)

b = minor axis of ellipse (inches)

C_D = drag coefficient

C_{P_f} = pressure coefficient, front of drag device

C_{P_i} = internal-pressure coefficient

C_1, C_2 = constants of integration

dA = differential drag area (square inches)

D = drag force

D_1 = drag on canister during second and third phases of deployment (pounds)

D_2 = drag on deployment bag during second and third phases of deployment (pounds)

E = modulus of deployment-bag line (pounds)

E_L = modulus of riser line (pounds)

f = fabric stress (pounds per inch)

$I_R = \int_0^1 \frac{x}{R} \frac{Px}{P} \frac{dx}{R}$

$k = nT_m/P\pi R^2$

ℓ = length of deployment-bag line (inches)

L = length of riser line (inches)

m_1 = mass of canister (lb-sec^2/in.)

m_2 = mass of decelerator (lb-sec^2/in.)

n = number of gores

P = value of P_x at x = R (pounds per square inch)

$P_{(ambient)}$ = ambient atmospheric pressure (pounds per square inch)

P_e = internal pressure on interstices between threads (pounds per square inch)

$P_{(local)}$ = local external pressure on drag (pounds per square inch)

P_ℓ = load in deployment-bag line (pounds)

P_L = load in riser line (pounds)

P_x = pressure difference on membrane at any point, x (pounds per square inch)

P_2 = internal pressure on threads (pounds per square inch)

q = dynamic pressure (pounds per square inch)

r_1, r_2 = principal radii of curvature (inches)

R = equatorial radius (inches)

R_i = inlet radius (inches)

R_o = radius of flat circle with same area as a parachute (inches)

T_H = tension in inlet hoop (pounds)

T_m = tension in each meridian cord (pounds)

T_s = tension in each suspension line (pounds)

V_o = canister ejection velocity (inches per second)

V_1 = velocity of canister and package after first phase of deployment (inches per second)

V_2 = velocity of canister and package after second phase of deployment (inches per second)

x = radial coordinate axis

x_2 = displacement of package at time, t (inches) (see Appendix IV)

y = axial coordinate

λ = geometric porosity

$\rho = F/\pi R^2$ (see Appendix II)

θ_i = suspension-line angle (degrees)

θ_t = angle of tangent to nominal parachute surface at inlet (degrees)

f = value of a quantity on the front of a drag device (subscript)

r = value of a quantity on the rear of a drag device (subscript)

3. THERMODYNAMIC

A_c = cross-section area (square feet)

A_s = surface area (square feet)

A_* = cross-section area at throat (square feet)

Bi = Biot number (dimensionless)

c^* = characteristic velocity (feet per second)

c = specific heat of material (Btu/lb-deg F)

c_p = specific heat of air at constant pressure (Btu/lb-deg F)

d = element diameter (inches)

D = diameter of burble fence (feet)

D_o = outer diameter of composite (inches)

D_{N_1} = outer diameter of Nomex element (inches)

D_{N_2} = core diameter of Nomex in composite (inches)

D_* = orifice throat diameter (inches)

F_o = Fourier number (dimensionless)

g = gravitational constant (32.2 fps^2)

h = convective heat-transfer coefficient (Btu/ft^2-hr-deg F)

k = thermal conductivity (Btu/ft-hr-deg F)

M = Mach number

Pr = Prandtl number

p = local pressure (pounds per square foot)

p_t = total pressure (pounds per square foot or per square inch)

q = heat-flux rate (Btu/ft^2-sec)

q_c = reference heat-flux rate (Btu/ft^2-sec) or heat flux into composite (Btu/ft^2)

q_N = heat flux into Nomex element (Btu/ft^2)

Q_{in} = total heat into specimen (Btu per pound)

Q_{abs} = total heat absorbed (Btu per pound)

Q_{eff} = effective heat absorbed (Btu per pound)

r = recovery factor

r_e = radius of roof-panel element

Re = Reynolds number

R_o = effective nose radius of cone (feet)

R = radius of BALLUTE (feet)

St = Stanton number

T_w = surface temperature (Rankin or Fahrenheit)

T_{aw} = adiabatic wall temperature (Rankin or Fahrenheit)

T^* = reference temperature (Rankin or Fahrenheit)

u = local velocity (feet per second)

w = weight of material (pounds)

x = characteristic surface length (feet)

y = surface depth (feet)

α = thermal diffusivity (square feet per hour)

ϵ = surface emissivity (dimensionless)

τ = time (seconds)

μ = absolute viscosity (lb-sec/ft^2)

ρ = density (lb-sec^2/ft^4)

ρ_c = coating material density (lb/ft^3)

ρ_N = Nomex material density (pounds per cubic foot)

σ = dimensionless factor accounting for density and viscosity variation in boundary layer as developed in Reference 16; also Stefan-Boltzman constant (0.173×10^{-8} Btu/ft^2-hr-deg R^4)

γ = ratio of specific heats for air (1.4)

SECTION I - INTRODUCTION

Space and the high-speed, high-altitude flight associated with it require new methods of stabilization and deceleration for the recovery of manned escape capsules and personnel ejected from these capsules, and of rocket boosters, nose cones, and instrument packages. Initial stabilization is required so that heat shields and ablation shields and drag devices of payloads tumbling or disoriented in space can be aligned with the flightpath. Initial deceleration is required for gradual reduction of aerodynamic heating, loading, and velocity in a varying dynamic loading regime. This essentially is done by decreasing the weight-to-drag ratio (the ballistic coefficient, W/C_DA).

If parachutes or sophisticated devices such as gliding and homing parachutes, paragliders, and expandable rotor blades are to be used in the final stage, the velocity of the payload must be reduced gradually to a dynamic pressure (q) and speed that will allow reliable deployment of the retardation devices. Missile and wind-tunnel tests show that conventional parachutes are not satisfactory for this first-stage deceleration because of aerodynamic heating and erratic loading under supersonic flow conditions.

This new requirement for high-speed recovery systems led to the USAF Aerodynamic Deployable Decelerator Performance Evaluation Program (ADDPEP). ADDPEP includes theoretical investigation, development of design methods, test, and evaluation of these new methods using newly designed deployable decelerators categorized in three groups: (1) large ribbon-type parachutes for recovery of heavy payloads at transonic and supersonic speeds at high dynamic pressures; (2) small specially designed supersonic parachutes for stable and reasonable high-drag performance up to Mach 5; and (3) balloon-type (BALLUTE[a]) decelerators for stable and high-drag performance up to Mach 10.

[a] TM, Goodyear Aerospace Corporation, Akron, Ohio.

As demonstrated by wind-tunnel model tests and full-scale free-flight tests, BALLUTEs show promise for stabilization and deceleration throughout the Mach number regime and for all decelerator-to-payload size ratios that have been tested.[1, 2, a] Similar tests of the truncated-cone parachute show promise at supersonic speeds and at low decelerator-to-payload size ratios.[3, 4] Large high-q parachutes have been under investigation by several agencies, and the ribbon types hold promise for low-level, high-speed recovery with large decelerator forces.

Under Contract AF33(657)-10955 from the Flight Dynamics Laboratory, Goodyear Aerospace Corporation (GAC), conducted Phase I of the ADDPEP program to determine the most effective analytical and empirical techniques for designing these three types of decelerators. Two test vehicle configurations were redesigned from Air Force drawings, and one of these was developed by vibration and static tests and utilized for free flights. Although no free-flight data were obtained, the vehicle demonstrated increased performance, payload, and data-assurance capability in comparison with prior decelerator test vehicles. Laboratory tests were conducted at GAC; the flight tests were conducted at the Air Force Missile Test Range at Eglin Air Force Base, Fla. In addition, GAC provided a consultant or observer for FDFR-conducted wind-tunnel tests at Arnold Engineering Development Center and for tests at the Langley Research Center to coordinate additional information for this report.

This report presents the results of the test vehicle design and development efforts as well as the analytical and empirical techniques found most applicable to the design of the BALLUTE and the small supersonic parachute. In the large parachute effort, wind-tunnel tests of promising supersonic configurations were studied and two systems were designed and fabricated for future testing. Table 1 summarizes the decelerator configurations and tests.

[a] Superior numbers in the text refer to items in the List of References.

TABLE 1 - DESIGN PARAMETERS

Decelerator type	Principal material	Coating	Test point data					
			Test method	M	Altitude (10^3 ft)	Dynamic pressure (psf)	Total temperature of air (F)	
Small parachutes			Vehicle "B/C"					
SP-1	Nylon, Perlon mesh roof	None	N-N boost	2.08	74	234	273	
			1st firing	. . .	. . .	. . .	. . .	
SP-2	Nomex, Mock Leno mesh roof	None	HJ-N	2.74	60	792	515	
			2nd firing	3.04*	39*	2660*	650*	
SP-3	Nomex, Mock Leno mesh roof	None	HJ-N	2.50	80	255	444	
		Silastic 131	Arnold PWT	2.60*	98*	120*	183*	
SP-3a (2nd unit)	Nomex, Mock Leno mesh roof	Silastic 131	HJ-N	2.50	80	255	444	
SP-5	Nomex, Mock Leno mesh roof	Dynatherm D-65	HJ-N-N	3.40	156	20	1150	
SP-7	Nomex, Mock Leno mesh roof	Silastic 131	HJ-N	2.74	60	792	515	
Ballutes			Vehicle "B/C"					
TB-1	Nylon	Neoprene	HJ-N	2.50	84	212	440	
			3rd firing	2.42*	87*	172*	398*	
TB-1a (2nd unit)	Nylon	Neoprene	HJ-N	2.50	84	212	440	
TB-2	Nomex	Silastic 131	HJ-N-N	3.80	104	197	1134	
Large parachutes			Vehicle "A"					
LP-1	Nylon	None	Airdrop	1.2	8.5	1350	170	
LP-2	Nylon	None	Airdrop	1.2	8.5	1350	170	

*Values at condition defined in remarks, actual test conditions.

+Total porosity instead of roof porosity.

BLE 1 - DESIGN PARAMETERS

Test point data				Remarks	S_{c_2} (ft)	Roof porosity (per sq ft at 1/2 in. H_2O or %)	Load factor (g)	C_DA (sq ft)
M	Altitude (10^3 ft)	Dynamic pressure (psf)	Total temperature of air (F)					
2.08	74	234	273		12.57	31.8	3.1	5.0
. . .	. . .	. . .	. . .	Second-stage ignition failure				
2.74	60	792	515		12.57	21.4	10.3	5.0
3.04*	39*	2660*	650*	Container failure				
2.50	80	255	444	Unit fabricated for test	12.57	750 cfm	3.8	5.7
2.60*	98*	120*	183*	H7 test from AEDC-TDR-64-120	12.57	9.0+ 450 cfm	. . .	3.2*
2.50	80	255	444	Unit fabricated for test	12.57	450 cfm	3.8	5.7
3.40	156	20	1150	Design completed	12.57	300 cfm	0.30	5.7
2.74	60	792	515	Unit fabricated for test	12.57	400 cfm	11.8	5.7
2.50	84	212	440		86.5	Negligible	10.9	19.6
2.42*	87*	172*	398*	No test item deployment				
2.50	84	212	440	Unit fabricated for test	86.5	Negligible	10.9	19.6
3.80	104	197	1134	Unit fabricated for test	86.5	Negligible	10.1	19.6
1.2	8.5	1350	170	Unit fabricated for test	201.1	29†	62.4	100
1.2	8.5	1350	170	Unit fabricated for test	201.1	15†	62.4	100

2

SECTION II - FREE-FLIGHT TEST CAPABILITY

1. VEHICLE/BOOSTER SYSTEM "A"

a. Requirements

(1) Test Objective

A basic goal in the evaluation program was to advance the state of the art of large supersonic-parachute performance at high dynamic pressure. The long-range objective is Mach 3 at low altitudes for a minimum parachute diameter (D_o) of 16 ft. By definition,[5] the requirements of this test regime could be fulfilled by land-surface recovery Vehicle "A," weighing (nominally) 2161 lb.

(2) Control

The test vehicle follows a ballistic trajectory when dropped from the bomb bay of a B-52 as well as when it is ground-launched by booster rockets. The mechanical functions leading to the deployment, data acquisition, test-item release, and recovery-parachute deployment are activated by a mechanical timer used in conjunction with pyrotechnic delay switches. The sequence schematic for drop-test flights is shown in Figure 1. The sequence schematic for ground-launched flight tests utilizing rocket boosters is shown in Figure 2.

(3) Test-Item Deployment

Test items are deployed by a pyrotechnic-initiated event controlled by a mechanical sequence. The deployment sequence is initiated by separation of the booster adapter and drag-cone assembly. The cone shape is desirable in the [illegible] environment for drag stability. The cone provides the force required to remove the aft section of the test-item compartment. The chain of events leading to the test-item deployment is presented in Figure 3.

(4) Data Requirements

To provide the necessary data for decelerator analysis and correlation, several

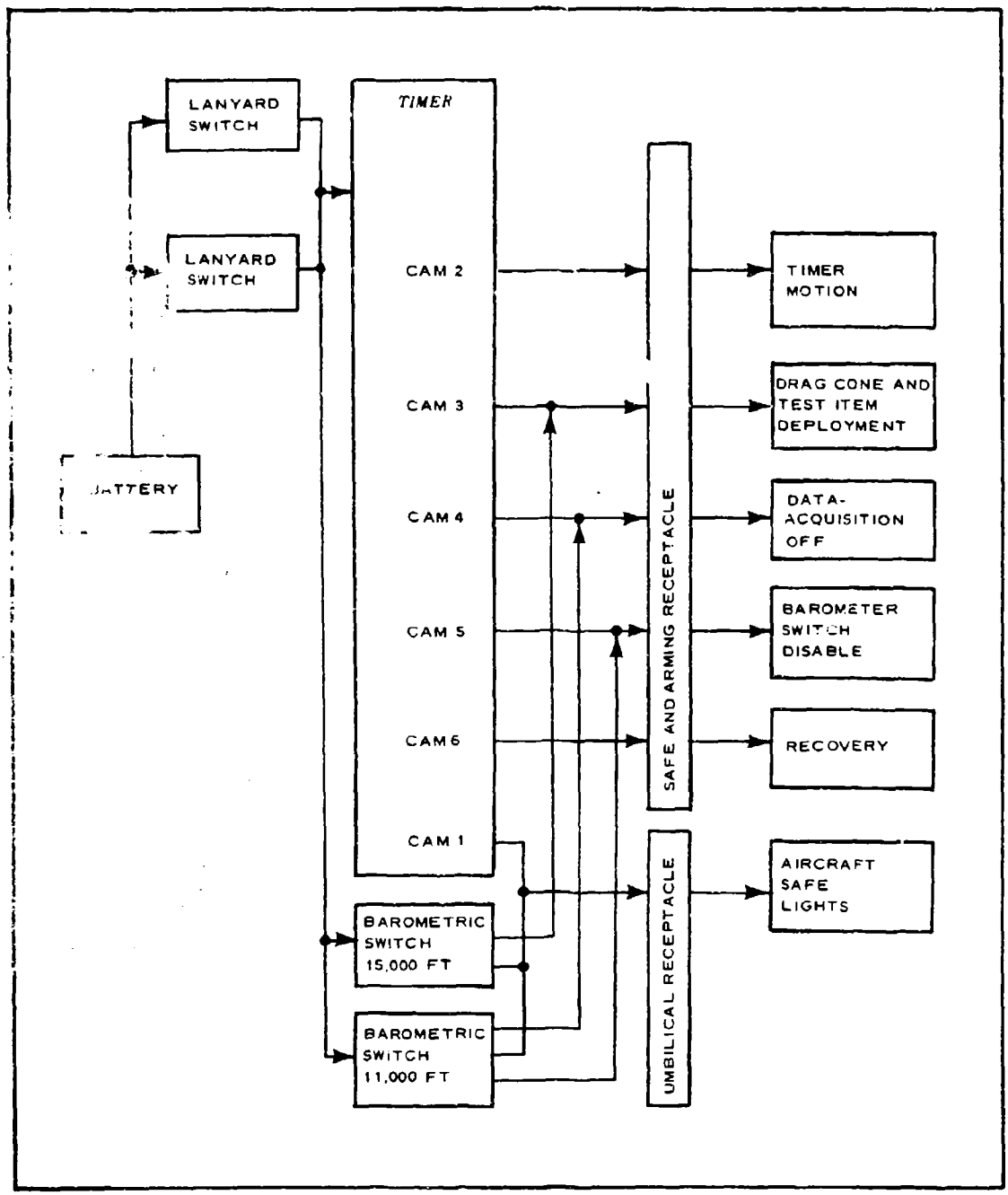

Figure 1 - Sequence Schematic, Vehicle "A" Airdrops

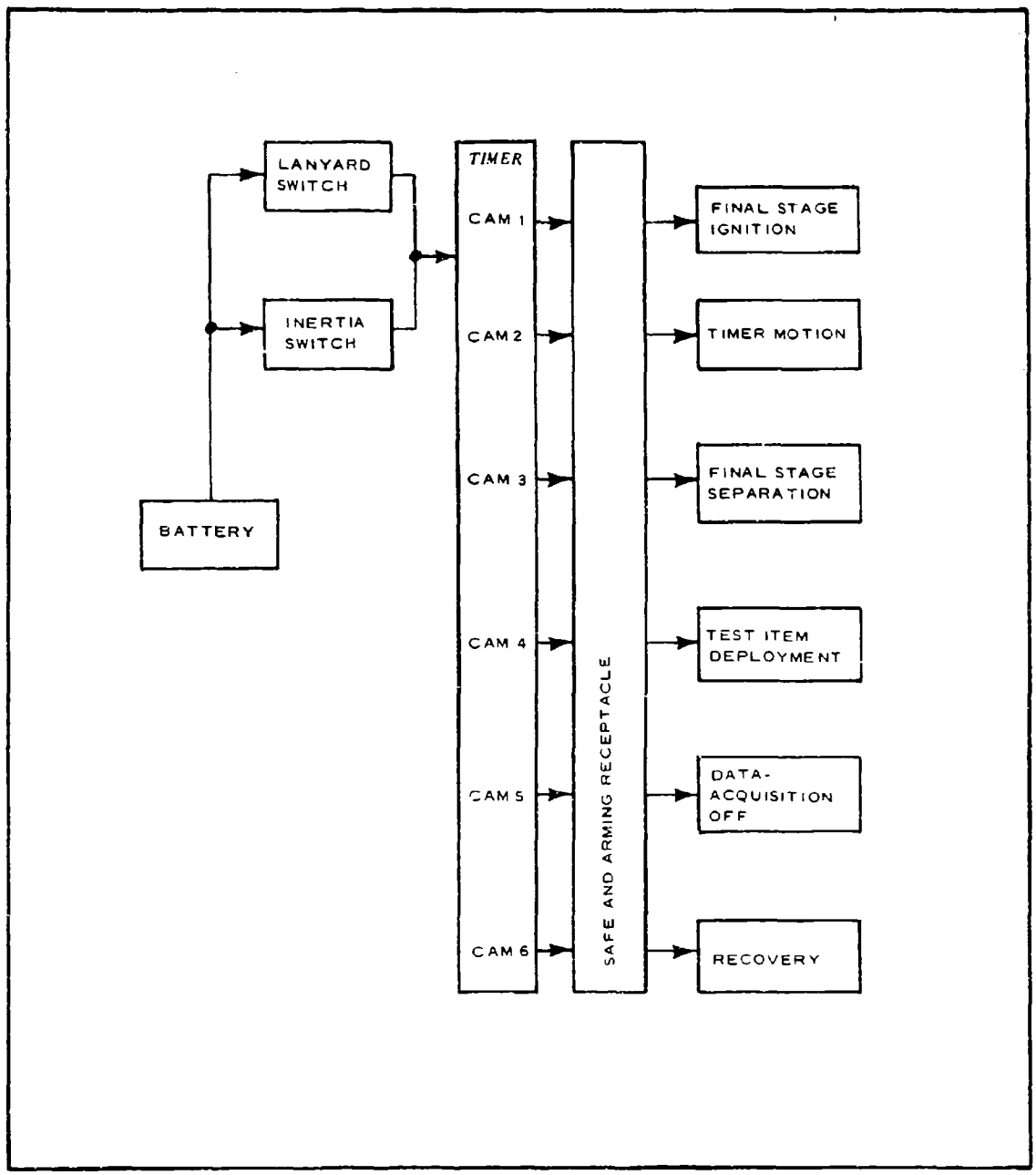

Figure 2 - Sequence Schematic, Vehicle "A" Ground-Launched Rocket-Boosted Flights

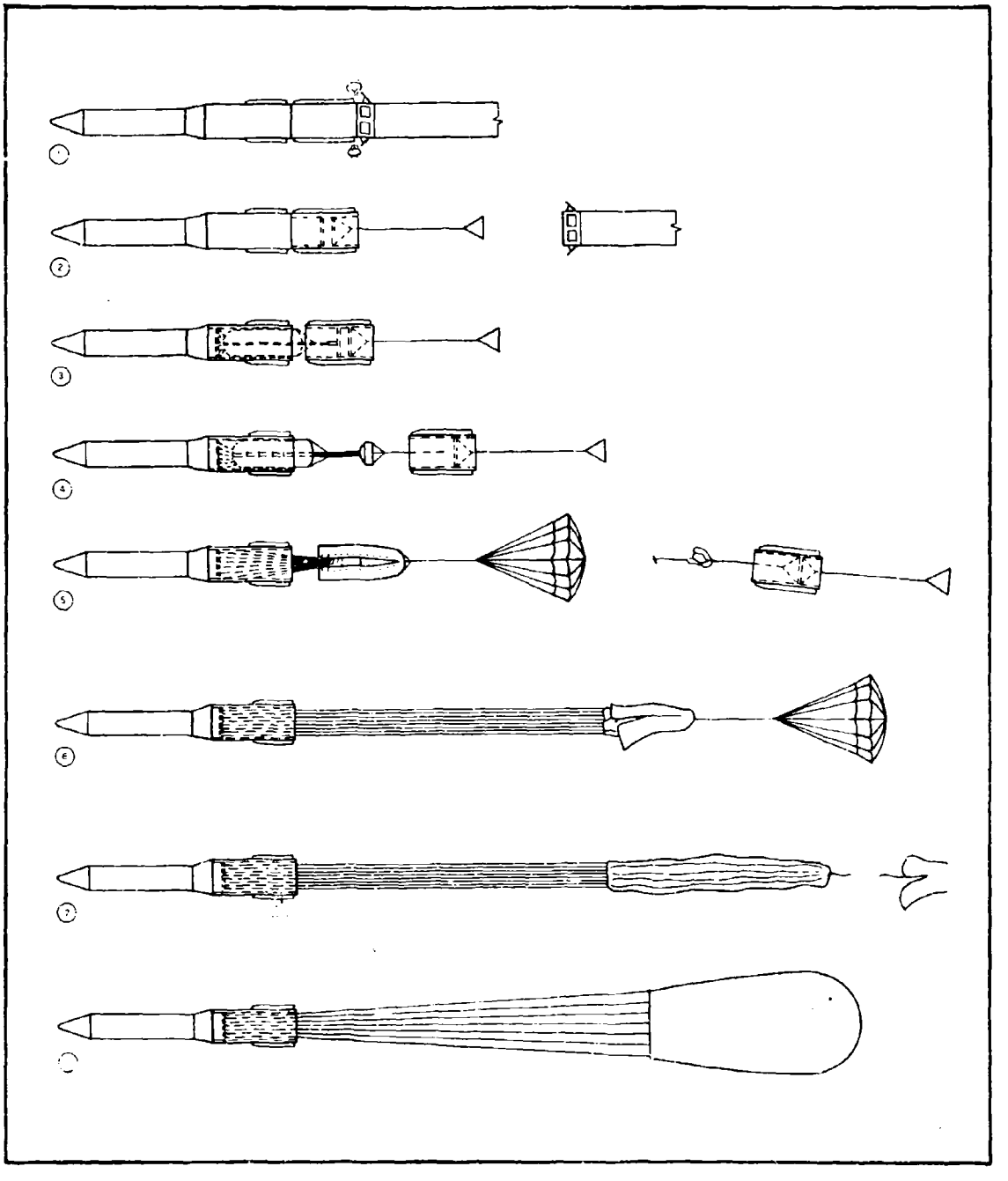

Figure 3 - Deployment Sequence of 16-Ft High-Q Parachute, Vehicle "A"

sources of data acquisition were required. GFE data-acquisition systems consist mainly of telemetry and phototheodolite devices. Theodolites provide position information, and telemetering provides force, temperature, and pressure data. In addition to telemetry equipment, the vehicle is equipped with two high-speed cameras for close examination of decelerator deployment and performance. The data-acquisition schematic is shown in Figure 4.

(5) Recovery

To prevent interference with deployment of the recovery parachute, the test item and test container assembly are separated from the vehicle before the recovery sequence is initiated. A typical flight profile is shown in Figure 5.

b. Characteristics

Figure 6 shows two booster configurations for Vehicle "A." Computer analyses established that these configurations were feasible from the standpoints of performance, stability, and structural integrity for operating at all test environments compatible with a Nike-plus-Nike-booster configuration when launched at 40 deg. The weight distribution of Vehicle "A" by flight sequence is given in Table 2. Figure 7 is a sketch of the vehicle illustrating component locations.

Information generated during Vehicle "A" design changes is given in Section 2 of Reference 6 under the following subheadings:

Payload Vehicle "A" Description
Vehicle "A" Design Analysis
Field Test Support, System "A"

c. Mission Capabilities

Vehicle "A," with a total weight of more than 2100 lb, is the payload-instrumentation missile for flight tests of large, high-dynamic-pressure supersonic parachutes. It is a ballistic type for airdrop or ground launching by an Honest John or Nike-Nike booster. It has a test decelerator storage capacity of 6.6 cu ft and is land-recoverable by means of a nose spike. The vehicle system

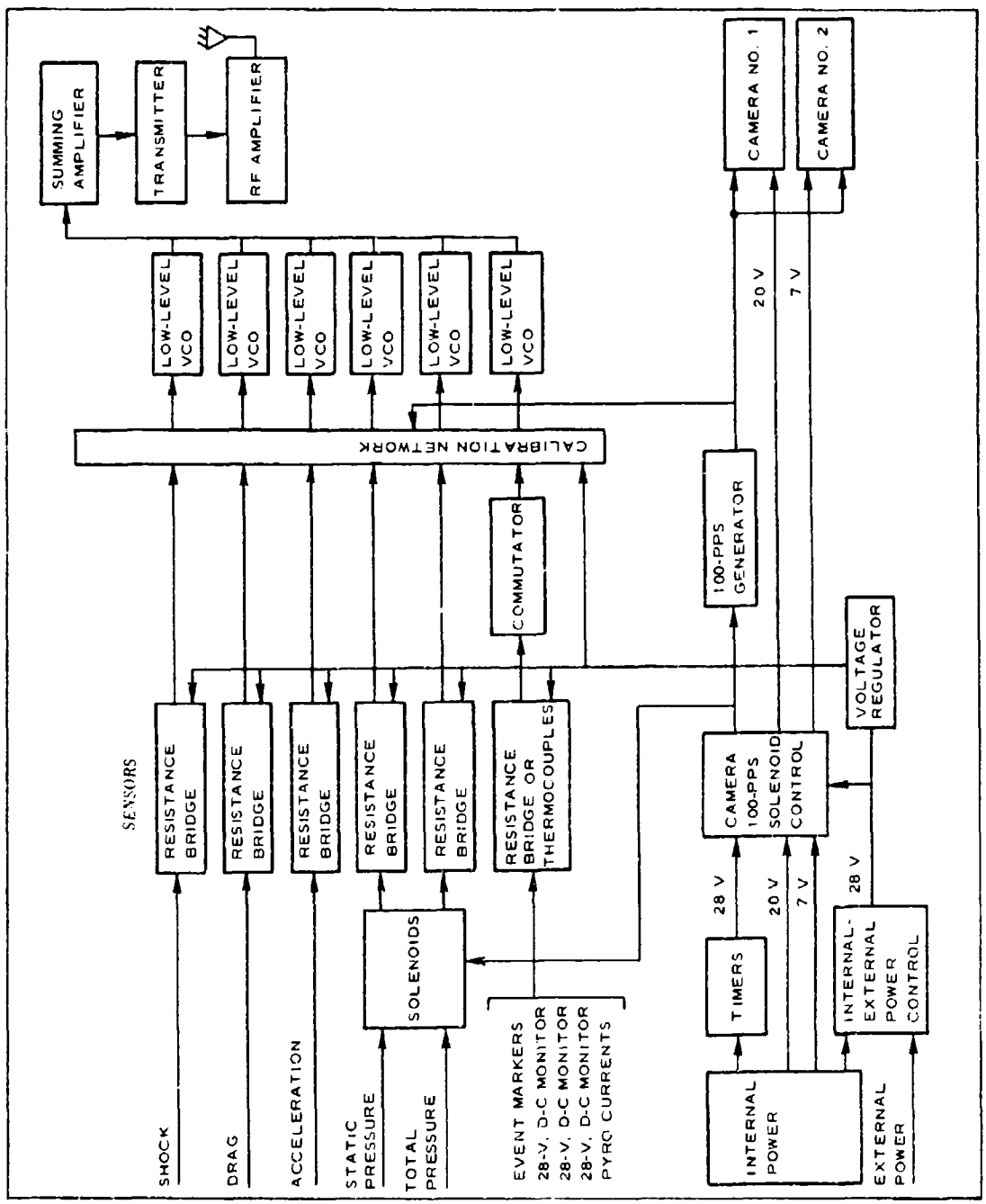

Figure 4 - Block Diagram of Vehicle "A" Data-Acquisition System

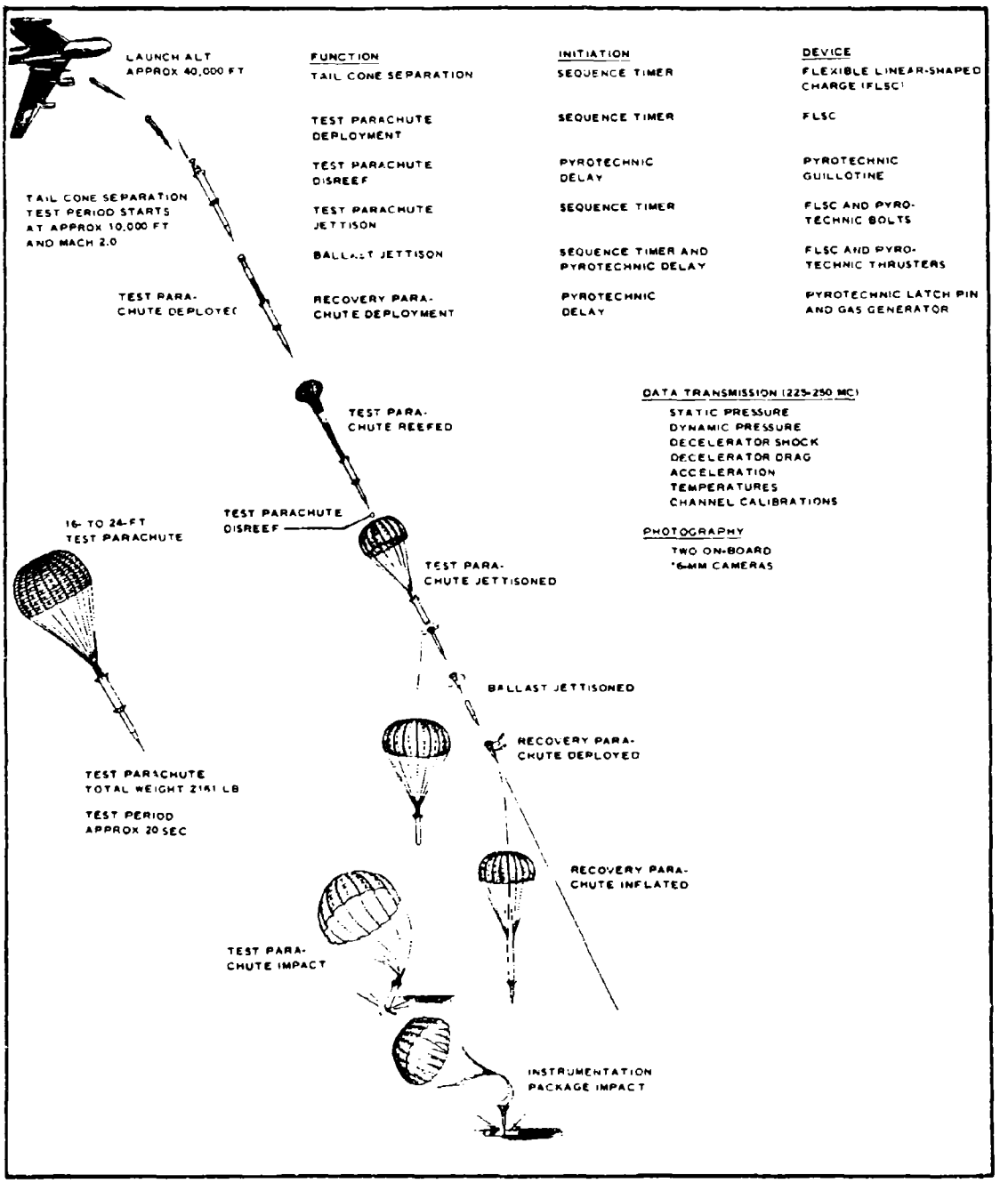

Figure 5 - Typical Vehicle "A" Flight-Test Profile

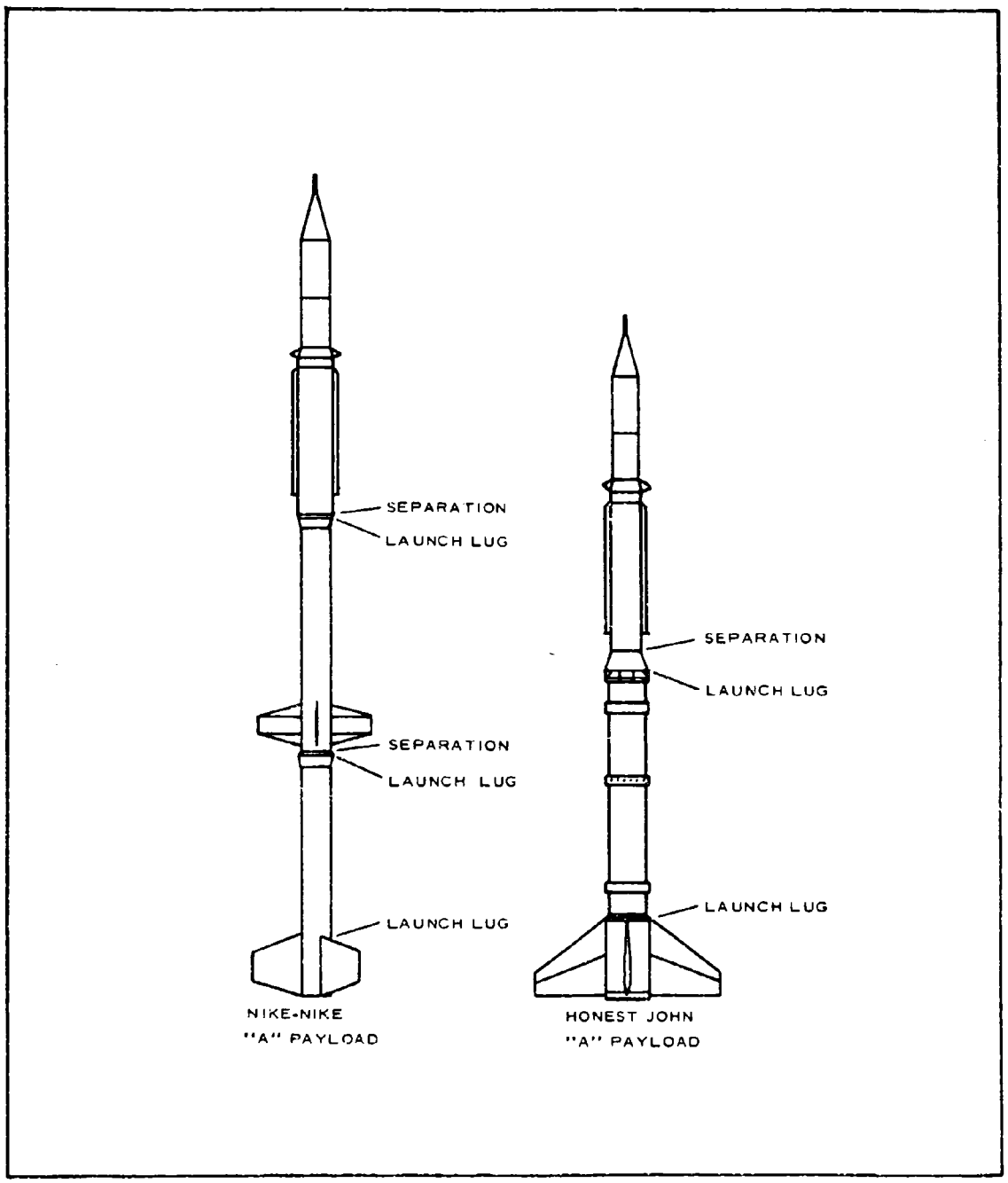

Figure 6 - Vehicle "A" Booster Combinations

TABLE 2 - VEHICLE A' WEIGHT, CENTER OF GRAVITY, AND MOMENT OF INERTIA

Item	Weight (lb)	Center of gravity from 0.00 (in.)	Moment of inertia (lb-in.^{2})		
			I_o (roll)	I_o (pitch)	I_o (yaw)
Total at launch	2103.3	119.43	65,439	3,736,475	3,737,107
Booster adapter assembly	-26.66	3.49			
Drag cone and riser line	-14.43	8.06			
Final stage separation	2062.21	121.71	63,213	3,186,529	3,187,161
Test container, aft end	-60.36	22.83			
Test item	-110.00	39.77			
Test item reefed	1891.85	129.63	55,651	1,704,446	1,705.078
Test container, forward end	-38.56	55.22			
Line attachment ring	-21.07	68.23			
Splice band	-7.06	69.49			
Attachment pin	-4.96	67.59			
Miscellaneous	-0.73	63.01			
Test item jettison	1819.47	132.34	51,119	1,347,682	1,348,314
Ballast separation ring	-8.28	83.84			
Forward probe tube assembly	-8.88	170.61			
Nose ballast	-1228.70	147.61			
Tube ballast	-164.70	108.88			
Bolts	-1.88	69.90			
Ballast jettison	407.03	96.20	13,816	240,989	241,621
Door assembly	-3.84	97.75			
Recovery parachute and bag	-31.12	98.01			
Instrument package at impact	372.07	96.03	12,393	239,293	239,925

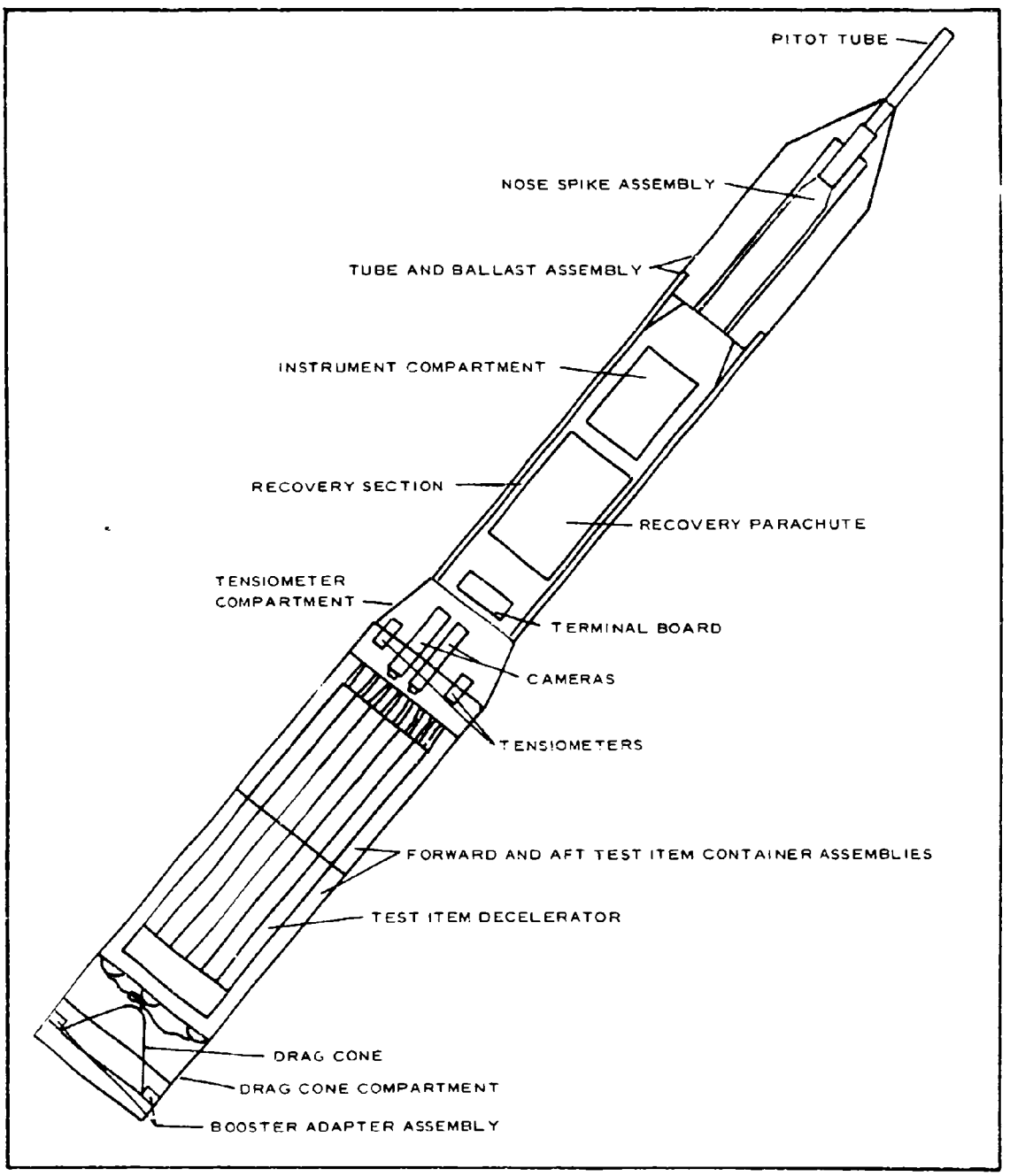

Figure 7 - Vehicle "A" Component Locations

provides f-m telemetry of the parameters given in Tables 3 and 4. Additional vehicle description is given in References 5 and 7.

Although not demonstrated during Phase I, the Vehicle "A," carrying a test item weighing 110 lb, is capable of reaching a series of test points with each system configuration. These capabilities, defined for the payload specified in terms of Mach number and altitude, are shown in Figure 8 for each designated combination. Figure 8 also indicates the loading conditions in terms of the dynamic-pressure isobars.

In addition to the airdrop capabilities, the following launch capabilities at a 40-deg boost-launch angle are possible for each configuration:

Nike-Nike - Vehicle "A"

$$1.1 \leqq \text{Mach} \leqq 2.0$$

$$8 \times 10^3 \leqq \text{altitude (ft)} \leqq 16 \times 10^3$$

Honest John - Vehicle "A"

$$1.1 \leqq \text{Mach} \leqq 1.9$$

$$8 \times 10^3 \leqq \text{altitude (ft)} \leqq 18 \times 10^3$$

2. VEHICLE/BOOSTER SYSTEM "B/C"

a. Requirements

(1) Test Objective

The basic goals in the evaluation program were to advance the state of the art in the direction of small supersonic parachutes and balloon-type hypersonic decelerator BALLUTEs. The ultimate capability desired for the parachutes was defined as Mach 5 at 80,000 ft minimum for a nominal parachute diameter of 2 ft minimum. By definition,[1] this test regime is accommodated by water-recovery vehicle "B," weighing (nominally) 541 lb.

The ultimate capability desired for BALLUTEs was defined as Mach 10 at 225,000 ft minimum for a nominal BALLUTE diameter of 5 ft minimum. This

TABLE 3 - TELEMETRY CHANNELS, VEHICLE "A"

Item	IRIG channel	Center frequency (kc)	VCO input (mv)
(Not used)	11	7.35	0 to 20
Static pressure	12	10.5	0 to 20
Differential pressure	13	14.5	0 to 20
Commutated data (PAM) (see Table 5)	14	22.0	0 to 20
Acceleration	15	30.0	-20 to +20
Drag	16	40.0	0 to 20
Shock	18	70.0	0 to 20

TABLE 4 - COMMUTATED DATA, VEHICLE "A" (IRIG CHANNEL 14, CENTER FREQUENCY 22.0 KC)

PAM segment	Data
1	Zero reference
2	Voltage monitor, Sequence A (28 v)
3	5 mv reference
4	Voltage monitor, Sequence B (28 v)
5	5 mv reference
6	Current monitor, Sequence A
7	5 mv reference
8	Current monitor, Sequence B
9	Timer running monitor, Sequence A
10	Timer running monitor, Sequence B
11	28-v, d-c, monitor (TM)
12	Event marker, final stage separation
13	Event marker, test item deployment
14	Event marker, nose ballast jettison
15	Event marker, test item jettison
16	Event marker, recovery parachute deployment
17	Sync pulse
18	Sync pulse

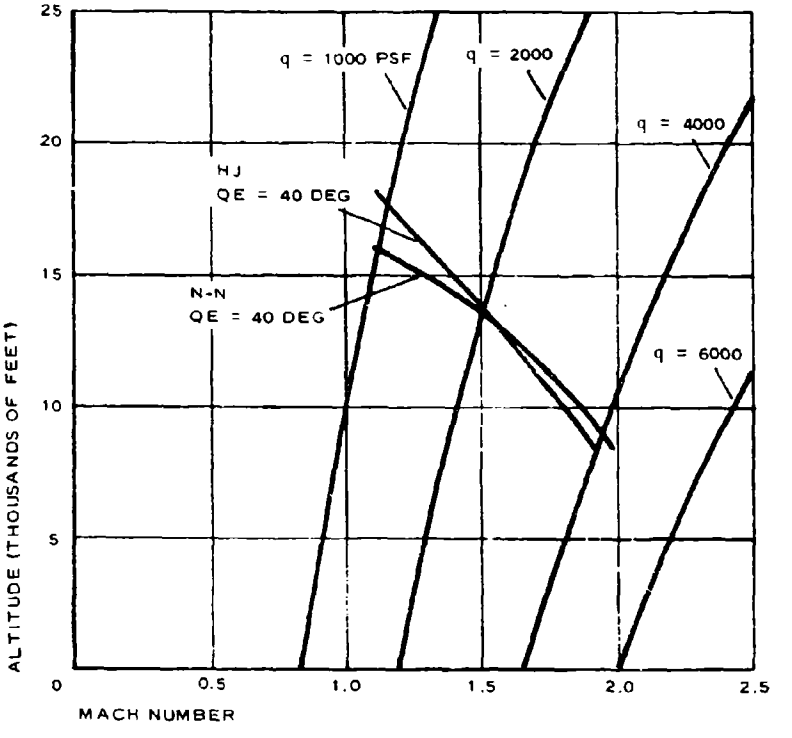

Figure 8 - Vehicle "A" Mission Capabilities

regime is accommodated by water-recovery vehicle "C," weighing 414 lb.

All test points listed in Tables 5 and 6 were determined to be attainable with the 414-lb vehicle designated "B/C." However, the scope of Phase I flight-test performance was limited to test points SP-1, SP-2, and TB-1.

(2) Booster Availability

Proved booster stages and booster hardware were known to be available for all tests listed in Tables 5 and 6.

TABLE 5 - PLANNED TEST POINTS FOR SMALL SUPERSONIC PARACHUTES

Test no.	Booster combination	Payload (lb)	Mach no.	Altitude (10^3 ft)	q (psf)	Site
SP-1*	N-N	414	2.08	74	234	Eglin AFB
SP-2*	HJ-N	414	2.74	60	792	Eglin AFB
SP-3	HJ-N	414	2.50	80	255	Eglin AFB
SP-4	HJ-N-N	414	4.20	80	715	Eglin AFB
SP-5	HJ-N-N	414	3.40	156	20	Eglin AFB
SP-6		Undefined				
SP-7		Undefined				
SP-8		Undefined				

*Flight-tested under Phase I; see Figure 1 for comments.

TABLE 6 - PLANNED TEST POINTS FOR BALLUTES

Test no.	Booster combination	Payload (lb)	Mach no.	Altitude (10^3 ft)	q (psf)	Site
TB-1*	HJ-N	414	2.40	84	200	Eglin AFB
TB-2	HJ-N-N	414	3.80	104	197	Eglin AFB

*Flight-tested under Phase I; see Figure 1 for comments.

Honest John and Nike combinations were appropriately staged for delivery to the above test points. A Castor-Recruit combination was originally considered for a possible hypervelocity test, and the need for consequent thermal protection of the test vehicle was recognized. The fins, interstage adapters and fasteners, and launching tees were selected to be compatible with the developed trajectories, aerodynamic analyses, and control requirements for the system. Requirements for the protection of control surfaces were ensured by aerothermodynamic analysis of the more critical test conditions for each booster combination.

(3) Control

Predicted test trajectories were computed from known booster performances, system aerodynamics, decelerator thermodynamic limitations, and range criteria. Sequencing was achieved by a programmed sequence timer. The sequence schematic is shown in Figure 9. Simplicity in attaining these trajectories without recourse to complicated guidance was effected by the following:

1. Programmed launch angles and coast times in the use of standardized configurations to achieve attainable test points
2. Flightpaths achieved through static and dynamic stability obtained from fin surfaces and fin-generated spin

Because spin was required to nullify system asymmetries during boost, despinning was necessary prior to test decelerator deployment.

(4) Test-Item Deployment

Deployment sequences for small parachutes and BALLUTEs are shown in Figures 10 and 11, respectively. The maximum forces applied to the vehicle were retained below 100 g by the controlled deployment sequence and the shock-absorbing qualities of the nylon riser and suspension lines.

(5) Data Requirements

To provide the necessary data for subsequent decelerator analysis and

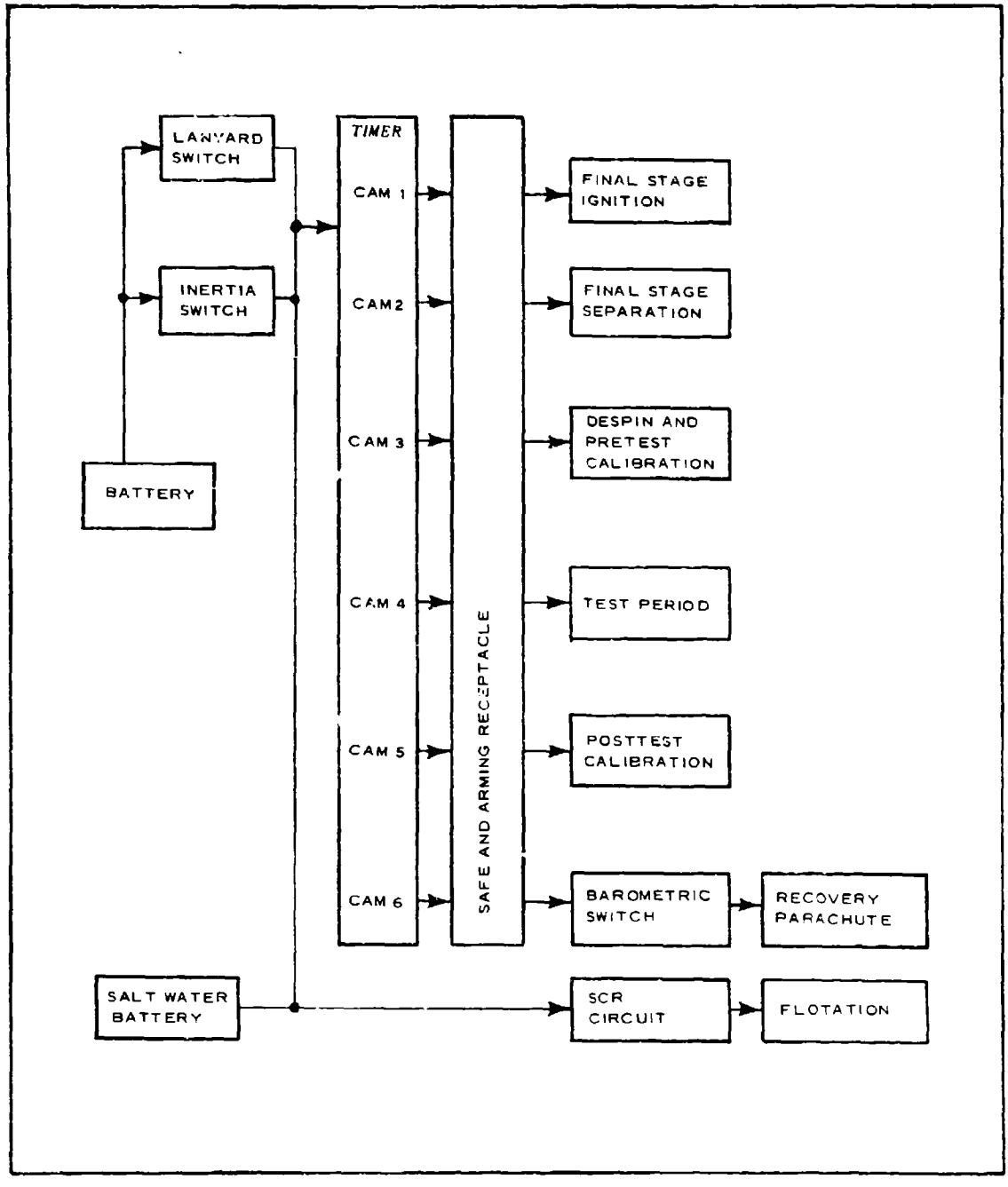

Figure 9 - Sequence Schematic, Vehicle "B/C"

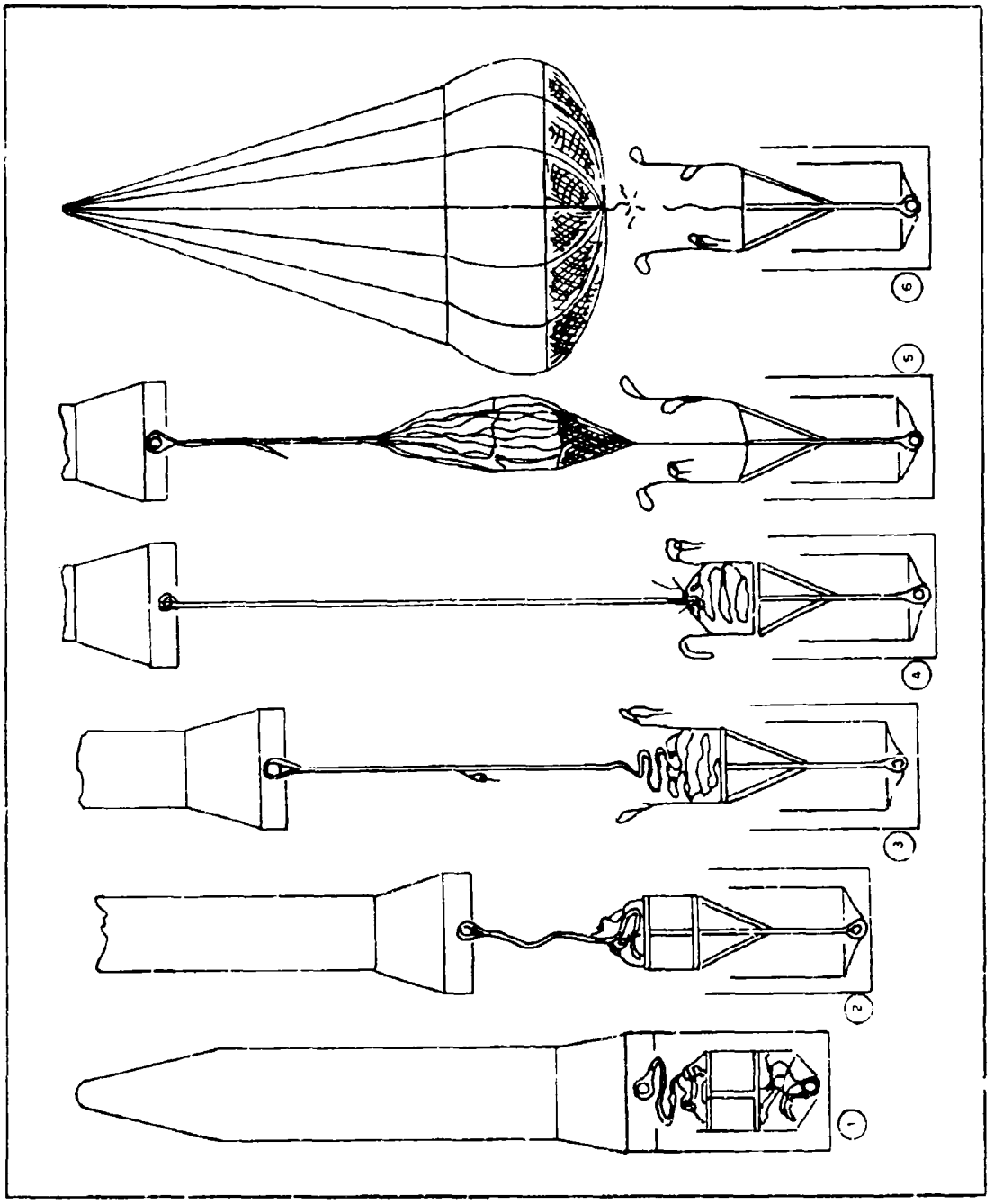

Figure 10 - Small-Parachute Deployment Sequence

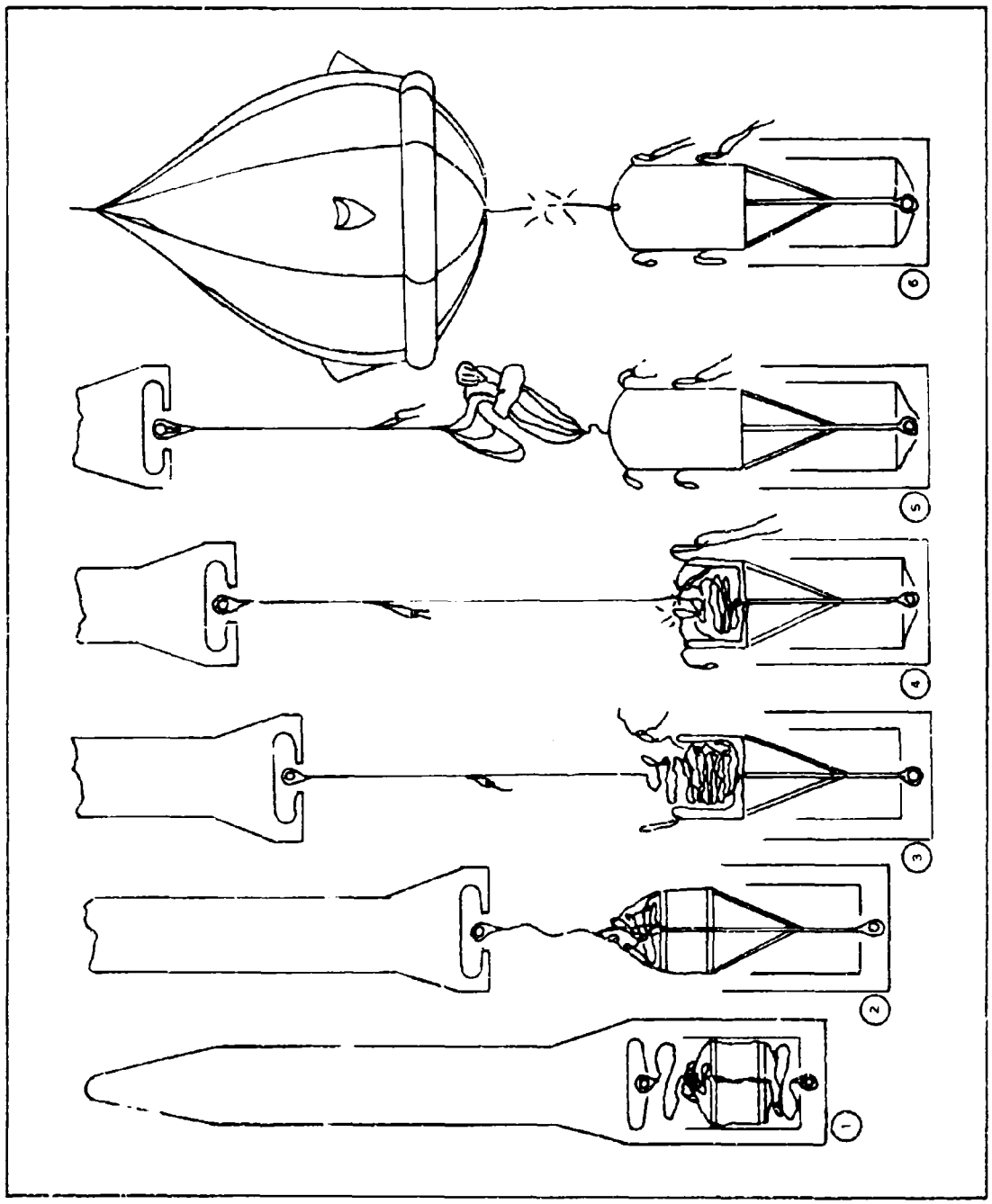

Figure 11 - BALLUTE Deployment Sequence

correlation, several sources of data acquisition were required. The GFE data-acquisition systems consisted of telemetry, skin tracking, beacon tracking, and phototheodolite facilities. The vehicle had two high-speed cameras to record decelerator deployment and performance. Via telemetry, the vehicle force, temperature, and pressure data were recorded. Ground-based radar and theodolites provided position information. Figure 12 shows the data-acquisition schematic.

(6) Recovery

To retain the decelerator with the recoverable vehicle, a pivoting arm is used to displace the test item from the vehicle axis. Upon immersion of the water-landing vehicle, a flotation bag inflates. Figure 13 shows the flight profile with a BALLUTE as the decelerator.

b. Characteristics

Figure 14 shows vehicle/booster configurations for System "B/C." Computer analyses predicted that the booster combinations were feasible from all

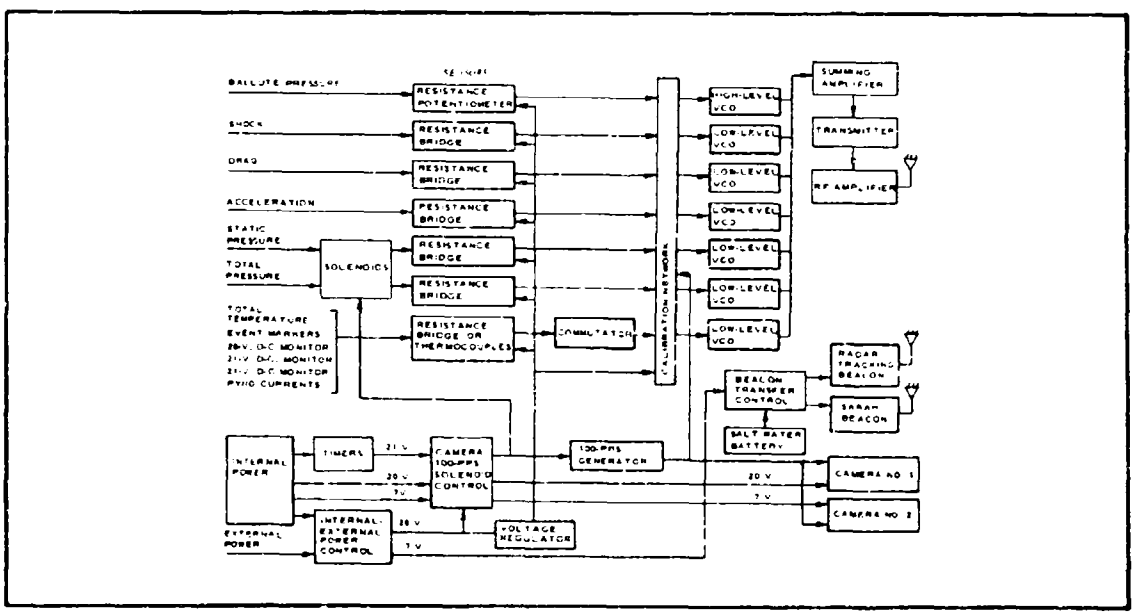

Figure 12 - Block Diagram of Vehicle "B/C" Data-Acquisition System

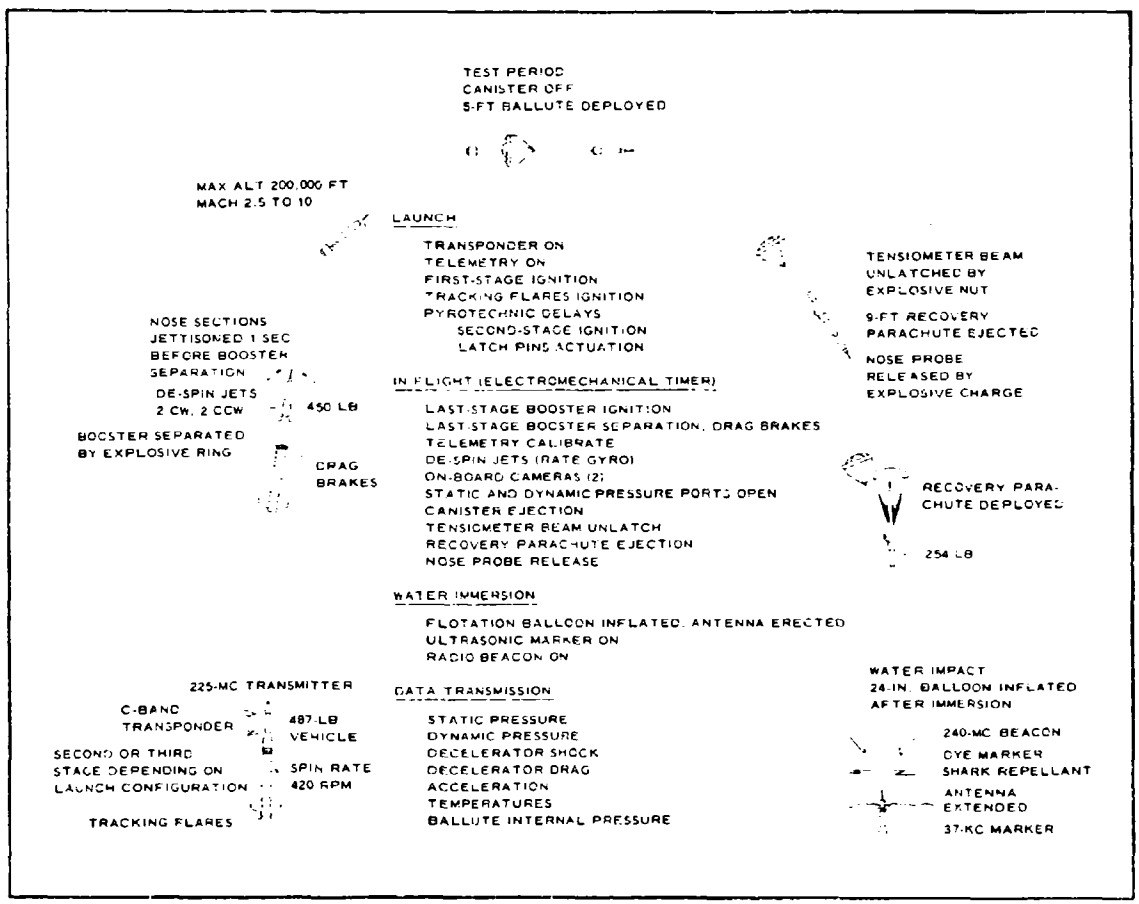

Figure 13 - Typical Vehicle "B/C" Flight-Test Profile

standpoints (performance, stability, and structural integrity) for meeting the test objectives. The weight breakdowns by flight sequence are given in Table 7 for Vehicle "B/C" and in Table 8 for System "B/C." Figure 15 shows the component locations. Information generated during changes in the design, development, and utilization of Vehicle "B/C" is given in Section 3 of Reference 6.

c. Mission Capabilities

Vehicle "B/C," with a minimum total launch weight of about 487 lb, is the

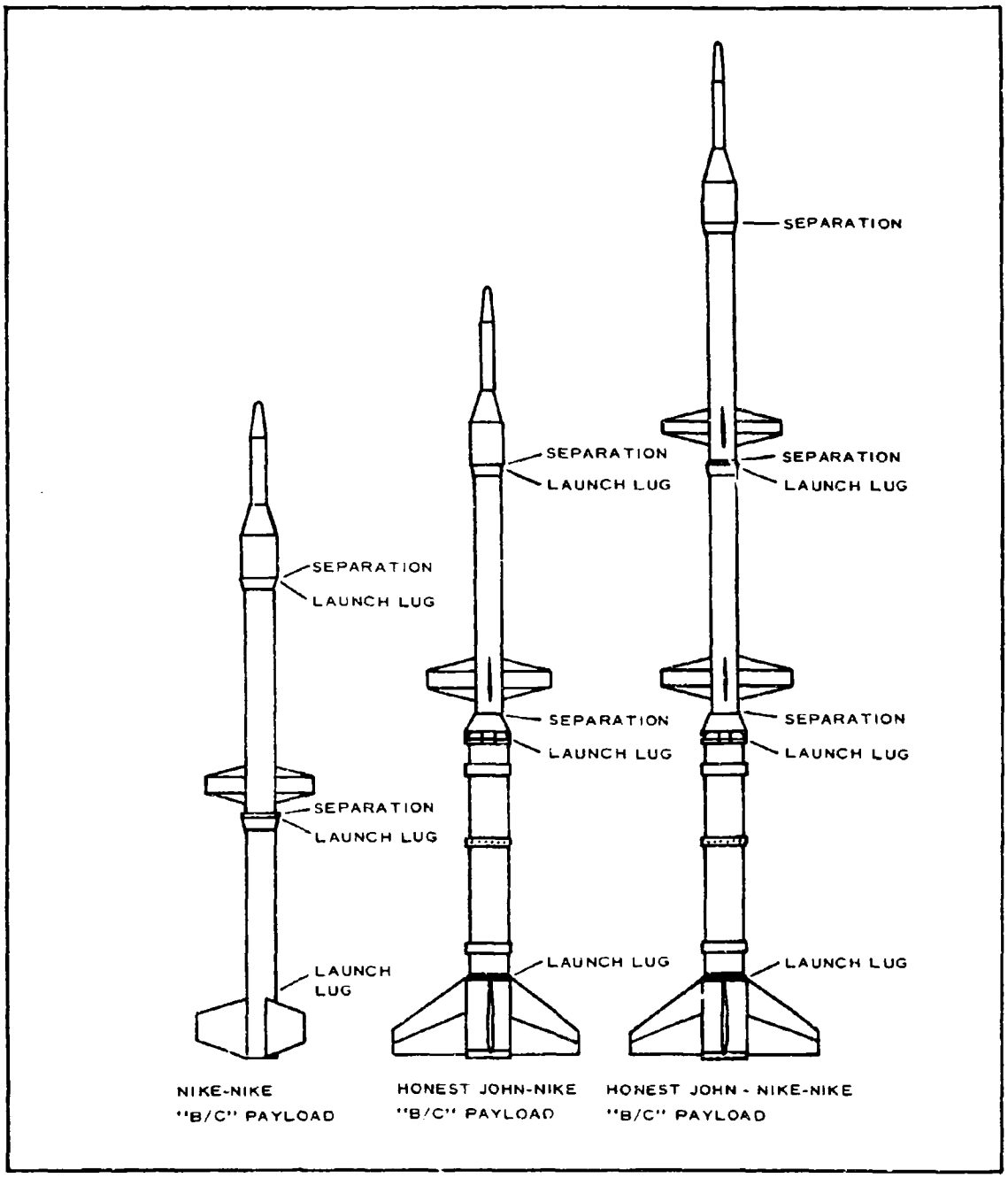

Figure 14 - Vehicle "B/C" Booster Combinations

TABLE 7 - VEHICLE "B/C" WEIGHT, CENTER OF GRAVITY, AND MOMENT OF INERTIA

Item	Weight (lb)	Center of gravity from 0.00 (in.)	Moment of inertia (lb-in.^{2})		
			I_o (roll)	I_o (pitch)	I_o (yaw)
Total at launch	487.15	46.73	13,843	410,732	410,805
Adapter ring	-13.62	-2.00			
Deceleration brake	-27.98	3.43			
Booster separation	445.55	50.94	11,016	314,355	314,428
N_2 despin system	-1.00	50.84			
Despin system activated	445.55	50.94	11,004	312,384	312,457
Test container	-40.25	14.36			
Test item	-25.00	14.74			
Test decelerator deployed	379.30	57.21	8,350	209,092	209,165
Recovery parachute and cover	-7.98	34.44			
Recovery parachute deployed	371.32	57.70	8,295	204,731	204,823
Spike assembly	28.87	92.98			
Spike retainer	-15.20	88.07			
Forward fairing bulkhead	-27.00	86.51			
Rear fairing bulkhead	-16.80	79.69			
Bulkhead standoff	-5.04	82.98			
Miscellaneous	-2.60	83.13			
Frangible skin	-12.00	76.59			
Ablation skin	-1.96	75.67			
Ablation closure	-1.53	71.73			
Pressure-probe assembly released	260.32	45.78	6,866	75,241	75,333
Balloon canister	-5.60				
Surface recovery	254.72	45.12	6,742	69,998	70,090

TABLE 8 - SYSTEM "B/C" WEIGHT BREAKDOWN

Booster and payload	Weight (lb)
Honest John - Nike-Nike-Vehicle "B/C"	
Stage 1	
Honest John case	1860
Honest John propellant	2050
Fin-shroud	260
Forward adapter	40
Stage 2	
Nike case	460
Nike propellant	740
Fin-shroud assembly (2-3/4 sq ft)	91
Forward adapter	25
Stage 3	
Nike case	460
Nike propellant	740
Fin-shroud assembly (2-1/2 sq ft)	86
Vehicle	487
Weight vs event	
First-stage ignition	7299
First-stage burnout	5249
Second-stage ignition	3089
Second-stage burnout	2349
Third-stage ignition	1773
Third-stage burnout	1033
Honest John-Nike-Vehicle "B/C"	
Stage 1	
Honest John case	1860
Honest John propellant	2050
Fin-shroud	260
Forward adapter	40

Third-stage burnout	1033
Honest John-Nike-Vehicle "B/C"	
Stage 1	
Honest John case	1860
Honest John propellant	2050
Fin-shroud	260
Forward adapter	40
Stage 2	
Nike case	460
Nike propellant	740
Fin-shroud assembly (2-1/2 sq ft)	86
Vehicle	487
Weight vs event	
First-stage ignition	5983
First-stage burnout	3933
Second-stage ignition	1773
Second-stage burnout	1033
Nike-Nike-Vehicle "B/C" Payload	
Stage 1	
Nike case	460
Nike propellant	740
Fin-shroud	125
Forward adapter	25
Stage 2	
Nike case	460
Nike propellant	740
Fin-shroud assembly (2 sq ft)	84
Vehicle	487
Weight vs event	
First-stage ignition	3121
First-stage burnout	2381
Second-stage ignition	1771
Second-stage burnout	1031

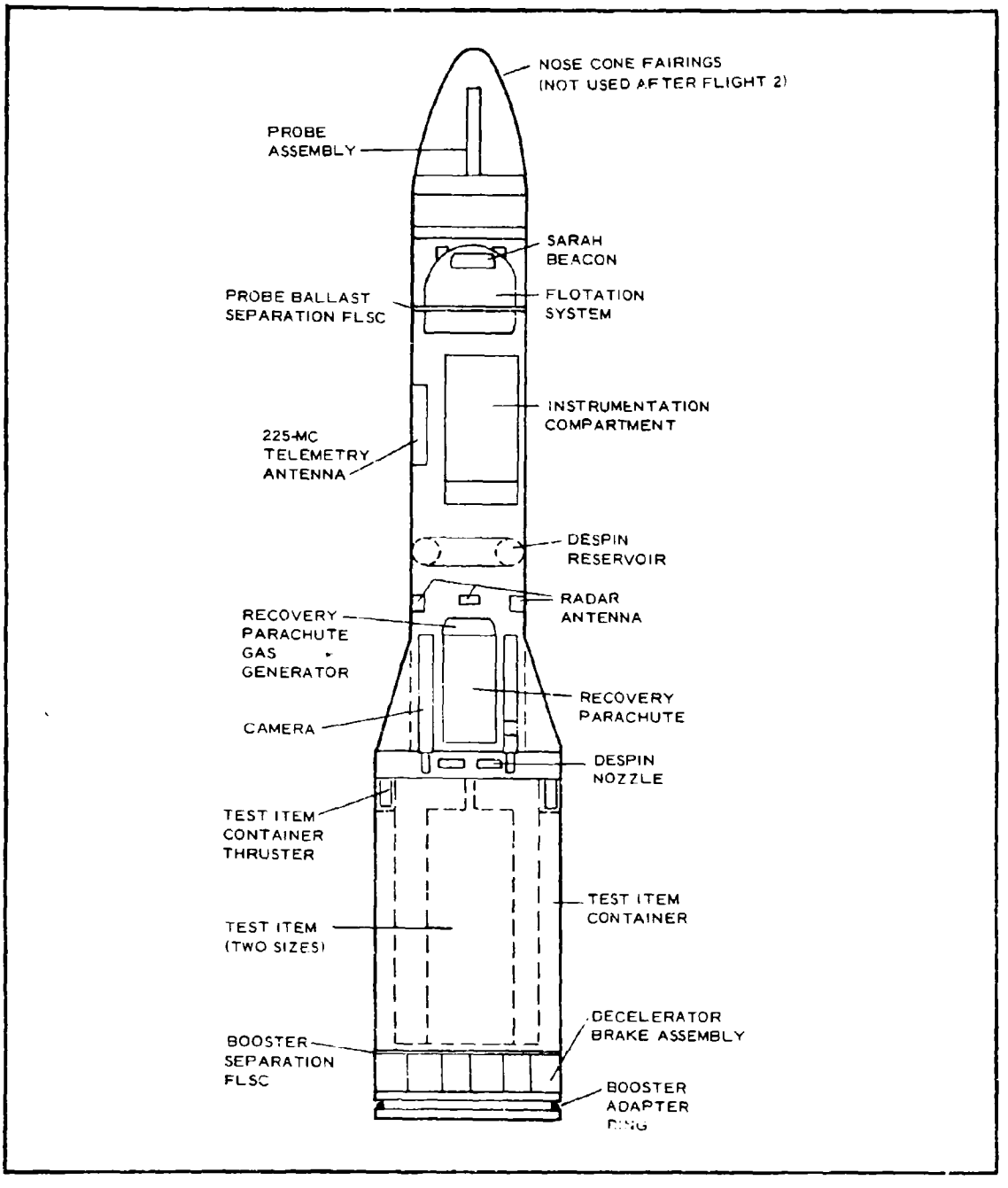

Figure 15 - Vehicle "B/C" Component Locations

payload-instrumentation-carrying missile for the flight tests of small supersonic parachutes and BALLUTEs. It is a ballistic-type missile boosted by the three combinations of standard rockets (Nike, Honest John) to attain the desired test points The vehicle has a test decelerator capacity of 1.3 cu ft and is water-recoverable by means of a flotation device. The vehicle system provides f-m telemetry of the measured parameters given in Tables 9 and 10. Additional vehicle description is found in References 5 and 7.

TABLE 9 - TELEMETRY CHANNELS, VEHICLE "B/C"

Data	IRIG channel	Center frequency (kc)	VCO input (mv)
BALLUTE pressure	11	7.35	0 to 20
Static pressure	12	10.5	0 to 20
Differential pressure	13	14.5	0 to 20
Commutated data (PAM) (see Table 10)	14	22	0 to 20
Acceleration	15	30	-20 to +20
Drag	16	40	0 to 20
Shock	18	70	0 to 20

Figure 16 defines the mission capabilities of this vehicle for the specified payload, in terms of Mach numbers and altitudes for each booster-rocket combination designated. It also indicates the loading conditions in terms of the dynamic-pressure isobars.

The following mission capabilities within 80 deg $< \gamma <$ 88 deg launch angles are possible for each configuration:

Nike-Nike - Vehicle "B/C"

$$0.3 \leqq \text{Mach} \leqq 2.2$$

$$46 \times 10^3 \leqq \text{altitude (ft)} \leqq 85 \times 10^3$$

TABLE 10 - COMMUTATED DATA, VEHICLE "B/C" (IRIG CHANNEL 14, CENTER FREQUENCY 22.0 KC)

PAM segment	Data
1	Zero reference
2	Voltage monitor, Sequence A
3	Nose temperature
4	Voltage monitor, Sequence B
5	Nose temperature
6	Current-pulse monitor, Sequence A
7	Nose temperature
8	Current-pulse monitor, Sequence B
9	Timer-position monitor, Sequence A
10	Timer-position monitor, Sequence B
11	28-v, dc, monitor (TM)
12	Booster separation-event marker and test-item container away
13	Test-item deployment signal
14	Booster away and flotation signal
15	Nose-probe separation and test-item thrusters
16	Recovery parachute
17	Synco pulse
18	Sync pulse

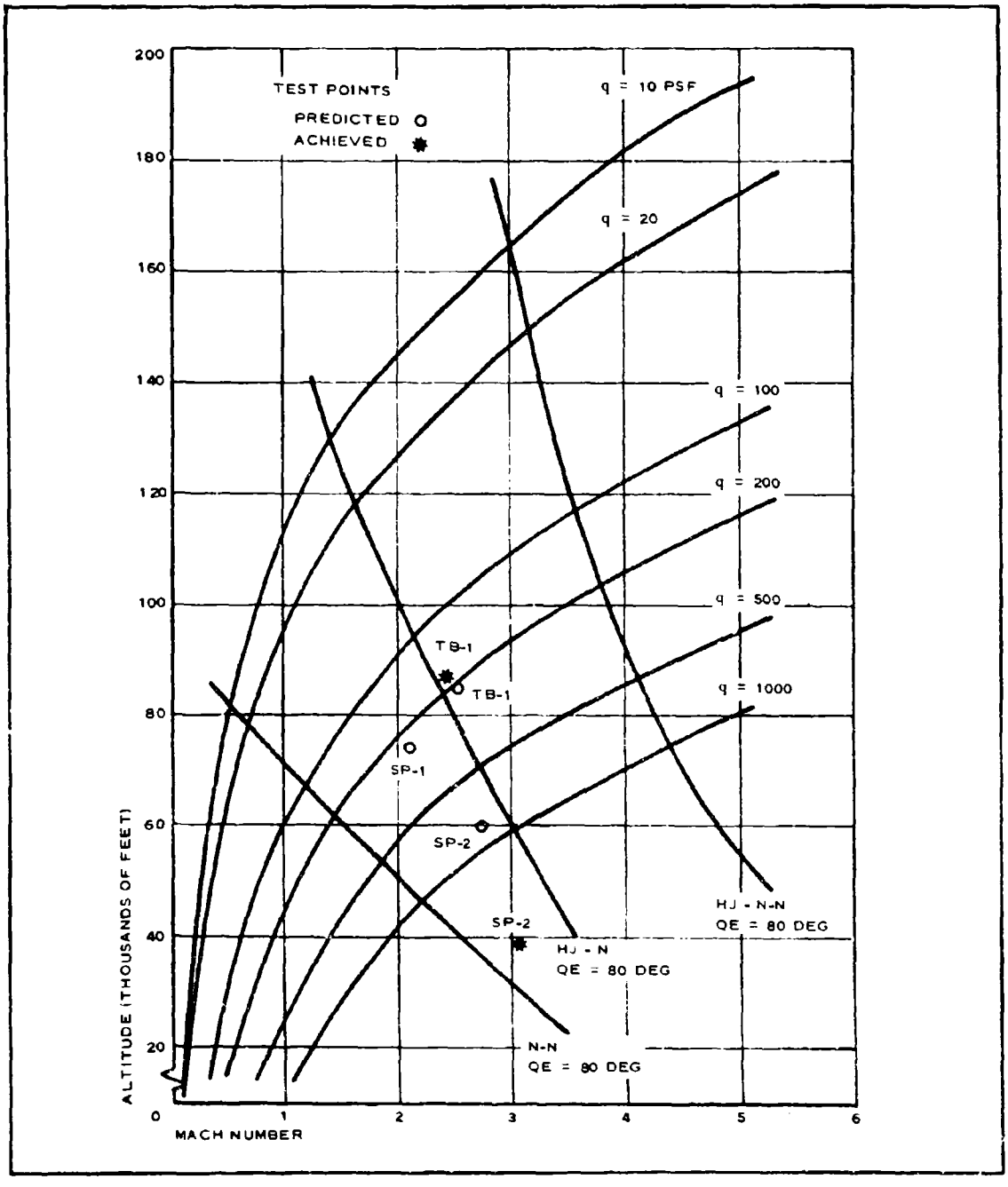

Figure 16 - Vehicle "B/C" Mission Capabilities

Honest John-Nike - Vehicle "B/C"

$$1.4 \leqq \text{Mach} \leqq 3.3$$

$$48 \times 10^3 \leqq \text{altitude (ft)} \leqq 130 \times 10^3$$

Honest John-Nike-Nike - Vehicle "B/C"

$$3.0 \leqq \text{Mach} \leqq 4.4$$

$$75 \times 10^3 \leqq \text{altitude (ft)} \leqq 166 \times 10^3$$

d. Evaluation

(1) Performance

(a) Test Points

The System "B/C" performance relative to test points, stability, and predictability has been evaluated for flights using either Nike-Nike or Honest John-Nike booster combinations. A concise comparison of test-point performances during Phase I is given in Table 11 and in Figure 16.

(b) Stability

The following flight tests performed during Phase I indicated stable performance of the booster/vehicle combinations.

1. Test SP-1 - Second-stage Nike remained with the vehicle from launch to impact. Phototheodolite indicated booster/vehicle combination was stable.
2. Test SP-2 - System was stable up to booster separation. Test-item deployment occurred prematurely at that time, and stability from the time of booster separation to normal test-item deployment could not be substantiated.
3. Test TB-1 - The test-item container never was ejected. There is evidence that satisfactory stability was achieved because the trajectory passed through the test point and the vehicle obtained a maximum altitude exceeding the prelaunch estimate.

TABLE II - SYSTEM "B/C" TEST-POINT PERFORMANCES

Test flight	Condition	Values		Remarks
		Predicted	Actual	
SP-1 with N-N	Mach number	2.08	. . .	Second-stage ignition failure
	Altitude (ft)	74,000	. . .	
	Dynamic pressure (psf)	234	. . .	
	Time (sec)	35.5	. . .	
SP-2 with HJ-N	Mach number	2.74	3.04	Premature test item deployment; test container, rear bulkhead failure
	Altitude (ft)	60,000	39,078	
	Dynamic pressure (psf)	792	2660*	
	Time (sec)	29.5	21	
TB-1 with HJ-N	Mach number	2.47	2.42	No test item deployment; container jammed
	Altitude (ft)	85,000	86,952	
	Dynamic pressure (psf)	195	172	
	Time (sec)	38.5	38.2+	
	Launch elevation (deg)	83	84.4	

*Dynamic pressure calculated, $q = 0.7pM^2$.

+Deployment initiation.

(c) Predictability

It has not been possible to compare three-stage booster flights with predicted trajectories and test points, since three-stage boosters were not employed during Phase I. However, the two-stage booster/vehicle system proved by the TB-1 flight that the performance can be within 5 percent at all planned events. The TB-1 booster/vehicle performance is plotted in Figure 17.

(2) Data

The data obtained during each test were governed by many factors. The factors that contribute to the accuracy and reliability of the data-gathering system are:

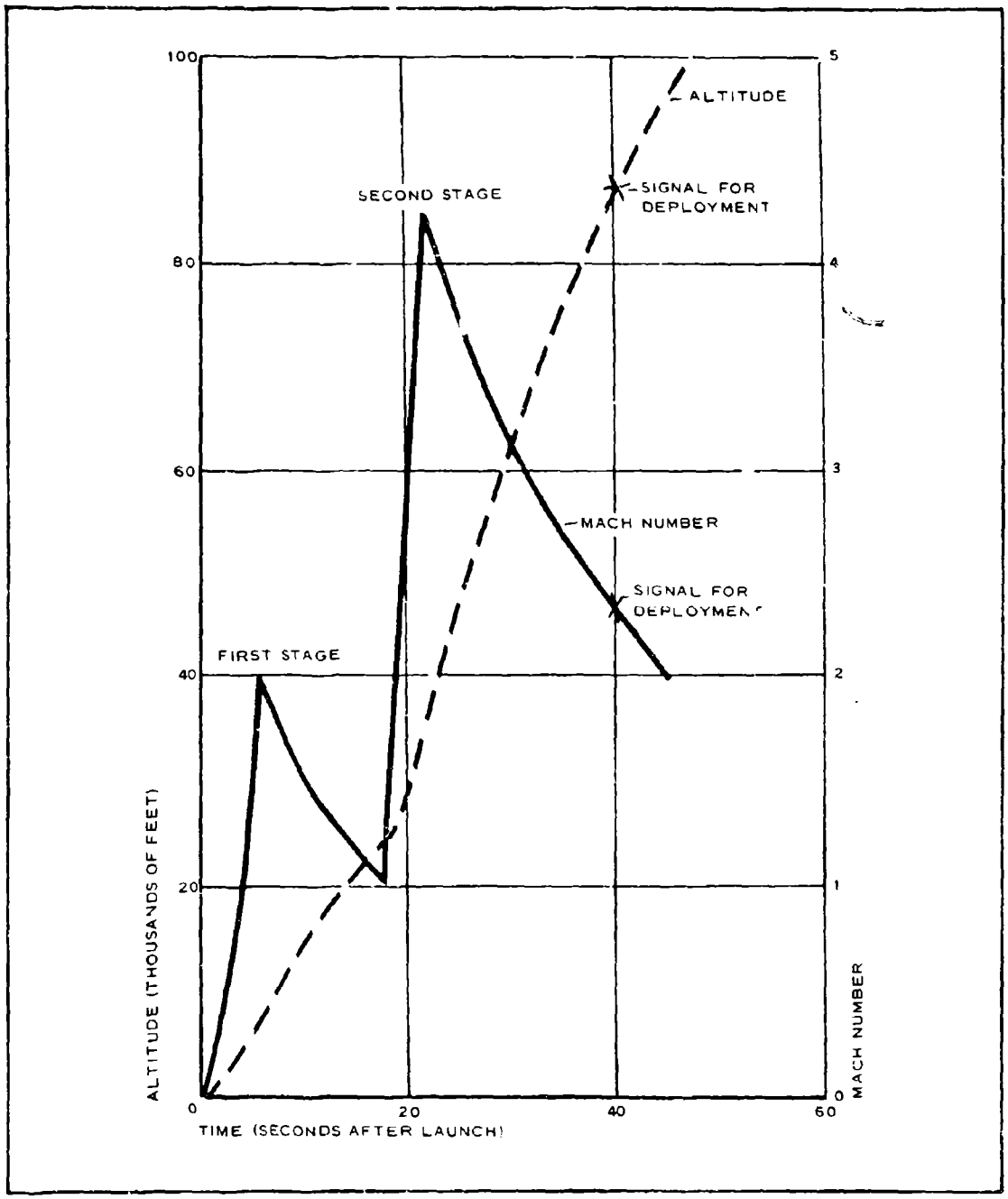

Figure 17 - Actual TB-1 Flight Conditions

- Booster performance
- Vehicle performance
  - Event programming
  - Data acquisition
    - Telemetry transmission
      - Shock
      - Drag
      - Acceleration
      - Pressures
      - Temperatures
    - Radar beacon
    - Cameras
    - Ground stations
      - Telemetry
      - Radar
      - Phototheodolite

Booster performance and ground station performance were satisfactory for all tests performed. Vehicle performance continued to improve throughout Phase I. Each flight was made with the vehicle in a different condition, and no flight was 100 percent successful. Valuable data on vehicle performance were provided by telemetry. The operation of the telemetry system was proved successful by these tests.

(3) Ground Support

The GAC field-test crew consisted of three engineers and two technicians. In addition, a pyrotechnics engineer was assigned part time. Basically, their responsibilities were as follows:

Project engineer - program management

Assistant project engineer - data and facility support, coordination, and contract administration

Instrumentation engineer - onboard data acquisition

Development engineer - vehicle systems and assembly

Electronics technician - assistance for instrumentation

Electrical technician - assistance for development

Pyrotechnics engineer - loading and assembly for explosive devices

Aerodynamics, telemetry, interstage buildup, documentation, and other required data were furnished to the APGC facilities by the field crew.

During the prelaunch and launch periods, close coordination was required between GAC and APGC. The APGC vertical-probe group was responsible for launcher preparation, launch programmer, interstage and rocket-booster buildup, and generating dispersion studies.

The APGC radar tracked the vehicle. The narrow C-band radar coupled with the broadband Agave provided a substantial amount of vehicle and decelerator performance data; phototheodolite coverage provided the most useful low-altitude data. APGC reduced the radar and theodolite data. In addition, APGC provided several telemetry receiving stations, reduced these data, and digitized and converted the information to engineering standards.

Data acquired by APGC and GAC ground-support personnel during this program were one of critical efforts in achieving the development of an operational test vehicle.

SECTION III - SMALL SUPERSONIC PARACHUTE

1. GENERAL

a. History

Wind-tunnel and free-flight tests previously had indicated that a truncated cone-type parachute held promise at supersonic speeds at low ratios of decelerator size to payload size.[3,4] Wind-tunnel tests of small models indicated that reasonable inflation and attitude stability could be attained with a fine-mesh roof material. Because of the limited temperature capability of this material, free-flight tests with it were limited to approximately Mach 2.1. Ribbon roofs of Nomex materials were tested at higher Mach numbers and with considerably degraded performance. Therefore, one of the first efforts under ADDPEP was to develop a Nomex mesh material and associated coatings for flight tests from Mach 2.1 to 4.

Because only limited engineering data were available at the start of the small-parachute efforts, two concurrent tasks to obtain engineering data were conducted. One, undertaken as an in-house program by RTD personnel, provided full-scale wind-tunnel data on past designs and on a newly generated ADDPEP design.[3] These parachutes, which had low- and high-temperature roof mesh materials, were tested over past and contemplated test regimes. The other task, undertaken under ADDPEP, was to establish free-flight data on past designs using old and new materials and analytical methods for designing small supersonic parachutes.

The wind-tunnel tests established the sensitivity of the parachute to the free-stream Mach number and to manufacturing tolerances. They indicated that an effective inlet area-to-exit area ratio approaching the critical for isentropic flow in a convergent rigid inlet is required to ensure full parachute inflation. The inlet area was based on the constructed diameter of the inlet,

and the exit area was based on the open percentage of the roof mesh (based on measurements at 1/2 in. of water) and the roof-mesh area.

ADDPEP initially used prior designs with a Perlon mesh roof for a planned Mach 2.08 test (SP-1) and a Nomex mesh roof for a planned Mach 2.74 test (SP-2). These were the first two free-flight shots for the "B/C" test vehicle. Missile malfunctions prevented successful deployment.

A newly constructed shape for the small parachute was generated, based on the inflated shape of a successful wind-tunnel model and loadings derived by analytical methods. The evolved shape is a composite of the analytical requirements for Mach 2 to 4. The roof material porosity was selected on the basis of isentropic requirements. Three parachutes were designed, and units were built of two of the designs. The designs were designated SP-3, SP-5, and SP-7. Two SP-3 units and one SP-7 unit were constructed. The major differences between SP-3 and SP-7 were the strength of the suspension lines and the porosity of the mesh roofs, which were coated to correspond to the test Mach number requirements.

b. Conditions

The conditions for designing the small parachutes were established by trajectory analysis, based on the estimated drag area in Figure 18. The contributing factors and predicted conditions that define the selected test points at the time of deployment are listed in Table 12 for each flight test considered.

c. Configuration Selection

Two small parachute configurations were investigated during this program, one that followed past practices and a second that was based on the inflated shape of a successful wind-tunnel model and loadings derived by analytical methods. The contructed configuration for SP-1 and SP-2 followed past designs. It was based on the general guidelines established by wind-tunnel tests of small parachute models trailing a simulated payload at Mach numbers from 2.3 to 4.65 (see Reference 4 and by one free-flight test behind a 9-in. missile at Mach 2.1 at 101,200 ft and dynamic pressure of 7.0 psf

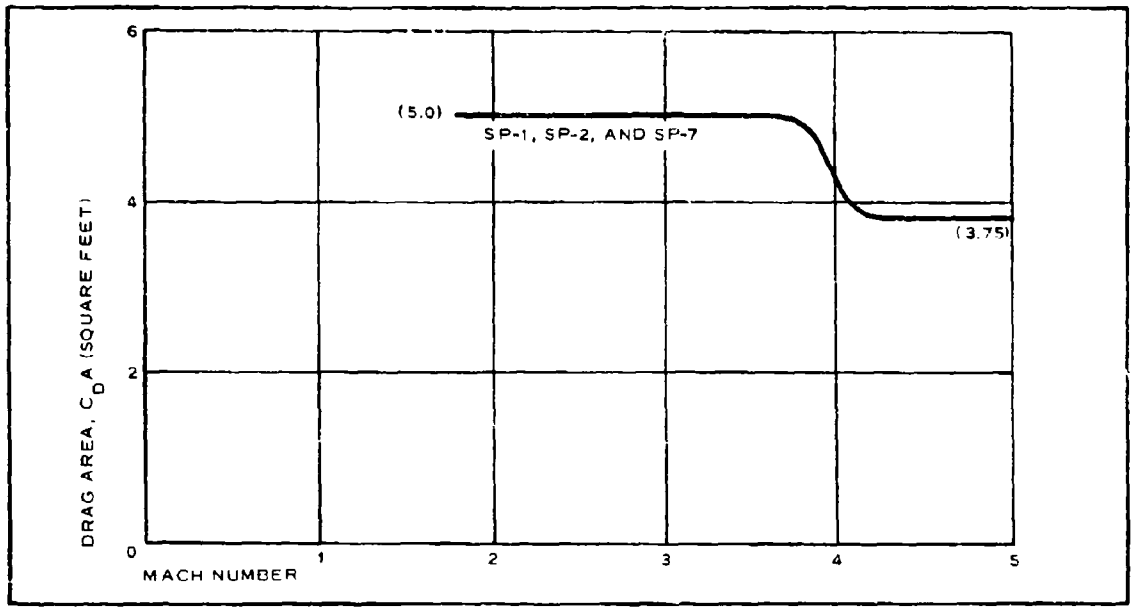

Figure 18 - Estimated Small Parachute Drag Area versus Mach Number

TABLE 12 - SMALL PARACHUTE INITIAL TEST CONDITIONS

Condition	Design configuration				
	SP-1	SP-2	SP-3	SP-5	SP-7
Mach number	2.08	2.74	2.5	3.4	2.74
Altitude (ft)	73,700	60,000	80,000	156,000	60,000
Dynamic pressure (psf)	234	792	255	20.8	792
Ascent flight path angle (deg)	76	77	71	69	77
Total weight (lb)	397	397	397	397	397
Ballistic coefficient of the system, payload plus parachute (psf)	79	79	79	79	79
Reynolds number (based on ℓ = 2.55 ft)	2.0×10^6	5.2×10^6	1.8×10^6	0.07×10^6	5.2×10^6
Booster combinations	N-N	JH-N	HJ-N	HJ-N-N	HJ-N

(see Reference 4). This flight-test model had a 2.71-ft D_o; it used 35-percent porous Perlon mesh for the roof gores and had a total roof porosity of 26 percent. The constructed configuration of SP-1 and SP-2 is shown in Figure 19.

A new configuration was evolved from the inflated coordinates of a stable model, while under test in the Arnold wind tunnel, and from analytical methods. The evolved configuration most nearly meets the shape requirements of an isotensoid design over the Mach 2 to 4 regime for the predicted loadings. The measured coordinates for the wind-tunnel model and the nominal coordinates for the evolved configuration are presented in Figure 20. This shape, known as Composite I, was used for the design of SP-3, SP-5, and SP-7.

d. Example (SP-5)

(1) Conditions

The predicated initial deployment conditions for test item SP-5 are presented in Table 12. The conditions following deployment are presented in Figures 21 through 23.

(2) Configuration

The nominal coordinates of the shape used for design, expressed as ratios of the parachute radius, are presented in Figure 20 as Y/R versus X/R.

2. AERODYNAMICS

a. General

The analysis and design of the small supersonic parachute is based on supersonic diffuser theory. However, certain deviations from this theory are required, since parachutes are not rigid (that is, the geometry changes); furthermore, the presence of the roof with variable porosity distribution and the attitudes the parachutes assume to the flow make them unique for the flow analysis.

The analysis can be divided into the separate phases of deployment, inflation,

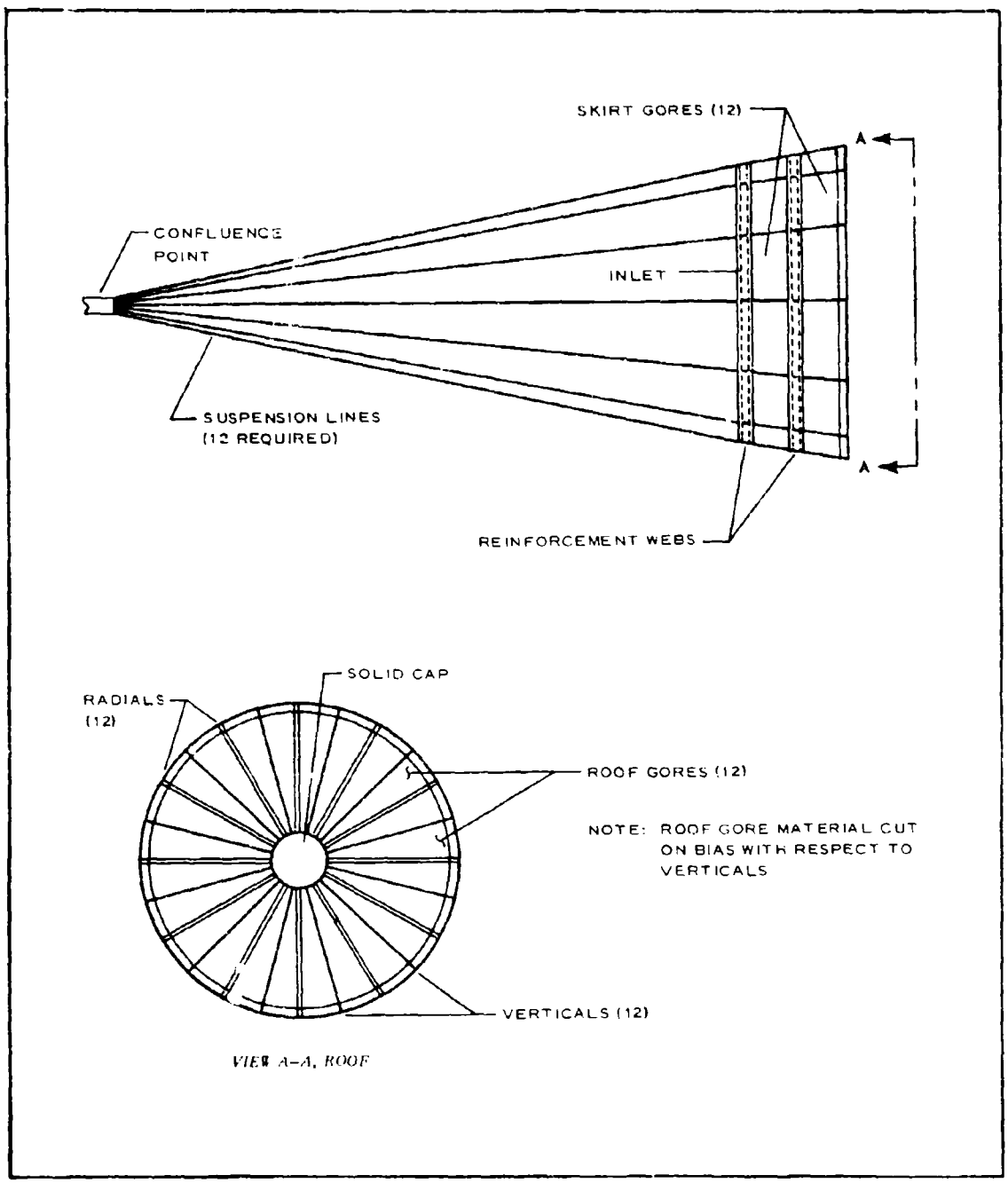

Figure 19 - Small Hyperflo Parachute, Configurations SP-1 and SP-2

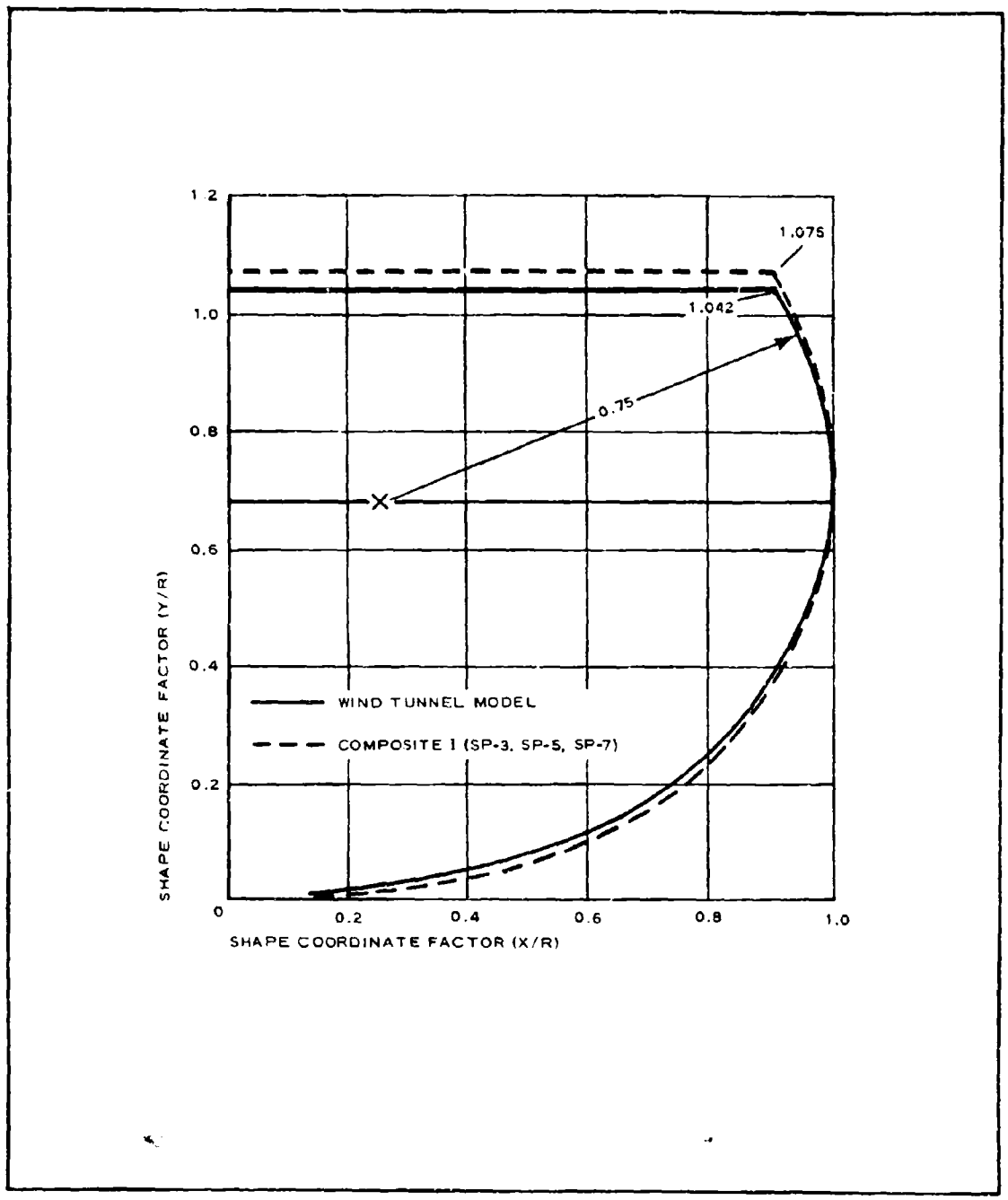

Figure 20 - Inflated Wind-Tunnel Model and Composite I Nominal Coordinates

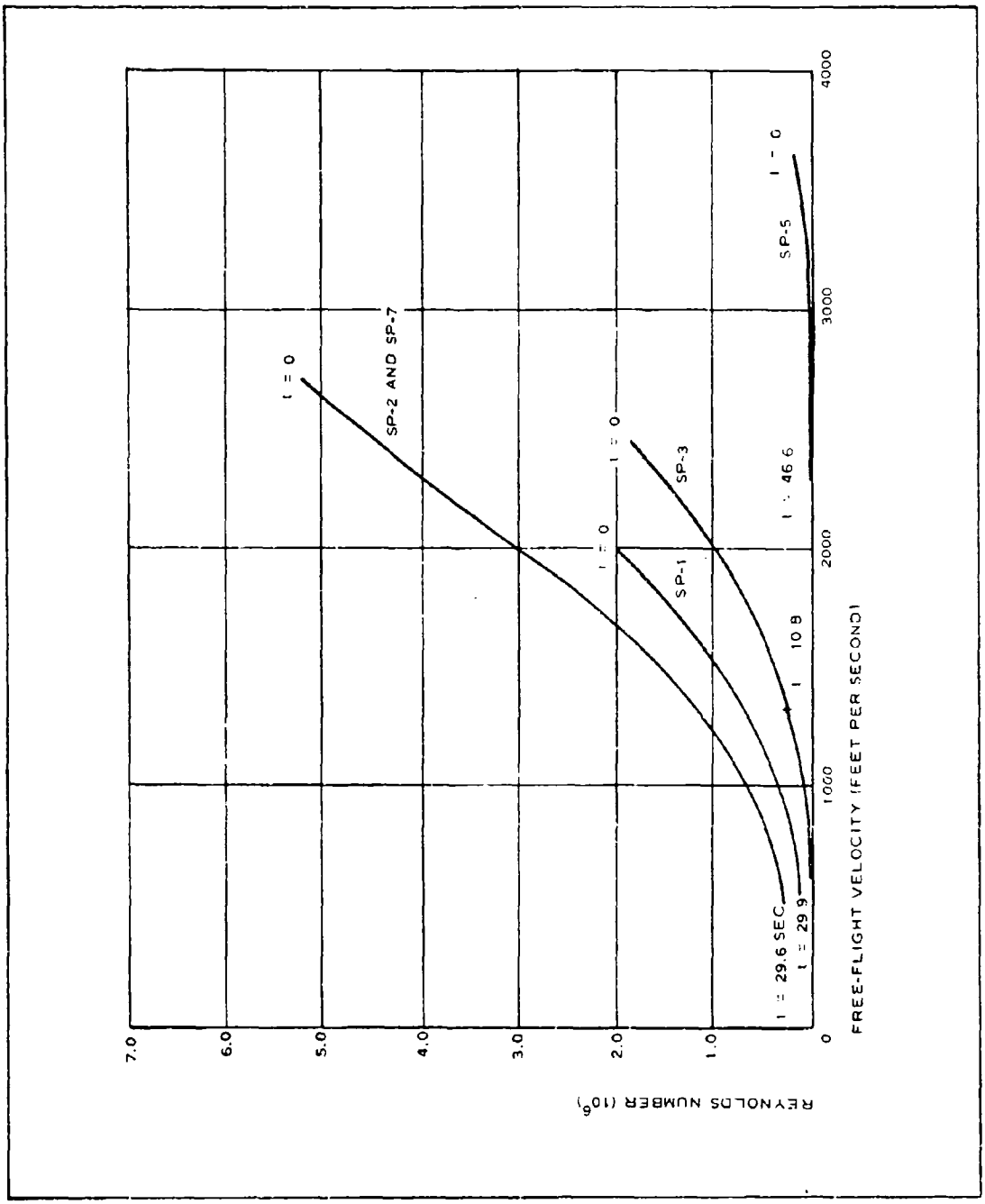

Figure 21 - Reynolds Number versus Free-Flight Velocity (Predicted)

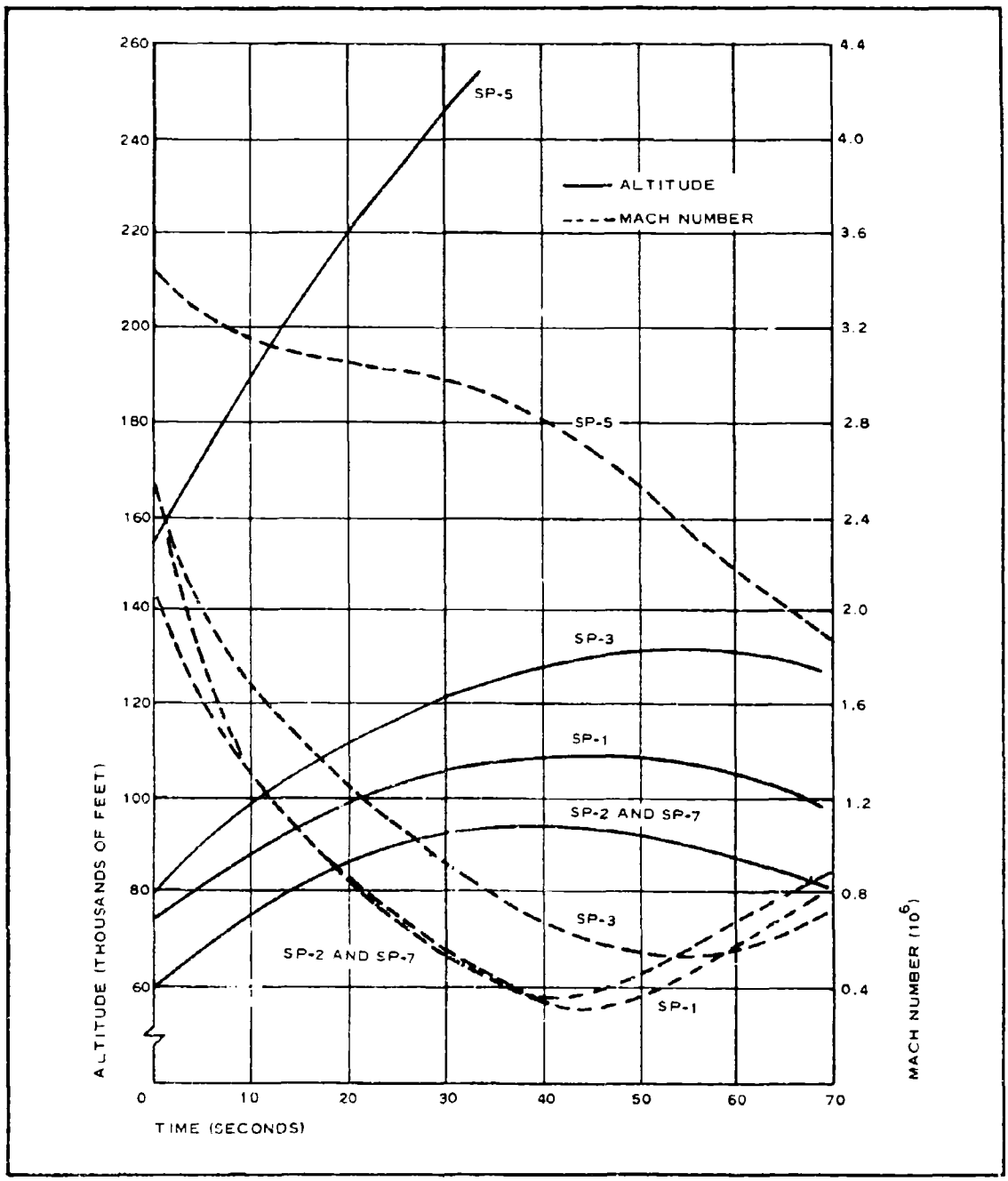

Figure 22 - Mach Number and Altitude versus Time (Predicted)

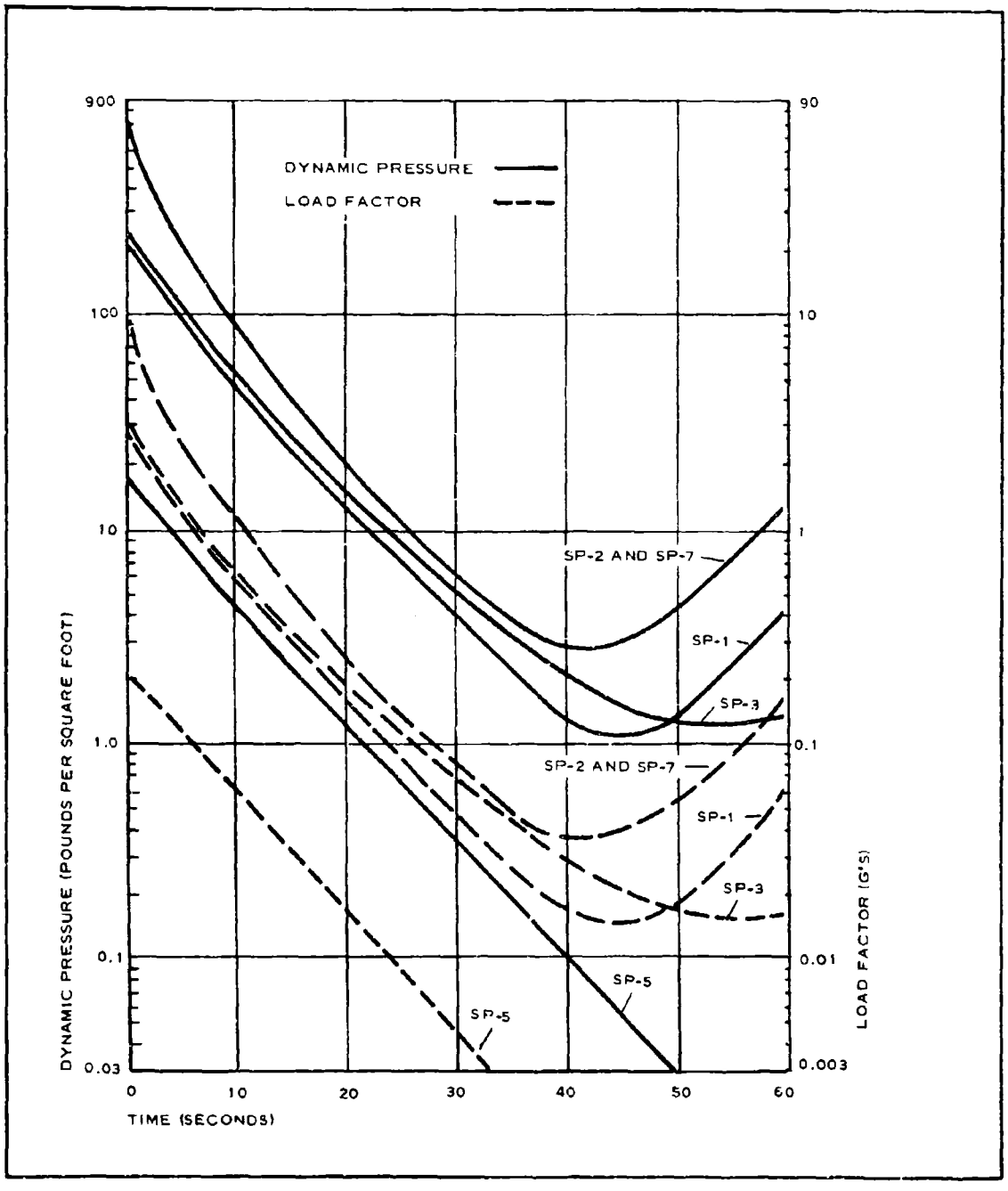

Figure 23 - Load Factor and Dynamic Pressure versus Time (Predicted)

operation, and performance. Each phase has a particular configuration, environment, and associated dynamics. Understanding the processes involved and the ability to predict and, if possible, to control them is the goal of the detailed configuration analysis. The problem essentially consists of the macro and micro environments. Logically, the macro environment should be resolved first since, if the general principles of operation and their evaluation are known, the details will be more obvious.

The success or failure of a parachute in performing properly is inseparable from its environmental conditions, which determine the two major qualitative criteria of a parachute performance - inflation and stability characteristics. Based upon the present state of the art, the following design factors influence the inflation and stability of small supersonic parachutes:

1. Porosity (in the general sense) and its distribution
2. Conical angle of the skirt (stabilization)
3. Length along the canopy (physical dimension)
4. Overall shape

Previous experience[4] indicates that some combinations of the parameters listed above provided the desired positive qualities of strong inlet inflation, good roof inflation, and a large drag force. However, the results were sporadic and no final conclusions were reached Canopy instability about the point of suspension and its center of gravity still was present, indicating a need for an adequate analysis. Insight into the flow field indicates that the problems involved are rather complex and their solution will require an extensive effort.

This effort in parachute analysis and design investigation recognizes the following important areas:

1. Free stream conditions - These are predicted from the trajectory studies.
2. Primary body wake profile - This is considered to be

one of the influencing factors not yet amenable to the rigorous solution. However, velocity and pressure profiles as a function of the distance downstream can be estimated by an approximate analytical empirical method.

3. Parachute shape and the associated shock type - This can be established experimentally or by considering the flow around and through bodies with porosity built into them.

4. Flow parameters (p, T, ρ, M) - These can be evaluated at desired stations for isentropic, steady, one-dimensional, fully developed, compressible flow.

5. Mass flow relations through the inlet and outlet can be used to determine the flow through the canopy.

6. Flow through the porous roof - This can be evaluated by nozzle-flow techniques.

7. Associated pressure loadings for structural design can be determined from the result of the above efforts.

The areas outlined above require extensive effort, using qualified data from previous work and generating new data as needed. The following conclusions were reached from the examination of the previous data.

1. No rigorous analysis technique is available.

2. Insufficient data are available to establish the effect of varying specific parameters (one at a time or in a logical combination) on parachute performance.

3. Data on configurations that performed satisfactorily are presently rather general.

b. Approach

(1) Analytical

Flow analysis of an inflated small supersonic parachute should consist of the following:

1. Flow ahead of an inlet including the wake effect of the payload (that is, modified free-stream conditions at the inlet, with special consideration given to the effect of riser lines on the flow)
2. Shock-wave system at the inlet
3. Conditions behind the shock (critical, supercritical, or subcritical regime of operation)
4. Flow through the skirt
5. Flow through the roof material

The canopy flow field was considered using the following assumptions:

1. A detached shock stands in front of the inlet.
2. The shock is not affected by the riser lines.
3. The flow is sonic at the roof.
4. One-dimensional duct analogy is applicable.

The following statements are in accordance with the gas-dynamics principles and details shown in Figure 24:

1. A_i/A_e controls M_i for choked flow.
2. M_2/M_i controls position of normal shock for choked flow.
3. When $M_2 > M_i$, the shock is detached.
4. As M_1 increases, M_2 will decrease and shock

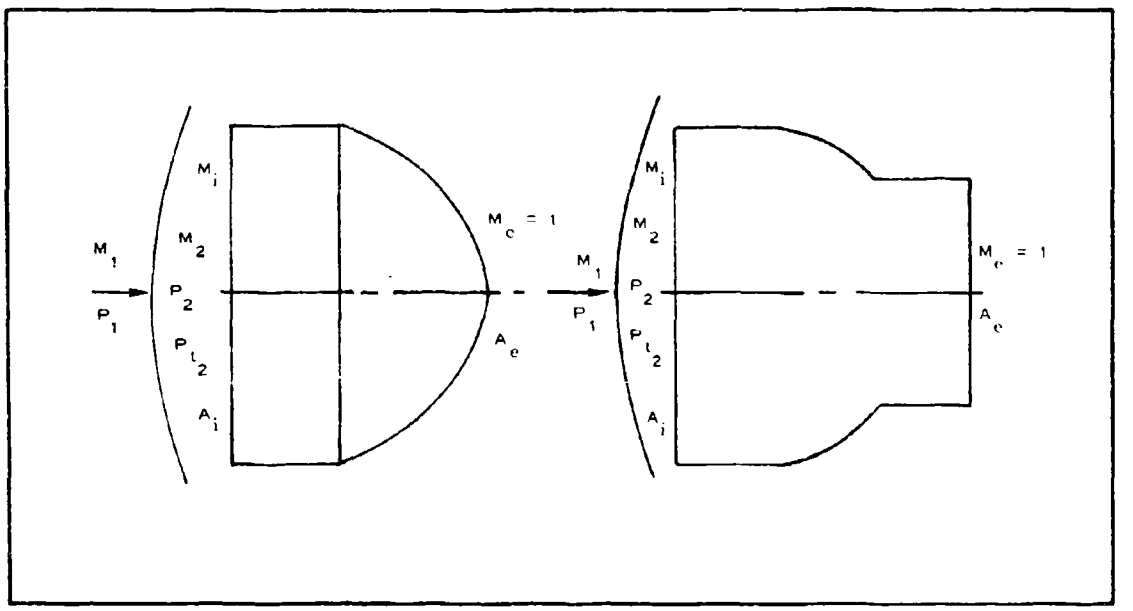

Figure 24 - Canopy Flow Field

will move downstream until $M_2 = M_i$ and the shock is attached.

Although the shock wave assumed ahead of the inlet has a bow shape, the portion of it directly in front of the entrance is essentially a normal shock, and the fluid properties downstream of the shock can be determined by the normal shock relations. The substantiation of the assumption of a detached shock in front of the canopy inlet is based on Reference 6.

The flow around the skirt resembles the flow about a parabolically cambered airfoil. The classical theory of flow for this airfoil indicates the total lift is directed outward and is given by the static derivative presented in Reference 7 as

$$\frac{\partial C_\ell}{\partial\left(\frac{a}{b}\right)} = -2\pi \ ,$$

where

a = camber and

b = cord for linear downwash.

It is also known that this parabolic airfoil forms a shroud or ring airfoil. The pressure on the outside of the ring-type airfoil is given in Reference 8 as

$$C_{p_{ext}} = \frac{2}{\beta}\left[\sigma_{ext} - (\alpha_o + \alpha \sin\theta)\right] \tag{2}$$

and

$$C_{p_{int}} = \frac{2}{\beta}\left[\sigma_{int} - (\alpha_o + \alpha \sin\theta)\right] , \tag{3}$$

where

σ = local slope of skirt surface with respect to cord,

α_o = angle between cord and skirt axis,

α = angle of attack,

β = Mach parameter, and

θ = cylindrical coordinate.

For a symmetric parabolic airfoil,

$$\sigma_{ext} = \frac{a}{b} ;$$

then

$$C_{p_{ext}} = \frac{2}{\beta}\left[\frac{a}{b} - (\alpha_o + \alpha \sin\theta)\right] . \tag{4}$$

For $\alpha = 0$,

$$C_{p_{ext}} = \frac{2}{\beta}\left(\frac{a}{b} - \alpha_o\right) . \tag{5}$$

The applicable range for the external pressure coefficient on the skirt is shown in Figure 25.

The flow through the roof is physically analogous to flow in the throats of a multinozzle grid.[9]

Calculation of the air loads is based upon the canopy geometry and the free-stream conditions. If one-dimensional diffuser analogy is applied, and normal shock relationships in front of the inlet are assumed, the pressures in the canopy can be determined readily.

The pressure in the mesh openings can be estimated assuming sonic flow. The pressure on the outside of the closed roof sections is essentially base pressure. The pressure on the outside of the skirt is estimated by using the ring-airfoil analogy and is given in Figure 25 as the C_p versus the Mach number. The procedure defines airloads on the parachute canopy for the isotensoid stress analysis.

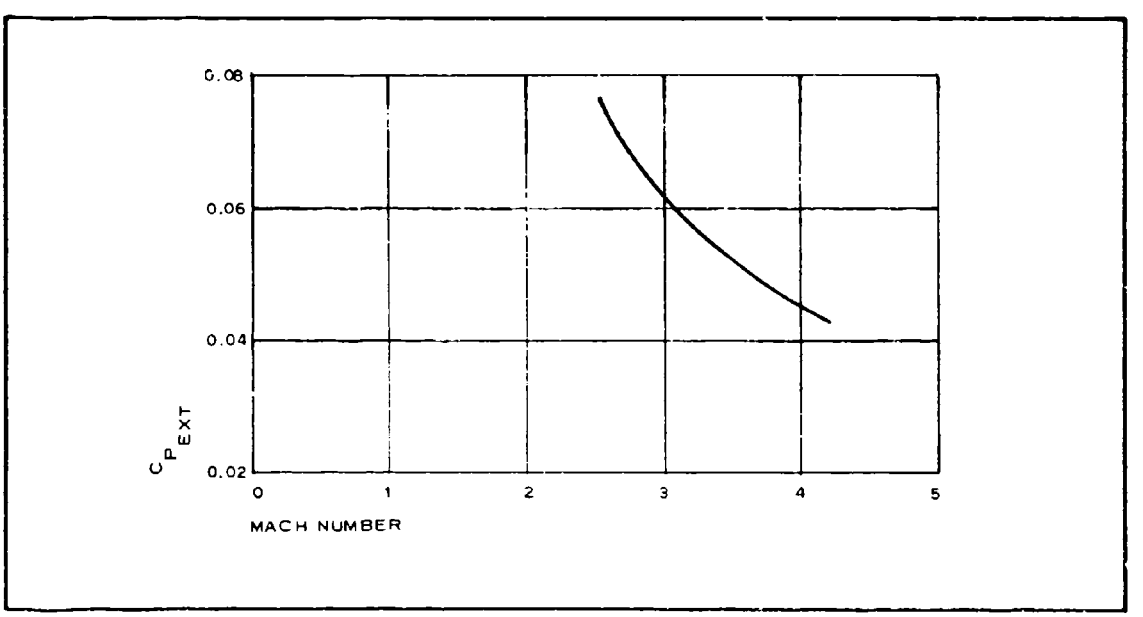

Figure 25 - External-Pressure Coefficient for Supersonic-Parachute Skirt

(2) Empirical

References 4, 10, 11, 12, and 13 document the results of the wind-tunnel tets using small models of supersonic parachutes. Reference 3 presents the results of tests using full-scale supersonic parachutes.

The results of the small model tests[4] indicated that, of the units tested, a canopy with a low conical angle and an extended skirt had the best directional stability while preserving strong inflation characteristics. This configuration had a ratio of contructed inlet to constructed maximum diameter of 0.9 with the roof starting at the maximum diameter. Flat-roof construction was found to provide performance equal to that of several other constructions tested.

The best canopy performance was attained with low-porosity skirt material and high-porosity roof material. The geometric porosity of the skirt was 2 to 3 percent, and that of the canopy roof material was approximately 30 to 45 percent.

The length of the suspension lines was between 1 and 2.6 times the constructed diameter of the canopy with the majority of the wind-tunnel models having line lengths of twice the constructed diameter. Only one model was tested at a length of one diameter, with unsatisfactory results. Eleven sled tests of models with line lengths of 2.6 times the constructed diameter with satisfactory results have been reported. The test results of References 4 and 5 indicated that the canopy inlet should be approximately seven payload diameters behind the payload and that the ratio of the constructed diameter to the payload's diameter should be approximately 2.5 for optimum operation.

The full-scale tests were conducted in the supersonic 16- by 16-ft propulsion wind tunnel facility at Arnold Air Force Station, Tenn.[3] The test setup for the full-scale tests is shown in Figure 26. The configurations used for the full-scale tests were derived from the results of small-scale tests, and one configuration was generated under this program.

Table 13 presents a summary of the most significant data obtained from the wind-tunnel tests.

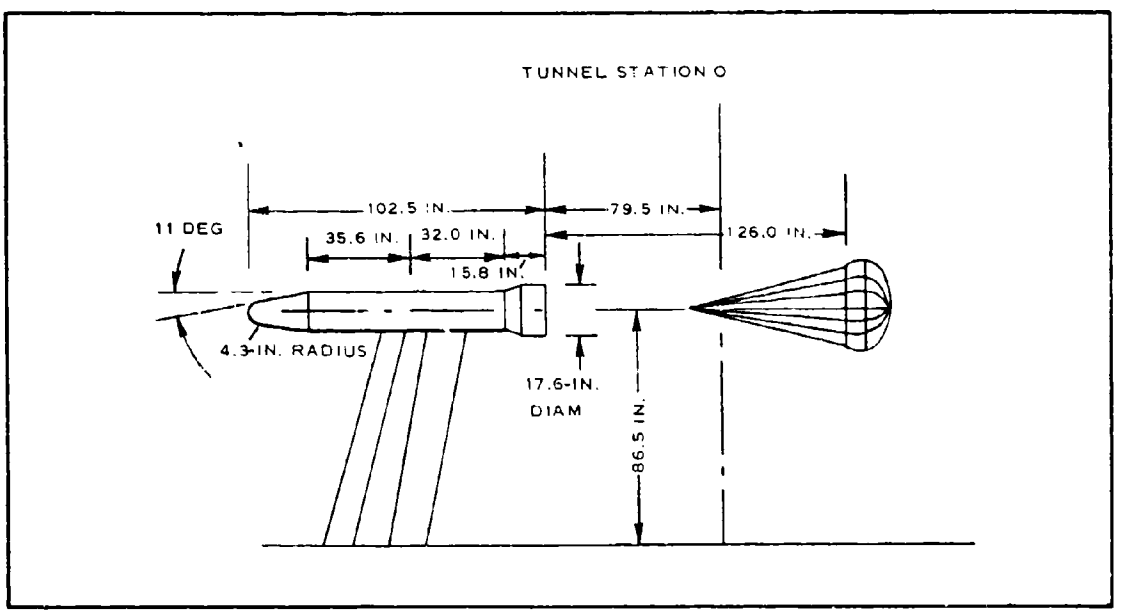

Figure 26 - SP-3 Test Setup

(3) Correlation

The available parachute results of ADDPEP, Phase I, are limited to wind-tunnel data and semianalytical estimates. These data are divided into the following parameters:

1. Type and shape - Hyperflo and isotensoid parachutes
2. Geometry - Areas (inlet and roof), diameters, and porosities
3. Test environmental and assumed physical conditions - Mach number, Reynolds number, position relative to payload, and free-stream conditions
4. Intercombination of finally reduced data (C_DA versus M, deployment shock force, and steady-state force versus time)

TABLE 13 - SUMMARY OF WIND-TUNNEL-TEST DATA

Test configuration designation		Geometry			Test condit			Results
Reference 3	ADDPEP	Parachute size, d_c (in.)	Total porosity (percent)	Description	Mach	q		
H-1	SP-1	33.16	13.3	Perlon mesh roof material with a 64/in. × 68/in. thread count and nylon skirt material	2.6	120.4	2.78	Fair stability, good inflation with heavy squiding, suspension line failed
H-2	SP-2	33.16	9.4	HT-1 mesh roof material with a thread count of 15/in. (4 strands per thread) × 22/in. (3 strands per thread) and nylon skirt material	2.6	120.6	3.00	Good stability, good inflation with slight squiding, suspension line failed
H-3	SP-3	30.63	9.0	HT-1 mesh roof material having a 24 percent porosity with an 11-in. radius circle from center of parachute, coated with silicone to give a porosity of 10.9 percent for the circle. HT-1 skirt material	2.6	120.0	3.19	Good stability, good inflation

Table 14 shows the design-area ratios and associated porosities of the roofs for the full-scale parachutes that were tested.[3] The roof-mesh porosity varied from 800 to 1148 cu ft per square foot per minute. From an analysis of the observed performance of Configurations 1 through 7 in terms of inflation, the following is apparent:

1. At $M_\infty = 2.6$, an $A_i/A_e \approx 3.0$ is the minimum ratio for good inflation.
2. The roof-mesh porosity values used to attain the desired A_i/A_e did not influence inflation appreciably.

The variation of drag area with time indicates the transient and steady-state forces acting. Typical dynamic variations are presented in Figures 27, 28, and 29 for selected conditions. Although there is no exact base for comparison, it is evident that drag variations are rather wide and cannot be ignored for design.

c. Example (SP-5)

The procedure used to determine aerodynamic loading on the canopy of the SP-5 parachute is described below.

The geometric parameters of the canopy are as follows:

1. Inlet diameter - $d_i = 27.6$ in.
2. Equator diameter - $d_{eq} = 30.62$ in.
3. Inlet cross-sectional area - $A_i = 4.16$ sq ft
4. Equator cross-sectional area - $A_e = 5.12$ sq ft
5. Roof total area - $A_r = 6.32$ sq ft
6. Roof solid area - $A_{r_s} = 1.15$ sq ft
7. Roof-mesh geometric porosity - $\lambda = 25$ percent

The critical area ratio (A_{cr}) for sonic flow at the exit, based on $M_1 = 3.4$ and a normal shock,[14] is

TABLE 14 - INLET-TO-EXIT AREA RATIOS (A/A^*)

Test configuration	Isentropic A/A^*	Mesh porosity, λ, cfm and geometric (percent)	Design			Measured A_i/A_e
			A_{inlet} (sq in.)	A_{exit} roof mesh (sq in.)	A_i/A_e	
H-1	2.89 at M = 2.6	1128 0.40 Perlon	697	611	$\frac{1.14}{\lambda \text{ mesh}} = 2.86$	3.2
H-2	2.89 at M = 2.6	795.8 0.284 Nomex	697	611	$\frac{1.14}{\lambda \text{ mesh}} = 4.02$	4.6
H-3	2.896 at M = 2.6	995 0.354 Nomex	697	611	$\frac{1.14}{\lambda \text{ mesh}} = 3.22$	3.4
H-4	2.005 at M = 2.2 1.439 at M = 1.8	1148 0.408 Perlon	602	745	$\frac{0.81}{\lambda \text{ mesh}} = 1.99$	. . .
H-5	2.896 at M = 2.6	916 0.326 Nomex	602	745	$\frac{0.81}{\lambda \text{ mesh}} = 2.48$	2.6
H-6	2.896 at M = 2.6 3.500 at M = 2.8	1028 0.365 Nomex	602	745	$\frac{0.81}{\lambda \text{ mesh}} = 2.22$	2.1
H-7	2.896 at M = 2.6	830 Nomex coating 22 in. diam 400 to 500 cfm 0.225 to 0.246 average	602	745	$\frac{0.81}{\lambda \text{ mesh}} = 3.19$ to 3.50	3.75

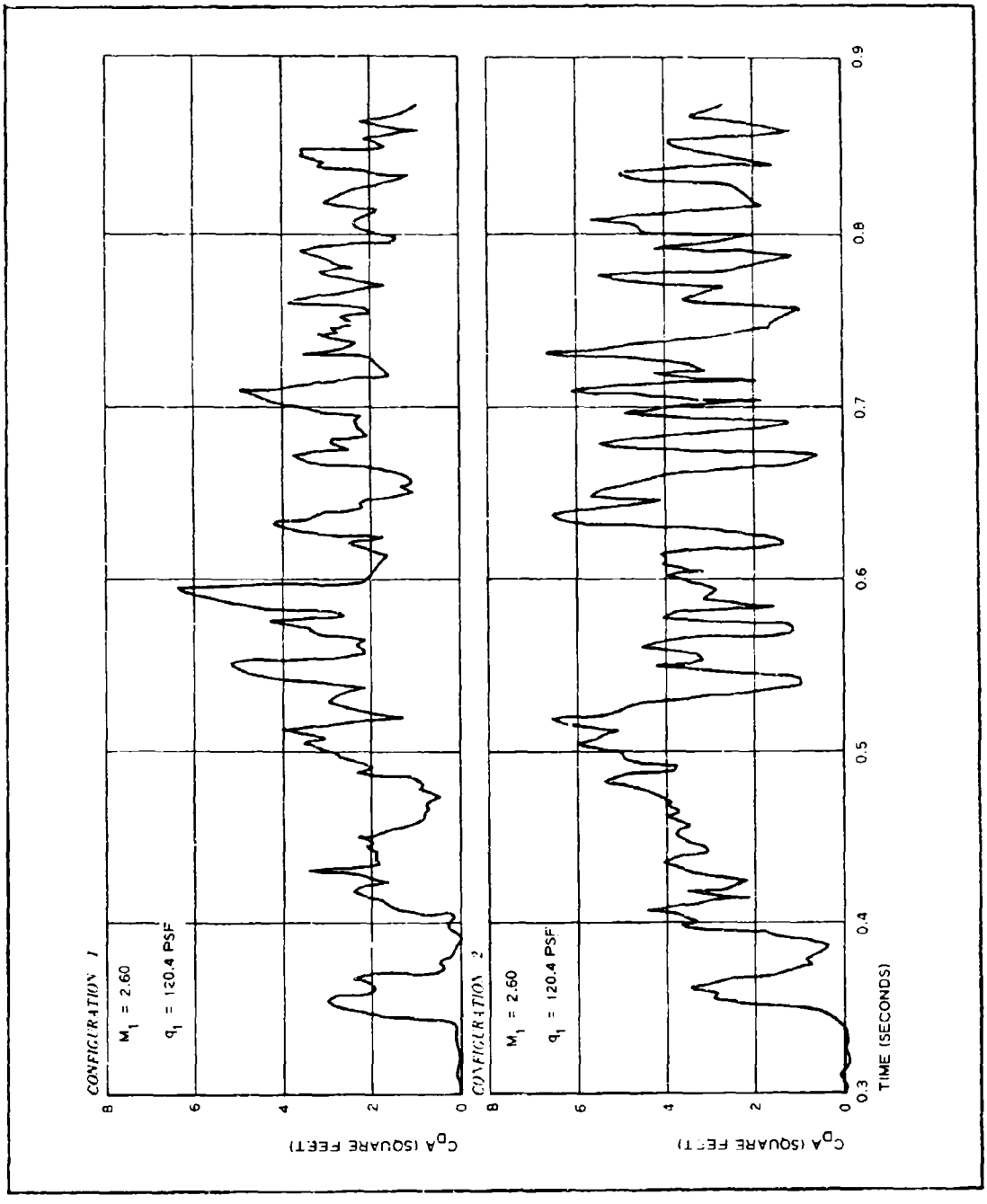

Figure 27 - Small Supersonic Parachute Performance, Configurations 1 and 2

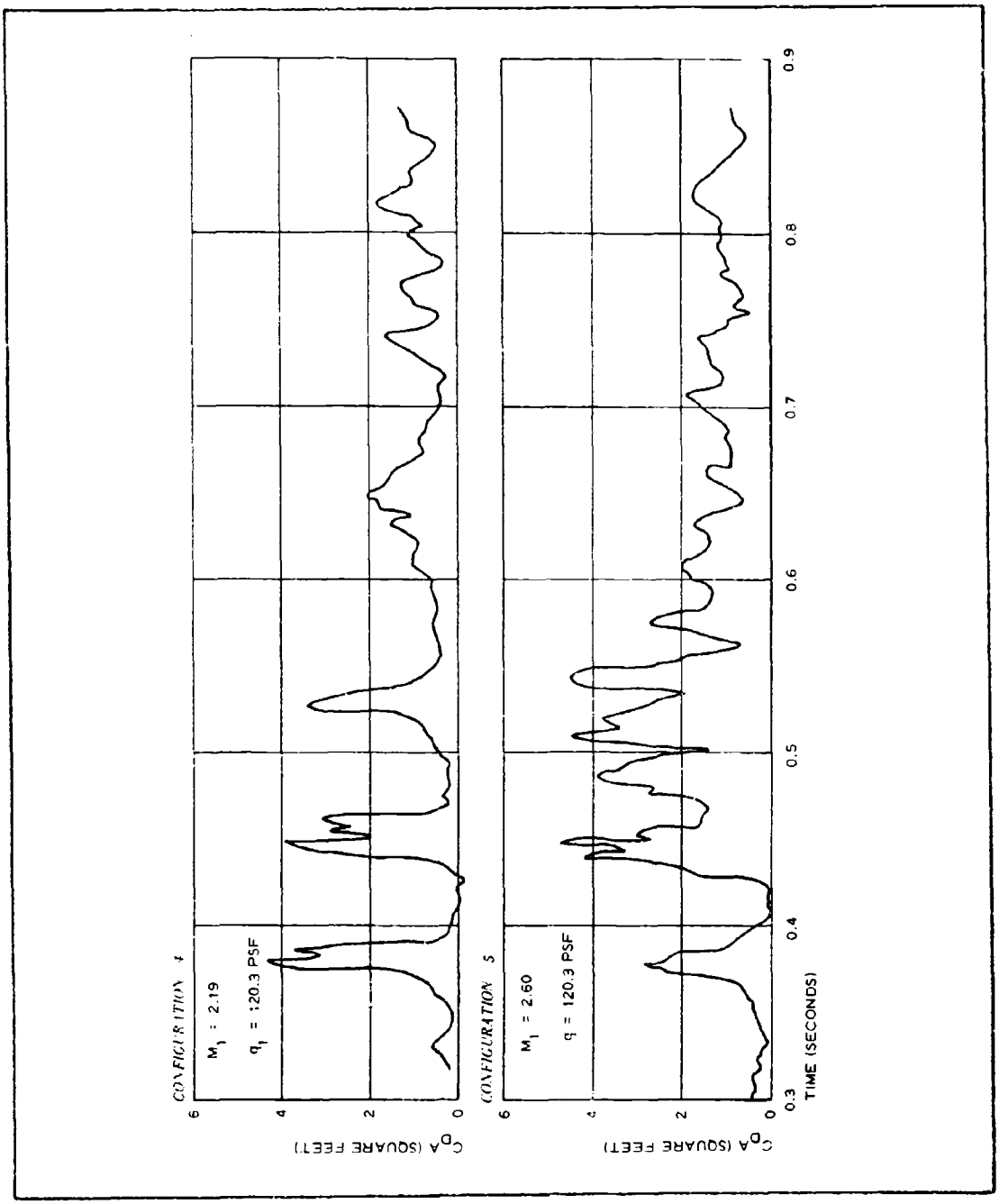

Figure 28 - Small Supersonic Parachute Performance, Configurations 4 and 5

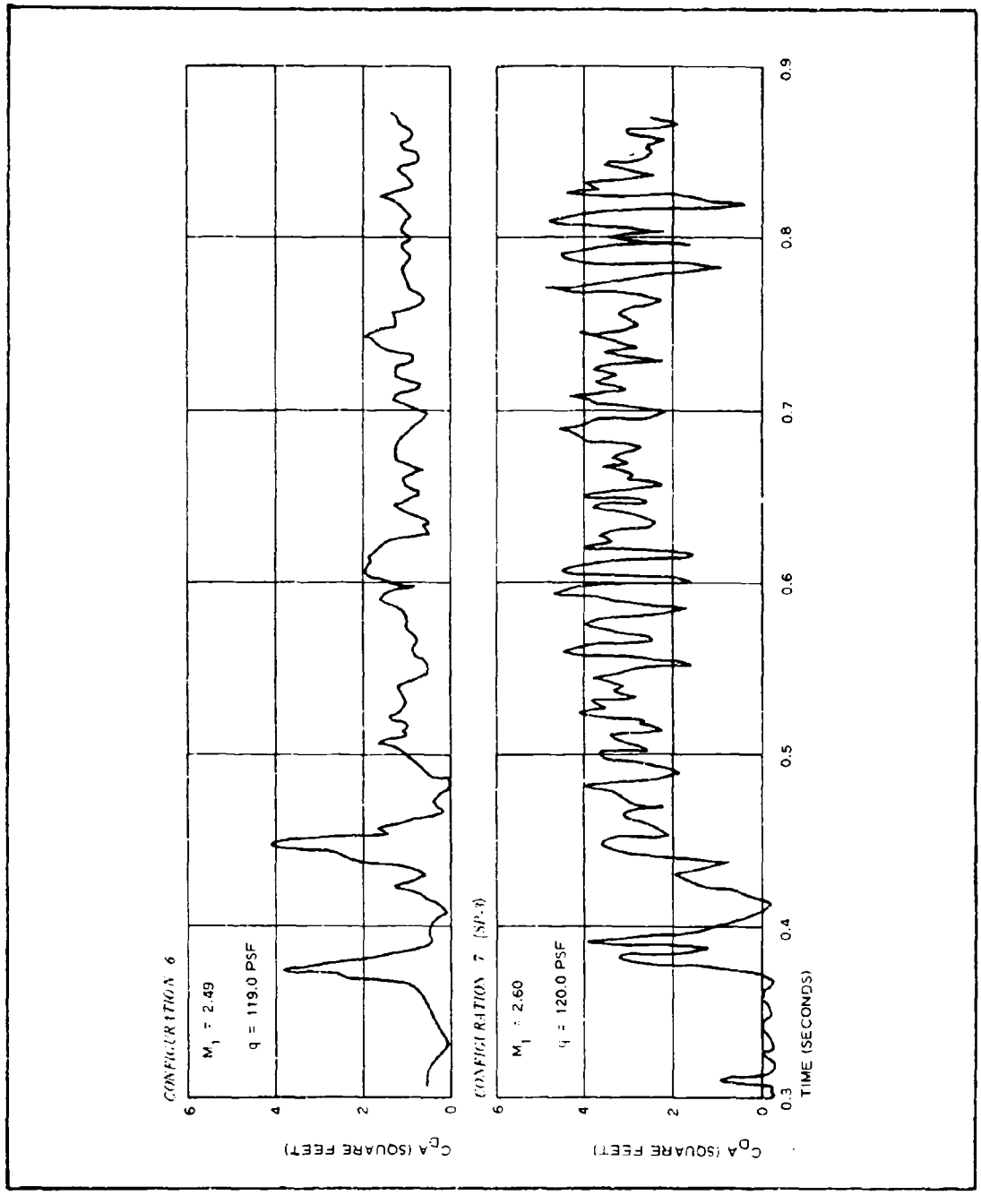

Figure 29 - Small Supersonic Parachute Performance, Configurations 6 and 7

$$\frac{A_i}{A_{r_{open}}} = 6.184. \tag{6}$$

$$A_{r_{open}} = \frac{4.16}{6.184}$$

$$= 0.674 \text{ sq ft.} \tag{7}$$

The area of the mesh portion of the roof is the total roof area (A_r) minus the solid-cloth portions, or

$$A_{r_{mesh}} = A_r - A_{r_{solid\ cloth}}$$

$$= 6.32 - 1.15$$

$$= 5.17 \text{ sq ft.} \tag{8}$$

The porosity (λ) required for sonic flow at the exit is

$$\frac{A_{r_{open}}}{A_{r_{mesh}}} = \frac{0.674}{5.17}$$

$$= 13 \text{ percent.} \tag{9}$$

The static pressure in the canopy, assuming one dimensional flow after the shock, is p_2. From Reference 14, then,

$$\frac{p_2}{p_1} = 13.32; \tag{10}$$

and substituting $p_1 = 2.56$ psf, then

$$p_2 = 13.32 \times 2.56$$

$$= 34.2 \text{ psf.}$$

The pressure at the grid openings (p_e) and at the canopy base (p_B) were calculated by the methods presented in References 14 and 15, as follows:

$$p_e = 0.528\, p_{t_2}$$

$$= 0.528 \times 39.4$$

$$= 20.8 \text{ psf} . \tag{11}$$

If

$$p_1 = 2.56 \text{ psf} ,$$

$$\frac{p_e}{p_1} = \frac{20.8}{2.56}$$

$$= 8.13 .$$

From Figure 5 of Reference 15, where

$$M = 3.4$$

and

$$\frac{p_e}{p_1} = 8.13 ,$$

$$C_{p_{Base}} = -0.04 \tag{12}$$

and

$$p_B = 1.73 \text{ psf} . \tag{13}$$

The pressure on the outside of the skirt was determined, with the skirt considered as similar to a ring-type airfoil.[8] For $\alpha = 0$,

$$C_{p_{ext}} = \frac{2}{\beta}\left(\frac{a}{b} - \alpha_o\right) \tag{14}$$

From the geometry of the wind-tunnel model,

$$\alpha_o = 5 \text{ deg}$$

$$= 0.0874 \text{ rad} .$$

For $M_\infty = 3.4$,

$$\beta = \sqrt{M_\infty{}^2 - 1}$$

$$= 3.25$$

and

$$\frac{a}{b} = 0.175 \ .$$

Substituting:

$$C_{p_{ext}} = \frac{2}{3.25}(1.75 - 0.0874)$$

$$= 0.054 \ ,$$

and

$$q_\infty = 0.7\, p_1 M_\infty{}^2$$

$$= 20.8 \text{ psf} .$$

Then

$$C_{p_{ext}} = \frac{p_{2_c} - p_\infty}{q_\infty}$$

and

$$p_{2_c} = 0.054\, q_\infty + p_\infty$$

$$= 3.67 \text{ psf} \ . \qquad (15)$$

Early approaches assumed that the skirt leading edge is similar to a wedge or cone. Under these assumptions, the loadings are:[14]

1. Wedge - $C_p = 0.4$ and $p_2 = 10.98$ psf
2. Cone - $C_p = 0.28$ and $p_2 = 8.38$ psf

The value of 3.67 psf, considered to be more realistic, was selected. The steady-state aerodynamic-pressure loadings are summarized in Figure 30.

3. THERMODYNAMICS

a. General

The procedures discussed in Items b and c, below, were used to evaluate the thermal environment around a small supersonic parachute and the thermal response of the parachute material during the deceleration period following its deployment behind a leading body. The procedures are primarily simple analytical techniques based on experimental and visual observations of analogous parachute components, since empirical and experimental data of actual deployed parachutes are very limited. Following the presentation of the thermal design procedure, evidence of several related substantive experimental reports is discussed as correlation information, followed by a presentation of an example of the SP-5 thermal design.

b. Approach

(1) General

An analysis of the aerodynamic heating of a small supersonic parachute trailing a leading body depends to a great extent on determining (1) the properties of the flow in the wake of the leading body and (2) how this flow is altered by the presence of the trailing body. Once these flow conditions are determined, the parachute components such as the riser and suspension-line assembly, the skirt panel, and the porous roof panel can be examined individually to determine the characteristics of the immediate thermal environment and its effect on the parachute material. However, since analytical methods of determining the wake-flow formation and air-property variation downstream along the wake have had only a limited degree of success in accurately predicting the state of the wake, wake flows currently are under investigation so that a better understanding of this flow can be attained. Therefore, simple analytical techniques have been used to determine the thermal environment at the

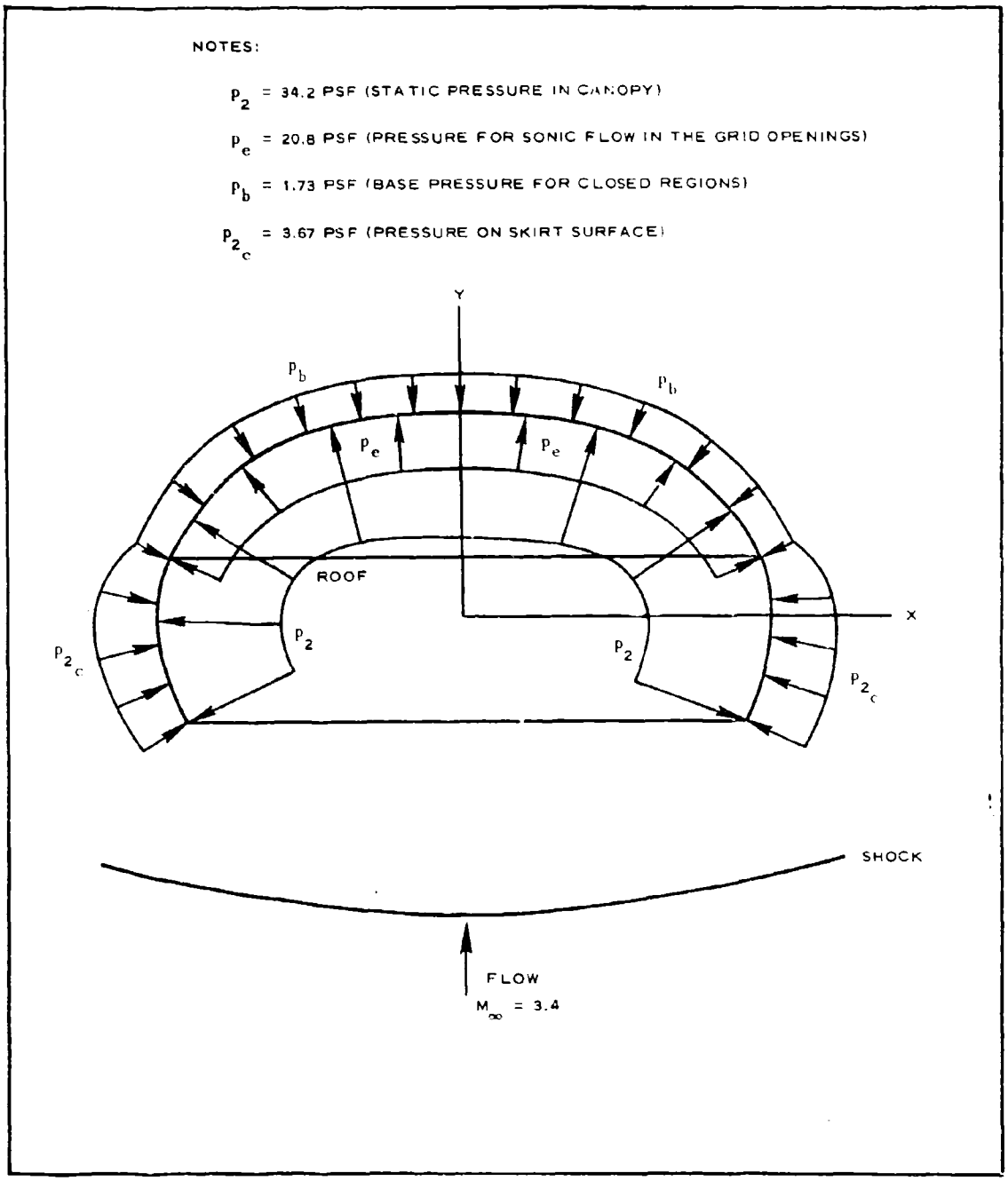

Figure 30 - Steady-State Loadings, Hyperflo Parachute SP-5

parachute components and their subsequent thermal response in this program.

(2) Analytical

One of the first considerations is the thermal environment generated by the following flow conditions. Immediately after deployment, the parachute is inflated and a strong shock develops and stands off from the inlet face of the parachute. The interference, or the effect of the leading body on the wake flow, is neglected. It then appears, if one assumes continuous flow, that stagnation or near-stagnation conditions are reached inside the decelerator, subject only to the mass flow rate of the air flowing out of the parachute envelope through the orifices in the porous roof. The roof, in fact, can be considered as comprising many individual orifices through which sonic flow exists. Furthermore, if the ratios between the total pressure inside the parachute and the local pressure on the back surface of the roof are greater than critical, sonic flow should exist in the flow through the porous roof. Therefore, it appears that the roof geometry can be examined on the basis of heat transfer to a surface analogous to flow through an orifice.

The skirt panel area can be examined on the basis of flow over a conical surface or a ring-type airfoil, as suggested in the aerodynamics discussion (Item 2, above). If one considers the air behind the strong shock at the parachute inlet as expanding from its compressed state behind the shock to the predicted local controlling-skirt pressures, then the local-flow field over the skirt can be evaluated. The flow over this surface then becomes analogous to flow over a flat plate. Similarly, the flow over the inlet lip of the skirt panel can be considered as flow over a cylinder that is oriented normally to the stream.

The local flow over the riser and suspension-line assembly can be handled in a manner similar to that over the skirt panel. However, for this case, the wake profile must be evaluated to establish local-flow parameters along these parachute components. Again, a flat-plate heat-transfer correlation can be used.

The next consideration is the heat transferred to the roof panel. A greatly enlarged roof-orifice geometry for a typical small supersonic parachute is shown in Figure 31. If the flow through the orifice is assumed to be turbulent, then the heat-transfer coefficient as a first approximation can be computed on the basis of the following equation, developed by Bartz in Reference 16:

$$h = \left[\frac{0.026}{D_*^{0.2}}\left(\frac{\mu^{0.2} c_p}{P_r^{0.6}}\right)_o\left(\frac{P_t g}{C^*}\right)^{0.8}\left(\frac{D_*}{r_e}\right)^{0.1}\right]\left(\frac{A_*}{A}\right)^{0.9}\sigma \qquad (16)$$

The orifice shown by the shaded area in Figure 31 can be assumed to be circular, so that a degree of similarity to those assumed in deriving Equation 16 can be realized between the case under analysis and the conditions used for establishing Equation 16. Once the geometrical relationships have been determined from the weave pattern selected for the roof panel (see Figure 31), the remainder of the parameters required for evaluating the heat-transfer coefficient can be determined on the basis of stagnation conditions within the parachute envelope at the instant of time under consideration.

The skirt can be analyzed on the basis of flow over a ring-type airfoil. From local pressure data such as presented in Item 2, above, and total temperature, local air-flow properties over the skirt can be generated. The heat-transfer coefficient then can be calculated by the Colburn correlation for turbulent flow over a flat plate,

$$h = 0.0296\frac{k}{x}R_e^{0.8}P_r^{1/3}, \qquad (17)$$

modified to include the reference temperature and reduced to terms of the local air properties

$$h = \frac{0.0334(pu)^{0.8}}{(T^*)^{0.576}(x)^{0.2}} \qquad (18)$$

This equation is derived from Equation 2 in Reference 1, where a complete discussion of the modification is available. A similar calculation of the

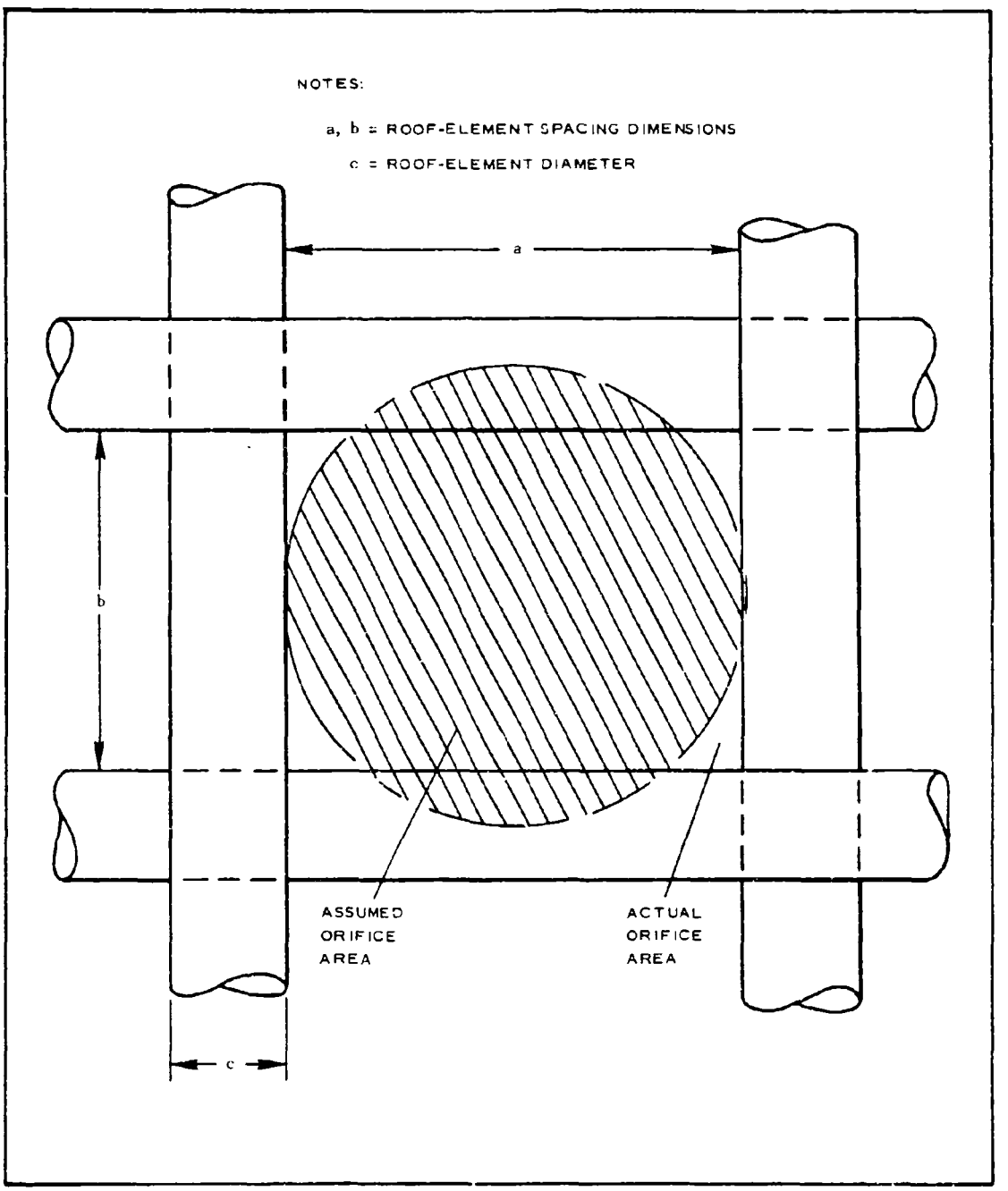

Figure 31 - Typical Roof-Orifice Geometry

heat-transfer coefficient to the skirt-panel lip and the riser and suspension-line assembly can be carried out, once a local-flow velocity profile and air-property variation within it are determined.

After the methods of determining the heat-transfer coefficients have been selected, a temperature variation with time as well as a heat-flux rate variation can be calculated based on the solution of equations typical of transient one-dimensional heat conduction. Since the deceleration times involved after deployment of a small supersonic parachute are usually quite short, the areas of interest subject to variable aerodynamic heating rates can be analyzed on the basis of transient heating. The first consideration is the roof area. The condition of heat input by convection along to a roof element at $r_e = d/2$ from a fluid stream at T_{aw} can be written as

$$h\left[T_{aw} - T(r_e, \tau)\right] = -k\left[\frac{\partial}{\partial r} T(r_e, \tau)\right] \qquad (19)$$

This equation implies that the element is subjected to a uniform thermal environment around its periphery. Thus, one can approximate the heating of the roof panel element by a cylinder subject to a constant temperature environment at the instant of time under consideration.

A particular solution of this transient heat-conduction equation is given in Reference 17. Furthermore, if one assumes that - as time from deployment is incrementally increased - the roof-panel elements are exposed to a uniform, average-temperature convective environment, a new temperature profile can be computed for each time interval. Thus, as time is increased from the instant of deployment, a new set of average convective heating parameters can be established and used as inputs to be used in Equation 19. However, the solution is subject to iteration procedure, since a balance must be achieved between the flow parameters and the heat-conduction mechanism. Once a balance is achieved, a time-temperature history of the element as well as the gradient through the element is generated over the deceleration time interval.

The temperature-time history of the skirt panel and the riser and suspension line assembly can be calculated in a similar manner, except that the transient heat-conduction equation is written for a flat slab. The condition for heat input by convection alone at the surface (y = 0) from a fluid at T_{aw} is

$$h\left[T_{aw} - T(0, \tau)\right] = -k\left[\frac{\partial}{\partial y} T(0, \tau)\right] \qquad (20)$$

The solution of this equation is generated in the same manner described above for Equation 19.

(3) Correlation

A discussion of a rigorous experimental examination of the nozzle-flow analogy for flow through porous roof fabrics, such as were incorporated in the several supersonic parachute decelerators fabricated under this contract, is given in Reference 18. The data presented in Reference 18 lead to the conclusion that once the parachute envelope is filled, a rise in pressure inside the parachute should be great enough to exceed the critical pressure ratio across the porous roof, and therefore the mass flow out of the envelope should become sonic and subject only to the porosity of the roof. Additional experimental data presented in Reference 19 showed a similar flow behavior at supersonic speeds. Thus, the selection of sonic flow through an orifice, as in the case of the porous roof, appears to have valid justification by experimental data. Additionally, it appears that Bartz's equation for evaluating the heat-transfer coefficient through such an orifice based on envelope-contained air-flow properties is reasonable as a first approximation.

Once the heat-transfer coefficient has been evaluated, the temperature-rise prediction in a porous roof element remains quite difficult, primarily because of the weaving arrangement of the elemental threads. In addition, a single-thread element also is composed of smaller filaments. Thus, the assumption of a single, homogeneous roof element subject to an additional simplification of constant-heat-transfer convective environment is at best an approximate approach to the transient-heat-conduction problem.

Another group of important parameters that are required before the temperature rise of cloth materials can be evaluated are the thermal properties of these materials. A comprehensive summary of cloth thermal properties is available in References 20 and 21. The evaluated thermal properties from these documents have been used where applicable in this program and should prove very valuable in a continued program for the evaluation of supersonic parachute decelerators.

As a result of these observations, it appears that although definitive flow observations and experimental tests have shown that flow through porous roofs is analogous to flow through a nozzle, and thermal-property evaluation of cloth fabrics has progressed to the point where these values are readily available, temperature-rise prediction in an elemental yarn material is quite complicated because of nonhomogeneity in the yarn material itself; therefore, the design criteria as outlined are recommended for analyzing supersonic parachute decelerators only until more explicit experimental or theoretical data become available.

c. Example (SP-5)

(1) General

A set of calculations used to establish the thermal design criteria for the small supersonic parachute, SP-5, is presented in Items (2) and (3), below, to illustrate the use of the calculation procedure.

(2) Applicable Techniques

A preliminary thermal-design analysis was conducted on the roof and skirt panels of test item SP-5. This small supersonic parachute is designed to be deployed at an altitude of 156,000 ft at Mach 3.4. According to the procedure outlined for analyzing the roof panel, it is necessary to calculate the flow-parameter inputs for calculating the heat-transfer coefficient to the roof panel at the orifice of a typical opening in the porous roof. This was done by programming Equation 16 onto a 1401 digital computer by FORTRAN language. In addition, the equations for calculating the state properties of air across a

normal shock were also programmed so that the solution of Equation 16 was dependent only on trajectory information such as Mach number, altitude, free-strean temperature, and pressure as a function of time after deployment. In addition, the ratio of wall to total temperature was varied along with the diameter of a roof element for a constant porosity factor. The result of such a computation yields a series of heat-transfer coefficients that are then a function of several geometrical roof-panel arrangements as well as a variable surface temperature. For example, the heat-transfer coefficient at $\tau = 0$, when the Mach number, M, is 3.4 and the free-stream pressure is 0.015 psi, is calculated as follows. Using the normal shock tables for air with a specific heat of 1.4 as given in Reference 14,

$$P_{t_2} = \frac{P_1}{0.0651}$$

$$= \frac{0.015 \text{ psi}}{0.0651}$$

$$= 0.24 \text{ psia} \quad , \tag{21}$$

$$T_{t_2} = \frac{T_1}{0.0319}$$

$$= \frac{487 \text{ deg R}}{0.0319}$$

$$= 1618 \text{ deg R} \quad , \tag{22}$$

$$C^* = \frac{\sqrt{\gamma g R T_{t_2}}}{0.8102}$$

$$= 2430 \text{ fps} \quad , \tag{23}$$

$$\sigma = \frac{1}{\left[\frac{1}{2}\frac{T_w}{T_o}\left(1 + \frac{k-1}{2}M^2\right) + \frac{1}{2}\right]^{0.7}\left(1 + \frac{k-1}{2}M^2\right)^{0.1}}$$

$$= 1.092 \quad , \tag{24}$$

and

$$\mu_o = 2.27 \times 10^{-8}(1618)^{0.5}$$

$$= 9.19 \times 10^{-7} \text{ lb-sec per square foot} \quad ; \tag{25}$$

then

$$h_g = \frac{0.026}{0.492} \frac{(9.19 \times 10^{-7})^{0.2}}{(0.70)^{0.6}} (0.24) \frac{(0.24)(32.2)^{0.8}}{(2430)} (23.3)^{0.1} (1)(1.092)$$

$$= 2.92 \times 10^{-5} \text{ Btu per square inch, second, and degree F} \tag{26}$$

The heat-transfer coefficients for the SP-5 roof panel are shown in Figure 32 as a function of time for various wall-to-total-temperature ratios and filament diameters.

The temperature rise of the element then can be evaluated by Equation 19. However Equation 19 was not solved directly, since a temperature solution of the assumed case - i.e., a cylinder subject to heating from a constant temperature environment - is available in Reference 17 as a function of the dimensionless parameters, the Biot number, and the Fourier number. For example, the Biot number and the Fourier number can be evaluated at τ = 0.1 sec for a Nomex roof panel whose filament diameter is 7 mils, as follows:

$$B_i = \frac{hd}{2k}$$

$$= \frac{(9.3)(0.007)}{(2)(0.9)}$$

$$= 0.0384 \tag{27}$$

$$F_o = \frac{4\alpha\tau}{2}$$

$$= \frac{(4)(1.2 \times 10^{-4})(0.1)}{(0.007)^2} = 0.875 \tag{28}$$

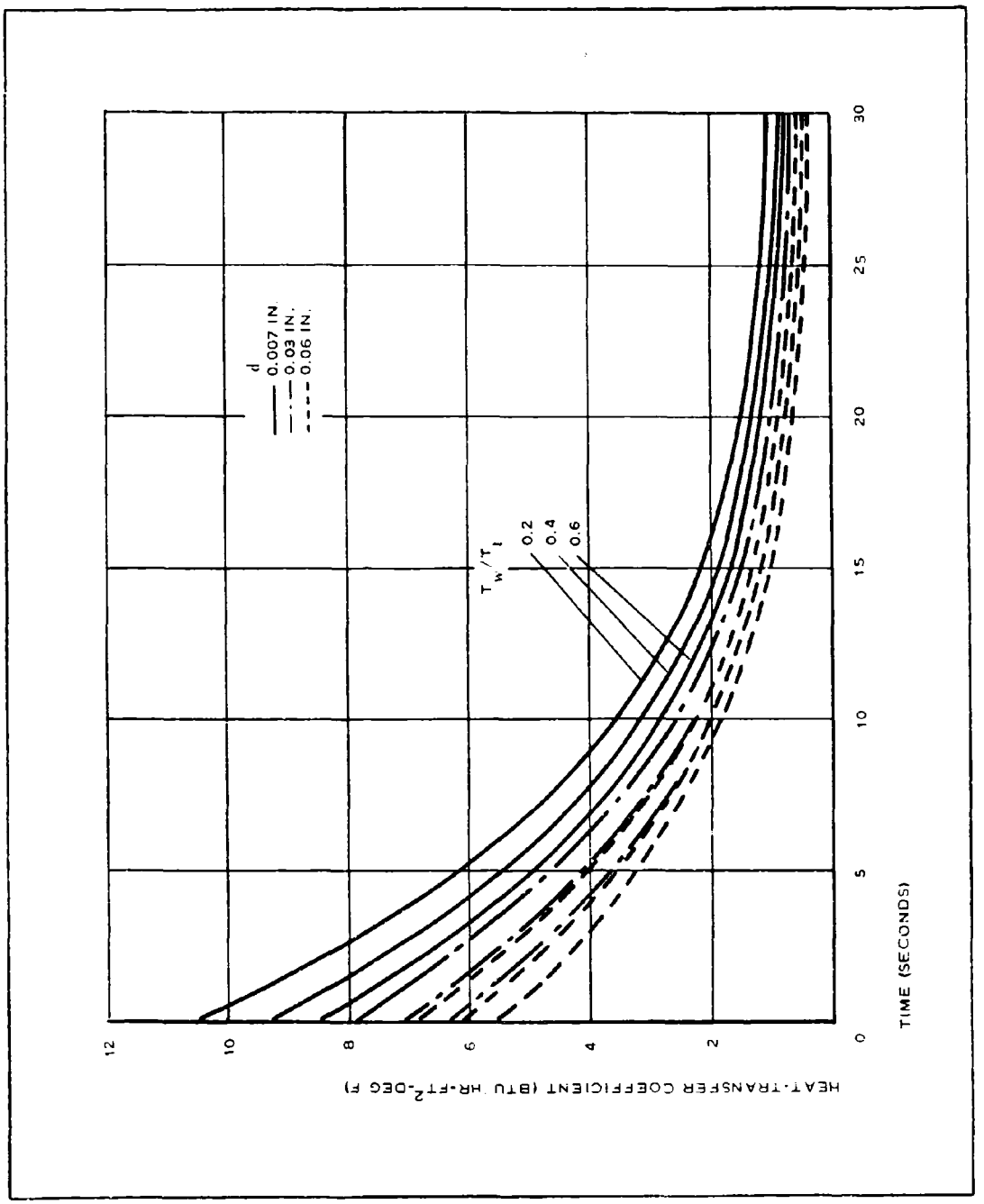

Figure 32 - Heat-Transfer Coefficient versus Time

From Chart 33 of Reference 17, the nondimensional temperature at the end of 0.1 sec is 0.07 for the calculated Biot and Fourier numbers. Then

$$\frac{T_w - 70}{T_{aw} - 70} = 0.07 \quad , \tag{29}$$

or

$$T_w = 0.07(1090 - 70) + 70$$

$$= 141 \text{ F} \quad .$$

This procedure is carried out over the time of deceleration to yield a temperature variation with time.

A similar type of calculation procedure is carried out for the other positions. Once the temperature variation with time has been computed from the heat-conduction equation, the heat-transfer rate can be computed from the following relationship:

$$\dot{q} = h(T_{aw} - T_w) \tag{30}$$

$$= \frac{9.3}{3600}(1090 - 141)$$

$$= 2.18 \text{ Btu/ft}^2\text{-sec}$$

(3) Results

The temperature-time history of the three roof-element diameters analyzed is shown in Figure 33; the surface heat input is assumed to be constant and equal to that at the orifice throat at the instant of time under consideration. The results show that a 7-mil-diameter roof element will experience a very rapid rise in temperature, reaching the critical temperature value of this material in about two seconds. The temperature rise of the other two diameters analyzed (30 and 60 mils) is less rapid because of the increased thermal mass of material available. From this temperature evaluation of the roof elements, it was concluded that a 30-mil-diameter roof element would be required to offset the effect of the aerodynamic heating during the deceleration phase of the flight.

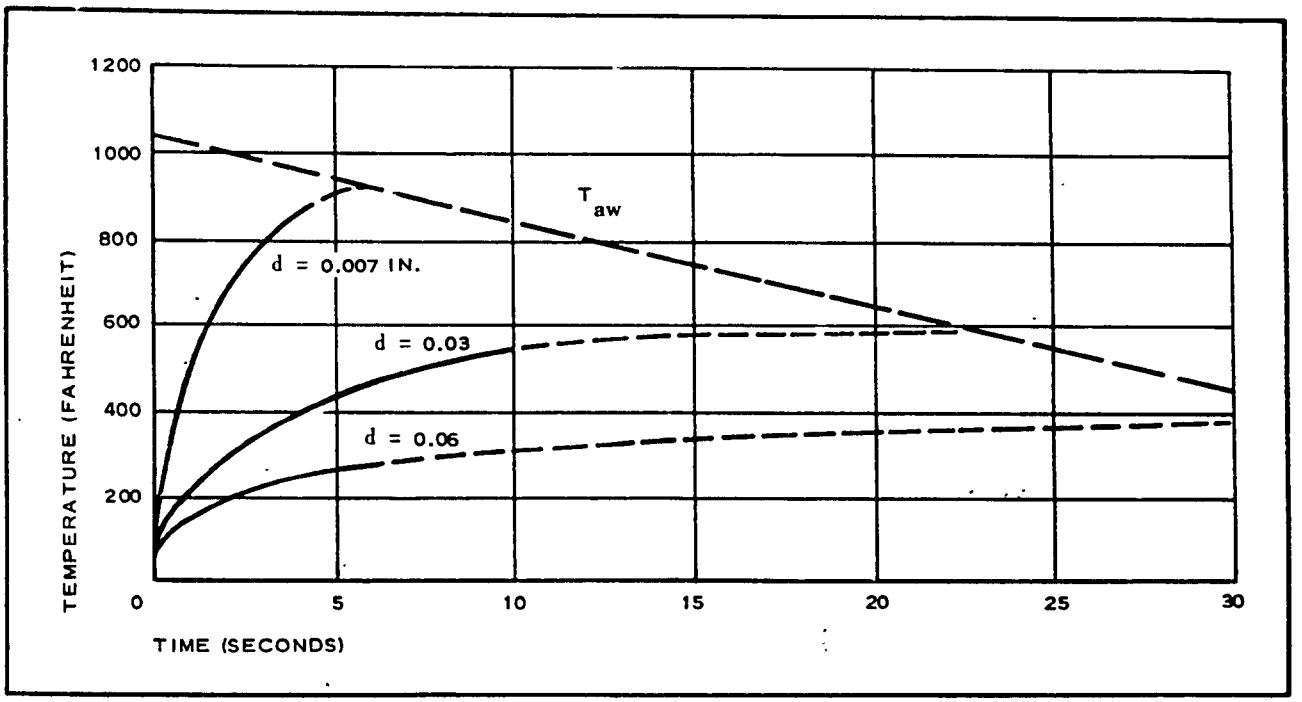

Figure 33 - Temperature versus Time (SP-5)

A temperature evaluation of the skirt was not conducted. Instead, a comparison of the thermal environment and the thickness of the material with these of the roof-panel conditions showed that the temperature along the skirt would not reach a critical value over the deceleration time period.

The resulting heat-flux rate to a 30-mil-diameter roof element is shown in Figure 34 for the orifice throat position. The heat-flux rate is maximum at the beginning of deceleration at about 2 Btu per square foot per second; it decreases quite rapidly as the test-flight vehicles slow down. At about 14 sec after deployment, the heat-flux rate is less than 0.1 Btu per square foot and per second.

The results of the thermal analysis of the small supersonic parachute (SP-5) show that a 30-mil-diameter roof-panel element is necessary to sustain the aerodynamic heating loads during the deceleration time period. Since increasing dimensions (30 mils instead of the planned 7-mil diameter) usually leads to placing limitations on other areas of the overall system design, it was decided

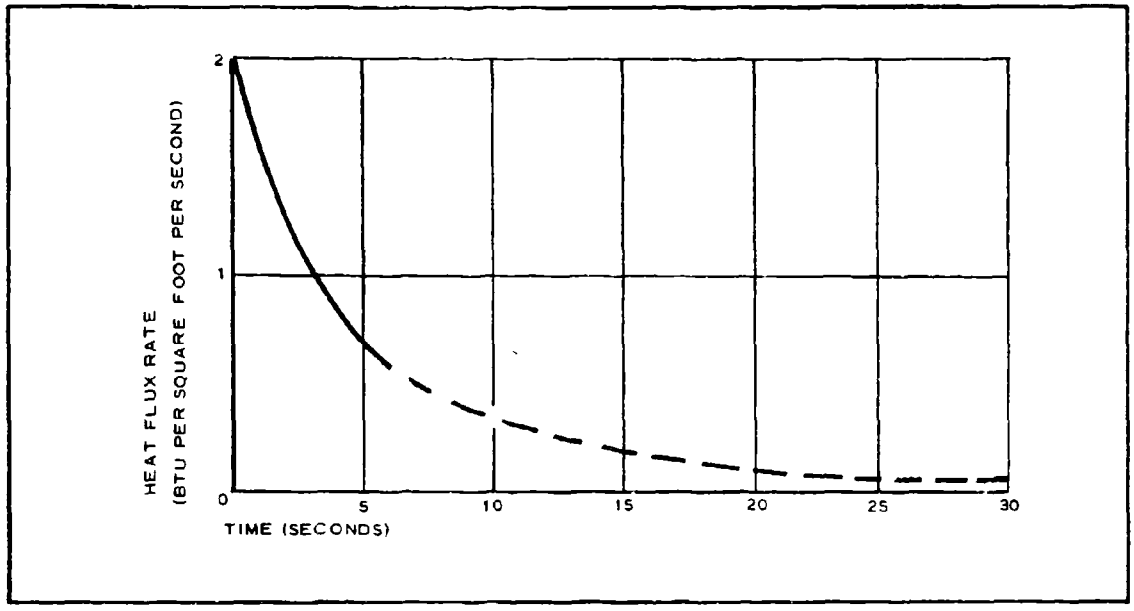

Figure 34 - Heat Flux versus Time (SP-5)

to investigate the possibility of using protective coatings on available Nomex elements. A series of experimental tests of Nomex elements covered with prospective heat-protection materials was initiated to yield the most efficient coating for a 7-mil-diameter element. The method of testing and the test results are given in Appendix I. The most significant conclusion from these tests as they affect the roof panel was that a 7-mil-diameter Nomex element coated with 9 mils of Dyna-Therm D-65 would be equivalent to the recommended 30-mil-diameter Nomex element. This experimentally determined diameter was also calculated by correlating the test results with an analytically established expression for calculating roof-panel diameters, as described in Appendix I. Applying the correlation procedure to the SP-5 case showed that a 7-mil-diameter Nomex element covered with 11 mils of Dyna-Therm D-65 would be sufficient to alleviate the heating load experienced during the deceleration period of the SP-5 parachute.

4. STRESS ANALYSIS

a. General

The following is a general discussion of membrane theory and the use of isotensoid theory in the design of parachute and BALLUTE decelerators.

Timoshenko (see Reference 22, page 433) gives the general equations for the stresses in a shell in the form of a surface of revolution with symmetrical loading. The stresses include both bending and compression. If the shell is relatively thin, the bending stresses can be neglected and the shell becomes a membrane; if the membrane is made of a flexible material such as fabric, compressive stresses cannot be carried, and a limitation is thus imposed on the number of structurally stable configurations. This latter category includes parachutes and BALLUTE; it is therefore worthy of more detailed discussion.

All-tension membranes include cones, cylinders, spheres, paraboloids, and some ellipsoids. Ellipsoids, in particular, are analyzed for a uniform internal pressure in Reference 22, page 441. It is found that all prolate spheroids (football shapes) are stable, whereas oblate spheroids (see Figure 35) have compressive hoop stresses at the equator if $a^2 > 2b^2$ (Reference 22, page 441).

The oblate spheroid is of some interest because it closely resembles the rear (from the equator back) of a BALLUTE or parachute; therefore, the same general principle for avoiding compressive stresses applies. However, the riser line applies a concentrated load to the membrane, either through the suspension lines, as on a parachute, or directly, as on a BALLUTE. The most convenient way to carry these concentrated loads is by providing the membrane with concentrated strength in the meridian direction throughout the surface, so that no heavy reinforcing is needed at the point or points of meridian-line attachment. The concentrated strength is in the form of cords or webs (straps), which lie along the meridians of the surface; therefore, a shape different from any of the simple shapes mentioned above must be used

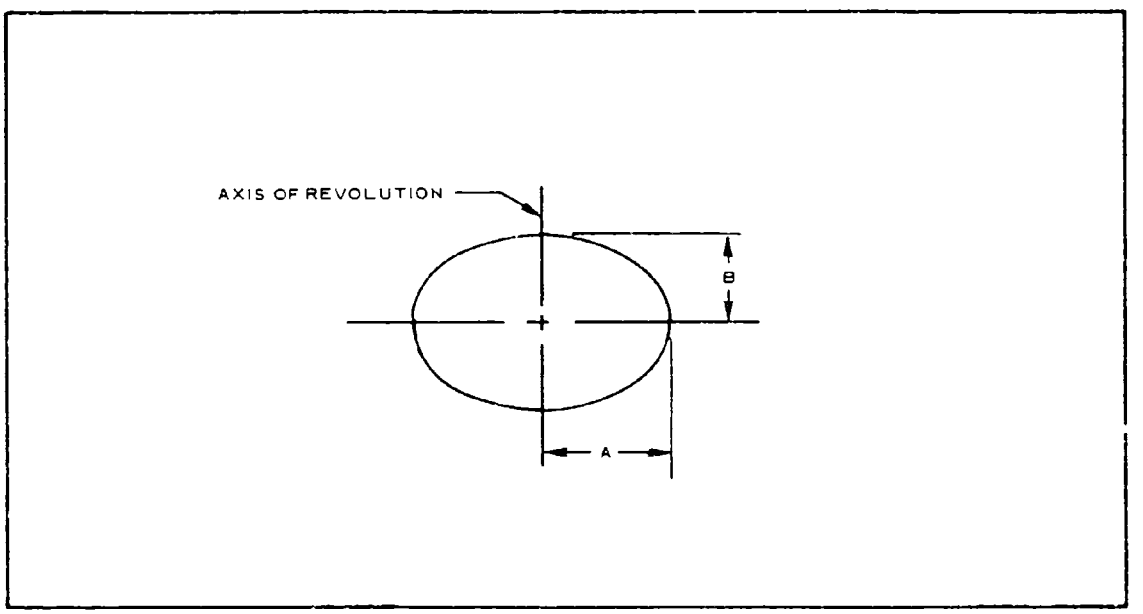

Figure 35 - Oblate Speroid

if efficient use is to be made of the meridian cords. The optimum shape for the usual method of construction (uniform cross-section cords and an envelope made of bias-cut gores of a single-ply fabric) is one in which the fabric stress is uniform in all directions throughout, and the cord tension is constant throughout. Such a surface is one form of an isotensoid.

By varying the relative loads carried by the fabric and the meridian cords, the family of curves in Figure II-3 (Appendix II) is obtained. This family is applicable to parachutes and to the rear of BALLUTES. The factor k in the figure is defined as $nT_m/p\pi R^2$ where n is the number of meridian cords, T_m is the tension in each cord, P is the internal pressure, and R is the equatorial radius of the membrane. The curve for k = 1.0 is the case in which the fabric stress goes to zero. Any curve flatter than the k = 1.0 curve would require compressive stress in the fabric and therefore cannot be obtained in a parachute or BALLUTE. Because it has the smallest surface area, the k = 1 curve might appear to be the optimum curve. To approach

zero fabric stress, however, a very small gore radius[a] would be required with the bias-cut gore construction described above. This would require a large number of gores and would make fabrication difficult. In practice, therefore, a compromise is necessary, depending on the number of gores, which in turn generally depends on the size of the parachute or BALLUTE. With 12 gores, for example, it has been found that k = 0.6 gives the smallest gore radius that can reasonably span the gore width at the equator; therefore, k = 0.6 is the practical maximum for 12 gores. The surface area of the k = 0.6 curve is $1.692\pi R^2$, which compares to $2\pi R^2$ for a hemisphere and $1.478\pi R^2$ for the limiting (k = 1.0) curve. A plane circle, of course, has a surface area of πR^2. It is clear, therefore, that a parachute constructed of a circle of cloth must undergo considerable distortion under load and must have an inflated diameter that is smaller than the constructed diameter. (Suppose the flat circle forms the limiting k = 1.0 curve, which has the minimum area for a given inflated radius. Equating surface areas before and after inflation gives $\pi R_o^2 = 1.478\pi R^2$, or $R = 0.824R_o$. If the circle forms one of the other curves of Figure II-3 of Appendix II, the ratio of R/R_o would be even less.) The inflated diameter of a parachute can nearly equal the constructed diameter if it has a large constructed skirt that can move aft of the equator after inflation.

Isotensoid design based on a steady-state internal and external pressure distribution is discussed in detail in Appendix II. The method usually requires a series of iterations, which proceed as follows:

1. Starting with a wind-tunnel model similar to the desired shape, a pressure distribution over the entire surface is obtained for conditions similar to the most critical loading condition in the trajectory. (In all cases

[a] The gore radius is the radius that lies in a plane normal to the meridian curve at any location on the parachute or BALLUTE. This plane also contains r_2, one of the principal radii of curvature of the surface of revolution, which approximates the BALLUTE or parachute surface. See Appendix III for additional details.

considered for this program the deployment conditions are the most critical.)

2. An isotensoid shape is obtained, if possible, for the above pressure distribution. If this shape closely approximates the shape of the wind-tunnel model, it becomes the design shape and no further iterations are required.

3. If it is not possible to derive an isotensoid shape that is similar to the wind-tunnel model, it may be necessary to build a new wind-tunnel model of the shape actually obtained and start over with Step 1. This can often be avoided by running Step 2 with various modified pressure distributions until the derived shape is similar to the wind-tunnel model. The shape then will not be an isotensoid for the actual loading condition and the stress distribution must be determined to ensure that there are no wrinkles or excessive stress concentrations. If the stress distribution is satisfactory with any configuration thus obtained, it becomes the design shape and no more iterations are required.

This is the procedure that was actually followed in all the decelerator designs. Margins of safety were calculated assuming the drag device to be fully inflated at the deployment conditions; because the dynamic pressure is usually decreasing while the drag device is inflating, this assumption is conservative.

The steady-state drag and internal pressure condition is not the only loading condition the decelerator experiences, however. During deployment the decelerator package is accelerated rearward by the air stream and is then accelerated to the payload velocity by the riser line. This condition is analyzed in general terms in Appendix IV, using the assumptions of rigid-body dynamics.

b. Approach

(1) Analytical

(a) Parachute Proper

Appendix II gives the general method of design of isotensoid drag devices, along with the definition of all symbols that are not defined in this discussion. The loading is given in terms of pressures over the internal and external surface of the parachute. The internal pressure is one value over the surface of the threads, P_2, and another value over the interstices between the threads, P_e. The external pressure varies over the surface as described in Section IV, Item 4, b, for the BALLUTE; for simplicity of analysis, however, the short length of the surface in front of the equator (the skirt) is assumed to have a constant external pressure.

The internal pressures P_2 and P_e exert a force on an element of area, dA, equal to $dA[P_2(1 - \lambda) + P_e\lambda]$, where λ is the porosity expressed as the fraction of the total area that is open. If a uniform pressure acted over the area, dA, that gave the same force, it would have the value $P_2(1 - \lambda) + P_e\lambda$. Therefore, this value could be used as a uniform pressure over the inside of the porous fabric. However, the analysis in Appendix II is based on an assumption of a uniform pressure over the entire inside surface; to conform to that assumption, it is necessary to add a constant pressure inside and out (which will not affect the analysis) over the porous area of the parachute. The value that must be added is $P_2 - P_2(1 - \lambda) - P_e\lambda$, or $(P_2 - P_e)\lambda$. Then the P_x values for substitution into the equations of Appendix II can be obtained directly by taking the difference between the internal and external pressures at any point.

Parachutes are analyzed by the parachute-analysis model of Figure II-8 (of Appendix II), which is obtained by extending the skirt (analytically) to the axis of revolution. The resulting structure is similar to the BALLUTE, and the methods of analysis (with the exception of the 80-deg boundary condition) are identical. Since there is no center cable to the rear pole, the quantity ρ_r

is zero. One more quantity must be chosen arbitrarily to define the isotensoid shape. In some cases it might be desired that the shape be similar to the inflated shapes of successful wind-tunnel models. The quantity k, therefore, is chosen by trial until a similarity is obtained.

The equations of Appendix II have been programmed (some in slightly different form) for digital-computer solution. To use the computer programs it is necessary to express the pressures as dimensionless ratios, which are obtained by dividing by the dynamic pressure, q. A first computer program requires the pressure ratios $P_{(local)}/q$ for the rear of the parachute, a value of k, the equivalent of $\rho_r = 0$, and the equivalent of I_{Rf} as input data. The program then can calculate the parameters and coordinates of the rear of the parachute. Because the skirt is assumed to have a constant external pressure, it is part of a uniform-pressure isotensoid surface that is defined by the quantity k = 0.6 and the value of 2f/PR given by Equation II-23 of Appendix II. Equation II-22 then gives ρ_f. Because only the portion of the front isotensoid surface in the region of the equator is used in the parachute, it can be closely approximated by a circular arc. Substitution of the expressions for dy/dx and d^2y/dx^2 in Equation II-10 yields

$$\frac{r_1}{R} = \frac{1 - \rho_f}{1 + k + \rho_f} \quad , \tag{31}$$

where

$$\frac{x}{R} = 1 \quad .$$

This value of r_1 is known as the skirt radius.

A general layout and loading distribution for the hyperflo parachute is shown in Figure 36. In many cases it is necessary to analyze the stress distribution for some loading condition other than the one that was used to derive the profile shape. Using the parameters that define the parachute shape and the new pressure values for the various values of x in a second parachute computer

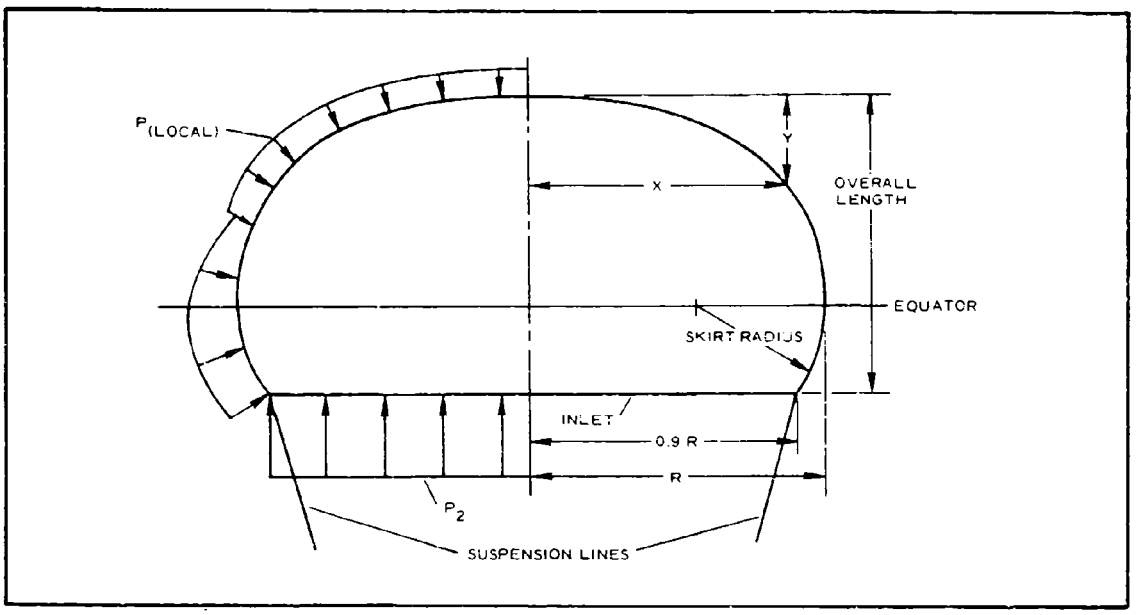

Figure 36 - General Layout and Loading for Hyperflo Parachute

program gives the stress parameters containing the fabric stress and meridian-cord loads for various points on the rear of the parachute. Values for points of interest then are converted to actual stresses and loads.

The loads in the inlet hoop and suspension lines are obtained by satisfying equilibrium of the loads at the inlet, as is shown in Figure 37.

The inlet hoop is not a perfect circle, but instead has "scallops," or arcs, between the meridians to transfer the fabric stress to the suspension lines at the inlet. The arc radius is obtained by dividing the inlet-hoop tension by the fabric stress at the inlet.

The gore pattern for the derived shape is obtained using the analysis of Appendix III. A cross section of a typical inflated parachute is shown in Figure 38. The calculated curves of the meridian and the gore centerline (top) are displaced to either side of the normal surface. At the inlet, however, all three curves must coincide; therefore, the meridian gore and top curves

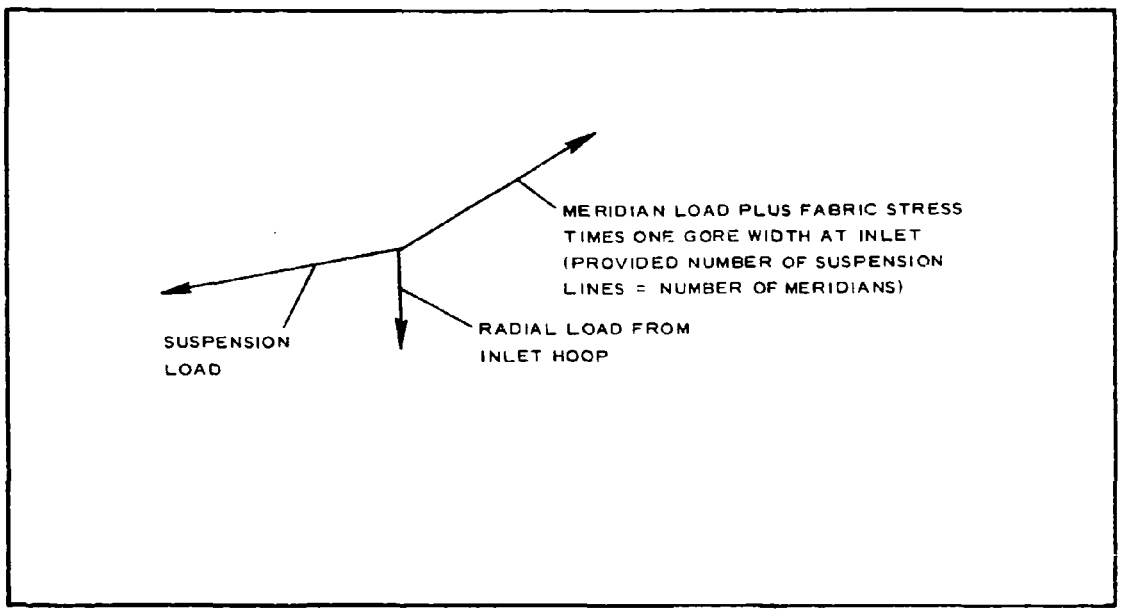

Figure 37 - Suspension-Line and Inlet-Hoop Loadings

are altered in the skirt region to make them intersect the nominal surface at the inlet. This, of course, requires a deviation in the gore pattern from the width given by Appendix III. The width at the inlet is equal to $2\pi R_i/n$, where R_i is the inlet radius and n is the number of gores. The width at the equator coincides with the calculation in Appendix III. Between these two points the gore pattern must be faired in by eye.

Wind-tunnel tests of SP-3 revealed wrinkles in the skirt in the area of the inlet. Examination of the method of determining the gore pattern then indicated that an improvement could be made in the method of fairing in the skirt area. Figure 39 shows a cross section of the inlet detail. The gore pattern detail then appears as shown in Figure 40.

The gore width at the inlet is shown as $2\pi R_i/n$. The faired section must be a tangent at an angle of θ_t with the gore centerline at the inlet. From Figure 40, $\sin \theta_t = \pi \sin \theta_i/n$.

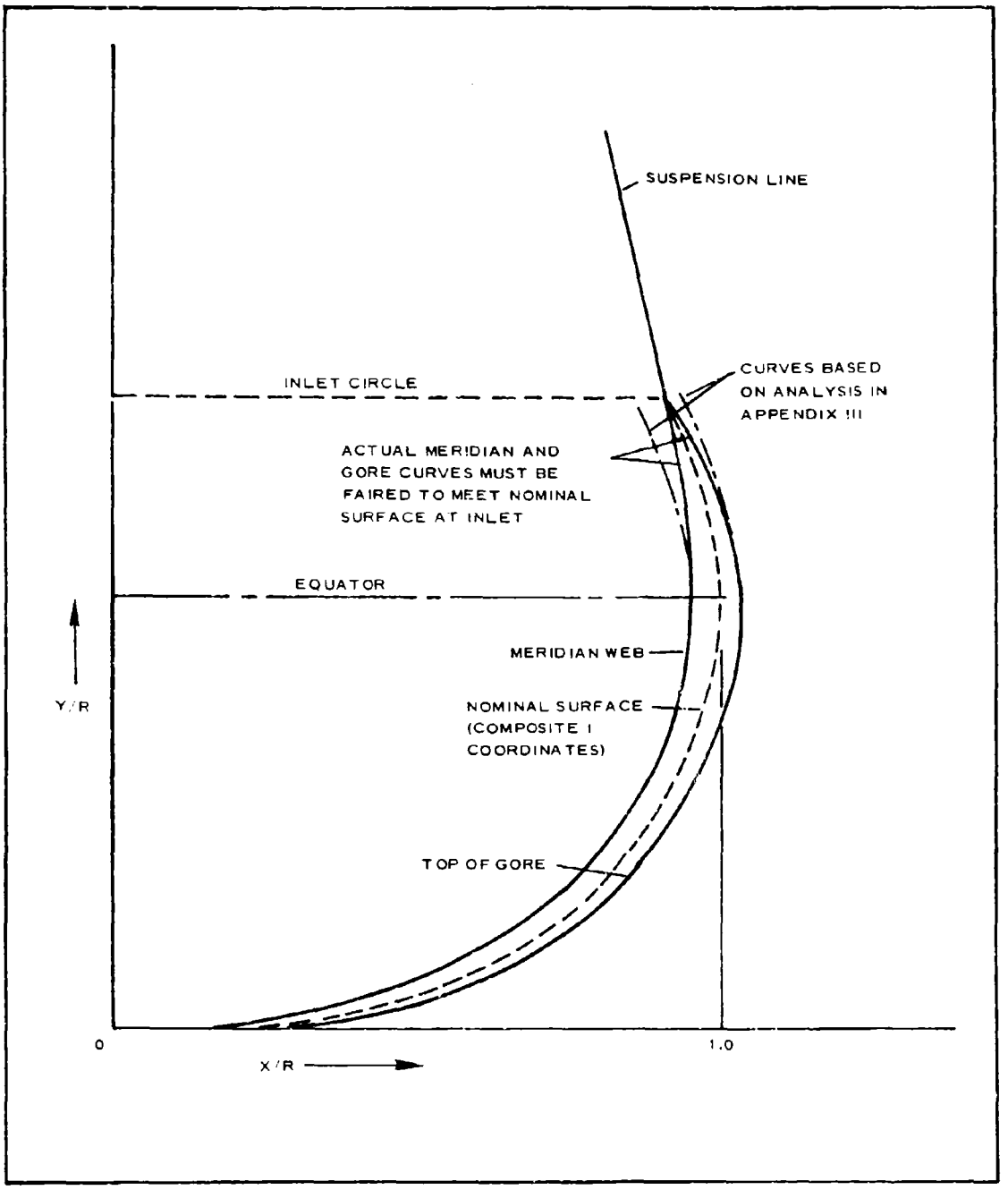

Figure 38 - Typical Parachute Cross Section

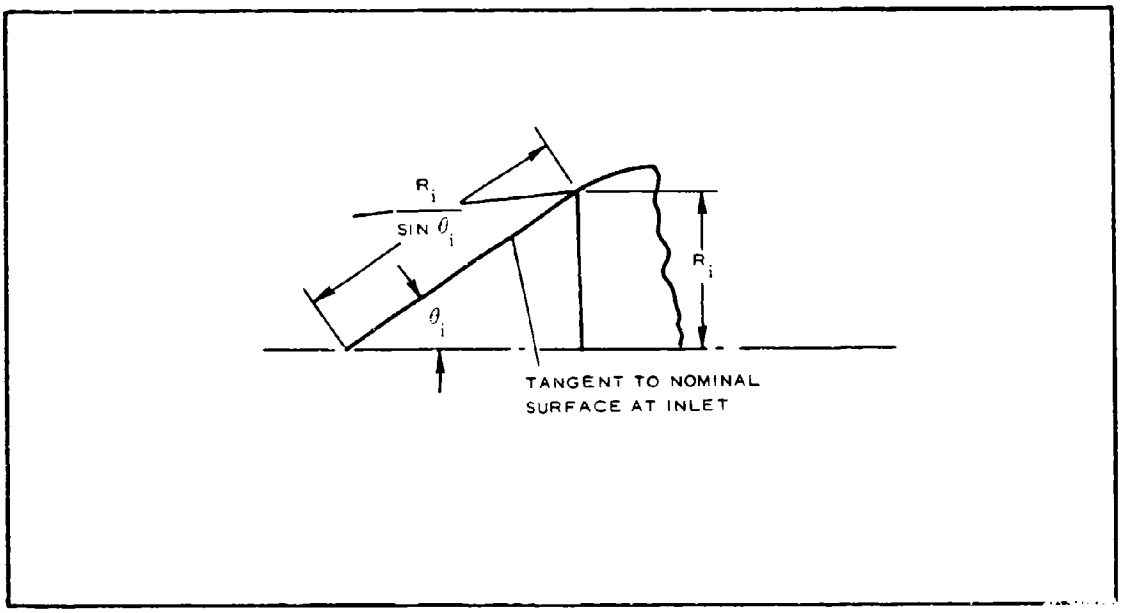

Figure 39 - Parachute Inlet Detail

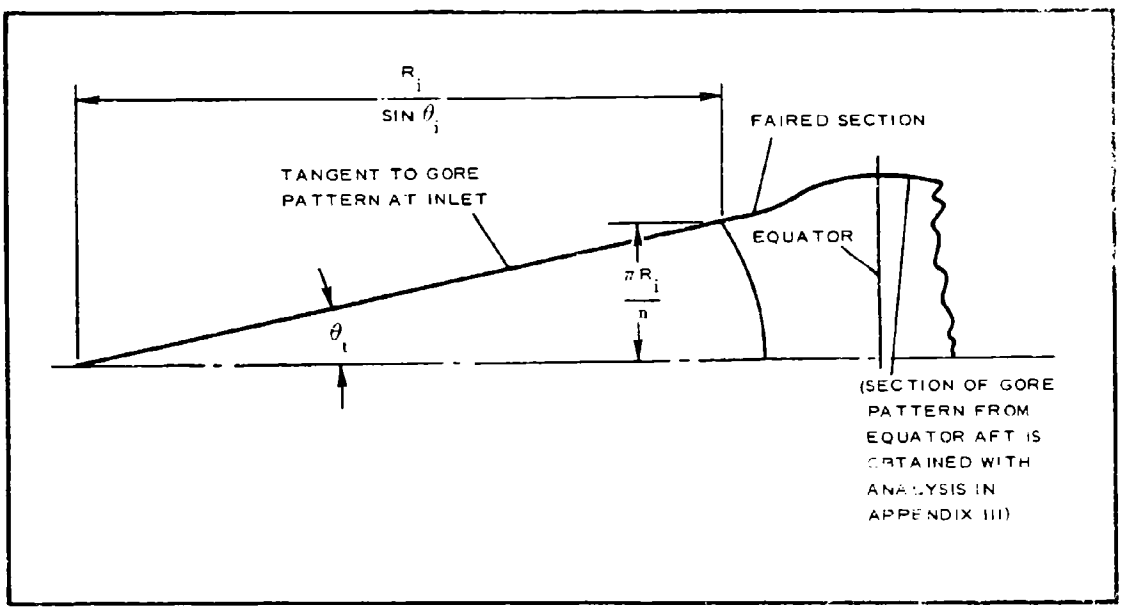

Figure 40 - Gore Pattern Detail at Inlet

(b) Deployment Analysis

The deployment analysis uses the assumptions of rigid-body dynamics, in which the canister, decelerator package, and payload are assumed to be rigid bodies and the deployment-bag bridle line and riser line are assumed to be massless springs. The canister is given an initial velocity by a set of explosive thrusters. It travels freely until the deployment-bag bridle line becomes taut; then the canister and decelerator package move rearward with the same velocity. They are accelerated rearward together by their aerodynamic drag until the riser is nearly taut, at which time the canister and deployment bag are cut loose. The parachute and payload then act as a two-mass system connected by the riser (spring); the riser absorbs the energy required to bring the parachute and payload to the same velocity. Equations for the motions and forces involved are developed in detail in Appendix IV.

(2) Empirical

The analytical methods described previously are based on classical membrane theory, which in itself does not require further experimental verification. The margins of safety used in the parachute designs are large and are similar to those used in the BALLUTE designs, the empirical background of which is discussed in Section 4, Item 4, b (2). It was not deemed necessary, therefore, to perform structural tests on the complete parachute prior to flight or wind-tunnel test, which will be the final verification of the design values.

c. Example (SP-5)

(1) Applicable Techniques

All the assumptions and equations that are discussed in Item b (1), above, are applicable to the design of SP-5.

(2) Results

(a) Parachute Proper

It is desired that the profile of SP-5 be aerodynamically similar to inflated

shapes of successful wind-tunnel models. The coordinates (scaled from a photograph) of the chosen shape are given in Figure 41. The procedure described previously could, if desired, be applied individually to each of the various test points for which small parachutes are used. However, the result would be five profile shapes, each slightly different from any of the others and each one optimum for only one particular loading condition. The disadvantage of having five different designs is obvious; in addition, any possible advantage from such a policy is nullified by two important factors.

1. Aerodynamic loads can be predicted with only limited accuracy.
2. Each parachute must pass through a range of aerodynamic loadings in its trajectory.

Therefore, it was desirable to obtain a design that is satisfactory for a range of aerodynamic-loading conditions, even though it is not absolutely optimum for all cases. It was decided to derive a composite shape that would be isotensoid for the average of the loading conditions for the SP-3 (λ = 20.5 percent), SP-4 (λ = 5.16 percent) and SP-5 (λ = 10.7 percent) test points. This loading condition was obtained by averaging the pressure ratios $P_{(local)}/q$ for the above three test points at each point on the surface.

The respective pressure and drag coefficients are given in Table 15.

The pressure ratios for the composite were used as inputs for the first computer program, along with various trial values of k. The value k = 0.6 gave a profile shape that is quite close to the wind-tunnel model. (The coordinates of both configurations are given in Table 16.) The composite shape then was analyzed under the loadings for the SP-5 test point for two different values of the roof porosity. The resulting values are given in Table 17.

The maximum values and values at the inlet then were converted to actual loads and stresses; these are given in Table 18. From equilibrium at the inlet, the hoop tension, scallop radius, and suspension-line tensions were obtained; these are also given in Table 18.

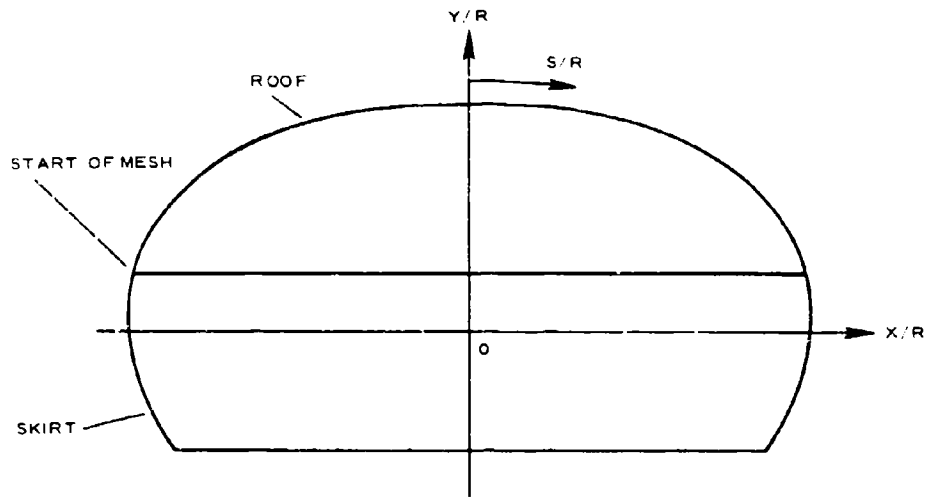

TABLE OF COORDINATES

X/R	Y/R	TAN $\theta_1 = \frac{Y}{X}$
0.000	0.6970	∞
0.082	0.6900	8.42
0.490	0.621	1.27
0.641	0.552	0.860
0.752	0.483	0.642
0.821	0.414	0.504
0.883	0.345	0.391
0.931	0.276	0.296
0.955	0.207	0.217
0.979	0.138	0.141
0.993	0.069	0.0695
1.000	0.000	0.000
0.993	-0.069	-0.070
0.983	-0.138	-0.140
0.966	-0.207	-0.214
0.938	-0.276	-0.294
0.907	-0.345	-0.380

Figure 41 - Wind-Tunnel Model Coordinates

TABLE 15 - PRESSURE RATIOS AND DRAG COEFFICIENTS OF HYPERFLO PARACHUTES FOR VARIOUS TEST POINTS AND POROSITIES

Item	SP-3 λ = 20.5 percent	SP-4 λ = 5.16 percent	SP-4 λ = 20.5 percent	SP-5 λ = 10.7 percent	SP-5 λ = 20.5 percent	Composite SP-3, SP 4, SP-5
$\frac{X}{R}$ (rear of parachute)						
0 to 0.95	0.251	0.081	0.202	0.149	0.212	0.16
0.98	0.150	0.150	0.045	0.090	0.090	0.090
0.995	0.230	0.080	0.080	0.140	0.140	0.150
1.0	0.306	0.124	0.124	0.178	0.178	0.203
$\frac{P_2}{q}$	1.637	1.655	1.655	1.645	1.645	1.64
$\frac{P_{(local)}}{q}$ for skirt	0.306	0.124	0.124	0.178	0.178	0.203
C_{D_P}	1.14	1.284	1.172	1.221	1.162	1.209

TABLE 16 - DIMENSIONLESS COORDINATES

Item	Composite	Wind tunnel model*
k	0.6	. . .
ρ_r	0	. . .
$\frac{\text{Skirt radius}}{R}$	0.660	0.75
$\frac{\text{Overall length}}{R}$	1.075	1.042
$\frac{X}{R}$	$\frac{Y}{R}$	$\frac{Y}{R}$
0	0	0
0.05	0.00010	. . .
0.1	0.00061	. . .
0.15	0.00188	0.007
0.2	0.0043	0.012
0.25	0.0080	0.020
0.3	0.0135	0.029
0.35	0.0210	0.038
0.4	0.0307	0.050
0.45	0.0430	0.063
0.5	0.0581	0.078
0.55	0.0764	0.095
0.6	0.1284	0.116
0.65	0.1245	0.142
0.7	0.1556	0.173
0.75	0.1926	0.213
0.8	0.2370	0.256
0.85	0.2914	0.310
0.9	0.3608	0.380
0.95	0.4587	0.470
0.98	0.5538	0.555
0.995	0.6438	0.635
1.0	0.7255	0.697

*Wind-tunnel model coordinates based on scaling photographs.

TABLE 17 - VALUES OF MERIDIAN-WEB TENSION AND FABRIC-STRESS PARAMETERS FOR COMPOSITE SHAPE UNDER SP-5 LOADINGS

		SP-5 loads on composite shape λ = 10.7 percent q = 20.8 psf		SP-5 loads on composite shape λ = 20.5 percent q = 20.8 psf	
	$\frac{X}{R}$	$\frac{nT'_m}{P'\pi R^2}$	$\frac{2f'}{P'R}$	$\frac{nT'_m}{P'\pi R^2}$	$\frac{2f'}{P'R}$
Roof	0 to 0.95	0.594	0.428	0.569	0.410
	0.98	0.609	0.412	0.499	0.483
	0.995	0.595	0.427	0.490	0.491
	1.0	0.575	0.447	0.465	0.517
Skirt	0.9	0.591	0.425	0.553	0.419

(b) Deployment Analysis

The following deployment analysis is for SP-3. The deployment conditions for SP-5 are much less severe. The general deployment analysis from Appendix IV is used here, with the same notation. The canister weight is estimated to be 35 lb, giving m_1 = 1.088 slugs. The parachute and suspension lines are estimated to weigh 2.4 lb, and the riser 1.1 lb. For purposes of analysis, these two values were added to obtain a conservative value of m_2. Thus,

$$m_2 = \frac{3.5}{32.2}$$

$$= 0.109 \text{ slugs} . \qquad (31)$$

The deployment-bag line is composed of four nylon webbings, each rated at 3000-lb ultimate strength. Values taken from the 1957 Man-Made-Fiber Table by Textile World indicate that the stiffness-to-strength ratio of high-tenacity nylon is 4.5, which gives

TABLE 18 - MAXIMUM FABRIC STRESSES AND MERIDIAN TENSIONS FOR SP-5 TEST POINT USING COMPOSITE CONFIGURATION

Test point	SP-5	SP-5	Composite of 1, 2, and 4
λ (percent)	10.7	20.5	. . .
q (psf)	20.8	20.8	. . .
P'/q	1.467	1.467	1.437
P'(psf)	30.5	30.5	1.437q
$\frac{nT'_m(max)}{P'\pi R^2}$	0.609	0.569	0.600
$\frac{2f'}{P'R}$			
Inlet	0.413	0.419	0.432
Maximum	0.447	0.517	0.432
T'_m(max) (lb)	7.91	7.39	0.368q
f'(lb/in.)			
Inlet	0.668	0.676	0.033q
Maximum	0.724	0.836	0.033q
D (lb)	130.0	124.0	6.18q
T_s(lb)	11.0	10.6	0.528q
T_H (lb)	8.1	7.8	0.388q
"Scallop" radius (in.)	12.1	11.5	11.77

$$E_{\ell} = 54,000 \text{ lb} . \tag{32}$$

Where

ℓ = 2 ft,

E_{ℓ} / ℓ = 27,000 lb per foot.

The line of length, L, is composed of three segments - the riser line, the suspension lines, and a short joint in which the two overlap. The material used is HT-1; as in Reference 42 the stiffness-to-strength ratio of HT-1 was taken as 8.66. The rated strength of the suspension lines is 1000 lb for each of the 12 lines. Multiplying by 8.66, the modulus of these lines is 104,000 lb. The effective length of these lines is 80.31 in., giving a stiffness for these lines of 104,000/70.31 = 1480 lb per inch. The riser line is composed of six webbings, each rated at 3000-lb ultimate strength. Multiplying by 8.66, the riser-line modulus is found to be 156,000 lb. Dividing by the effective length of 52.76 in., the stiffness is 2960 lb per inch. The overlap joint is 8 in. long. In this region the modulus was assumed to be the sum of the moduli of the suspension lines and riser line (104,000 plus 156,000 = 260,000 lb). The stiffness then is 260,000/8 = 32,500 lb per inch. Because the riser line, suspension lines, and overlap joint are in series, the stiffness of the composite was obtained by adding the reciprocals of the individual stiffness and then taking the reciprocal of the sum. Thus,

$$\frac{E_L}{L} = \frac{1}{\frac{1}{32,500} + \frac{1}{1480} + \frac{1}{2960}}$$

$$= 957 \text{ lb per inch}$$

$$= 11,500 \text{ lb per foot.} \qquad (33)$$

The important values above were rewritten for convenience as follows:

$$m_1 = 1.088 \text{ slugs}$$

$$m_2 = 0.109 \text{ slugs}$$

$$E_\ell/\ell = 27,000 \text{ lb per foot}$$

$$E_L/L = 11,500 \text{ lb per foot}$$

The equations referred to in the following discussion are in Appendix IV. Because the thrusters and canister are the same as in the analysis of test

item TB-1, the initial velocity, V_o, is also the same. Thus,

$$V_o = 32.6 \text{ fps.} \tag{34}$$

Substituting into Equation IV-16,

$$P_{\ell_{max}} = 1682 \text{ lb} \tag{35}$$

This was the maximum load in the deployment-bag line, giving a large margin of safety. The velocity, V_1, was obtained by substituting into Equation IV-17. Thus,

$$V_1 = 29.6 \text{ fps.} \tag{36}$$

The drag values, D_1 and D_2, were obtained by multiplying the values from the TB-1 analysis by the ratio of the dynamic pressures. Thus,

$$D_1 = (104.5)\left(\frac{255}{200}\right) = 133 \text{ lb} \tag{37}$$

$$D_2 = (425.5)\left(\frac{255}{200}\right) = 542 \text{ lb} \tag{38}$$

$$D = D_1 + D_2 = 675 \text{ lb} \tag{39}$$

The drag, D, was assumed to act over a length of approximately 10 ft. Substituting into Equation IV-20 gives

$$V_2 = 110.2 \text{ fps.} \tag{40}$$

This is the velocity of the parachute pack and canister at the instant of riser line stretch. The deployment bag is held shut at the front by a very light cord; therefore, the breakaway load was neglected. Proceeding to the second phase, the initial conditions were

$$V_2 = 110.2 \text{ fps}$$

$$X_2 = 0$$

Equation IV-32 gives

$$C_1 = -0.00579 + \frac{0.17}{i} \tag{41}$$

Equation IV-33 gives

$$C_2 = 0.00579 - \frac{0.17}{i} \tag{42}$$

Equation IV-36 gives

$$P_{L_{max}} = 4043 \text{ lb} . \tag{43}$$

This is the maximum load in the riser line and suspension lines during deployment. Table 19 summarizes the results of the preceding analysis.

TABLE 19 - APPLIED LOAD SUMMARY OF SP-5 COMPONENTS*

Item	Gore fabric (lb/in.)	Meridian webs (lb)	Suspension lines (lb)	Inlet hoop (lb)	Riser (lb)	Deployment bag line
Static loads						
λ = 10.7 percent	0.724	7.91	11.0	8.1	130	. . .
λ = 20.5 percent	0.836	7.39	10.6	7.8	124	. . .
Deployment loads*	. . .	. . .	. . .	. . .	4043	1682

*Deployment loads are for SP-3.

5. MATERIAL QUALIFICATION

a. General

Features of the free-flight environment, together with characteristics peculiar to textiles, required the consideration of several criteria influencing the selection of materials for decelerators. To select the materials to be used in the construction of small supersonic parachutes, it was necessary to consider the effects of probable overloading, static and dynamic loading, seam efficiency, temperature, and safety. After the basic material and its required strength were determined from the above factors, the parameters of cloth

weight, thickness, porosity, flexibility, and weave were considered, together with fabricating and coating techniques, in the selection of the cloth.

b. Approach

(1) Design Factors

Initially, material for the parachutes was selected upon the basis of tenacity (strength-to-weight ratio) versus temperature. Figure 42 indicates (1) that at temperatures below approximately 320 F, cloth woven from nylon provides the most efficient structure and (2) that at much above this temperature, Nomex cloth is required. Once the basic material was selected, the required room-temperature strength was determined by increasing the calculated working load for the cloth by the appropriate design factors.

Test points attained in previous programs using the later versions of the Cree missile were normally at lower altitudes and lower Mach numbers than expected. This resulted in loadings up to twice as great as had been expected. It seemed reasonable to anticipate similar overloads in dynamic pressure

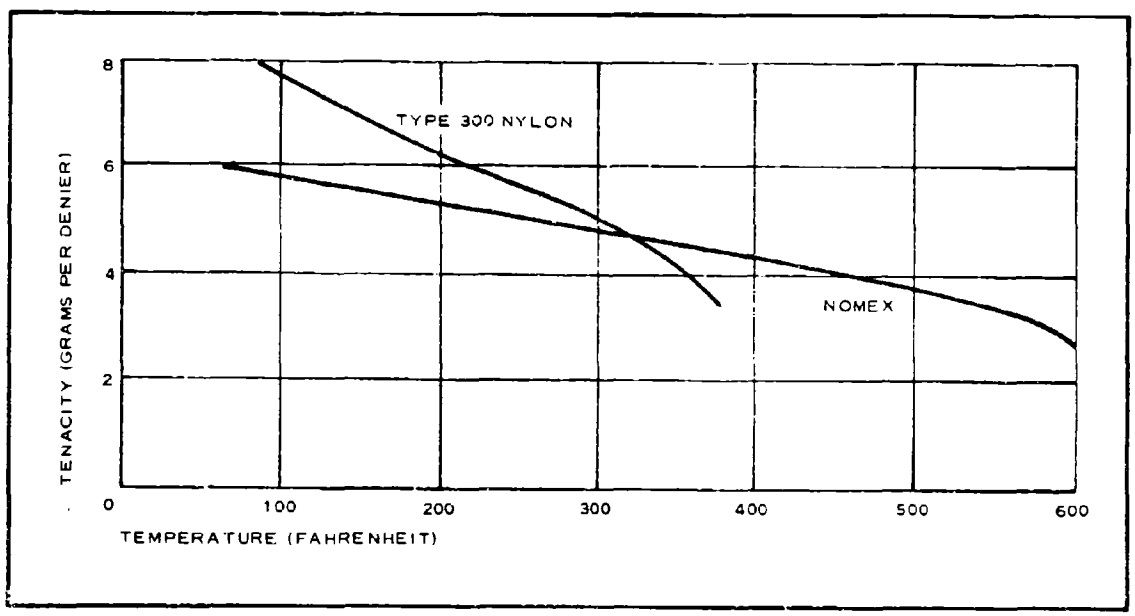

Figure 42 - Yarn Tenacity versus Temperature

when a new missile is used. Thus, an overload range of 1.6 to 2 was estimated.

It is a well-established fact that rapid or dynamic loadings on an elastic structure result in higher stress values than does an equal-valued static load. These stress values are typically twice as great with the dynamic loadings; a factor of 2 was applied to the calculated static stress to account for this effect.

Previous tests to establish seam efficiencies indicated that the selected sewn seam ran 80 to 85 percent efficient. Thus, a seam-factor range of 1 to 1.2 was established.

Since listed material strength data are generally based on room temperature results, it is necessary to convert these data for use at other temperatures. The temperature conversion can be determined from the results presented in Figure 42 for the materials listed. A temperature-factor range of 1 to 2 was used initially with further refinements being based on the thermodynamic analysis. A normal safety factor of 1.5 was selected.

To select initially the materials needed, the static stress value was multiplied by the product of the following design factors:

1. Test-point overload - 1.5 to 2
2. Dynamic loading - 2
3. Seam efficiency - 1 to 1.2
4. Temperature - 1 to 2
5. Safety - 1.5

(2) Cloth Selection

Once the cloth strength was determined, a specific cloth was selected. In making this selection several parameters were considered, including cloth weight, thickness, porosity, flexibility, and weave.

The weight, thickness, and flexibility are interrelated and are considered

from a packaging standpoint. Maximum flexibility and minimum cloth thickness are desirable to facilitate packaging and to keep the required package volume to a minimum. The cloth porosity and weave also are interrelated. To obtain the desired roof porosity and yet maintain adequate cloth strength requires the use of weave constructions that are not too commonly used. It was found that a mock leno weave in combination with high-twist yarns (14 turns per inch) best served this purpose. The mock leno weave involves the weaving of groups of yarns in both the warp and fill directions. The fill yarns are locked in place by having a portion of the warp-yarn group woven both over and under each fill-yarn group. The relative positions of the warp yarns change as they cross each successive fill-yarn group. This method of locking yarns eliminates the sleaziness of the open-mesh weave. The porosity can be varied by varying the yarn counts, the yarn twist, and the coating. Variation of the yarn count affects the cloth strength, which is not always desirable; as an alternative, the yarn twist can be varied. Increasing the yarn twist decreases the diameter of the yarn, thereby increasing the porosity of the cloth for a given warp and fill count. This latter method is useful only within a limited range.

Elastomeric coatings were used as a means of sufficiently reducing the porosity of existing weaves and protecting the basic material in accordance with temperature requirements. At moderate temperatures, neoprenes and polyurethanes were most common; at elevated temperatures, silicone rubbers and fluorinated elastomers were used. (See Appendix I for an investigation of high-temperature coatings.) In addition, the individual coatings were considered on the basis of their flexibility and their function of locking loose-weave yarns in place.

(3) Seam Development

In the fabrication of the flight article, both adhesive systems and the use of sewn seams were considered. The fact that most flexible adhesive systems tested had little strength at elevated temperatures precluded their use. Those that did develop moderate strength at higher temperatures required

an excessive seam lap. High-strength, high-temperature adhesives were too rigid to be used. For these reasons, sewn seams were given primary consideration.

To establish sewn-seam and joint details, several parameters were considered. These parameters included joint configuration, thread size, number of rows of stitching, and number of stitches per inch. In general, seam or joint efficiencies will benefit by the following:

1. Use of a double-felled seam, instead of a French or simple lap seam
2. The use of more stitches per inch to an optimum of about 11
3. Use of the lock stitch (301) rather than a chain stitch (401)
4. Maximum number of rows of stitching in accordance with sound design principles
5. Use of heavier thread, within certain limitations, even where lighter thread does not rupture under application of load

(4) Material Tests

The above axioms provided a basis for the selection of a base cloth from which to initiate seam designs. Since several different cloths and seam designs were available, it was necessary to select the most suitable by tensile testing with an Instron machine.

The candidate base cloths and the seam designs were tested in a similar manner. The specimens were approximately 1-1/2 in. wide with the test width raveled to 1.0 in. The gage length was 6 in. and the load rate was 50 percent or 3 in. per minute. The candidates were screened at room temperature; the final seam design and cloth were validated at elevated temperatures. This was accomplished by using a Missimers oven in conjunction with the Instron tester. The test specimens were allowed to condition for 15 min at temperature and an additional 5 min after they were placed in the test jaws of the machine.

The coatings were selected upon the basis of their temperature capability. The porosity of the base cloths and the leak rate of the coated fabrics were measured. The cloth porosity was established in accordance with method 5450 of Federal Specification CCC-T-191B. The fabric leak rates were measured with a Cambridge fabric permeameter. Where the leak rate was greater than the capacity of this equipment, the equipment was modified and the rate was established by a flowrator.

At elevated temperatures, leak rates were determined by use of a high-temperature-premeability vacuum chamber. In this chamber the specimen is heated by quartz lamps; the pressure differential is obtained by the proper vacuum in the chamber with the high-pressure side of the specimen vented to the atmosphere. The leak rate was measured with a flowrator.

Major decelerator components such as riser lines, riser-line attachments to the decelerator and payload, and keeper rings were tested to ensure adequate strength. Wherever possible, a Baldwin testing machine was used. In cases where biplanar loading was required, such as in testing keeper rings, special test setups were used.

c. Example (SP-3)

(1) Applicable Techniques

Specific values for the design factors described in Item b (1), above, were chosen for each of the parachute components of SP-3. These values were used, together with the structural requirements, to determine the required quick-break strengths of candidate materials at room temperature.

Candidate materials and jointing techniques selected by earlier tests were applied to actual components. The components were tested to failure, and their static margins were computed.

A cloth weave was chosen to satisfy the porosity parameter of the roof, and when required (for SP-3a), the roof was coated to reduce the flow rates to correspond to the requirements at higher Mach numbers.

(2) Results

The values of the design factors, strengths, and static margins for the SP-3 parachute components are presented in Table 20 for the static loads and in Table 21 for the dynamic loads

Important roof-material design parameters included strength at temperature, porosity, and capability of fabrication. These parameters are all interrelated. A minimum Nomex cloth strength, at room temperature, of 100 lb per inch and a porosity of 1100 cfm was desired originally to duplicate a prior low-temperature roof material. The desired porosity could be met exactly only by fabricating a special-weave cloth. Since this involved 4 to 6 weeks lead time, it was decided to use an available Stern and Stern pattern No. HT-68. This is a Nomex cloth, 3.38 oz per square yard, with a porosity of 840 cfm and a strength of 183 lb per inch in the warp direction and 149 lb per inch in the fill direction. To minimize the lower porosity effects, 1/2-in.-wide roof-gore seams and tapes were used rather than conventional 1 in.

Roof-gore seam specimens were fabricated from similarly constructed nylon materials to evaluate various seam configurations. Once the Nomex materials were available, seams corresponding to the best of the screened specimens were fabricated and tested. The selected seam configuration is shown in Figure 43.

The test specimens were sewn with Size E Nomex thread at 7 and 11 stitches per inch. At 7 stitches per inch, a seam strength of 133 lb per inch was obtained; at 11 stitches per inch, a 129-lb-per-inch average was obtained based on five test specimens each. On the production item the thread size was increased to Size F-F and 9 to 11 stitches per inch at no sacrifice in strength. Size F-F Nomex thread was not available for the earlier tests.

The parachute-skirt material selected was a specially woven Nomex cloth. This cloth carries Stern and Stern pattern No. HT-72. This is an 8.67-oz-per-square-yard cloth, with a warp strength of 374 lb per inch and a fill strength of 352 lb per inch, as measured at GAC.

A procedure similar to that used in screening roof-gore seams was used to

TABLE 20 - MATERIAL SELECTION AND STATIC MARGINS FOR SP-3

Item	Gore fabric		Suspension (meridian) lines	Riser	Inlet hoops
	Skirt	Roof			
1. Design factors					
Overload	2.0	2.0	2.0	2.0	2.0
Dynamic load	2.0	2.0	2.0	2.0	2.0
Seam efficiency	1.2	1.2	1	1	1
Temperature	1.43	1.43	1.25	1.11	1.43
Safety	1.5	1.5	1.5	1.5	1.5
2. Product of factors	10.3	10.3	7.5	6.66	8.6
3. Static strength (lb)	6.82 per inch	6.82 per inch	124.7	1458	85.5
4. Required strength lb (Item 2) × (Item 3)	70.5 per inch	70.5 per inch	930	9730	735
5. Allowable strength, lb (room temperature)	352	149	1000	18,000	1000
6. Safety margin $\frac{\text{Item 5}}{\text{Item 4}} - 1$	4.0	1.12	0.07	0.85	0.36
7. Materials used	Stern and Stern No. HT 72-58 Nomex	Stern and Stern No. HT 68-46 Nomex	MIL-W-5625 1/2-in.-wide Nomex	MIL-W-5625 Nomex (6 lines)	MIL-W-5625 Nomex (1000 lb)

determine the best roof-to-skirt seam. Similar nylon materials were used for screening, and verification was later carried out using Nomex materials. The seam configuration that was adapted is shown in Figure 44.

Because Size F-F Nomex thread was not available, Size E thread was used for the test specimens. At 7 stitches per inch a seam strength of 130 lb per inch was obtained; at 11 stitches per inch, the average strength was 113 lb

TABLE 21 - DEPLOYMENT LOADS AND STATIC MARGINS FOR SP-3

Item	Suspension lines	Riser
Design factors		
Temperature	1.00	1.00
Seams (based on rated strength)	1.00	1.00
Overload	2.0	2.0
Safety	1.5	1.5
Product of factors	3.0	3.0
Deployment load (lb)	4043	4043
Required strength (lb)	12,129	12,129
Available strength (lb)	12,000	18,000
Safety margin	-0.01	0.49

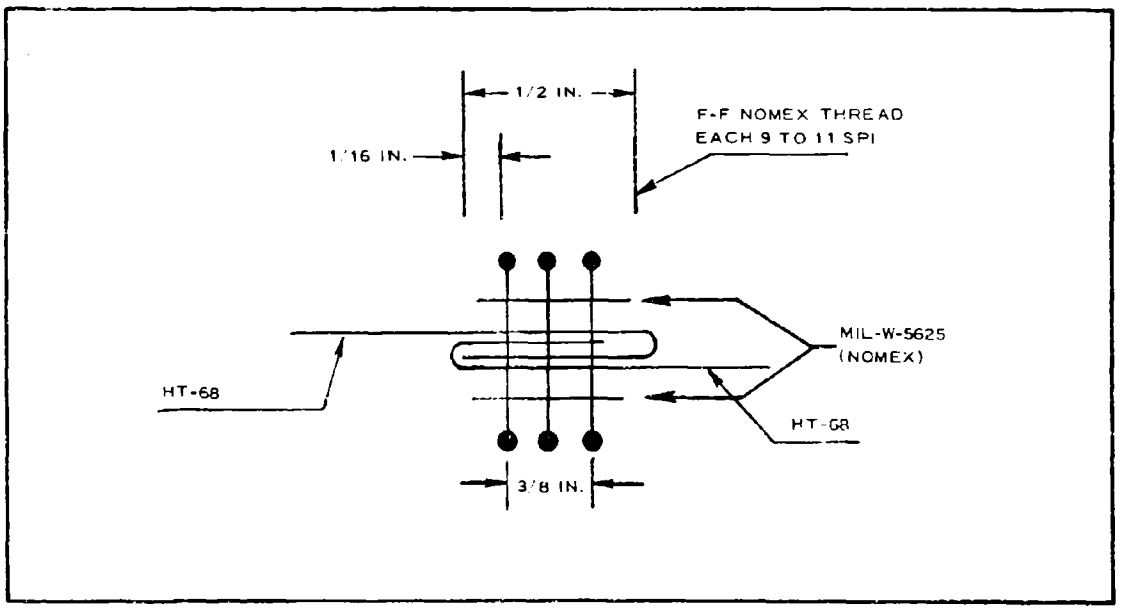

Figure 43 - Roof-Gore Seam

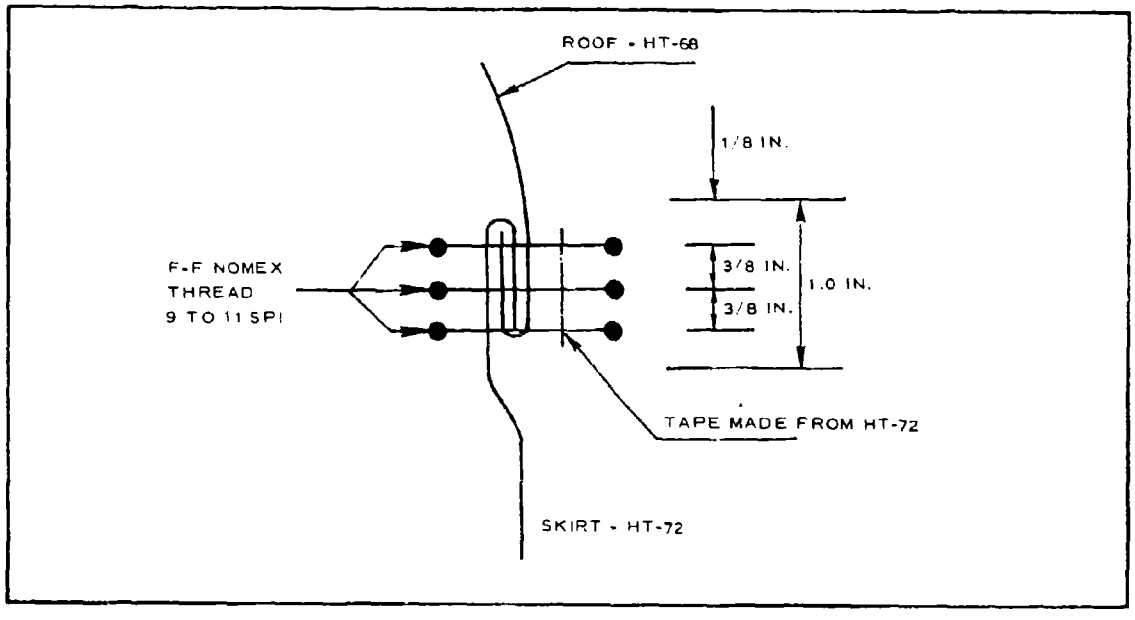

Figure 44 - Roof-to-Skirt Seam

per inch. These results represent an average of five tests each. It should be noted that the seams described above had a gage length of 6 in. and were loaded at a rate of 3 in. per minute.

Specially woven Nomex webbings and tapes were obtained for use in fabricating the unit. They were woven in accordance with the specifications governing nylon webbings and tapes. MIL-W-6525 1/2-in.-wide Nomex webbing had a room-temperature strength of 1120 lb. Nomex tape woven in accordance with MIL-T-5038 Type IV specifications had a strength of 1020 lb. These values are an average of five specimens each. The specimen gage length was 12 in. and loaded at a rate of one inch per minute.

The splice joining two radial lines to one riser has the configuration shown in Figure 45. The 1/2-in.-wide MIL-W-5625 Nomex webbing failed at the edge of the sewing at a total average load of 2060 lb.

Test Item SP-3a was identical structurally to Item SP-3 in all respects except that HT-86 was substituted for HT-68 roof material. HT-86 is also

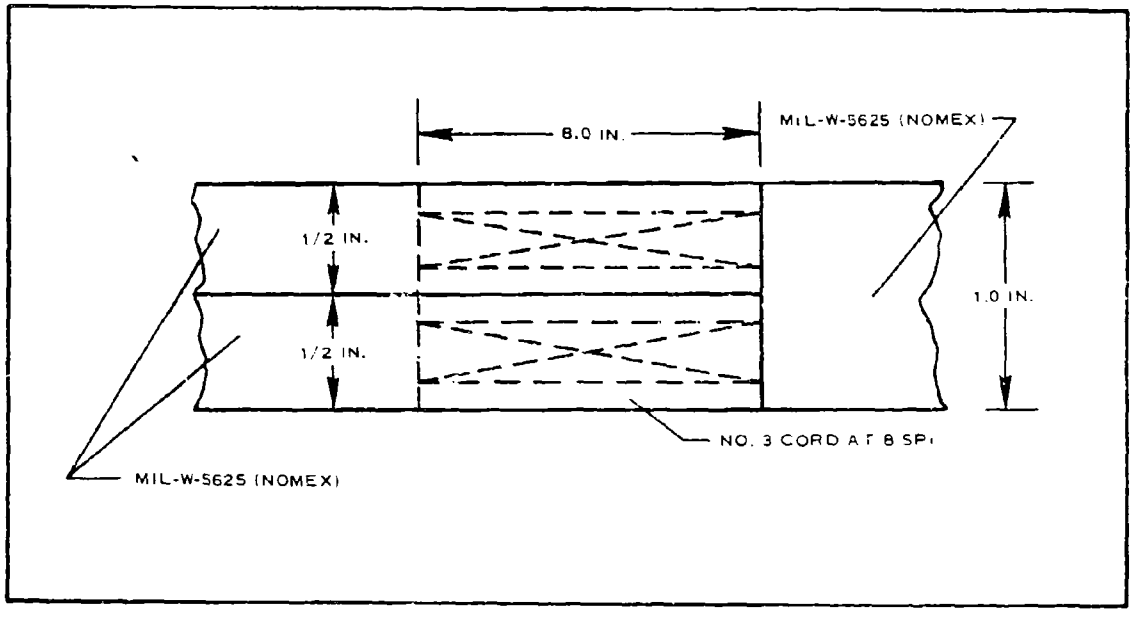

Figure 45 - Radial-to-Riser-Line Attachment

Nomex, of the same weight, but with a porosity of 799 cfm per square foot minimum at 1/2 in. H_2O and a warp strength of 172 lb per inch and a fill strength of 185 lb per inch. Since there is very little difference between HT-86 and HT-68, the seam-validation effort carried out under SP-3 is applicable to SP-3a.

After this unit was fabricated, it was learned from the wind-tunnel tests of Reference 3 that a lower roof porosity was required at the anticipated operational Mach number. Therefore, the inside of the roof, excluding the end cap, was coated to reduce the porosity. The area coated was 22 in. in diameter. The coating used was Dow-Corning Silastic 131. This coating was selected because of its high-temperature capability and its ease in handling. The roof porosity after coating was between 400 and 500 cfm as measured on a Frazier Permeameter.

6. DESIGN AND FABRICATION

a. General

During Phase I, two parachutes (SP-1 and SP-2) were fabricated to prior designs for free-flight tests. Units SP-3, SP-5, and SP-7 were newly designed to their inflated (isotensoid) shapes. Two units of SP-3 (SP-3 and SP-3a) and one unit of SP-7 (designed for function at the test point of SP-2) were fabricated and delivered for wind-tunnel tests. The designs of all parachutes, with the exception of SP-1, required Nomex. The isotensoid parachute is described in Items b and c, below.

b. Approach

(1) Decelerator

The isotensoid parachute shown in Figure 46 is constructed of 12 gores, which are patterned to provide the desired canopy contour and to provide the correct lobe radius for the isotensoid structure. The porous roof portion of each gore (Item 6 in Figure 46) is made of a woven-mesh cloth, and the skirt portion (Item 4) is made of a heavier, tightly woven cloth. Both sections are arranged with the yarn direction at a 45-deg bias at mid-gore to facilitate the forming of the lobe radius.

The 12 radial suspension lines are formed by placing six continuous webs around the canopy and all the way forward to the confluence point (see Item 2 in Figure 46). Over the canopy, each web is sewed into, and becomes a part of, a gore main seam. Forward of the canopy, the suspension lines are folded and stitched into approximately a round cross section to minimize adverse aerodynamic effects. At the confluence point, the 12 webs are stitched in pairs to the six web ends of the riser line. The riser line is constructed from three heavy webs doubled back to form the attachment loop and to provide the six webs of the riser.

The inlet reinforcing web (Item 3 in Figure 46) and the outer edge of the skirt are arranged in a scalloped pattern forming a catenary between each pair of

suspension lines. This construction is required to balance the fabric stresses properly in the inlet area.

The roof cap (Item 7 in Figure 46) is a circular patch of the tightly woven cloth. This six-inch-diameter patch not only terminates the ends of the gores but also provides a nonporous area at the apex of the parachute.

All gore seams are the double-felled type. Seams joining two or more pieces of mesh require the addition of a tape against the mesh surface to provide adequate material area for stitching. For the main seams, the radial web running over the top side of the seam, as described above, takes the place of this tape. A light tape is placed on the inner side of the seam in the roof section. The roof-to-skirt seam is a one-inch-wide double-felled seam with the roof mesh placed on the outer fold, thus requiring that a folded bias tape be added over the seam.

(2) Deployment Bag and Sequence

The deployment bag for deploying all the small supersonic parachutes is a nylon cylindrical bag 8 in. in diameter and 12 in. long. Four heavy nylon webs are sewed to the outer surface, running longitudinally and equally spaced around the bag. They extend into a bridle at the back end of the bag for attachment to the deployment canister.

The schematic of the parachute deployment system is given in Figure 47. This system is illustrated with a series of six sequences that represent various times and events from the start of container separation to parachute inflation. Design considerations were for a simple and reliable deployment system that would progressively deploy first the riser, then the suspension lines, and then the canopy.

Figure 48 shows a test-unit assembly. It illustrates the outer lock-cord and cutter arrangement at the forward end of the bag and the bridle at the aft end.

Figure 49 shows a partially packed parachute. It illustrates the inner lock loops tied with the light linen break cord, which surrounds the bundle of

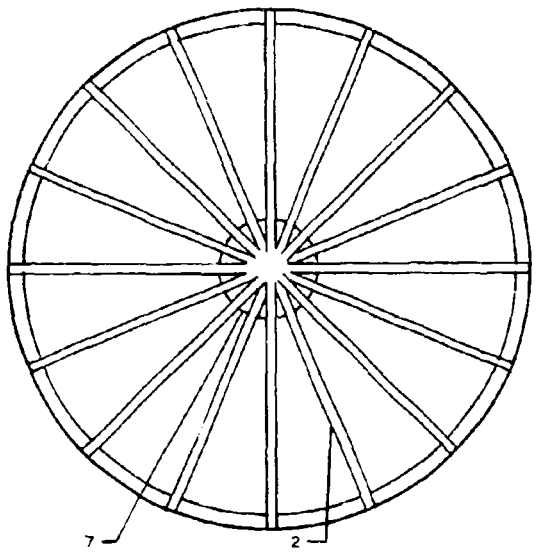

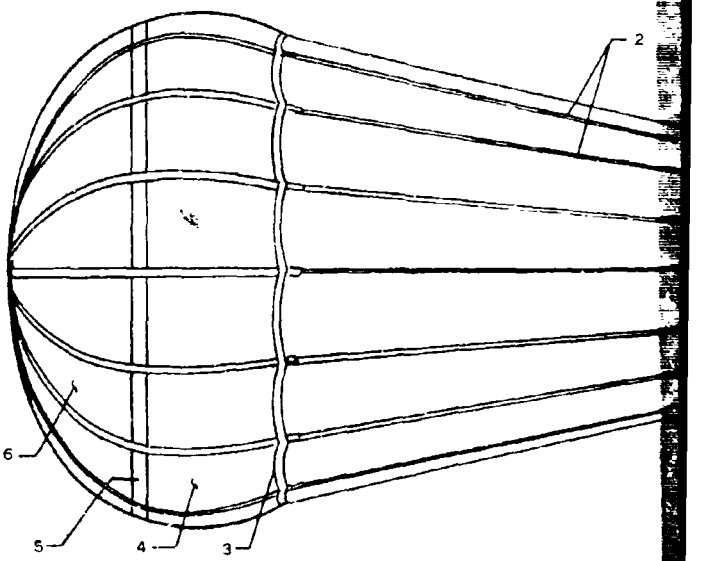

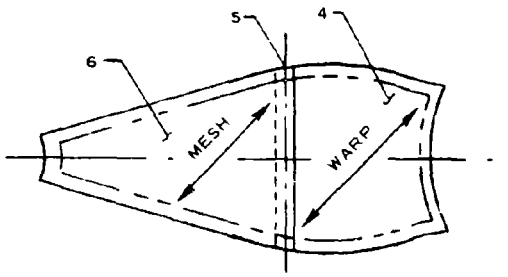

CANOPY GORE PATTERN

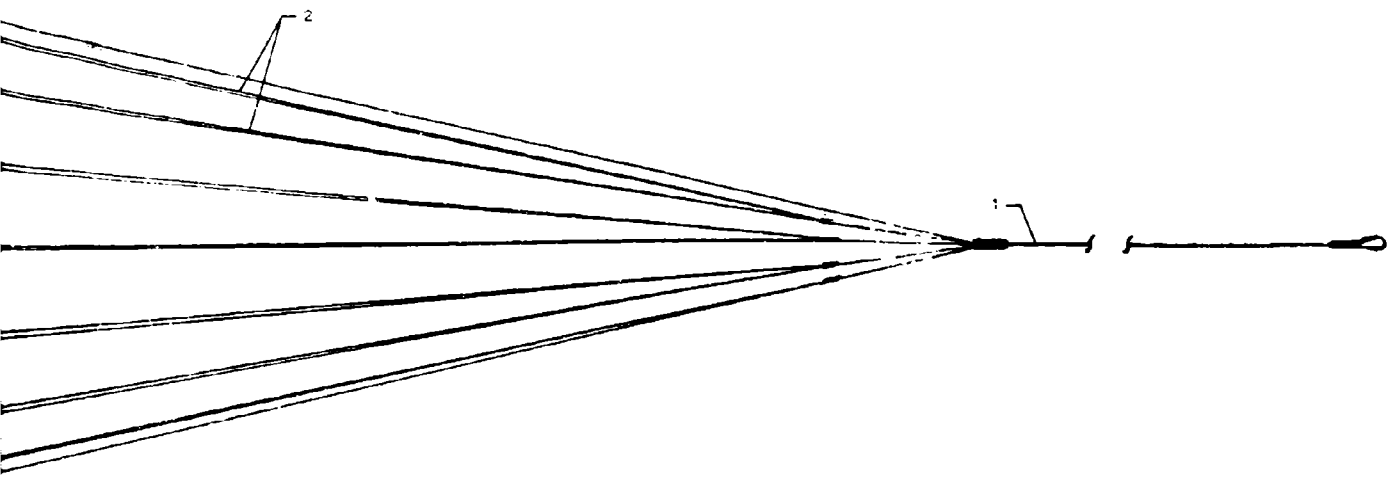

KEY:

1. RISER LINE
2. RADIAL/SUSPENSION LINES
3. INLET REINFORCING WEB
4. SKIRT-GORE PANEL
5. CENTER-LINE ROOF-TO-SKIRT SEAM
6. ROOF-GORE PANEL
7. ROOF CAP

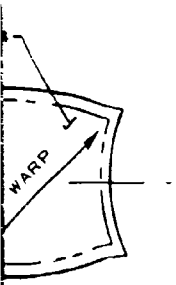

TERN

Figure 46 - Small Supersonic Parachute (Isotensoid)

2

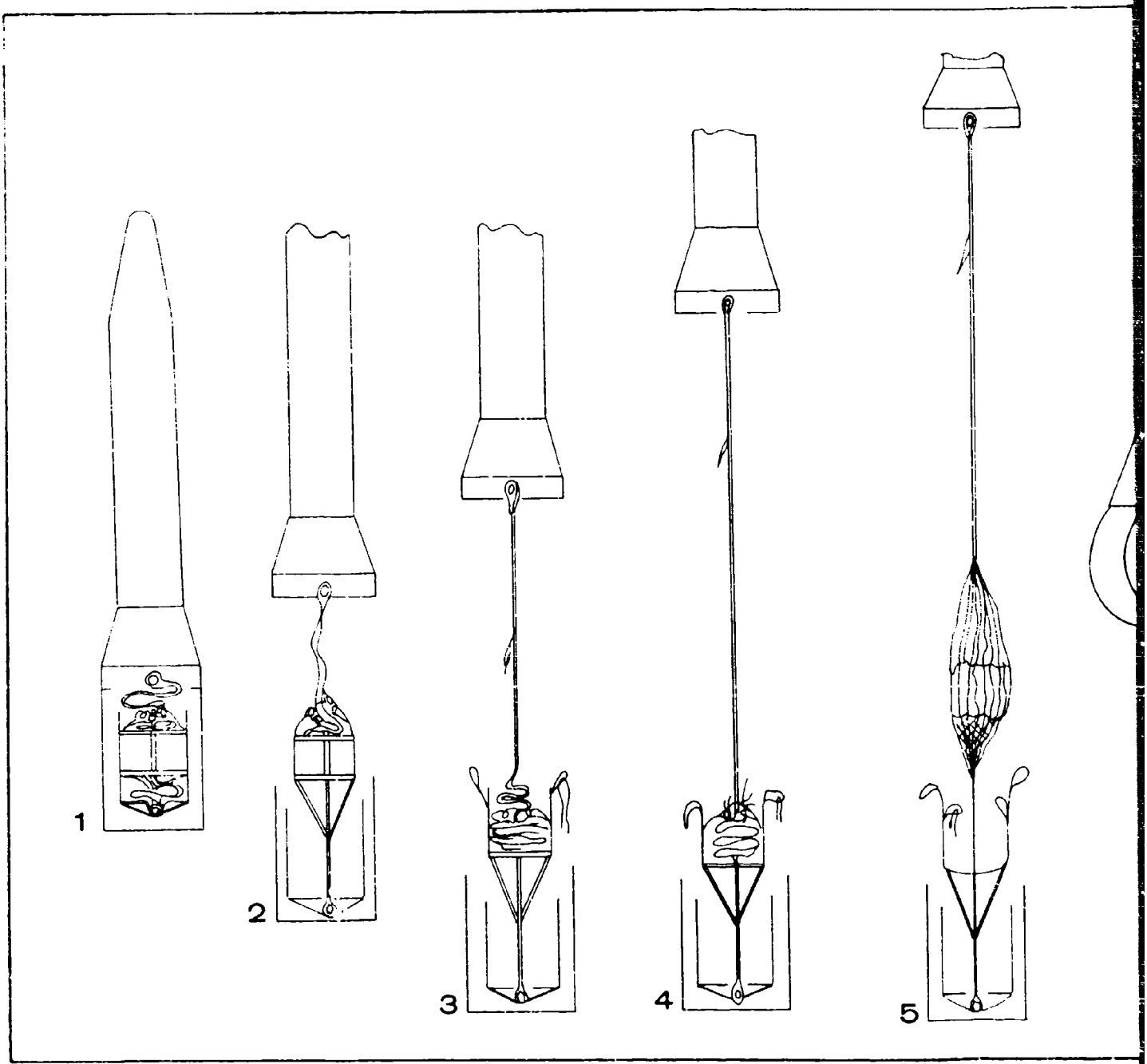

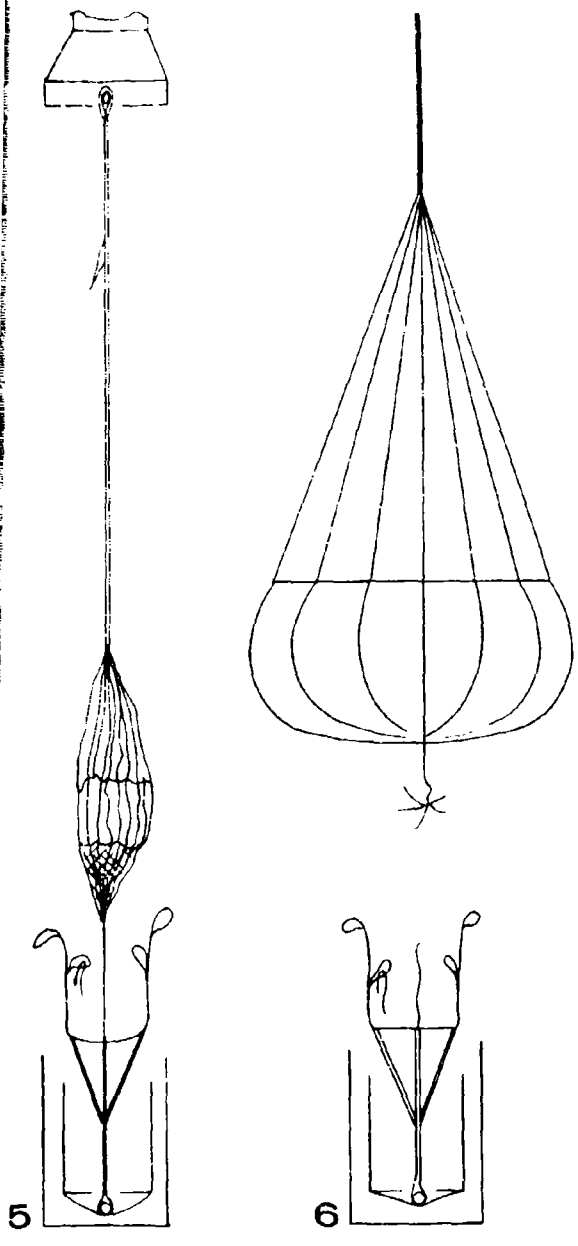

1 VEHICLE IN FLIGHT BEFORE DEPLOYMENT BEGINS. PARACHUTE PACKAGED IN DEPLOYMENT BAG; RISER ATTACHED TO VEHICLE; BAG-BRIDLE LINE ATTACHED TO AFT SECTION OF CANISTER.

2 CANISTER SEPARATED FROM VEHICLE. DEPLOYMENT BAG OUT OF CANISTER, BEING ACCELERATED BY CANISTER THROUGH BRIDLE LINES. RISER LINES SLIGHTLY EXTENDED; ONE RISER LINE HAS METAL CORD-CUTTER KNIFE. NYLON CORD LACED THROUGH OUTER LOCK LOOPS OF DEPLOYMENT BAG AND THROUGH KNIFE. FUNCTION OF CORD IS TO CLOSE END OF BAG, RETAINING PARACHUTE AND RISER IN DEPLOYMENT BAG WHEN ACCELERATING LOADS ARE APPLIED TO BAG BY CANISTER.

3 CANISTER AND DEPLOYMENT BAG FURTHER AFT OF MISSILE; KNIFE HAS CUT LOCK CORD, ALLOWING RISER LINES TO DEPLOY.

4 FOUR INNER LOCK LOOPS SEWED INSIDE BAG; LIGHT LINEN BREAK CORD LACED THROUGH LOOPS JUST FORWARD OF CANOPY INLET. THIS LOCK LOOP AND BREAK CORD ARRANGEMENT HOLDS CANOPY IN BAG UNTIL LINES ARE FULLY EXTENDED.

5 DEPLOYMENT BAG OFF PARACHUTE. APEX OF CANOPY STILL ATTACHED TO BAG WITH LIGHT NYLON BREAK CORD TO ENSURE FULL CANOPY EXTENSION.

6 PARACHUTE FULLY INFLATED; BREAK CORD BROKEN; DEPLOYMENT BAG AND CANISTER ENTIRELY SEPARATED.

Figure 47 - Details of Parachute-Deployment Sequence

2

Figure 48 - Small Supersonic Parachute in Deployment Bag

Figure 49 - Partially Packaged SP-3A Parachute

suspension lines. It also shows the stowage of the suspension lines in the loop-retainer tray. The retainer tray is attached to the bag to ensure progressive line deployment from the forward end of the retainer.

c. Example (SP-3)

The configuration and general construction of the SP-3 parachute have been described in the previous paragraphs. It was constructed entirely of Nomex materials explained in Item 5c, above, except for the use of nylon in the riser because of availability. Figure 50 shows the roof side of the SP-3 parachute, and its deployment bag and the apex-to-bag break cord, as well as the data aids added to the roof. The heavy black nylon yarn, stitched around at a 20-in. diameter, serves as a dimensional reference and, considering the shrinking and melting properties of the nylon, it could serve as a temperature indicator. The large dot and the concentric ring, at two places, are marked with temperature-indicating paints, which are rated to change color when temperatures are exceeded. The SP-3a parachute was constructed identical to SP-3 except that the riser line is Nomex and the roof-gore material and porosity treatment are as described in Item 5c, above.

Figure 50 - SP-3 Parachute

SECTION IV - BALLUTE

1. GENERAL

a. History

Work performed under Contracts AF33(616)-6010 and AF33(616)-8015 demonstrated by model tests and full-scale test that the BALLUTE was a promising device for stabilization and deceleration to Mach 10 for all decelerator-to-payload-diameter ratios tested. Wind-tunnel tests of both pressure-bottle-inflated and ram-air-inflated BALLUTEs indicated excellent performance, with the ram-air inflation offering significant weight advantages. Full-scale tests were conducted under these contracts at transonic and low supersonic speeds using the earlier pressure-bottle-inflated designs.

Two concurrent tasks were conducted during the ADDPEP program. One, undertaken by RTD and NASA personnel, was laboratory tests using 7-in. models at the Arnold Engineering Development Center and at Langley Research Center to extend the pressure data over a greater Mach-number range and to aid in describing the payload wake. The second, by GAC, was to fulfill the need for full-scale data at higher speeds and loadings. Two BALLUTEs were designed and fabricated. Because Design TB-1 was not deployed during the test, a third unit, TB-1a, was fabricated as a replacement and tested as planned. Design TB-2 was designed and fabricated. It will be tested under ADDPEP Phase II.

b. Conditions

The flight conditions used for designing the BALLUTEs have been established by trajectory analyses. The contributing factors and the conditions that define the test point at the time of BALLUTE deployment are listed for each flight-test item in Table 22.

With ASD approval, GAC chose the diameter of the BALLUTE (without fence)

TABLE 22 - BALLUTE TEST CONDITIONS

Item	TB-1	TB-1a	TB-2
Mach number	2.5	2.5	3.8
Altitude (ft)	84,000	80,000	104,000
Dynamic pressure (psf)	212	255	197
Flightpath angle (ascent)	70	70	72
Total weight (lb)	397	397	397
Ballistic coefficient of system, payload plus BALLUTE (psf)	18	18	18
Reynolds number (based on ℓ = 5 ft)	2.8×10^6	3.3×10^6	1.6×10^6
Booster combinations	HJ-N	HJ-N	HJ-N-N

to be 5 ft for all tests, based on estimated weights and available missile volume. The weights of the BALLUTEs were 15 to 20 lb. The combined missile and BALLUTE drag area versus Mach number (M), used to predict flight conditions is presented in Figure 51.

Plots of predicted Reynolds number, Mach number, altitude, dynamic pressure, and load factor after deployment of the BALLUTE are presented in Figures 52, 53, and 54.

c. Configuration Selection

The BALLUTE shape selected was based on the results of wind-tunnel tests at supersonic velocities [23] and isotensoid requirements. This structural-analysis method obtains an all-positive, nearly uniform stress structure; it was used to define the basic shape to meet specific test points (see Appendix II). The analysis indicated that slight changes in BALLUTE shape and inlet positions from those of the solid wind-tunnel model satisfy the all-positive, nearly uniform-stress principle for the test-point conditions.

If the stress-aerodynamic requirement is not satisfied there are two methods to fulfill it. One is to conduct additional wind-tunnel tests of new shapes and

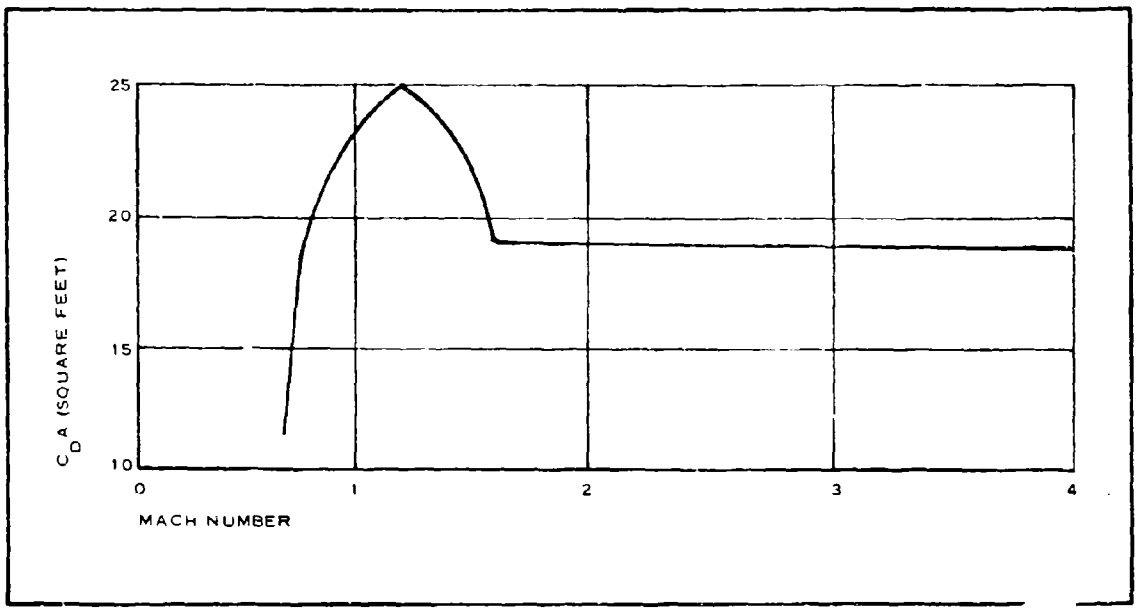

Figure 51 - Test-Configuration Drag Area versus Mach Number (Predicted)

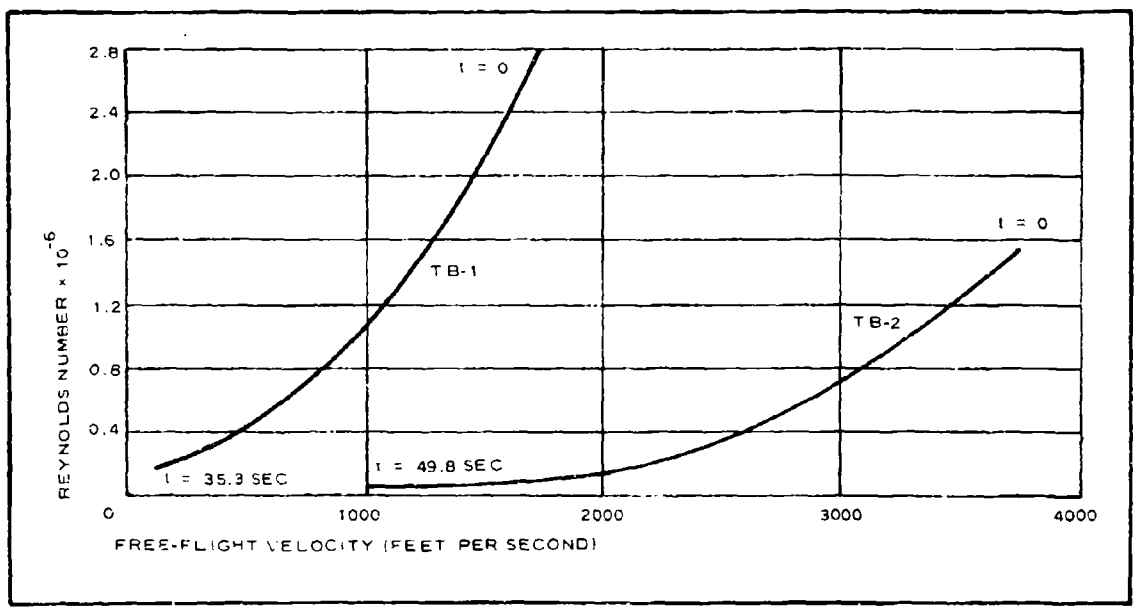

Figure 52 - Reynolds Number versus Free-Flight Velocity (Predicted)

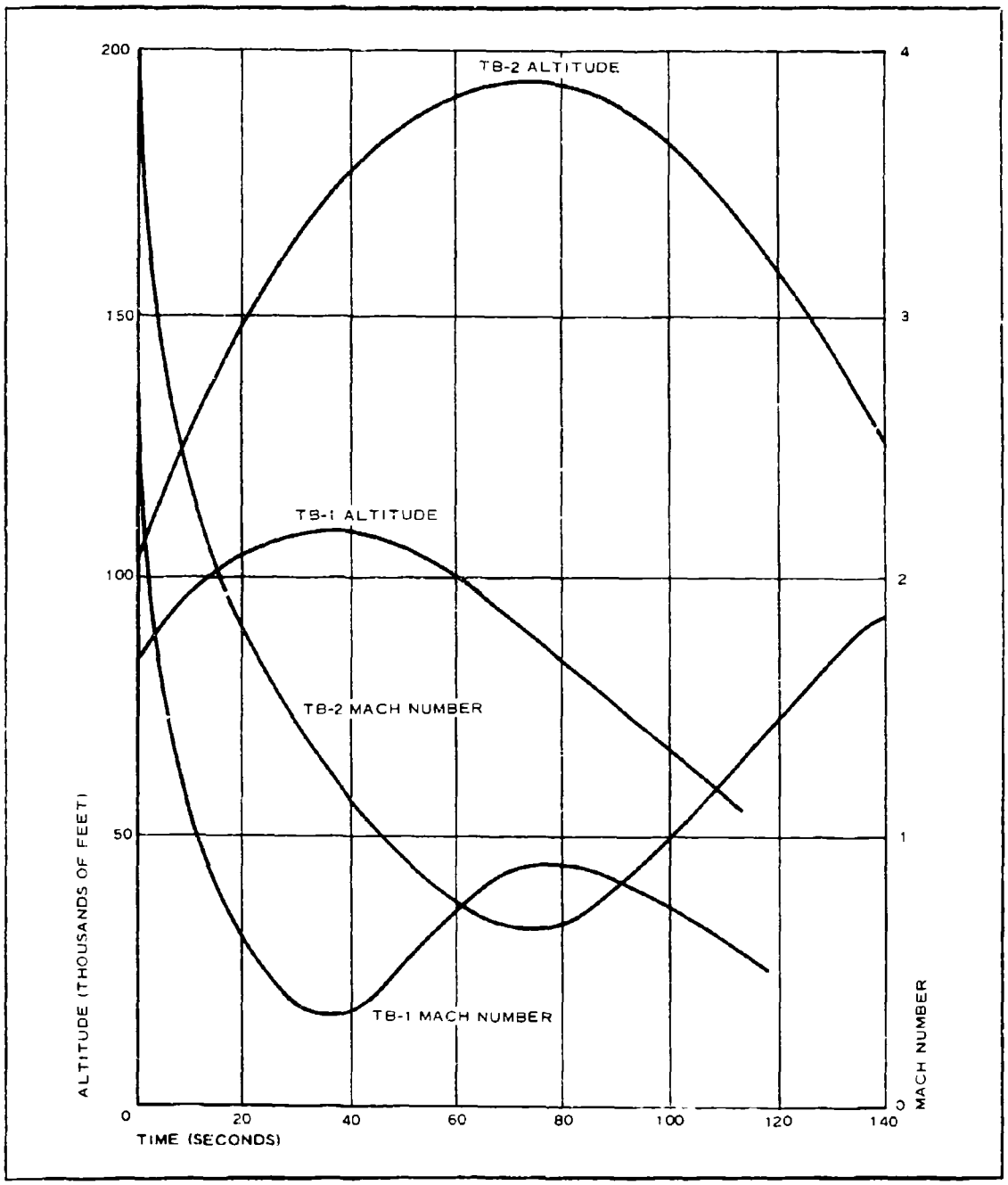

Figure 53 - Mach Number and Altitude versus Time (Predicted)

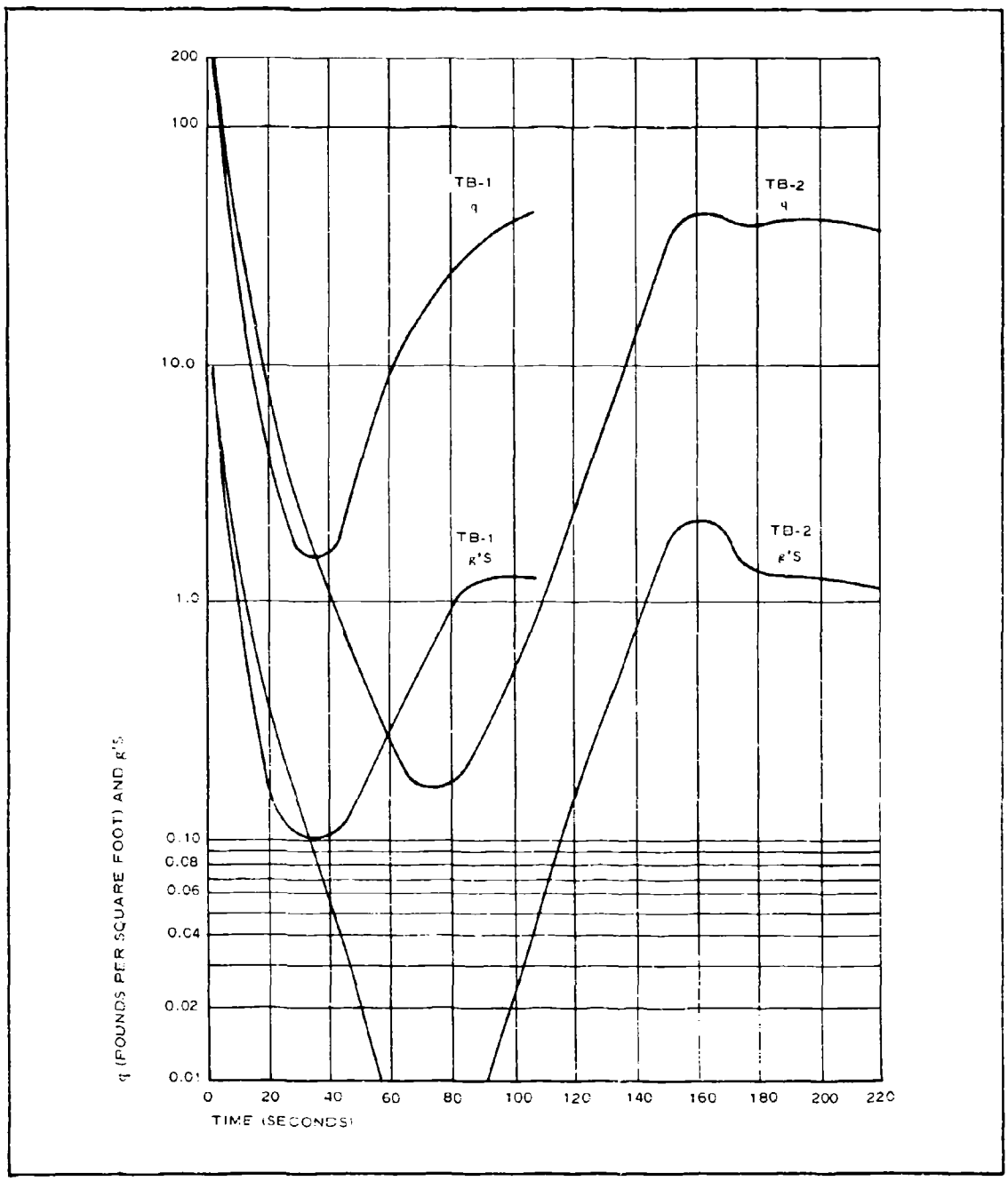

Figure 54 - Dynamic Pressure and Load Factor versus Time (Predicted)

determine the pressure distributions; the other is to extrapolate from available data.

The shape of a BALLUTE can be described by geometric coordinates and ratios. The following are used to describe BALLUTE geometry:

1. Cartesian planar coordinates: y - along center-line, with origin at nose; x - normal to y
2. Maximum radius - R (inches)
3. Linear distance along the surface - S (inches)
4. Surface-inclination angle - θ (degrees)
5. Dimensionless ratios - X/R, Y/R, and S/R

Values of X/R versus Y/R coordinates for TB-1, TB-1a, and TB-2 are presented in Figure 55.

d. Example (TB-1)

(1) Conditions

The design conditions for test item TB-1 are shown in the first column of Table 22. The actual flight conditions at the test-point time (t = 39.2 sec) for TB-1 are presented in Figure 17. The values are very close to the deployment-design values. The values predicted for design, starting after BALLUTE deployment, are indicated on Figures 52, 53, and 54.

(2) Configuration

The coordinates normally are presented as X/R versus Y/R and X/R versus S/R (see Figures 55 and 56).

2. AERODYNAMICS

a. General

The procedure for aerodynamic analysis must establish estimates for wake effects, pressure distribution, base pressure, inlet local velocity, and inflation time. The estimates are based on both analytical and empirical methods.

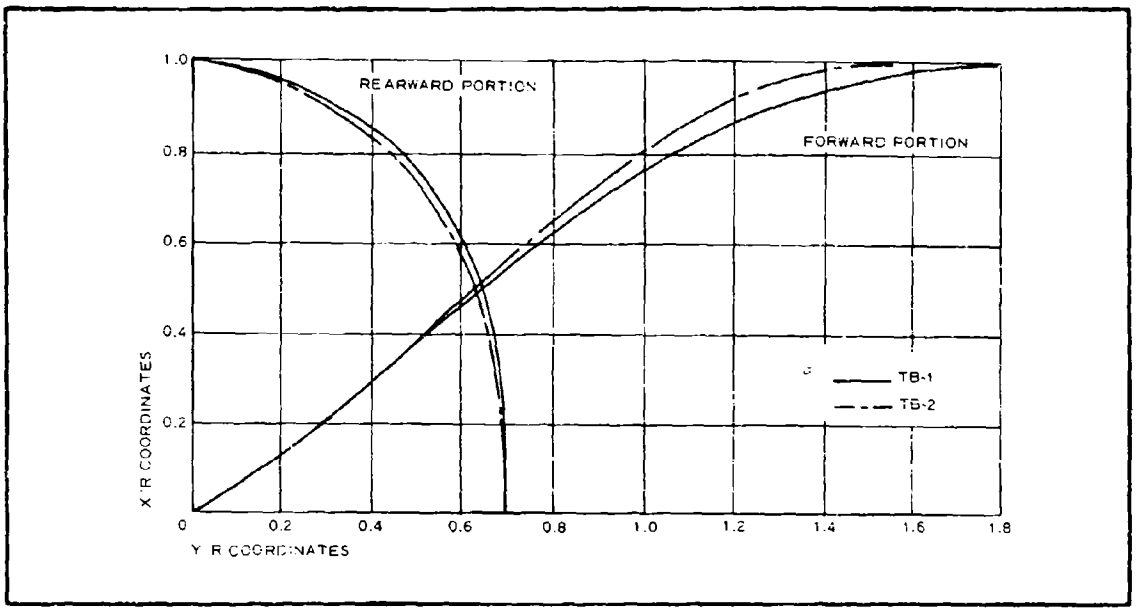

Figure 55 - BALLUTE Coordinates

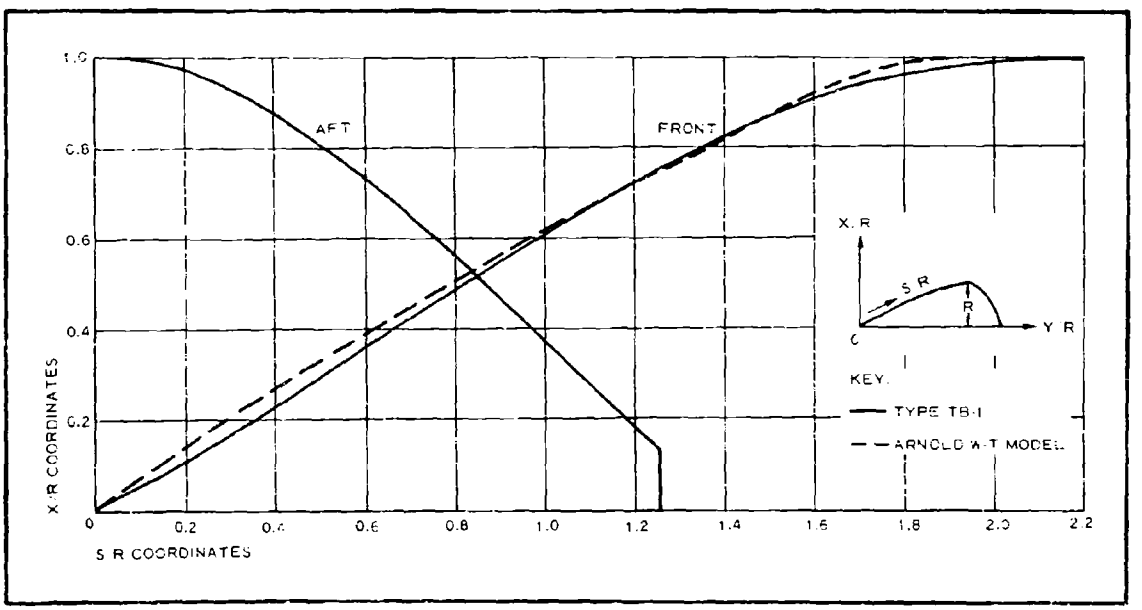

Figure 56 - BALLUTE Geometry Evolution - X/R versus S/R Coordinates

During the program, analytical methods were reviewed and evaluated for application. These methods were evaluated by comparison with each other and with wind-tunnel data.

b. Approach

(1) Analytical

(a) Payload Wake

The aerodynamic approach to the BALLUTE analysis started with initial flow conditions that are influenced by a region consisting of a decelerated inner fluid layer striving to reach free-stream condition by mutual interaction with the outer layer. This region is called the wake. Although the problem of motion of a viscous fluid in a separated boundary layer is not yet solved explicitly, wakes possess some common characteristics such as the following.

1. The wake is separated into two distinct regions - the outer region, where isentropic conditions prevail, and the inner wake, where viscosity is dominant.

2. The free-shear layer between these regions initiates the development of the neck region, which has steep gradients due to the recompression shocks and viscous inner wake.

The important feature of the wake generated by the payload is its influence upon the decelerator placed in its path. Previous experience and wind-tunnel data indicate a significant decrease in pressure coefficient on the forward part of a decelerator.

A typical structure of the flow field in which the decelerator performs is shown in Figure 57. The region of interest is classified as the "near" wake ($6 \leq x/d \leq 12$). In this region at M_∞ (free-stream Mach number)$< < 1$, the wake consists of vortices and the flow is unsteady [24], changing from laminar to turbulent at low Reynolds numbers. Boundary-layer solutions give poor results for the turbulent case. If the flat plate is assumed, however, the wake is then laminar

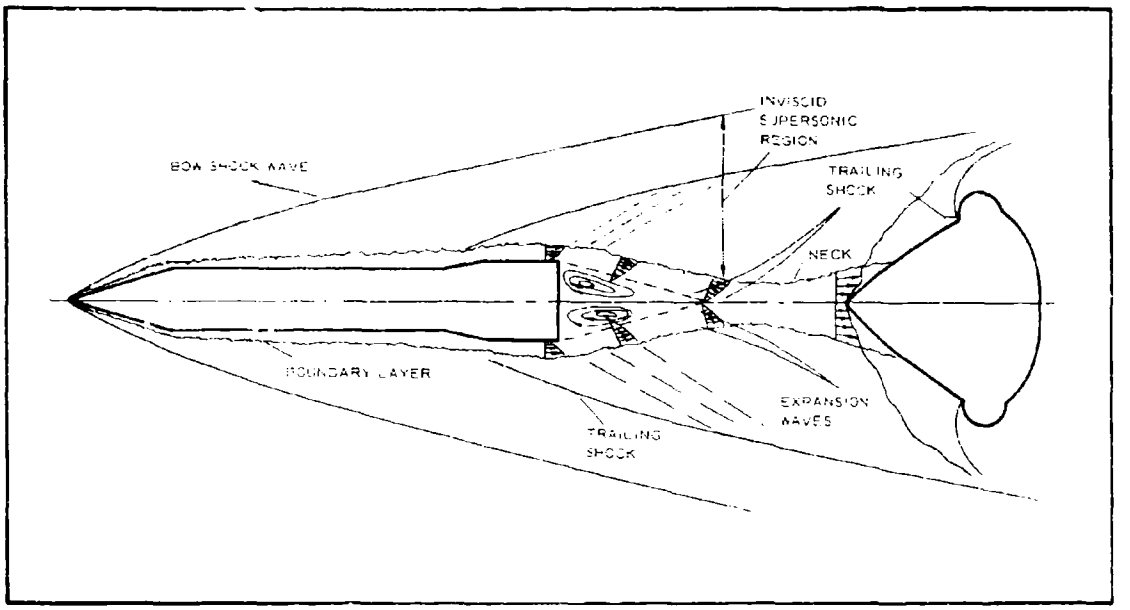

Figure 57 - Typical Payload-Decelerator Flow Field

and analytical solution exists for the far wake (Schlichting). The near wake at $M_\infty < 1$ is formed by two free-shear layers, which converge and form a "neck." In the outer region the Mach number varies. For slender bodies it is close to the free-stream value, but for blunt bodies it "freezes" at about Mach 3, according to Reference 25.

At the supersonic Mach numbers, the laminar shear layer and neck region are rather stable.[26, 27] Boundary-layer approximated solutions are applicable for the inner wake but not near the neck region where rapid changes in the mean profiles occur.[25] The boundary-layer solutions are significant for three main reasons:

1. Detail flow visualization at the decelerator surface
2. Information for inlet geometry, location, and flow inside
3. The nature of the flow in a wake

Theoretical treatment of the wake depends on the conditions existing at the edge, which can be determined either by the inviscid flow field or from wind-tunnel experiments. The pressure distributions in the wake take essentially two shapes - the Gaussian type for the laminar part, and the parabolic for the turbulent.

(b) BALLUTE Flow Field

The equation for the streamline in supersonic flow, as given in Reference 28, is

$$Y_{str} = C + \sqrt{M_\infty^2 - 1}\ (f_1 - f_2)\ , \qquad (44)$$

where

str = Y coordinate of streamline, and

C = constant.

If Function f_1 or f_2 is considered to be constant for the entire field, the particular solutions can be obtained as "waves of one family" or "simple waves."

The concept of the Mach lines, being the lines of propagation of pressure waves generated by the changes of the angles along the body surface, states that these waves physically can be propogated only in the downstream direction. Examination of the BALLUTE forward portion shows that its surface is concave. As a result the Mach lines cross each other at a point forming the Mach-line envelopes.[29] The conclusion is that the shock is formed in the envelope, with its strength decreasing as the distance from the body is increasing. But if the shock strength is not too large, a good approximation is to neglect the gain in entropy at the shock and apply the simple-wave theory behind the shock, treating the surface of the body as being convex to the stream.

Since the local angles of surface inclination to the flow are known and hence the values of Mach angles can be determined, the pressure distribution in terms of the local pressures can be estimated on the basis of Bernoulli's equation, when entropy is assumed to be uniform.[29] Figure 58 shows the typical streamline pattern in the approximate flow field of the forebody.

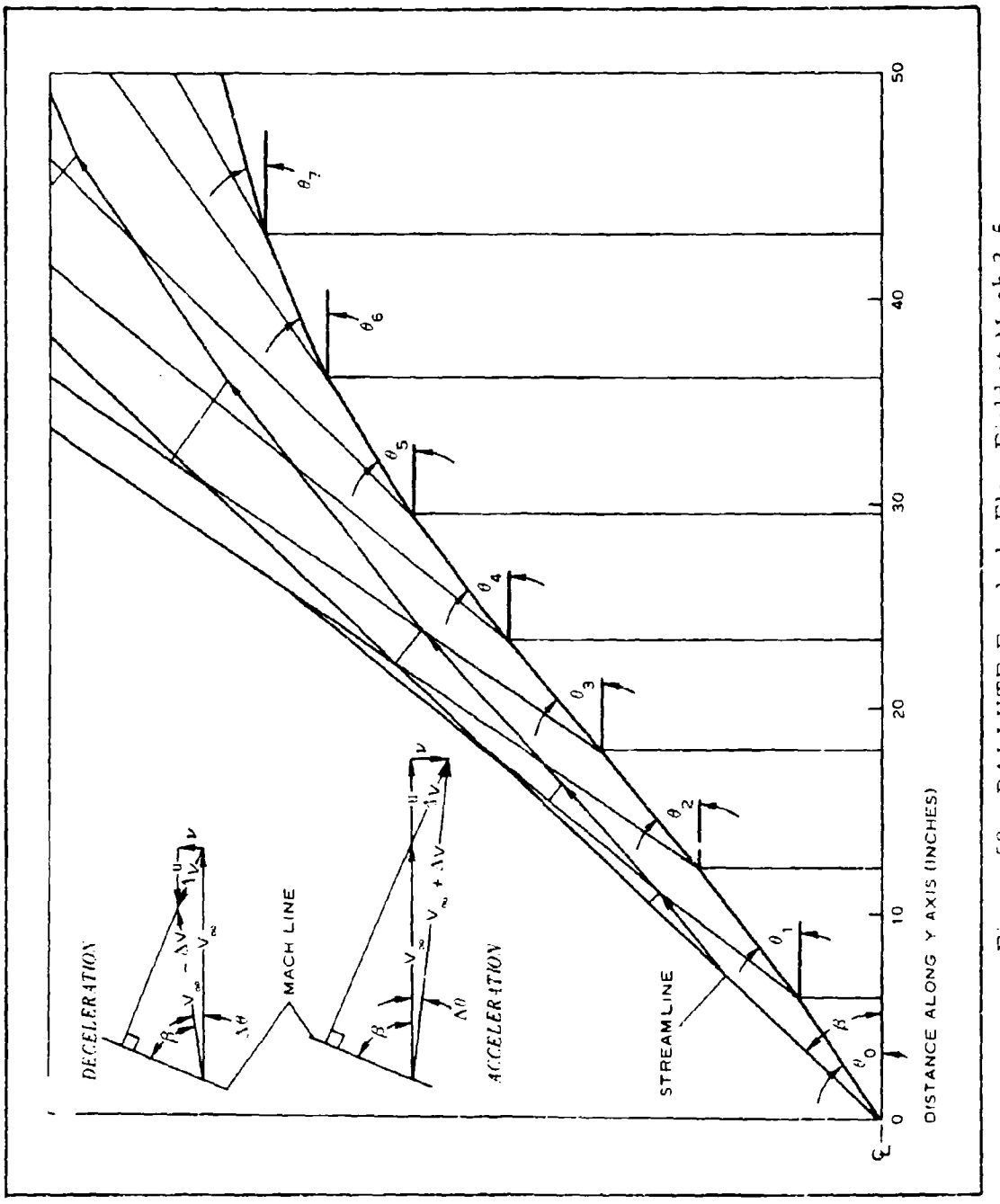

Figure 58 - BALLUTE Forebody Flow Field at Mach 2.5

The forebody pressure distribution can be evaluated by the following methods:

1. Small-perturbations method - Based upon the simple wave theory[29] and linearization of the equations of motion. The boundary conditions for this method are:
   a. Two-dimensional flow
   b. Irrotational flow
   c. Flow approximately isentropic, or $ds << 1$ for oblique shock
   d. Flow uniform and parallel, or $d\psi << 1$
   e. Range of free flow not to exceed $M_\infty^2 \leqq 10$

   The method is limited in its applicability for rather slender bodies of revolution.

2. Conical-shock-expansion method[30] - Based on the fact that Mach number on the surface varies with surface-inclination angle downstream of the vertex approximately according to the Prandtl-Meyer relations for two-dimensional flow when similarity parameter K is greater than unity ($K > 1$). Thus, for a given free-stream Mach number, the surface Mach number corresponding to the semivertex cone angle equal to that of the tip of the BALLUTE is determined. Flow parameters downstream of the vertex are obtained by the Prandtl-Meyer expansion, which is bounded by two rules: (1) Flow properties are uniform on straight lines emanating from the corner; and (2) these lines are inclined at the local Mach angle to local-flow direction. Therefore, the pressure distribution on a BALLUTE is a function of the vertex angle and free-stream Mach number only.

3. Tangent-cone method[31] - Based on the exact flow solutions for cones whose semivertex angles correspond to the local surface angles of inclination of the body. The method has

two approaches. One is based on the local total-pressure ratio ($p_o/p_{o\,\infty}$); i.e., the surface-pressure coefficient is a function of the local $p_o/p_{o\,\infty}$ ratio for each station; its limitation is inability to predict negative pressure coefficients. The other approach is to use vertex $p_o/p_{o\,\infty}$ ratio across the shock wave and subsequent local Mach-number distribution for cones tangent to a body at each station.

This method shows the following error values versus the similarity parameter, K:

Ratio	K < 1	K > 1
Local $p_o/p_{o\,\infty}$	$\sigma \geq +10$ percent	$\sigma \leq +10$ percent
Vertex $p_o/p_{o\,\infty}$	$\sigma > +10$ percent K = 1 → o = 0 percent	$\sigma > -10$ percent

Pressure distribution on the aft body of a BALLUTE is determined according to the considerations of Appendix V. Although the pressure cannot be below absolute zero, the pressure coefficient (C_p) can have a negative value. By definition:

$$C_p = \frac{p_L - p_\infty}{0.7 M_\infty^{\,2} p_\infty}$$

$$= \frac{(p_L/p_\infty) - 1}{0.7 M_\infty^{\,2}}$$

and

$$0.7\, C_p M_\infty^{\,2} + 1 = p_L/p_\infty \qquad (46)$$

Analysis shows that the pressure coefficient at a given point de-ends on the free-stream Mach number (M_∞) and the body shape. Then, if p_L is always to be greater than absolute zero, (p_L/p_∞) must be equal to or greater than zero and $0.7C_pM_\infty^2 + 1$ must be equal to or greater than zero.

Most BALLUTEs are equipped with a burble fence to establish the flow separation point at given flow conditions. Its location and size also influence drag and stability.

The flow behavior in the region of the inlet and the fence can be considered similar to that of the forward-facing steps in an accelerating supersonic flow. The inlet position causes a discontinuity that results in a normal shock standing forward of the inlet. The local Mach number and normal shock relationships offer insight into the local pressures existing at the inlet.

Flow separation is anticipated ahead of a step. The flow is assumed to be turbulent (also evidenced on the schlieren pictures); that is, transition has already taken place upstream.

The selection of the position for the BALLUTE inlets and the fence is influenced by the internal-pressure requirements for a stable shape. The internal-pressure coefficients for a range of Mach numbers are presented in Appendix V. The flow in the fence region depends on the transition location relative to a reattachment position. The problem consists of determining the dead-air pressure in front of the fence.

According to Reference 27, the basis of the process is a balance between the scavenged mass flow from the dead-air region by the mixing layer and the reversed mass flow back into a dead-air region from the pressure rise in the reattachment zone.

According to the laminar-mixing-layer theory, which also has been applied to turbulent cases, the stream with the uniform velocity u_e, the Mach number M_e, and the pressure p_e mixes with the dead-air region. Thus, a particle along the streamline within the mixing layer must possess total pressure (p_t) greater than terminal static pressure (p^1) at the end of the reattachment zone. The particle

that is slower and therefore has a lower total pressure is reversed before the pressure goes from p_d to p^1.

Derivation of the dead-air pressure is based upon the procedure employed by D. Chapman,[27] who in turn employed the Busemann isoenergetic integral and the work of Crocco. To determine the dead-air pressure, one more requirement must be satisfied; the total pressure along the dividing streamline as it approaches the reattachment zone must be equal to the terminal static pressure (p^1).

Flow in a mixing layer is divided into two regions: (1) constant pressure (viscous) region, and (2) reattachment zone, where compression values are assumed that do not consider most of the total pressure loss along the dividing streamline.

In the final form, the dead-air pressure is

$$\frac{p_d}{p^1} = \left(\frac{1 + \frac{\gamma - 1}{2} M^{12}}{1 + \frac{\gamma - 1}{2} \frac{M^{12}}{1 - u_x^2}} \right)^{\frac{\gamma}{\gamma - 1}} , \qquad (47)$$

Where:

p_d = dead air pressure,

p^1 = pressure downstream of reattachment region, and

M^{12} = Mach number downstream of reattachment region.

In general, the Reynolds number (RN) influences the drag coefficient at subsonic and transonic velocities, while the Mach number has pronounced effect in the supersonic range.

Thus, if

$$C_D = C_D (RN, M, 1/d, Sh), \qquad (48)$$

where

l/d = position of decelerator with respect to payload, and

Sh = shape,

the shape (body geometry) affects the nature of the flow.

Placing a fence changes the flow field in terms of local velocities and pressures, decreasing velocity and increasing the local static pressures immediately in front of the fence. The consequence is the increasing value of drag, as supported by Reference 32. The amount varies, however, depending on the body geometry and flow condition. For example, for Bodies 1 and 2 in Figure 59, if the maximum diameter is the same and F_1 equals F_2 (fence height), and if both are subjected to the same flow conditions (Mach number, Reynolds number, and l/d), the local flow forward of the fence will be decelerating at Body 1 and accelerating at Body 2. Hence, C_p at F_1 will be greater than C_p at F_2; the strength of normal shock formation at F_1 will be greater than F_2; and drag increases due to F_1 will be greater than those due to F_2.

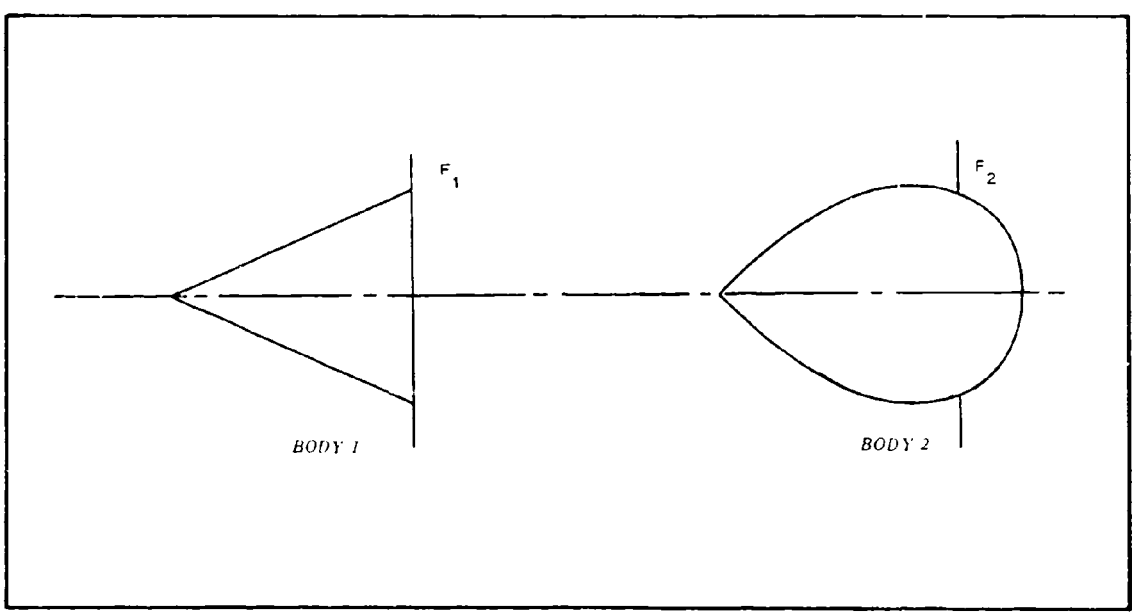

Figure 59 - Body Geometrics

The BALLUTE inflation and time required can be analyzed on the basis of the isentropic flow relations applied to the problem of filling a vessel with a gas (porosity losses included). The methods are given in Appendixes VI and VII.

(2) Empirical

(a) General

The qualitative influence of the payload wake is shown in Figure 60. The flow field in the near wake is indicated in Figures 60 and 61 with information taken from Reference 33. Figure 61 gives the Mach-number distribution in the wake calculated by the use of the wind tunnel Pitot-pressure measurements. It indicates the local flow expectation.

Although the precise location of the neck is usually not known, its region has high Pitot- and static-pressure gradients. This nebulous quality is best indicated, at present, from the measured Pitot-pressure coefficient profiles shown in Figures 62 and 63 (taken from Reference 34).

An important parameter to consider is the width of the wake neck. Lees and Hromas[35] indicate that neck width varies as $(RN_d)^{-1/2}$, shown in Figure 64 with a data point from Reference 34.

(b) Local-Flow Field

The flow field can be analyzed (first approximation) by the considerations of the conical-flow theory and the Prandtl-Meyer flow expansion.

(c) Airloads

The external airloads on the forebody are obtained from the given or estimated pressure distributions according to methods given in Item b(1) (b), above. The separated regions (dead-air pockets) in front of the burble fence, are estimated by the first-order perturbation theory.[36] Figures 65 and 66 show pressure distributions obtained in the wind tunnel.[33]

The location, size, and shape of the inflation inlet will determine the inside pressure of a BALLUTE. Figure 67 shows the results obtained in the Arnold Tunnel

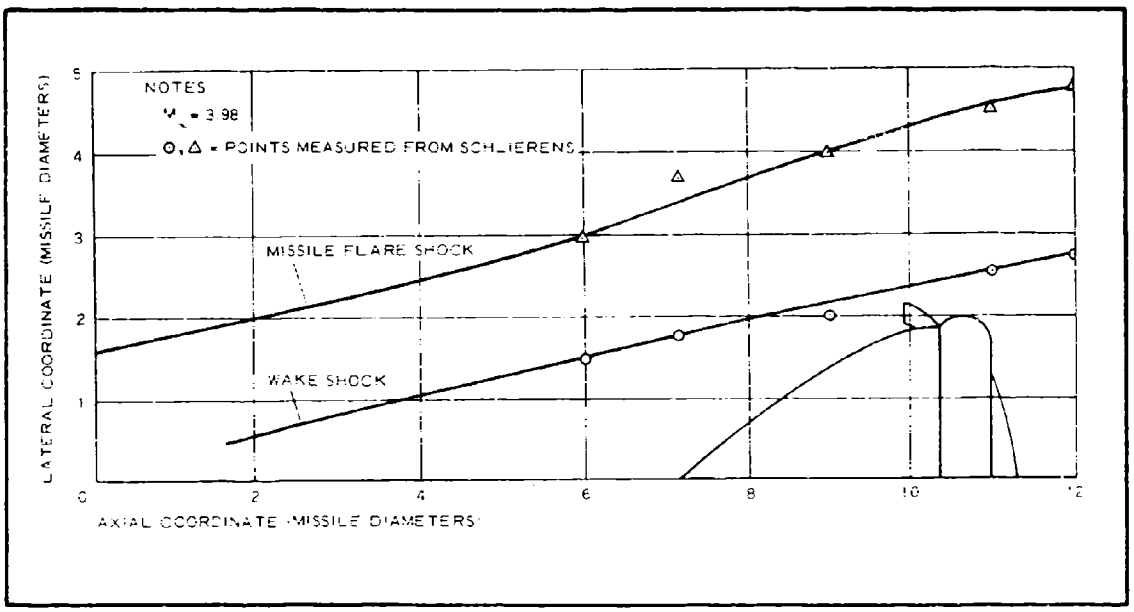

Figure 60 - Shock-Wave Shapes from Missile

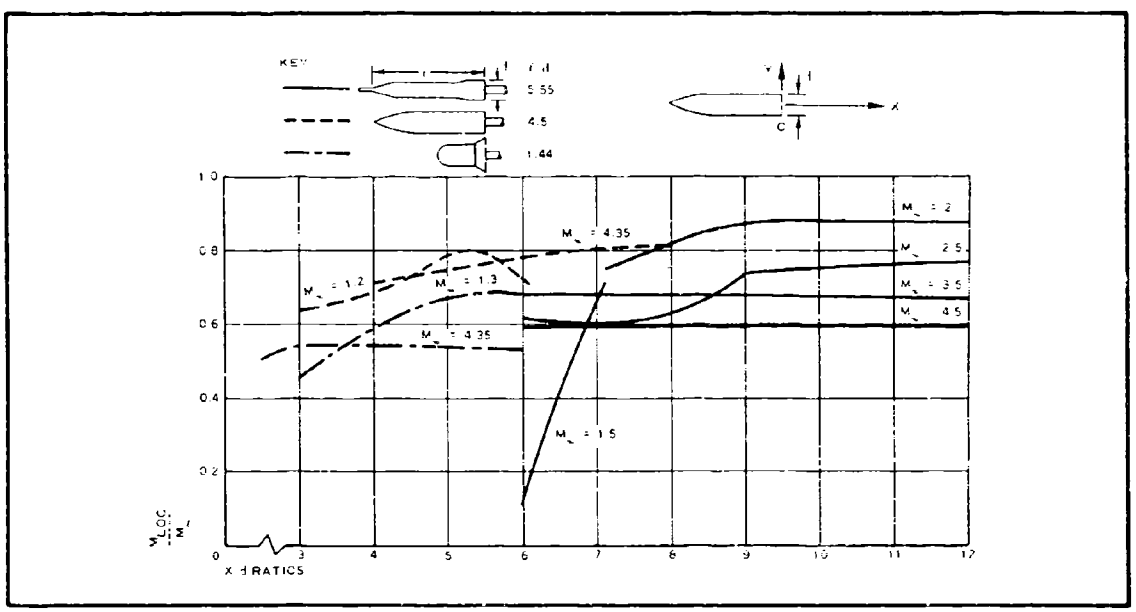

Figure 61 - Estimated Mach-Number Distribution near Centerline of Payload Wake

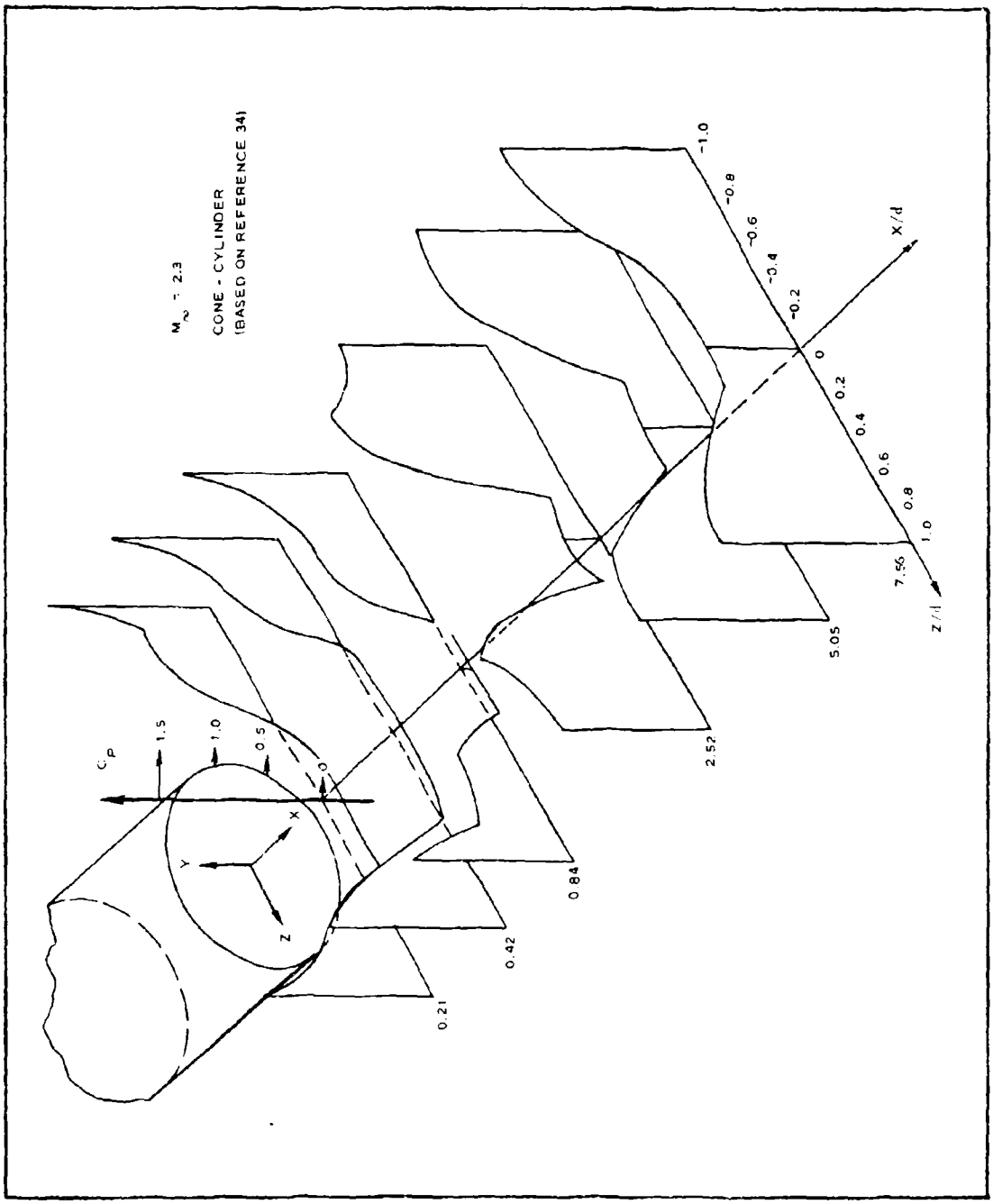

Figure 62 - Isoaxiometric Traces of Pitot-Pressure Coefficients in Wake at M_∞ = 2.3

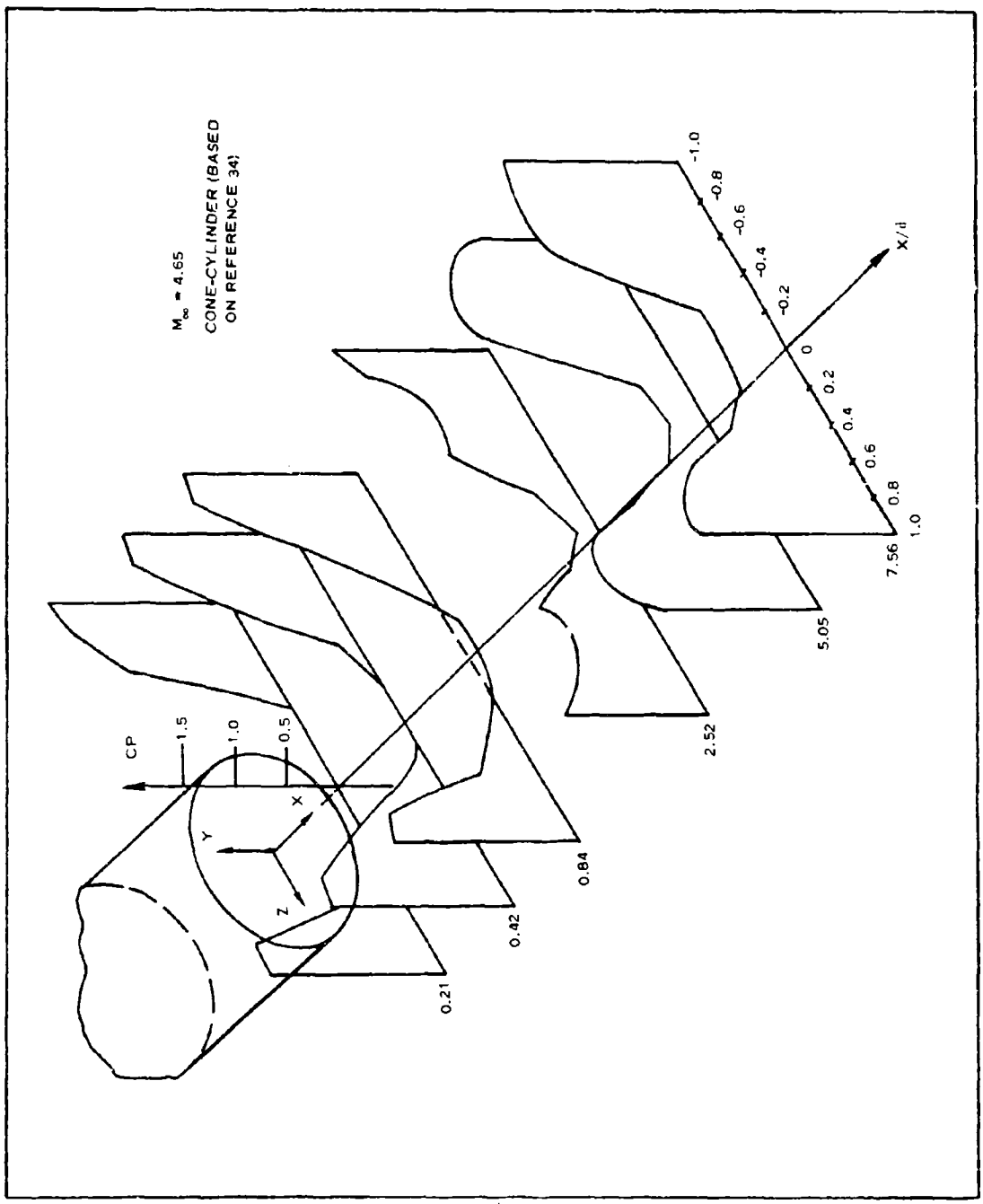

Figure 63 - Isoaxiometric Traces of Pitot-Pressure Coefficients in Wake at M_∞ = 4.65

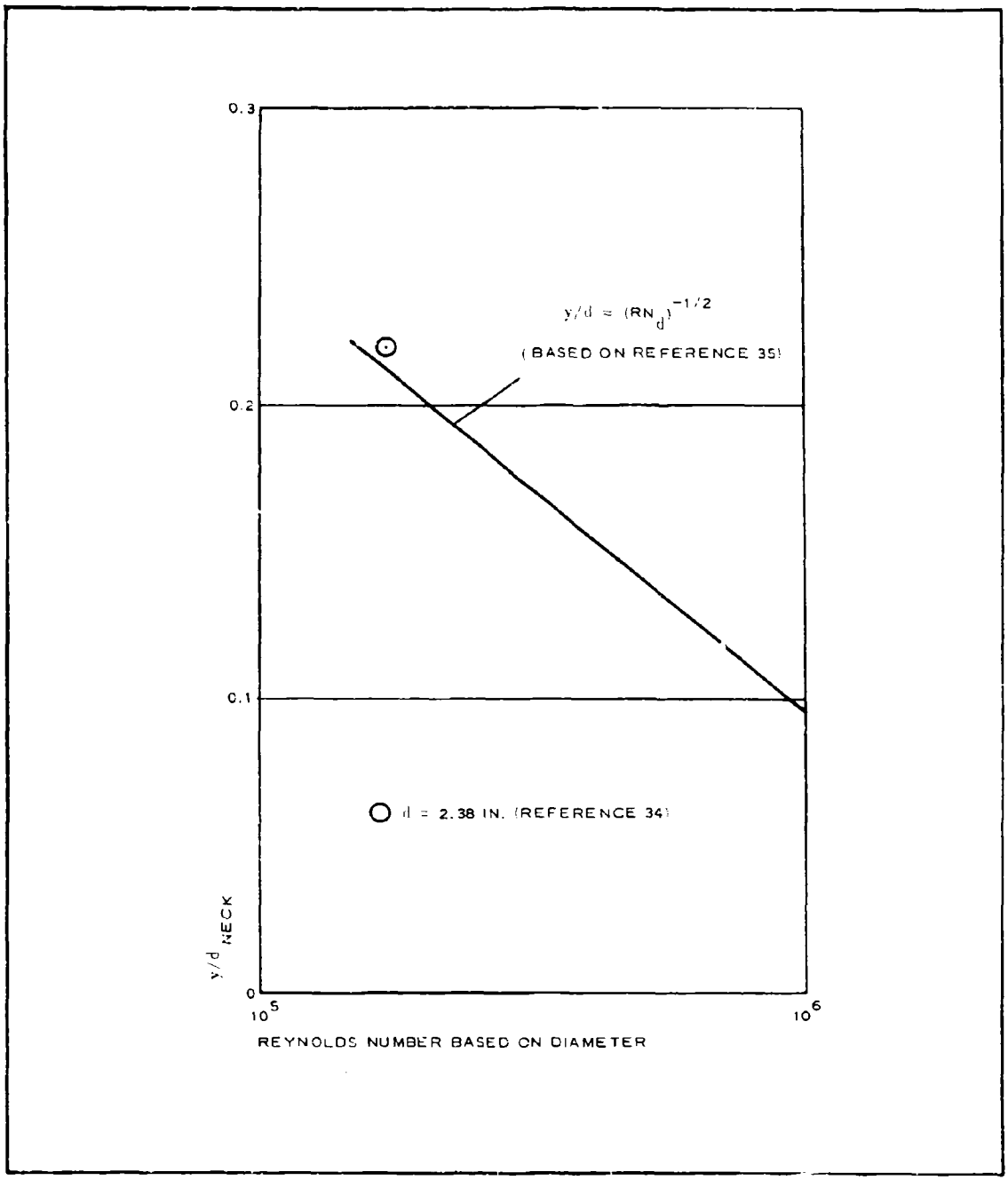

Figure 64 - Estimated Wake-Neck Width

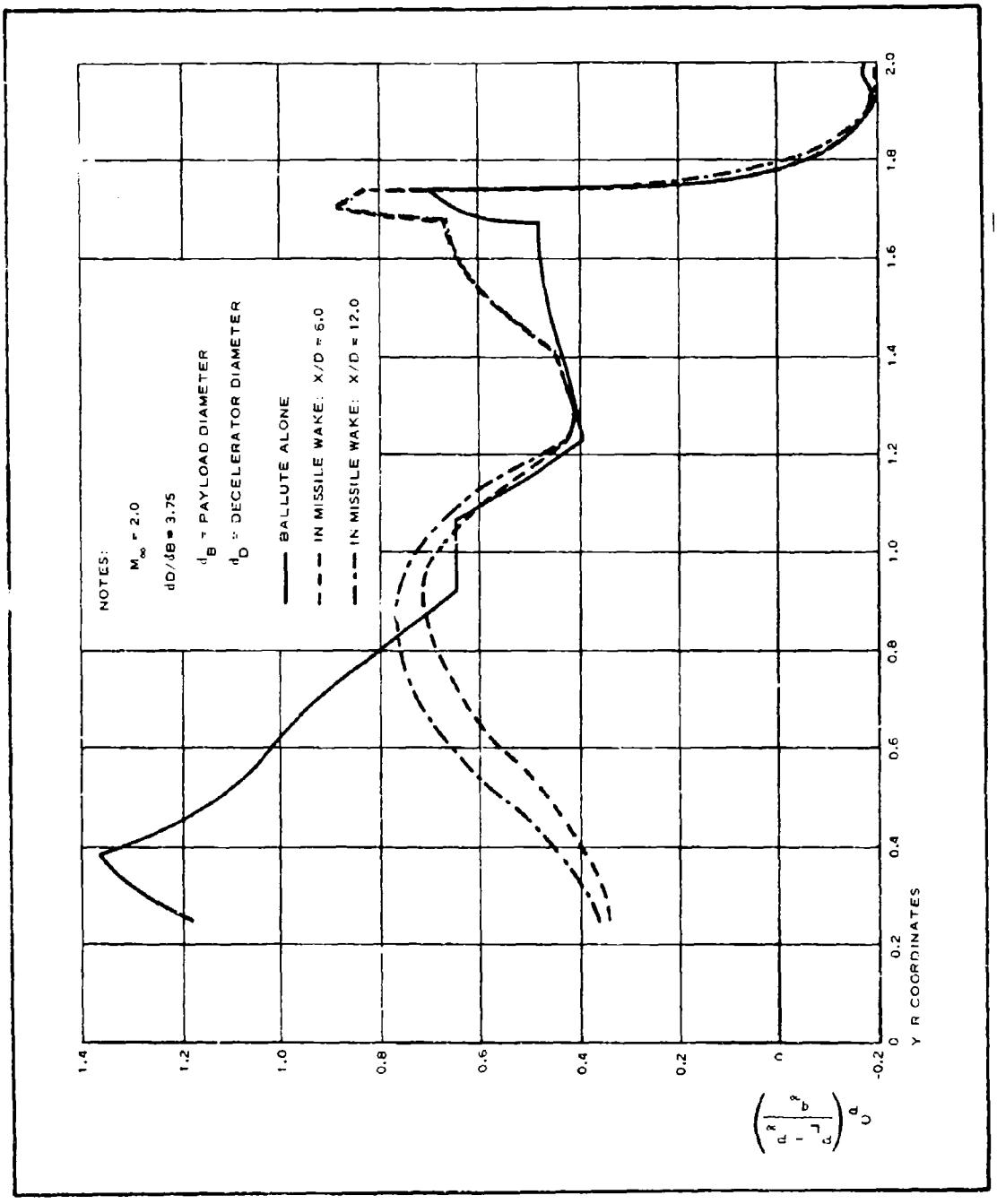

Figure 65 - BALLUTE Pressure Distribution at $M_\infty = 2.0$

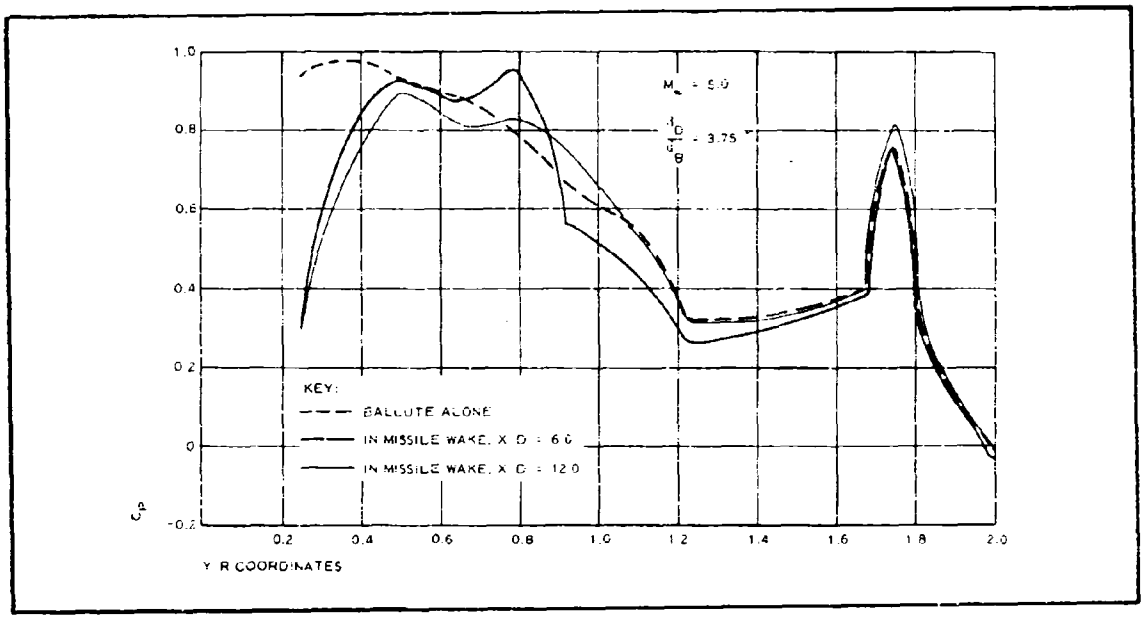

Figure 66 - BALLUTE Pressure Distribution at M_∞ = 5.0

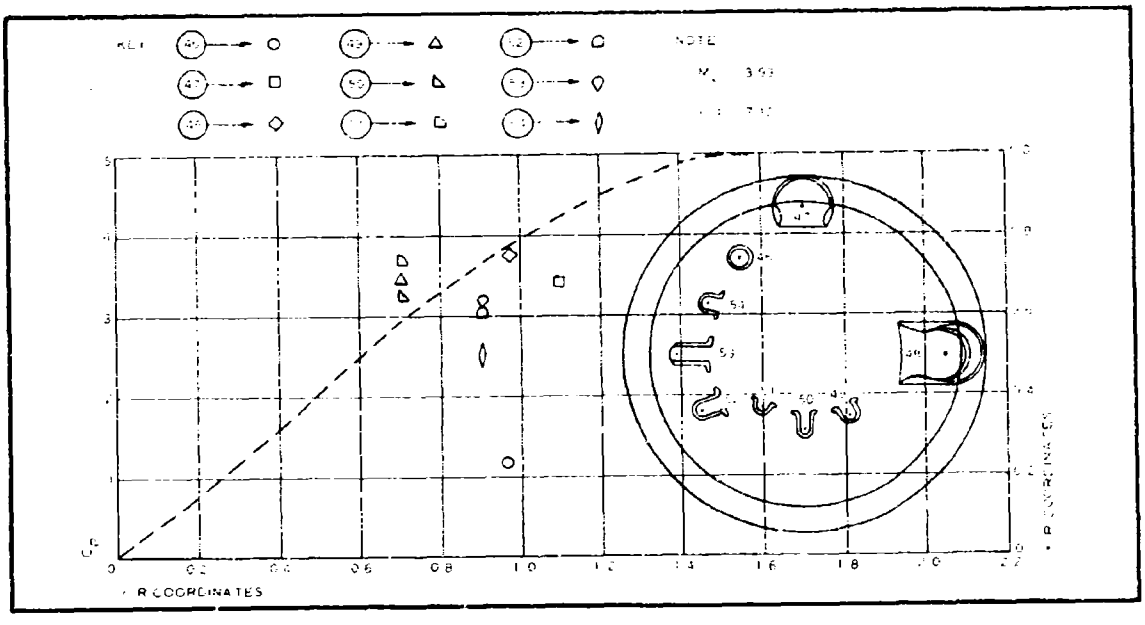

Figure 67 - Inlet Leading-Edge Locations at Pressure Coefficients

for the variety of inlets.[33] The loading on the base (aft of fence) is either estimated or obtained in the wind tunnel.

The use of the above approaches will produce a reliable set of loads to satisfy the strength requirements.

(3) Data Correlation

The correlation of wind-tunnel data with analytical estimates is the next step in aerodynamic evaluation of the decelerometer. Its purpose is to validate the conformity with the principles of fluid flow. The correlation between the analitical estimates obtained by the methods described and wind-tunnel data is presented below.

For Case I, free-stream Mach number 2.5, the difference in geometrics of the model and prototype resulting in a deviation from the principles of similitude must be kept in mind during correlation. Figure 68 shows this geometry comparison. Figure 69 shows the correlation between wind-tunnel data and

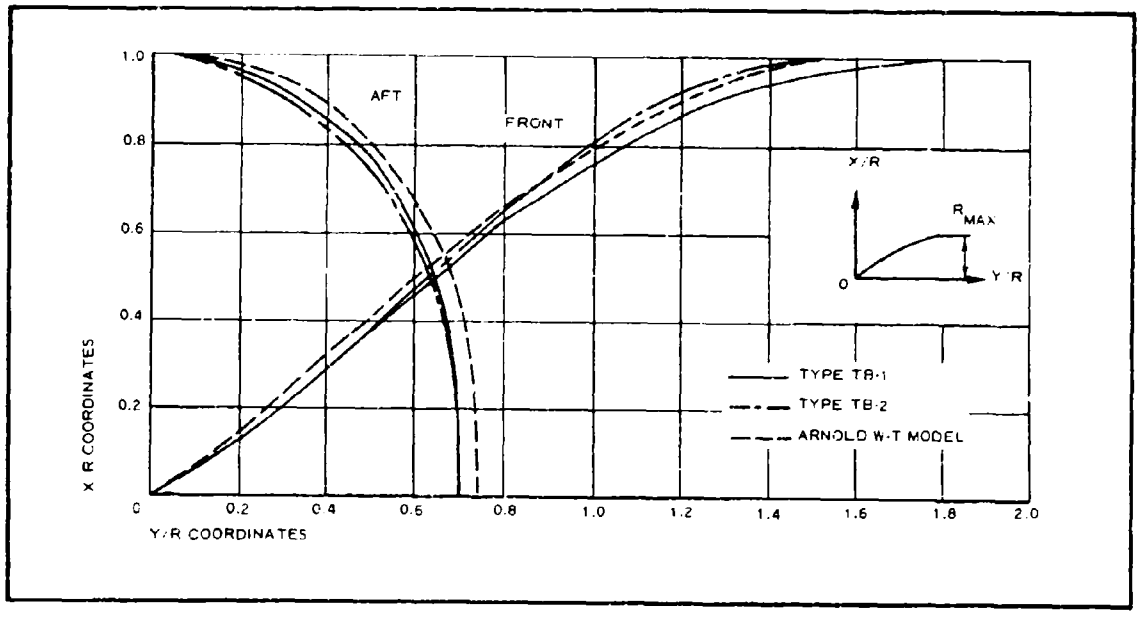

Figure 68 - BALLUTE Geometry Comparison

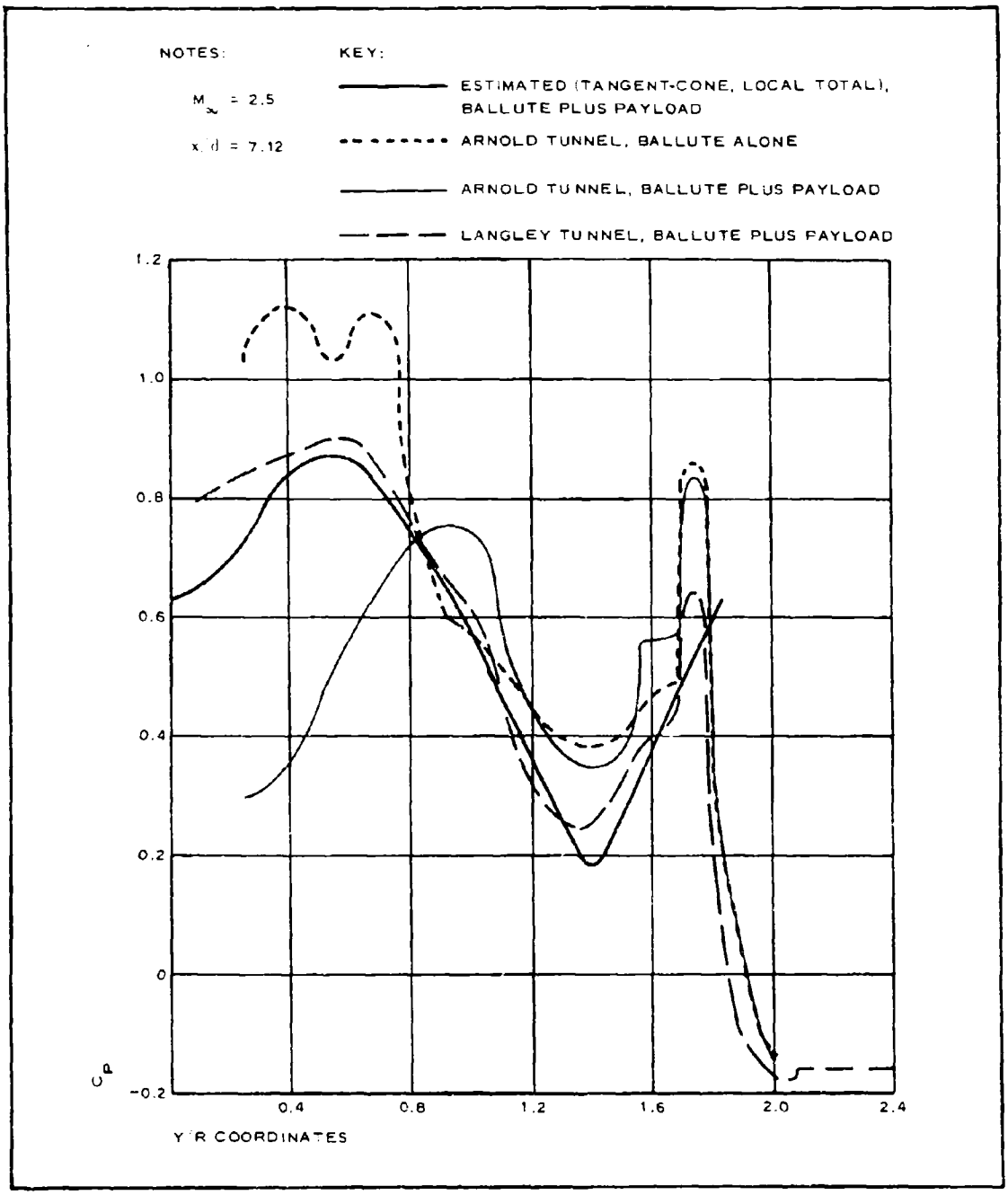

Figure 69 - BALLUTE Pressure Distribution, Correlation of Data

analytical estimates performed according to the methods given in Item b(1)(b), above.

The data from Figure 69 indicate:

1. Excellent correlation for the characteristic shape of a typical BALLUTE pressure distribution
2. Sensitivity of the pressure distribution to changes in the flow brought about by the presence of the payload wake, the type of connection between the payload and BALLUTE, and the presence of the burble fence

The significant variation in the magnitudes of pressure coefficients is in the first one-third of the Y/R ratio span. Aside from the obvious "BALLUTE-alone" plot, the Arnold data show lower values due to the favorable continuity that the support sting provides for the flow aft of the missile base. Hence, the boundary-layer-like flow and associated shock-wave system alter the typical wake flow, thus leading to the accelerated flow and lower pressures at the BALLUTE vertex. Both the Langley and the estimated data neglect the presence of the riser line; therefore, the flow at the tip has typical characteristics of the wake (greater velocity defect) and thus higher pressures.

For Case II, free-stream Mach number 3.8 to 4.0, correlation between the wind-tunnel data and the analytical estimate is shown in Figure 70. The correlation and comparison indicate that analytical methods of conical-shock expansion and tangent cone are acceptable to predict external steady-state loads on the forward body of a BALLUTE within the limits of each method.

The wake effect was estimated as previously discussed, with due regard for the size and shape of the riser line.

The base pressure variation with the Mach number is given in Figure 71. It shows that the curve fitted by the equation

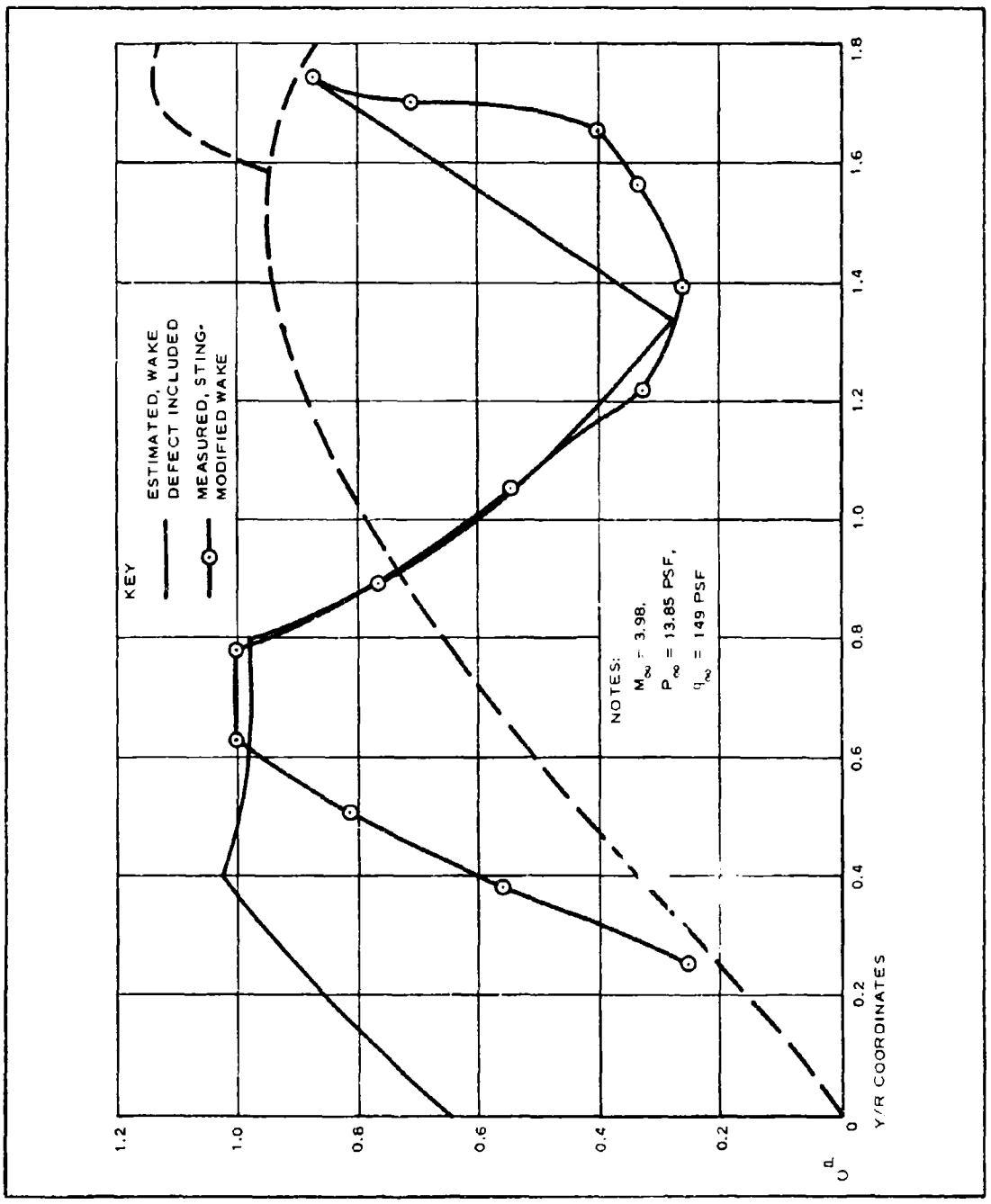

Figure 70 - BALLUTE Model Pressure Distribution

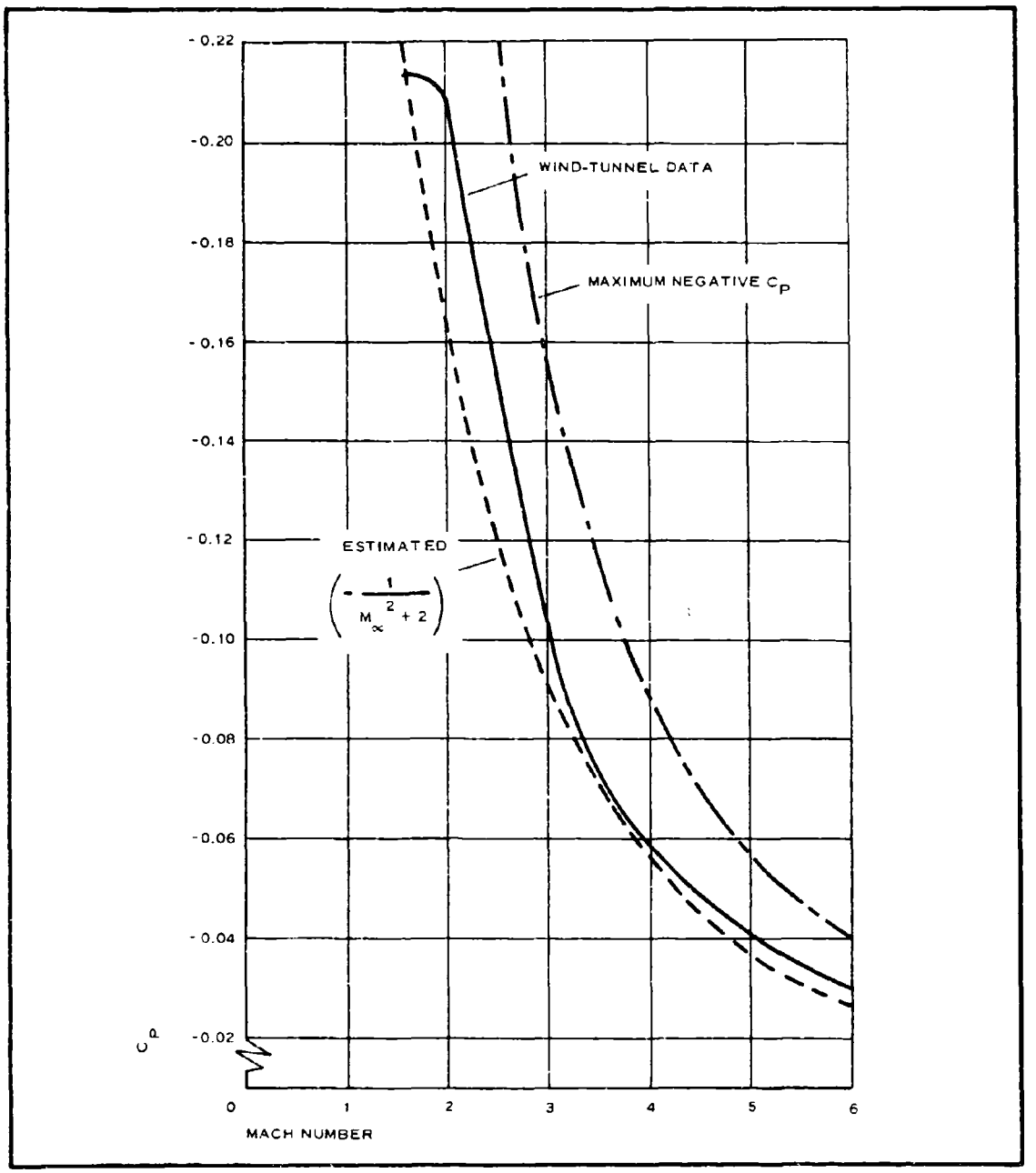

Figure 71 - BALLUTE Pressure Variation versus Mach Number

$$C_p = -\frac{1}{M_\infty^2 + 2} \tag{49}$$

asymptotically approaches the wind-tunnel values at $3 \leqq M \leqq 5$.

The free-flight test of the TB-1 item did not produce any aerodynamic data.

c. Example (TB-1)

The pressure distribution for the TB-1 design was obtained from the early wind-tunnel tests of a modified force model. The limited number of orifices indicated an approximate pressure field, as shown in Figure 72. Subsequent efforts showed that in the region of the burble fence the values were somewhat lower than would be expected. The TB-1 forebody flow field showing the typical streamline path is given in Figure 73.

The maximum allowable negative-pressure coefficient at the base, referenced for free-stream conditions, is

$$C_p = \frac{\frac{1}{48.5} - 1}{4.37}$$

$$= -0.229 \tag{50}$$

Based on empirical data for the sphere (at Mach 2.5) from Reference 37,

$$C_{p_b} = -0.1 \text{ (sphere)} ; \tag{51}$$

$$\frac{C_{p_b}}{C_{p_{b\,max}}} = \frac{-0.1}{-0.229}$$

$$= 0.436 ; \tag{52}$$

or 43.6 percent of the maximum allowable negative-pressure coefficient was applied at the rear.

The pressure coefficient at the inlet indicates the level of inflation (internal

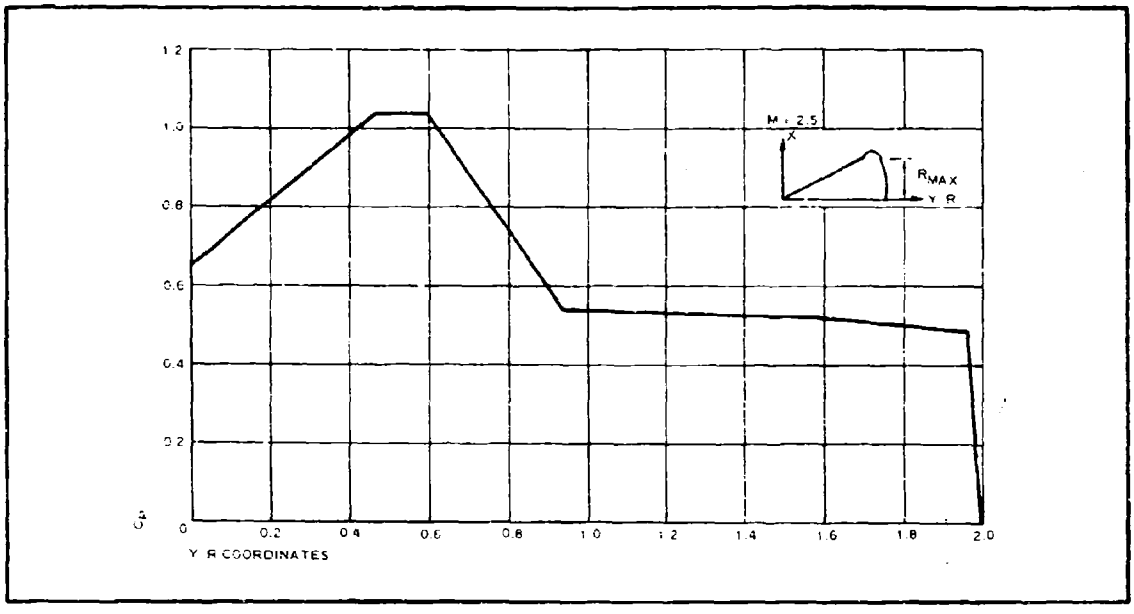

Figure 72 - Pressure Distribution of BALLUTE at Mach 2.5

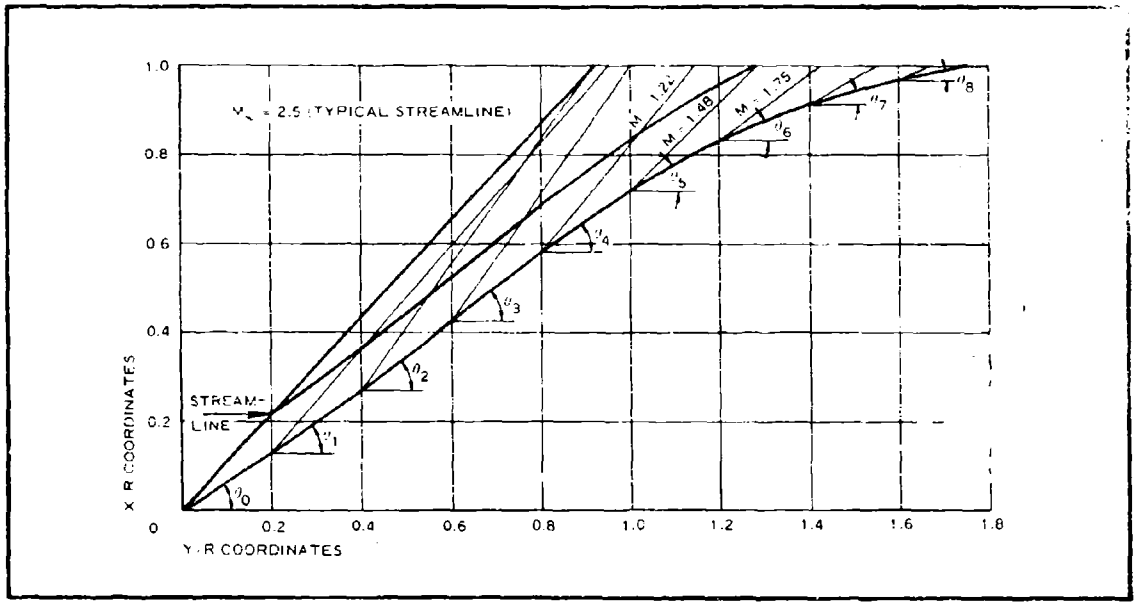

Figure 73 - BALLUTE Forebody Flow Field

pressure). The results were compared with wind-tunnel data on a rigid model. The inlets are located in the range of local surface-inclination angles where 15 deg $\leqq \theta \leqq$ 33 deg. The shock at the inlet leading edge is assumed to be normal. The local-flow conditions are summarized in Table 23.

TABLE 23 - LOCAL FLOW CONDITIONS (TB-1)

Condition	Local Mach number		
	1.42	1.82	2.10
ν local (sq ft per sec)	24.5×10^{-4}	17.7×10^{-4}	15×10^{-4}
ρ local (lb-sec per ft^4)	0.122×10^{-3}	0.169×10^{-3}	0.199×10^{-3}
δ local (in.)	0.595	0.504	0.465
θ local (deg)	33	23	15
Local station	θ_5	θ_6	θ_7

Since velocity at θ_7 is affected by the proximity of the burble fence and local boundary layer, it is considered that local velocity at θ_6 is representative for the inlet leading-edge area. Thus, the local velocity (including velocity change due to surface variation) is

$$V_{loc} = \sqrt{(1380 + 173)^2 + 242^2}$$

$$= 1520 \text{ fps at } \theta_6 , \qquad (52)$$

and local pressure conditions are

$$q_{loc} = 0.5 \rho_2 V_{loc}^2$$

$$= 0.0845 \times 10^{-3} \times 1520^2$$

$$= 195 \text{ psf} , \qquad (53)$$

$$p_{loc} = \frac{q_{loc}}{0.7M_{loc}^2}$$

$$= \frac{195}{0.7(1.82)^2}$$

$$= 88 \text{ psf} \qquad (55)$$

and

$$\frac{P_L}{P_{t_{loc}}} = 0.210 ; \qquad (56)$$

therefore

$$P_{t_{loc}} = \frac{88}{0.21}$$

$$= 420 \text{ psf} . \qquad (57)$$

If inlet-pressure coefficient is defined as

$$C_{P_i} = \frac{P_{t_{loc}} - P_\infty}{q_\infty} , \qquad (57)$$

then

$$C_{P_i} = \frac{420 - 48.5}{12}$$

$$= 1.75.$$

The inlet-pressure coefficient does not reflect any additional losses of pressure due to flow. Therefore, the assumption that the inside pressure is approximately equal to 2q is considered valid. Wind-tunnel test data indicate the value of C_{P_i} as 1.96. However, the configurations are not exactly similar.

3. THERMODYNAMICS

a. General

A thermal analysis of BALLUTEs following in the wake of a leading body depends largely on defining the local-flow conditions over the BALLUTE surface and then using these flow conditions to determine the magnitude of the aerodynamic heating present, by using available heat-transfer theory and empirical data. However, since the definition of the wake flow and local conditions of trailing bodies is a relatively new area of investigation, data are rather limited. Recently published studies of wake formation behind various types of bodies show that the wake is a function of the body geometry, the flight regime, and the type of flow conditions generated in the wake formation. Since these wake parameters can vary considerably from one set of flight conditions to another and are a function of body geometry as well, the data contained in these studies has had limited application in this program. Therefore, the methods used in establishing thermal design criteria have followed rather simple analytical techniques. These techniques are described below, along with an empirical approach for determining heat-transfer coefficients. An example calculation then is presented to outline the use of the methods used for generating BALLUTE thermal-design criteria.

b. Approach

(1) Analytical

The first consideration is a BALLUTE following a trajectory path calculated for the composite bodies - that is, the leading body and the trailing BALLUTE. If it is assumed (1) that effects of the leading body are nonexistent and (2) that the flow ahead of the BALLUTE returns to normal free-stream flow conditions, then the local-flow properties over the BALLUTE can be valuated on the basis of these stream conditions. If, in addition, the BALLUTE is assumed to have a conical forebody, the local-flow properties on the BALLUTE can be evaluated by conical-flow data.

Normally, both laminar and turbulent boundary-layer flow over the BALLUTE can be considered; however, only turbulent flow was considered in this analysis.

Thus, only the most severe heating case was used for the preliminary design analysis. On this basis, the heat-transfer coefficients over the BALLUTE envelope can be calculated with the following equation:

$$h = \frac{0.0384}{(T^*)0.576} \frac{(p \times u)^{0.8}}{x^{0.2}} \tag{59}$$

This equation is a modification of the well-known Colburn correlation for heat transfer to a flat plate with a turbulent boundary layer present:

$$h = 0.0296 \frac{k}{x} R_e^{0.8} P_r^{1/3} \tag{60}$$

Equation 60 has been modified to the form shown in Equation 59 by introducing the concept of a reference temperature - that is, a weighted value of the boundary-layer temperature. The introduction of this reference temperature into the equation has been shown to improve the correlation of theoretically predicted heat-transfer coefficients with those obtained experimentally. Equation 59 has been modified further to account for flow around a cone; it has been multiplied by $2^{0.2} = 1.15$, a correction factor accounting for conical flow rather than flow over a flat plate. Therefore, Equation 59 requires insertion of local cone-flow conditions. The basis for these modifications of Equation 60 is contained in Reference 38. Equation 59 thus is in a form consistent with the geometry of a BALLUTE, which in essence approaches a conical type of forebody.

The heat-transfer coefficients for the inlet lip and the burble fence are calculated on the assumption that these elements are cylinders subjected to the local-flow conditions on the BALLUTE immediately preceding the components. Since it can be assumed that turbulent flow exists over the BALLUTE surface, the following equation, taken from Reference 39, for turbulent flow over a cylinder normal to the flow was selected to evaluate the average heat-transfer coefficients on the inlet lip and the burble fence:

$$h_{avg} = 0.385 \frac{k}{D} (R_e)^{0.56} (P_r)^{0.30} \tag{61}$$

Once the method for calculating the heat-transfer coefficient is selected, an appropriate heat-balance solution must be applied. Either of two procedures can be used, as follows.

1. One-dimensional transient-slab solution - Consider the fabric wall as a slab exposed to aerodynamic heating on one surface and extending infinitely in the other direction. A heat balance then can be written for the conditions at the outer surface. The condition for heat input at the outer surface by convection alone from a fluid at an adiabatic wall temperature (T_{aw}) is

$$h(T_{aw} - T_w) = k \frac{\partial}{\partial y} T(0, \tau) \tag{62}$$

The radiation away from the outer surface is neglected but can be included if necessary as surface temperatures reach values where they become an important factor. The rate of heat conduction into this slab then can be calculated in conjunction with one of the suggested methods for calculating the heat-transfer coefficient, by iteration over a finite time interval. This equation is solved over the critical deceleration time with the aid of a computer, or it is estimated by using thermal-response charts such as those available in Reference 17. This transient type of heat-balance solution is useful particularly in situations where the deceleration takes place over a short time interval. In such a situation, the aerodynamic heating rates may be so high that there is a delay in conducting heat away from the outer surface. This is particularly true of materials that have a low coefficient of thermal conductivity, such as the textile-fabric cloths used in this program.

2. Heat-balance solution - Again, consider the fabric wall as a slab exposed to aerodynamic heating on one surface, which behaves like a heat sink with practically no temperature gradient through its thickness. Then, the following heat balance can be written:

$$h(T_{aw} - T_w) - \epsilon \sigma T_w^4 = \rho c t \frac{d T_w}{d \tau} \tag{63}$$

This heat balance is written at the outer surface on the assumption that there is no internal radiation-energy interchange. This equation, combined with the method selected for calculating the heat-transfer coefficient, can then be solved by iteration, by assuming various wall temperatures for the instant of time under consideration until a balance is achieved (i.e., a quasi-steady-state condition is reached along the trajectory path for a finite time interval). This heat-balance solution is useful particularly in situations where the material has practically no temperature gradient within it. Thus, a simple estimate of the surface-temperature rise can be made if one assumes that such a temperature gradient does not exist. Once the temperature response of the material under consideration is evaluated on the basis of Equation 62 or 63 over the selected time interval, the heat-flux rate into the material can be evaluated from an equation such as the following:

$$q = h(T_{aw} - T_w) \tag{64}$$

The adiabatic wall temperature, $T_{aw} = T_\infty \left[(1 + r) \times (\gamma - 1)/2 M_\infty^2\right]$, is calculated from trajectory predictions, and the wall temperature is calculated as prescribed above. The heat-transfer coefficient is calculated during the evaluation of temperature rise, so that all inputs

to Equation 64 are known. A heat-flux-rate variation with time then can be calculated simultaneously with the temperature evaluation.

(2) Empirical

The alternative to the theoretical approach for calculating the heat-transfer coefficient on the BALLUTE surface is to use experimental test data, primarily those in Reference 23.[a] On the basis of these data, a set of generalized heat-flux-rate curves for BALLUTE were calculated. These curves present nondimensional heat-flux rates to a BALLUTE surface as a function of the position on the surface for both a laminar and a turbulent boundary layer. The laminar-boundary-layer heat-flux rates were nondimensionalized by using a reference laminar-stagnation-point heat-flux rate; the turbulent-boundary-layer heat-flux rates were nondimensionalized by using a reference turbulent heat-flux rate at a specified BALLUTE position (S/R = 2). In both cases, the reference heat-flux rates were calculated for a BALLUTE without a leading body. The heat-transfer data for Mach 10 were found to be independent of the tunnel free-stream Reynolds number and were assumed, therefore, to apply for the range of supersonic flight conditions up to Mach 10. No correlation exists that compares theoretical predicted heat-transfer coefficients with recorded experimental data; however, GAC is conducting a study to determine the possibility of such a correlation. The results of this study will be available soon. The heat-transfer characteristics, then, can be evaluated by using the generalized heat-flux-rate curves to a BALLUTE surface (Figures 137 and 139 of Referencd 23), assuming that flow is similar between the experimental pressure data and the design under consideration, so that, for a turbulent boundary layer,

$$\frac{\dot{q}}{\dot{q}_c} = \frac{h(T_{aw} - T_w)}{h_c(T_{aw} - T_w)}$$

[a] This report presents experimentally recorded local pressure and heat-transfer rates over a typical BALLUTE, with and without the presence of a typical leading body, at Mach 10, taken in the Arnold Von-Karman tunnel "C" facility.

The ratio of heat-flux rates can be found in the curves as function of position for both the cases (with and without a leading body). Equation 65 can be solved for the heat-transfer coefficient to a BALLUTE surface with a leading body by ratioing the two values of heat-flux rate as given below:

$$h_w = \frac{\left(\frac{\dot{q}}{\dot{q}_c}\right)_w}{\left(\frac{\dot{q}}{\dot{q}_c}\right)_{wo}} (h)_{wo} \frac{(T_{aw} - T_w)_{wo}}{(T_{aw} - T_w)_w} \tag{66}$$

where the subscripts "w" and "wo" designate with and without a leading body, respectively.

If the temperature differences are assumed to be approximately equal, the heat-transfer coefficient for a BALLUTE with a leading body can be estimated by (1) calculating the heat-transfer coefficient to the BALLUTE surface without a leading body and (2) modifying this heat-transfer coefficient with the experimental data - that is, the ratio of the heat-transfer rates. This in effect will establish a means of empirically estimating a heat-transfer coefficient to a BALLUTE surface that will take into account the characteristics of the wake.

c. Example (TB-1)

(1) General

To demonstrate the calculation procedure that was followed, a set of typical calculations for the design of the TB-1 test item are presented in Items (2) and (3), below.

(2) Applicable Techniques

A schematic sketch of the BALLUTE is shown in Figure 74. Four positions on the BALLUTE are analyzed. Positions 1 and 2 are on the forebody; Position 3 is on the burble fence; and Position 4 is the leading edge of the inlet lip. The material of the BALLUTE envelope is a coated nylon fabric weighing 10 oz per square yard. The basic nylon polymer from which this fabric was

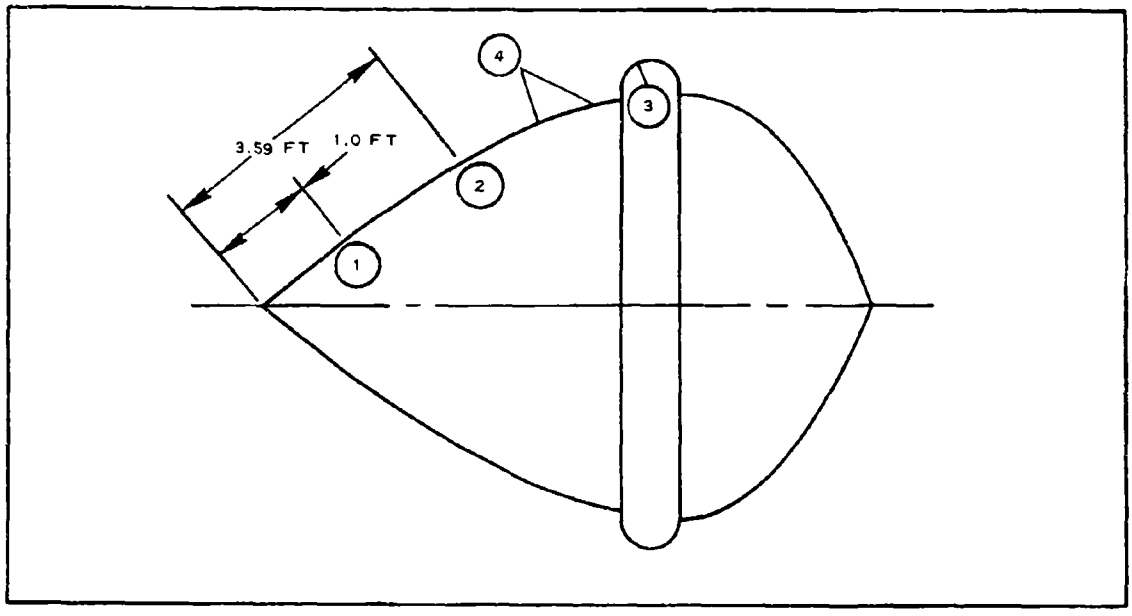

Figure 74 - Test Item TB-1 Schematic

woven has a specific heat of 0.4 Btu per pound and per degree F at room temperature. This value of the specific heat was assumed to be constant for the fabric cloth over the expected temperature rise. At 1 sec after deployment, trajectory predictions for the combined bodies show that they are at an altitude of 86,062 ft, moving at 2050 fps. The heat-balance method, using Equation 62, was selected for calculating the temperature response at Position 1 because of its usefulness in providing a fairly quick method of ascertaining the temperature rise. The heat-transfer coefficients were calculated using Equation 59. First, the local pressure and velocity over the BALLUTE forebody surface were calculated. It was assumed that the forebody was conical and the semivertex angle was 40 deg, which is approximately the BALLUTE shape upon inflation. The local pressure and velocity were evaluated by using the conical-flow data in Reference 14, with a perfect gas relationship assumed for the flow through the shock. The temperature inserted into Equation 59 is a reference temperature; a simple form of the reference temperature taken from Reference 40,

$$T^* = T_\infty (1 + 0.133 M_\infty^2) , \tag{67}$$

was used to evaluate this quantity. These properties then were calculated and substituted into Equation 59. Thus,

$$h = \frac{0.0384}{(630)^{0.576}} \times \frac{(189 \times 1315)^{0.8}}{(1)^{0.2}}$$

$$= 19.4 \text{ Btu per hour, square foot, and degree F.}$$

The temperature rise was estimated by solving Equation 63 for the surface temperature, as follows. Let the differential

$$\frac{d T_w}{d \tau} = \frac{\Delta T_w}{\Delta \tau}$$

$$= \frac{T_{w_2} - T_{w_1}}{\Delta \tau} , \tag{68}$$

where T_{w_2} is the surface temperature at the end of the time interval, $\Delta \tau$, and T_{w_1} is the surface temperature at the beginning of the time interval. In addition, let the product of the material density and its thickness equal the weight per unit area ($\rho t = w$). Then, substituting into Equation 63 and solving for the surface temperature gives

$$T_{w_2} = T_{w_1} + \frac{\Delta \tau}{wc} h(T_{aw} - T_{w_2}) - \epsilon \sigma T_{w_2}^4 . \tag{69}$$

By assuming values of T_{w_2} until a balance is attained,

$$T_{w_2} = 595 \text{ F} + \frac{0.5}{100} 19.4(711 - 603) - 0.8 \times 0.173 \left(\frac{603}{100}\right)^4$$

$$= 603 \text{ R}$$

$$= 143 \text{ F} ,$$

where the surface emissivity is assumed to be 0.8 and T_{w_1} is the surface temperature from the previous calculation at 0.5 sec after deployment.

This procedure can be followed over the period of deceleration to establish surface temperature variation with time. Similar calculations were carried out at the other positions designated; however, the local flow at the inlet lip and the burble fence required further definition since the airflow over these positions is altered from that over the BALLUTE forebody. (The inlet lip is encompassed by a strong shock, and the burble fence is in an expanding-flow region.) Once the local flow properties had been ascertained, the calculation of the heat-transfer coefficient and the surface temperature proceeded as described above.

(3) Results

The resulting temperature-time history of the four positions on the BALLUTE is shown in Figure 75. The envelope temperature was predicted to reach 152 F at Point 1 and 100 F at Point 2 at about three seconds after deployment. The burble fence was predicted to have a temperature-time history similar to that of Point 2 on the BALLUTE envelope; the lip of the ram-air inlet was predicted to peak at 251 F about two seconds after deployment. The greater temperature of the latter is due to the small radius of curvature of the inlet lip, which in turn led to a higher heat-transfer coefficient since the coefficient is inversely proportional to this dimension raised to the 0.44 power.

An attempt was made to estimate the effect of the leading body on the characteristics of heat transfer to the BALLUTE by directly comparing the wind-tunnel heat-transfer data taken at Mach 10 with the heat-transfer coefficients calculated empirically at the test Mach-number range. Evaluating Equation 66, with Figure 139 of Reference 23 at an S/R_o of 7, shows that the heat-transfer coefficient can be increased by approximately 20 percent because of the presence of a leading body. This estimate is based on a cold-wall temperature difference at Mach 10. If it is assumed that this effect is present at the Mach number under consideration here, then a 20-percent increase

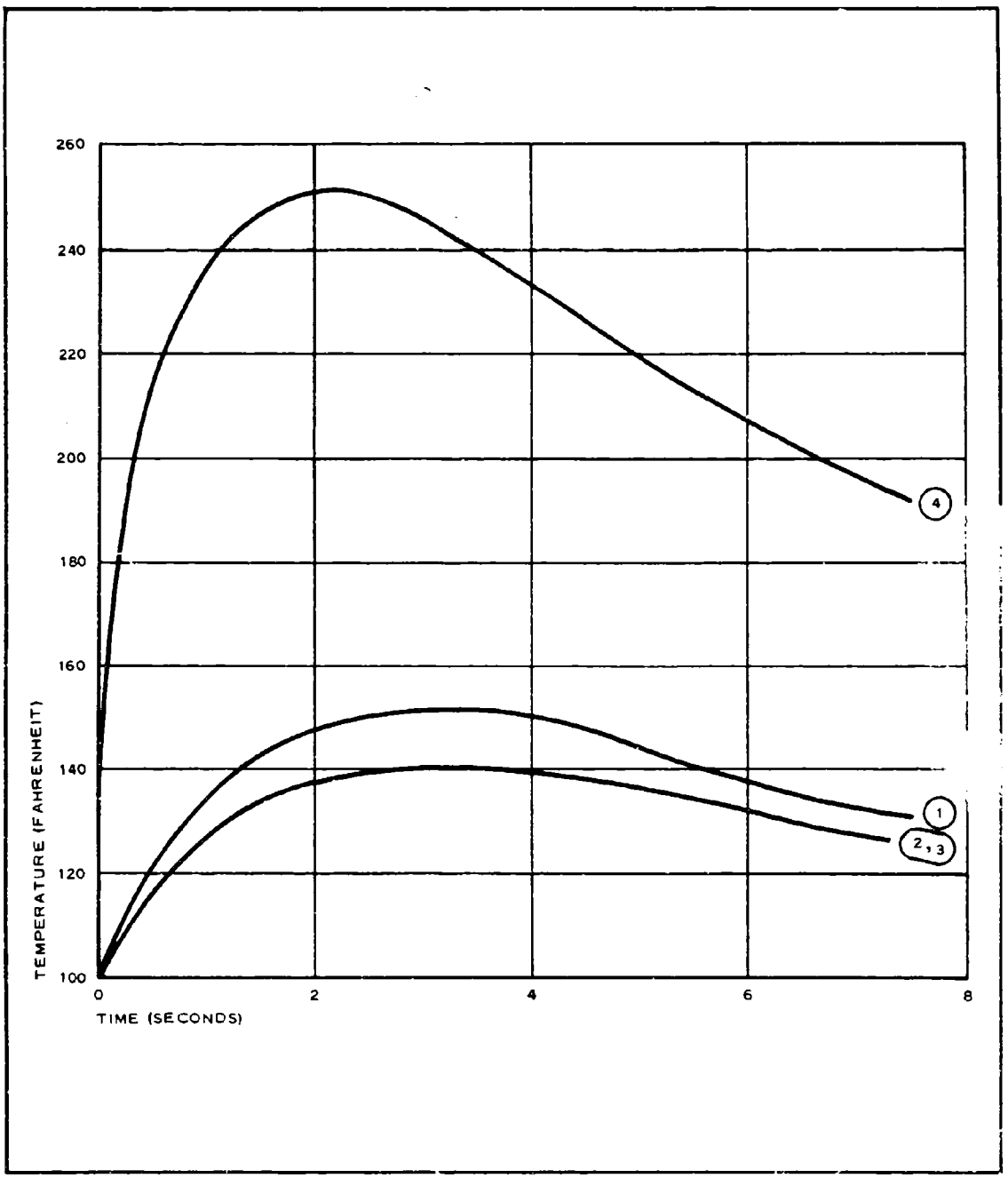

Figure 75 - Temperature versus Time for Test Unit TB-1

in the heat-transfer rate can be expected in the region of Point 2 because of the presence of the leading body. This increase in the heat-transfer coefficient at Point 2 will increase the maximum expected temperature at this point to about 170 F.

4. STRESS

a. General

Applicable background for the following analysis is the general discussion of membrane theory and the use of isotensoid theory in Section III, Item 4. Appendix II gives the method and the definitions of symbols not otherwise defined.

b. Approach

(1) Analytical

(a) BALLUTE Proper

The pressure distribution over the surface of the BALLUTE is expressed in terms of coefficients, which are defined as follows:

$$C_P = \frac{P_{(local)} - P_{(ambient)}}{q} , \qquad (70)$$

where

$P_{(local)}$ = local pressure,

$P_{(ambient)}$ = free-stream static pressure, and

q = dynamic pressure.

The external-pressure coefficients are always variable over the front of the BALLUTE and are sometimes variable over the rear half. For convenience, however, a constant coefficient is used in all cases for the rear. The pressure difference, P_x, at any point, x, on the BALLUTE is obtained by taking the difference in the $P_{(local)}$ values in Equation 70. Thus,

$$P_x = q(C_{P_i} - C_P) \quad , \tag{71}$$

where C_{P_i} is the coefficient for the internal pressure and C_P is the coefficient of the external pressure at any point, x.

Many of the equations of Appendix II that apply to BALLUTEs are programmed (some in slightly different form) for digital-computer solution. A first computer program requires values of k, ρ_r, the equivalent of I_{Rr}, and values of C_{P_f} for various values of x as input data.[a] The computer then calculates C_D, the equivalent of P/q, and the parameters of the front of an 80-deg BALLUTE for various values of x ending with a table of y versus x. The coordinates of the constant-pressure rear curve are defined by the given values of k and ρ_r and are obtained from Equation II-14 of Appendix II.

If the value of P/q obtained from the program does not agree with the actual value, the stress distribution must be analyzed for the actual value to ensure that there are no wrinkles or locally high stresses. This is done with the equations of Part 6 of Appendix II, which are solved by a second program. This program uses data defining the shape of the BALLUTE from the first computer program, along with any symmetrical loading condition (C_P values and C_1) and calculates the variation of stresses in the fabric and meridian cables over the front of the BALLUTE. (The back always has essentially constant pressure and therefore remains an isotensoid.)

(b) Inlets

Each inlet is a segment of a circular torus. The torus is oriented so that the

[a] Most BALLUTEs are fitted with a toroidal burble fence near the equator. Its effect must be considered in determining the proper value of I_{Rr}. A graphical integration of the pressure over the back of the BALLUTE (which for purposes of analysis is assumed to contain the burble fence) yields a drag coefficient (based on the area = πR^2) for this portion of the BALLUTE only. If the BALLUTE had no fence but had a constant pressure coefficient equal to minus this drag coefficient over the rear, the front of the BALLUTE (which is aerodynamically more significant than the rear) would be unaffected. For convenience, therefore, this simplification is made in the analysis.

meridian direction in the torus corresponds to the hoop direction in the BALLUTE proper. The pressure in the inlet is equal to the internal pressure in the BALLUTE; the pressure around the outside of the torus is conservatively assumed to be zero (gage). The meridian stress is approximately equal to the pressure times the radius of the torus cross section; the fact that this value is nearly always much less than the fabric stress in the BALLUTE proper, gives a large factor of safety. The hoop stress in the torus is smaller than the meridian stress; this also gives a large factor of safety.

(c) Burble Fence

Unlike the BALLUTE proper, the burble fence does not have any meridian straps. Because the warp and fill threads are at 45 deg to the principal stress axes, the stress ratio must be one to one if substantial thread racking and distortion are to be avoided. A surface with a one-to-one stress ratio can be obtained with the equations of Appendix II by letting $k = 0$. A family of contours for such a surface is obtained with Equation II-14 of Appendix II by choosing various values of ρ, depending on the size of burble fence desired. If the burble fence has a nearly constant pressure from the top forward and a different constant pressure from the top rearward, it is possible to obtain a uniform stress throughout the fence by joining two surfaces with different values of ρ at the top of the fence. One of these values can be chosen to obtain a fence of the desired size; the other must then be chosen to give equal fabric stress in the front and rear portions. Equation II-7 of Appendix II gives the fabric stress as

$$f = \frac{PR}{2}(1 - \rho) \quad , \tag{72}$$

where R is the outer radius of the burble fence. Inserting the subscripts r and f and equating fabric stresses gives

$$P_r(1 - \rho_r) = P_f(1 - \rho_f) \quad ,$$

or

$$\rho_f = 1 - \frac{P_r}{P_f}(1 - \rho_r) \quad . \tag{73}$$

If the desired value of ρ_r is given, ρ_f can be found by Equation 73.

(d) Deployment Analysis

The deployment analysis uses the assumptions of rigid-body dynamics, in which the canister, the BALLUTE package, and the payload are assumed to be rigid bodies, and the deployment-bag bridle line and riser line are assumed to be massless springs. The canister is given an initial velocity by a set of explosive thrusters. It travels freely until the deployment-bag bridle line becomes taut, at which time the canister and the BALLUTE package move rearward with the same velocity. They are accelerated rearward together by their aerodynamic drag until the riser is nearly taut, at which time the canister and deployment bag are cut loose. The BALLUTE and the payload then act as a two-mass system connected by the riser (spring). The riser absorbs the energy required to bring the BALLUTE and the payload to the same velocity. Equations for the motions and forces involved are developed in detail in Appendix IV.

(2) Empirical

The analytical methods described previously are based on classical membrane theory, which in itself does not require further experimental verification. The validity of its application to BALLUTE design has been established by successful wind-tunnel and airdrop tests of BALLUTEs in previous development programs; in many of these tests the margins of safety were lower than those used in this program. It was not deemed necessary, therefore, to perform structural tests on the complete BALLUTE prior to the flight test, which will be the final verification of the design values.

c. Example (TB-1)

(1) Applicable Techniques

All the assumptions and equations that are discussed in Item 4, b (1), above, are applicable to the design of TB-1.

(2) Results

(a) BALLUTE Proper

The external pressure distribution is shown in Figure 72. In addition, the following values were given:

C_{P_i} = 2.0, based on a two-shock system (80-degree conical shock followed by a normal shock)

q = 200 psf

Figure 74 shows that the BALLUTE was fitted with a toroidal burble fence, which materially increased the drag and had to be accounted for in the analysis. A graphical integration of the pressure over the back half (which for purposes of analysis is assumed to contain the burble fence) yielded a pressure drag coefficient of 0.34 for this portion of the BALLUTE only. This drag force is applied as a uniform tension to the envelope half, forward of the maximum envelope diameter. A simplification of the C_P curve presented in Figure 72 yielded the following values for C_{P_f}:

X/R	0	0.05	0.1	0.15	0.2	0.25	0.3	0.35	0.4	0.45	0.5	0.55
C_{P_f}	0.80	0.825	0.85	0.87	0.89	0.91	0.92	0.915	0.920	0.910	0.850	0.805

X/R	0.6	0.65	0.7	0.75	0.8	0.85	0.9	0.95	0.98	0.995	1.0
C_{P_f}	0.755	0.705	0.66	0.605	0.55	0.53	0.53	0.525	0.52	0.51	0.50

The above coefficients yielded values of P_{x_f} and the constant value of P_{x_r}. These values were then substituted into the definition of I_x in Appendix II to obtain the I terms in Equation II-26a of Appendix II. The BALLUTE does not have a center cable, so ρ_c = 0. Equation II-26a then gives k = 0.451. This value of k yielded a plain-back, isotensoid BALLUTE, which satisfied the 80-deg boundary condition of Equation II-26a. The resulting shape, however, was longer than desired; therefore, a value of k = 0.6 was chosen arbitrarily for determining the BALLUTE shape. This value of k produced a shape that would

be isotensoid for a value of the internal-pressure coefficient lower than the given value of 2.0. The first computer program gave the shape for k = 0.6, and the second program analyzed the stresses for the actual internal pressure of 2.0, as described in the general BALLUTE analysis. The resulting maximum values are

$$k_f' = 0.506 \tag{74}$$

and

$$\frac{2f'}{P'R} = 0.559 \ , \tag{75}$$

where

$$\begin{aligned} P' &= \Delta P \\ &= \left(C_{P_{internal}} - C_{P_{base}}\right) q \\ &= 2.34q \ , \end{aligned}$$

and where

$$C_{P_{internal}} = 2.0$$

and

$$C_{P_{base}} = -0.34 \ ,$$

from

$$\begin{aligned} Drag_{base} &= C_{D_{base}} qS \\ &= C_{P_{base}} qS \ ; \end{aligned}$$

eliminating q and s gives

$$C_{P_{base}} = C_{D_{base}}$$

Substituting $P' = 2.34q$, $q = 200$ psf, $n = 16$, and $R = 2.5$ ft gives

$$T_m' = 291 \text{ lb}$$

and

$$f' = 27.2 \text{ lb per inch.}$$

Numerical integration of the given pressure-coefficient values yields

$$C_D = 1.025 \quad . \tag{76}$$

The corresponding drag force is

$$D = (1.025)(200)\pi(2.5)^2$$

$$= 4030 \text{ lb}$$

The given maximum value of $T_m' = 291$ lb occurs near the nose of the BALLUTE in the region of the keeper ring. With the meridian tension and the geometry known, the keeper ring and keeper-ring tie-loop loads are obtained with the equations of statics. The resulting values are:

$$\text{Keeper-ring tension} = \frac{\text{Unbalanced radial force by meridians}}{\text{Unit length of keeper hoop}} \times$$

$$\text{keeper hoop radius}$$

$$= 321 \text{ lb}$$

$$\text{Tie-loop loads} = 49 \text{ lb each}$$

(b) Inlets

The pressure in the inlet is assumed to be equal to 2.0 q or 400 psf, based on a two-shock system (80-deg conical, followed by a normal shock). Assuming zero external pressure, a conservative stress value was calculated. The meridian stress is approximately equal to the pressure differential times the radius, or

$$\frac{(400)(2\text{-}1/8)}{144} = 5.8 \text{ lb per inch} \quad . \tag{77}$$

This value is much less than the fabric stress in the BALLUTE proper, giving a large static factor of safety. The hoop stress in the torus is smaller

than the meridian stress; this also gives a large factor of safety. The hoop stress is 5.8/2 due to pressure plus a smaller amount due to the spring [Torque (30 lb in.)/inlet perimeter and moment arm].

(c) Burble Fence

The burble-fence analysis follows the general method outlined in Item 4, b (1) (c), above. By trial it has been found that the curve for $\rho_r = 0.8$ gives approximately the desired size of the rear of the fence. The pressure difference over the rear is q(2.0 + 0.08). On the front of the fence the pressure difference is q(2.0 - 0.49). The equation derived in Item 4, b (1) (c), above, gives

$$\rho_f = 1 - \frac{2.08}{1.51}(1 - 0.8)$$

$$= 0.724$$

Substituting q = 200 psf, R = 36 in., P = 2.08 q, $\rho = 0.8$, and $I_{Rr} = 1$ into Equation II-7 of Appendix II gives f = 10.4 lb per inch, which is much lower than in the BALLUTE proper.

(d) Deployment Analysis

The calculations below are based on the equations and notation of Appendix IV. The following values are given:

$$m_1 = \frac{35 \text{ lb}}{32.2 \text{ fps}^2}$$

$$= 1.088 \text{ slugs (test-item container)}$$

$$m_2 = \frac{10}{32.2 \text{ fps}^2}$$

$$= 0.311 \text{ slugs (test item)}$$

$$\ell = 2 \text{ ft}$$

$$L = 10 \text{ ft}$$

$$q = 200 \text{ psf}$$

The material used in both the riser line and the deployment-bag line for the calculation is a 3/4-in.-wide webbing, woven from HT-1 fiber. A typical stress-strain curve for this fiber is shown in Figure 2 of Reference 42. Because the curve is nonlinear, it is necessary to make a linear approximation for the analysis. It is desired not to load the material to more than half of its ultimate strength, which corresponds to an elongation of about 18 percent; therefore, if a secant modulus line is drawn at an elongation of 10 percent, the area under the actual curve is always greater than the area under the straight line for the operational loading range. From the referenced figure, the 10-percent secant modulus is 52 grams per denier and the ultimate strength is 6 grams per denier. The spring-type stiffness-to-strength ratio is therefore 8.66. Ultimate strength of the 3/4-in.-wide webbing is given as 2550 lb (Reference 43, p. 7). The riser line is made up of 16 of these webbings, and the deployment bag is composed of 4. It follows that

$$E_\ell = (4)(2550)(8.66)$$

$$= 88,400 \text{ lb} \tag{78}$$

and

$$E_L = (16)(2550)(8.66)$$

$$= 353,000 \text{ lb} . \tag{79}$$

The canister is deployed by a set of explosive thrusters, which are capable of imparting a velocity of 30 fps to a 45-lb weight. In this case, however, only m_1 is accelerated initially. If the thrusters impart the same energy to the 35-lb weight m_1 as they do the 45-lb weight, it follows that $V_c = 32.6$ fps. Substituting into Equation IV-16 of Appendix IV gives

$$P_{\ell_{max}} = 3380 \text{ lb} . \tag{80}$$

Equation IV-17 gives

$$V_1 = \frac{(1.088)(32.6)}{(1.088 + 0.311)} = 25.4 \text{ fps} . \tag{81}$$

The canister diameter is 1.5 ft. With a flat-plate type of drag coefficient (1.5), the drag has a constant value of

$$D = (1.5)(200)\pi(0.75)^2$$
$$= 530 \text{ lb} . \quad (82)$$

This drag is assumed to be divided between the canister and the deployment bag in proportion to their areas. Thus, if the deployment bag is eight inches in diameter,

$$D_2 = 104.5 \text{ lb}$$

and

$$D_1 = 425.5 \text{ lb} .$$

Substituting into Equation IV-20 of Appendix IV gives

$$V_2 = 93 \text{ fps} . \quad (83)$$

Equation IV-32 gives

$$C_1 = \frac{\frac{-104.5}{35,300} + \frac{93}{337i}}{2}$$
$$= -0.00148 + \frac{0.138}{i} . \quad (84)$$

Equation IV-33 gives

$$C_2 = \frac{\frac{-104.5}{35,300} - \frac{93}{337i}}{2}$$
$$= -0.00148 - \frac{0.138}{i} . \quad (85)$$

Equation IV-36 gives

$$P_{L_{max}} = 9855 \text{ lb} . \quad (86)$$

Table 24 summarizes the results of the preceding analysis.

TABLE 24 - APPLIED LOAD SUMMARY OF TB-1 COMPONENTS

Item	Gore fabric (lb per inch)	Fence (lb per inch)	Meridian webs (lb)	Keeper ring (lb)	Keeper loops (lb)	Riser (lb)	Deployment bag line (lb)
Static loads	27.2	10.4	291	321	49	4030	. . .
Deployment loads	. . .	. . .	. . .	. . .	. . .	9855	3380

5. MATERIAL QUALIFICATION

a. General

The critereria and procedures followed for selecting material and establishing fabrication techniques for small supersonic parachutes are discussed in Section III, Item 5. These same criteria and techniques with the addition of more stringent leakage criteria are applicable for BALLUTE design.

b. Approach

(1) Design Factors

Seam raking is one factor to be considered in attempting to limit leakage to low rates. Under load, sewn seams tend to rake the filling yarns, causing gaps to form perpendicular to the seam; these gaps permit leakage of the inflation gas. Openings in excess of 1/16 in. wide were considered unacceptable from a gas-loss standpoint. It was determined by seam tests that this limit is reached at approximately 75 percent of the ultimate seam strength for tightly woven fabrics (see Table 25).

Cloth construction, or weave, and cloth porosity are additional factors to be considered. The cloth porosity is considered from the standpoint of vehicle gas loss. The porosity can be reduced to the desired limits of 0.02 cu ft per square foot per minute by high-pressure calendering or elastomeric coatings, or both. However, it is desirable to keep the basic cloth porosity to a minimum

TABLE 25 - DOUBLE-FELLED-SEAM TENSILE TEST*

Fabric	Ultimate load (lb/in.)	Temperature (F)	Results
2604/2	300	73	Raking appeared at 160 lb and did not exceed 0.0625 in. at ultimate load; fabric failed at seam
2604/2	240	170	Raking began at 100 lb and did not exceed 0.10 in. at ultimate load; fabric failed at seam
2634/7	177	73	Fabric was coated with one light coat of 1497C to reduce raking; raking began at 75 lb
2634/7	141.6	170	Raking began at 80 lb and was 0.250 in. at ultimate load; fabric was coated with 3 coats of 1497C to reduce raking; failure was in fabric
2634/7A	186	73	Material was calendered to reduce raking, but raking was still excessive; raking appeared at 80 lb and exceeded 0.125 in. at ultimate load
3382	186	73	Fabric showed less raking than 2534/7; raking began at 90 lb and reached 0.10 in. at ultimate load; fabric failed at seam
3382	142	170	Raking began at 80 lb and reached 0.18 in. at ultimate load; failure was in fabric
4137/2	302	73	Raking appeared similar to 2604/2; fabric failed at seam
4152	228	73	Raking started at 125 lb and did not exceed 0.125 in. at ultimate load; failure was at seam
HT-72	354	73	Warp direction, Size F Nomex thread - 0.125 in. edge distance
HT-72	316	73	Fill direction, Size F Nomex thread - 0.25 in. edge distance

*All seams were constructed as follows:

1. Seam width - 0.625 in.
2. Rows of stitching - 4
3. Stitches per inch - 10
4. Sewing thread - Size E, VT-295 Type II Class 1

since either of the above porosity-reduction techniques increases weight or packing volume. A plain woven fabric has the least tendency to rake at the seam area while under load, since each fill yarn is woven under consecutive warp yarns; this induces maximum yarn crimp and therefore locks the yarns. However, in selecting a particular fabric weave, a tradeoff may be necessary between the locking mechanism and maximum strength. For a given yarn size, greater fabric strength can be obtained in a basket or twill weave than in a plain weave. This is because less yarn crimp is involved, and a greater number of picks per inch can be set in the "beat-up" operation of the loom. Therefore, these tradeoffs were considered in the selection of the base fabric.

In addition to temperature capability, the coatings for the BALLUTEs are selected on the basis of (1) their effectiveness as a gas barrier, (2) their effect on flexibility of the fabric, and (3) their ability to prevent raking of the cloth in the seam area. The porosity of the base cloths and the leakage rate of coated fabrics are measured by the same procedures outlined for the small supersonic parachutes in Section III.

(2) Load Tests

Several candidate cloths were obtained and evaluated for strength. Results of the tests are listed in Table 26. In addition, seams of these materials were sewn and tested. All seams were 5/8-in.-wide double felled, with four rows of stitching, using Size E nylon thread spaced at 10 stitches per inch (see Table 25). Stern and Stern pattern No. 2604/2 was used for further seam evaluations. Both Size E and Size F nylon thread were used, and the effect of edge distance of the outer row of stitching on seam efficiency and raking was evaluated. The edge distances used were 0.06 and 0.125 in. The results of these tests are shown in Table 27.

The need for efficient webbing seams led to the design and testing of seam configurations. The testing was done on MIL-W-5625B webbing, which is 0.75 in. wide and has a rated breaking strength of 2300 lb (see Table 28). Tensile testing of the webbing indicated a breaking strength of 2950 lb based on an average of five samples. The tests were made in a Baldwin testing

TABLE 26 - RESULTS OF FABRIC TENSILE-STRENGTH TEST*

Fabric	Ultimate load warp (lb/in.)	Ultimate load fill (lb/in.)	Fabric manufacturer
Nylon 2604/2	337	322	Stern and Stern
Nylon 2634/7	211	203	Stern and Stern
Nylon 2653	450	438	Stern and Stern
Dacron 3382	214	200	Wellington-Sears
Nylon 4137/2	336	292	Stern and Stern
Nylon 4152	269	236	Stern and Stern
Nylon 8373	428	. . .	Stern and Stern
Nylon 1347	270	195	Burlington Mills
Nomex HT-72	376	352	Stern and Stern

*All specimens were one-inch raveled strips, tested at 73 F.

TABLE 27 - EFFECT OF EDGE DISTANCE ON SEAM STRENGTH*

Fabric	Edge distance (in.)	Ultimate load (lb/in.)	Size sewing thread	Temperature (F)
2604/2	0.06	287	E	73
2604/2	0.06	285	F	73
2604/2	0.06	265	E	170
2604/2	0.125	293	E	73
2604/2	0.125	240	E	170
2604/2	0.125	242	F	170

*Notes:

1. Seam width - 0.625 in.
2. Rows of stitching - 4
3. Stitches per inch - 10
4. Test results - all specimens failed at seam

TABLE 28 - NOMEX WEBBING TENSILE STRENGTH

Type webbing	Load (lb)			Remarks
	Average	High	Low	
MIL-W-5625, 1/2 in. wide	1050	1110	1020	Failed over 1-in.-diam pin
MIL-W-5625, 3/4 in. wide	2282	2470	2098	Failed over 1-in.-diam pin
MIL-W-5625, 1 in. wide	3000	3100	3050	Failed over 1-in.-diam pin
MIL-T-5038 Type IV, 1 in. wide	1050	1110	1020	Failed over 1-in.-diam pin

machine at a load rate of one inch per minute. The webbing was sewn into an 18-in.-diameter loop and pulled over two 1-in.-diameter pins at room temperature.

Of the seams tested, Designs 7, 9, and 10 of Table 29 resulted in webbing failures; all others failed in the sewing thread.

The strengths of various Nomex webbings and tapes are shown in Table 28. The joint constructions used were similar to seam design No. 10. For the MIL-W-5625 one-inch-wide webbing, the seam was the same using Nomex thread.

The tensile strength of the Nomex sewing thread is shown in Table 30.

(3) Permeability Tests

Several candidate coatings were tested for reducing the fabric leakage to 0.02 cu ft per square foot per minute at a differential pressure of 1/2 in. of water. Coatings were tested on 2604/2 nylon and HT-72 Nomex. The coatings were evaluated based on (1) weight added to obtain the desired porosity, (2) the resulting fabric stiffness, and (3) stability at temperature. The results are presented in Table 31 and Table 32.

TABLE 29 - TENSILE-STRENGTH RESULTS OF WEBBING SEAM CONFIGURATIONS

No.	Seam Design	Total stitching	Load (lb)		Size thread
			Per stitch	Total	
1	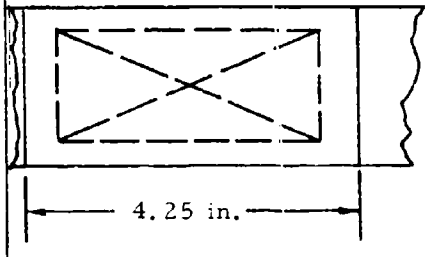 Sewing Failure	160	9.75	$\frac{3125}{2}$	F-F
2	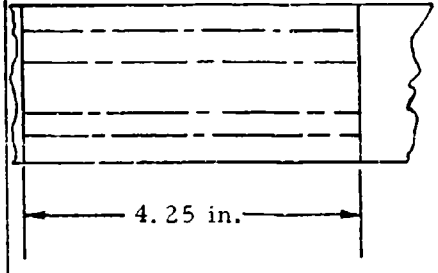 Sewing Failure	160	10.25	$\frac{3245}{2}$	F-F
3	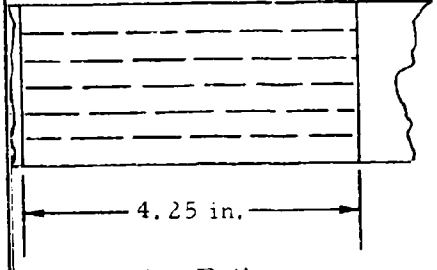 Sewing Failure	206	9.07	$\frac{3625}{2}$	F-F

TABLE 29 - TENSILE-STRENGTH RESULTS OF WEBBING SEAM CONFIGURATIONS (Continued)

No.	Seam design	Total stitching	Load (lb)		Size thread
			Per stitch	Total	
4	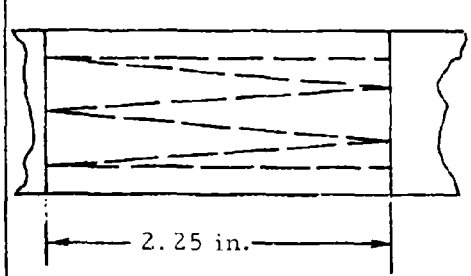 Sewing Failure	120	16.42	$\frac{3940}{2}$	3 Cord
5	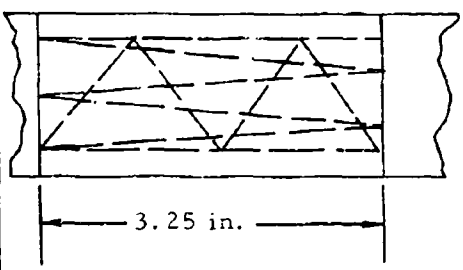 Sewing Failure	175	16.35	$\frac{5360}{2}$	3 Cord
6	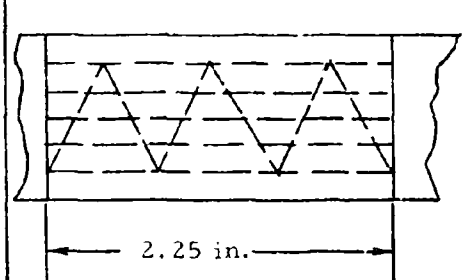 Sewing Failure	135	17.25	$\frac{4670}{2}$	3 Cord

TABLE 29 - TENSILE-STRENGTH RESULTS OF WEBBING SEAM CONFIGURATIONS (Continued)

No.	Seam design	Total Stitching	Load (lb)		Size thread
			Per stitch	Total	
7	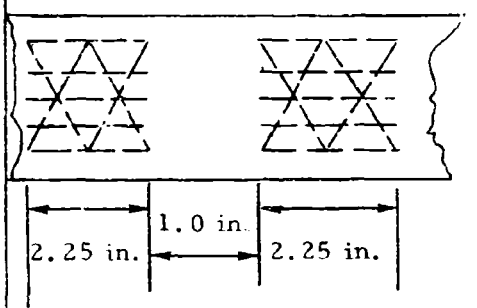 Fabric failure at seam	180	. . .	$\frac{5690}{2}$	3 Cord
8	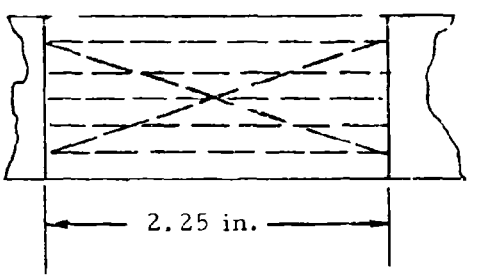 Sewing failure	140	15.80	$\frac{4430}{2}$	3 Cord
9	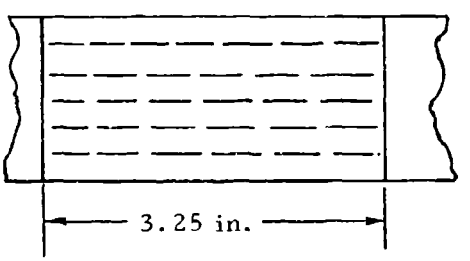 Fabric failure at seam	150	. . .	$\frac{4970}{2}$	3 Cord

TABLE 29 - TENSILE-STRENGTH RESULTS OF WEBBING SEAM CONFIGURATIONS (Continued)

No.	Seam design	Total stitching	Load (lb)		Size thread
			Per stitch	Total	
10	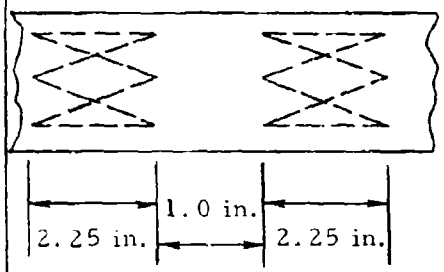 Fabric failure at seam	190	. . .	$\frac{5710}{2}$	3 Cord

TABLE 30 - TENSILE STRENGTH OF NOMEX SEWING THREAD

Size	Tensile strength (lb)
E	7.46
F	16.68
F-F	23.00
3 cord	23.50

c. Example (TB-1)

(1) Application Techniques

The values of the design factors were determined in a manner similar to that described in Section III for the small supersonic parachutes. These values

TABLE 31 - LEAKAGE RATES OF 2604/2 CLOTH*

Coating (1497C)	Diffusion rate (cu ft/sq ft/min)	Type of test	Gas	Total fabric weight (oz/sq yd)
Uncoated	5.0	Cambridge with Flowrator	Air	5.6
1 wash coat	0.66	Cambridge with Flowrator	Air	6.2
2 wash coats	0.0003	Cambridge	Helium	6.5
1 regular coat	0.05	Cambridge with Flowrator	Air	6.6
2 regular coats	0.1824×10^{-5}	Cambridge	Helium	7.0
3 regular coats	0.02964×10^{-5}	Cambridge	Helium	7.4

*Notes: (1) wash coat is one regular coat of 1497C thinned with an equal amount of solvent; (2) weight is for both fabric and coating; (3) two and three regular coats make sample stiff; (4) diffusion rate is measured at differential pressure of 1/2 in. of water.

TABLE 32 - LEAKAGE RATES OF HT-72 CLOTH COATED WITH DIFFERENT ELASTOMERS*

Coating	Diffusion rate (cu ft/sq ft/min)	Type of test	Gas	Fabric weight (oz/sq yd)
Uncoated	3.07	Cambridge with Flowrator	Air	8.67
One coat, Dow-Corning RTV-731	0.004	Cambridge with Flowrator	Air	9.77
One coat, Dow-Corning RTV-102	0.02	Cambridge with Flowrator	Air	9.75
One coat Polyurethane, Goodyear Tire and Rubber Co. CUR-71A	0.06	Cambridge with Flowrator	Air	9.55
Two coats, Dow-Corning Silastic 131	0.00	Cambridge	Helium	10.6

*Notes: (1) substrate material - HT-72; (2) all RTV coatings very flexible; (3) polyurethane coating stiff; (4) two coats of silastic value not measurable on equipment; (5) diffusion rate measured at differential pressure of 1/2 in. of water.

were used, together with the structural requirements, to determine the required quick-break strengths of candidate materials at room temperature. Candidate materials and jointing techniques selected by earlier tests were applied to actual component fabrication. The components then were tested to failure. The leakage rate was determined by using laboratory samples and inflating the complete BALLUTE to low pressures.

(2) Results

The selected values of the design factors and resulting strengths used for selecting materials, seams, and joints for the various TB-1 BALLUTE components are presented with the in-plant-test results in Table 33 for the static loads and in Table 34 for the dynamic case. The selected design factors relative to quick-break room-temperature strength were as follows:

TABLE 33 - MATERIAL REQUIREMENTS AND STATIC MARGINS FOR TB-1

Item	Gore fabric (lb/in.)	Inlet and fence (lb/in.)	Meridian webs (lb each)	Keeper ring (lb)	Keeper-ring loops (lb each)	Riser (lb total)
Static load based on Mach 2.5 pressure distribution	27.2	10.4	291	321	49	4,030
Design factors						
Overload	2	2	2	2	2	2
Dynamic	2	2	2	2	2	2
Seam efficiency	1.2	1.2	1.2	NA	NA	1.2
Temperature	1.3	1.3	1.1	1.1	1.1	1.1
Raking	1.3	1.3	NA	NA	NA	NA
Safety	1.5	1.5	1.5	1.5	1.5	1.5
Product of factors	12.2	12.2	7.93	6.6	6.6	7.93
Material strength requirements						
Basic	332	127	2310	2119	323	32,000
Seam	277	106	1925	NA	NA	26,667
Raking	213	81	NA	NA	NA	NA
Material test results						
Basic	322/337	322/337	3050	2400	1600	48,800
Seam	267/300	To envelope 163*	2855	NA	NA	28,400†
Raking	Min at seam ultimate	Min at seam ultimate	NA	NA	NA	NA
Static margins						
Basic	-3 percent	154 percent	+32 percent	+13 percent	+400 percent	+52.5 percent
Seam	-2 percent	To envelope +54 percent	+48 percent	NA	NA	+6.5 percent
Raking	+25 percent	To envelope 101 percent	NA	NA	NA	NA

NA - Not applicable

*Jaw break.

†Four-foot specimen.

TABLE 34 - DEPLOYMENT LOADS AND STATIC MARGINS FOR TB-1

Item	Riser
Deployment load, calculated peaks	9,855 lb
Design factors	
Overload	2
Seam	1.2
Safety	1.5
Product of factors	3.6
Material strength requirements	
Basic	35,500 lb
Seam	27,917 lb
Static-test values	
Basic	47,200 lb
Seam	28,400 lb
Margin based on static values	
Basic	+33 percent
Seam	+2 percent

1. Overload - 2, based on past test-point q dispersions
2. Dynamic - 2, based on possible rapid flexing of BALLUTE material
3. Seam efficiency - 1.2, based on anticipated efficiency of 83 percent (actual was 80 and 89 percent)
4. Temperature - 1.3, based on reduction in room-temperature strength of nylon at temperature
5. Raking - 1.3, based on seam raking at 75 percent of ultimate seam strength
6. Safety - 1.5, standard value

Tables 35 and 36 present the results of TB-1 cloth and seam tests.

TABLE 35 - STRENGTH OF 2604/2 CLOTH USED IN TB-1 FABRICATION

Temperature (F)	Ultimate load - average (lb/in.)	Ultimate load - high (lb/in.)	Ultimate load - low (lb/in.)
73	336.9	342	328
170	278	285	271
170	322	330	317
170	247	260	239

TABLE 36 - STRENGTH OF SEAMS SEWN ON 2604/2 CLOTH USED IN TB-1 FABRICATION*

Ultimate load - average (lb/in.)	Ultimate load - low (lb/in.)	Ultimate load - high (lb/in.)	Temperature (F)	Remarks
300	295	310	73	Tested in warp direction
267	253	276	73	Tested in fill direction
264	252	271	170	Tested in warp direction
240	233	250	170	Tested in fill direction

*Notes:

1. Edge distance - 0.125 in.
2. Seam width - 0.62 in.
3. Rows of stitching - 4
4. Stitches per inch - 10
5. Thread - Size E
6. All failures were in the fabric at the seam

The selected gore seam was a 5/8-in. double-felled seam, using Size E nylon thread at 10 stitches per inch with 4 rows of stitching. The edge distance used was 0.125 in. This seam was selected because it met the strength requirements and induced minimum raking in the cloth.

The 3/4-in.-wide MIL-W-5625D webbing was found to have an actual tensile strength of 3050 lb. Lap splices of this webbing sewn in accordance with Configuration 10 of Table 29 had a strength of 2855 lb, resulting in a seam efficiency of 93.5 percent.

Two suspension-line specimens incorporating Configuration 10 of Table 29 and simulating the riser-line attachment to the payload were tensile-tested in the Baldwin testing machine. The specimen failed at 13,650 lb and 14,750 lb for an average strength of 14,200 lb. Both specimens failed at the edge of the sewing.

Two test specimens simulating the gore-to-burble-fence seam were fabricated and tested. The seam configuration was identical to that used in assembling the gores. The test was conducted as shown in Figure 76 to provide biplanar

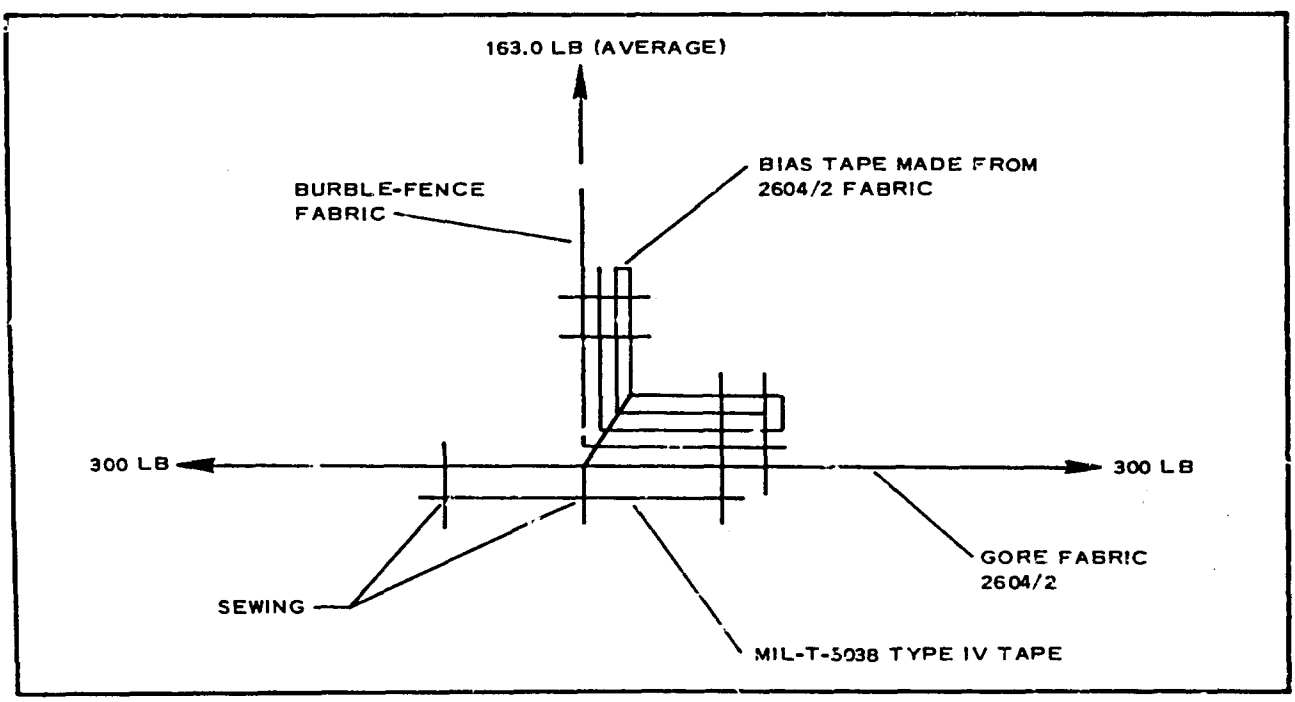

Figure 76 - Burble Fence Fabrication and Test

loading. The gore fabric was preloaded to 300 lb per inch, and the fence fabric was gradually loaded to failure. The strengths obtained were 181 and 145 lbs per inch, for an average of 163 lb per inch. Both failures occurred in the gore fabric in the clamping jaws, indicating jaw damage. Examination of the seams showed no indication of undue stress. Various weights of Goodyear Tire and Rubber Company 1497C neoprene elastomer were applied to the 2604/2 material to determine the minimum weight of coating required to meet the leakage-rate requirements (0.02 cu ft per square foot per minute, measured at a differential pressure of 1/2 in. of water). The results of these tests are shown in Table 31. Two wash coats of 1497C having a weight of 0.90 oz per square yard met the required leakage rate and still gave adequate flexibility for packaging.

6. DESIGN AND FABRICATION

a. General

During Phase I, two basic designs of similar construction but slightly different configuration were completed, one specifying nylon and the other, Nomex. Two units of the nylon (TB-1 and TB-1a) and one of the Nomex (TB-2) were fabricated and delivered for flight test.

b. Approach

(1) BALLUTE

The envelope contour of the BALLUTE approaches an isotensoid shape with 16 gores and 16 meridional webs. The gores are patterned to provide the correct lobe radius for this structure. The 16 meridional webs and the riser are formed by placing 8 webs continuously around the envelope and into the riser, forming the 16 riser webs. The webs end at the riser-attachment loop. At the front of the BALLUTE the webs are brought through a 6-in.-diameter keeper ring. The keeper ring is constructed of a large number of turns of light cord, forming a bundle with a cross section of approximately 1/2-in. diameter. The meridional webs are served together at a point 14-1/2 in.

forward of the keeper ring, forming the confluence point. This arrangement of keeper ring plus a confluence point is intended to keep the meridional webs oriented and loaded equally and to decrease the angle change at the keeper ring.

The gore cross seams, just forward of the maximum diameter, are alternated in a zigzag pattern and shingled to the rear to provide symmetry and to reduce aerodynamic spin forces. The gores also are arranged so that the main seams reduce aerodynamic-spin forces. The gore main seams and cross seams are double felled and 5/8 in. wide, with four rows of straight stitching. The meridionals are located on the centerline of the gores; the main seams are at the top of the lobes. This construction permits the formation of the lobes with very little racking or change of thread-set angle.

The cloth material (excluding webs) is lightly coated with elastomer for two reasons: to decrease the porosity of the fabric for proper inflation, and to alleviate raking of the cloth in the seams. The two nylon BALLUTEs are coated with a clear colored neoprene, and the Nomex BALLUTE is coated with a silicone elastomer.

The BALLUTEs have four inflation inlets located forward of the burble fence and near the maximum diameter of the envelope. Each inlet is a segment of a fabric torus with a spring-loaded wire frame at its base and mouth. Although the fabric torus is essentially a stable-pressure body, the wire frame is required for increased stability; the spring loading is required to ensure initial inflation and to aid the torus body in reacting to the drag force on the inlet.

Each inlet assembly includes a sock-type check valve to prevent reverse flow through the inlet. If reverse flow starts, the "sock" collapses against the envelope and against the cords extending across the base frame, preventing further reverse flow. Although the sock-type constructions vary somewhat from one BALLUTE to another, they have the same function and approximately the same size. The cross-sectional area of each inlet is approximately 14 sq in.

throughout, except for the exit or aft portion of the sock, which converges to approximately 12 sq in. The purpose of this convergence is to ensure that the sock is fully inflated during initial high-flow rates by maintaining the highest velocity and lowest pressure at the exit.

In general, the pattern of the fence gores provides a cross-sectional contour that, when subjected to the determined pressure distribution, loads the fabric to approximately equal tension stress throughout, thereby creating a stable shape.

The cross-sectional radius at its forward surface is considerably larger than the radius at the aft surface. The rear-fence attachment seam to the envelope is designed to be loaded in shear. By necessity, the front attachment seam is in tension. To alleviate this problem, a reinforcement tape is placed circumferentially around the inside of the envelope; a single row of Size F-F thread, plus additional rows of lighter thread, is sewn into the tape.

A pressure transducer is provided to indicate the inflation pressure within the BALLUTE. Because of g-load limitations on the transducer, it is mounted on the riser near the attachment loop, where shock loads are lowest. A flexible pressure tube is attached to the riser to transmit the inflation pressure from the BALLUTE to the transducer. The tube consists of a surgical-rubber tube with a 3/32-in. inside diameter; a coil of 0.015-in.-diameter music wire is inserted in the tube to prevent its collapsing. Pure gum rubber was selected as the best elastomer material for this tube because (1) it has a much lower percentage of volatile plasticizers than most other elastomers and therefore is less subject to "gassing off" errors at high altitudes; (2) it has much better recovery from creases than most materials; and (3) it has good temperature characteristics. (It can endure 300 F for long periods and 350 F for several minutes with little damage).

(2) Deployment Bag and Sequence

The deployment bag for the BALLUTEs is a cylindrical nylon bag, 13 in. in ameter and about 14 in. long. Four heavy nylon webs, attached longitudinally

and equally spaced around its diameter, extend into a bridle at the back end of the bag for attachment to the deployment canister. Two hoop webbings are attached at each end of the deployment bag; in the packaged position, these webbings are spaced 12 in. apart.

The bag in the packaged position consists of two compartments or sections. The inner, or bottom, section is the larger and contains the BALLUTE envelope. Four lock loops, attached to the inside of the bag and to the bridle, are secured over the envelope pack with one turn of MIL-C-5050 Type II cord (350 lb) through the loops and through the break loop, which is attached to two riser webs just forward of the keeper ring (see Figure 77).

The other section of the bag, forward of the inner lock loops, contains the riser. A large rectangular flap of fabric, attached to the inside of the bag, is provided for retaining the riser in an orderly arrangement. The riser is laid onto this flap in a zigzag fashion and hand tacked to the flap with light linen cord (see Figure 77). The retainer flap then is folded into the bag, and the four outer lock loops, which are the ends of the bridle webs, are secured with four turns of MIL-C-5050 Type II cord through the four loops and through the cutter knife provided on the riser (see Figure 78). The bag is closed by gathering the outer flap of the bag in pleats and stitching two turns of Size E nylon thread through the pleats and through the riser, thus providing an initial break for protection of the cutter knife. The BALLUTE assembly is shown in Figure 79.

The BALLUTE deployment system is shown in Figure 80. The system is illustrated with a series of six sequences that represent various times and events from the start of container separation to full BALLUTE inflation.

(c) Example (TB-1)

The TB-1 (Figure 81) is an all-nylon BALLUTE coated with clear neoprene. Its general external contour is shown in Figure 82. This BALLUTE has a 10-percent burble fence located slightly aft of the maximum diameter. The fence is located so that a line at 25 deg to the axis is tangent to both fence and envelope, as shown in Figure 82.

Figure 77 - Partly Packaged BALLUTE

Figure 78 - Partly Packaged BALLUTE with Riser

Figure 79 - Packaged TB-1 BALLUTE

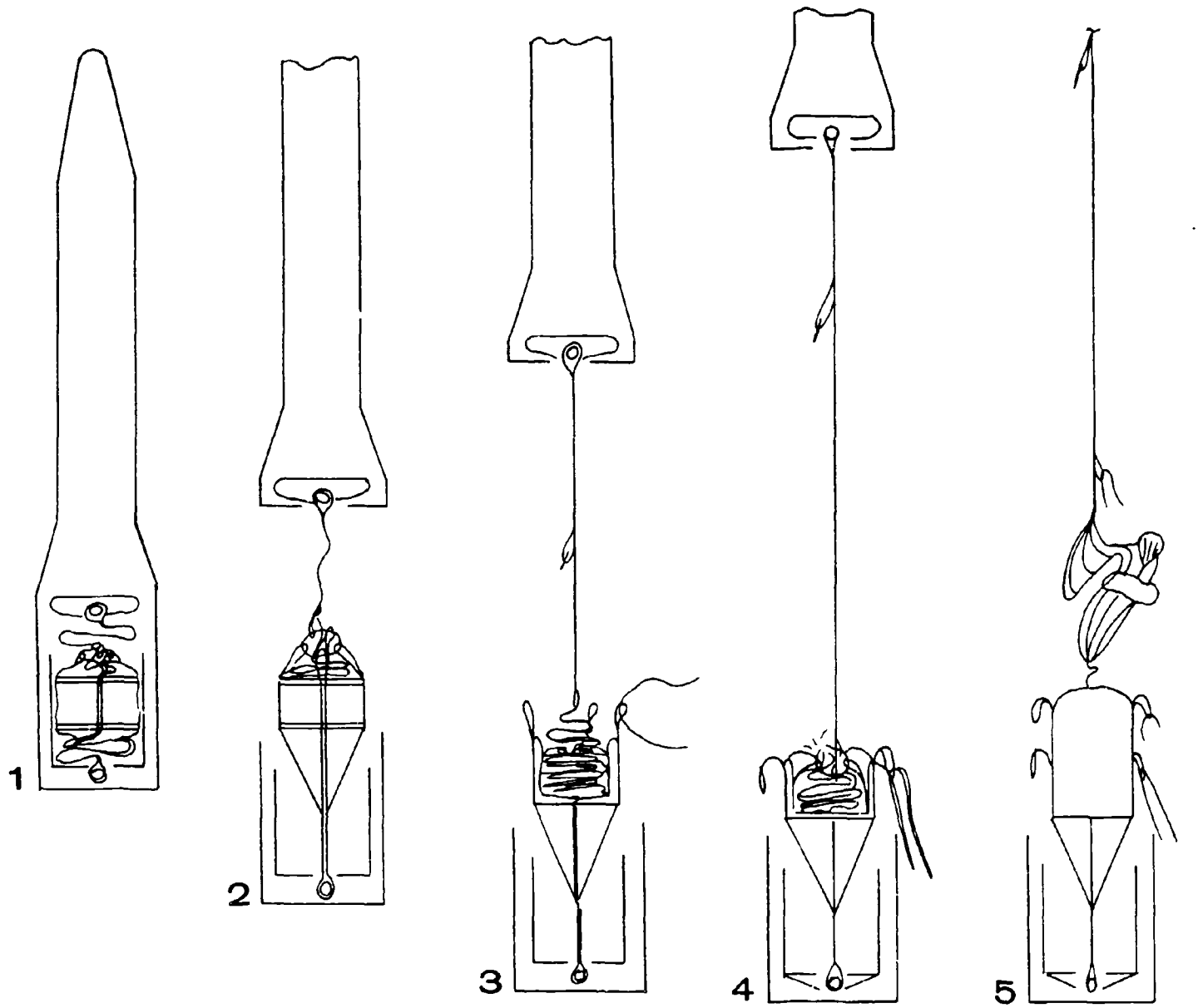
1
2
3
4
5

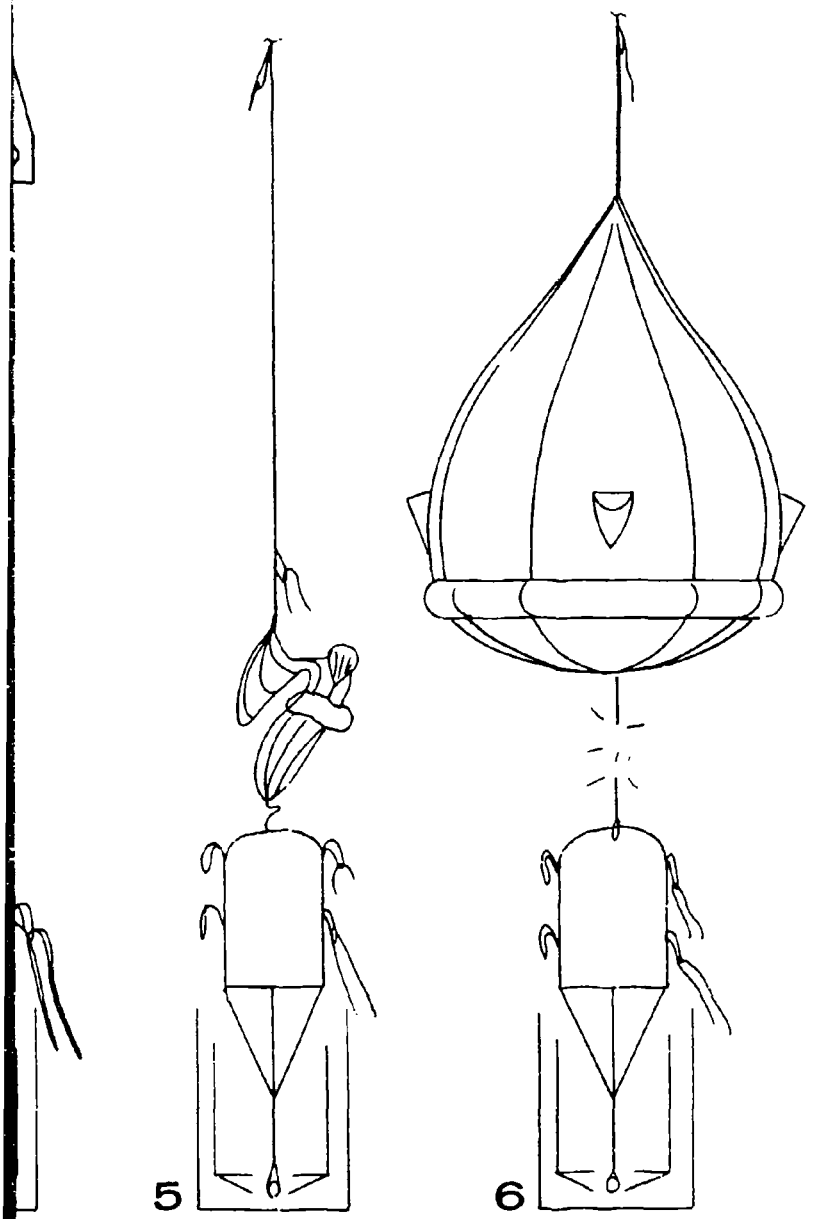

1 MISSILE IN FLIGHT, ALL COMPONENTS INTACT. BALLUTE PACKAGED IN DEPLOYMENT BAG AND CONTAINER. RISER LINES ATTACHED TO MISSILE. DEPLOYMENT-BAG BRIDLE LINES ATTACHED TO THE AFT SECTION OF CONTAINER

2 CONTAINER SEPARATED FROM MISSILE; DEPLOYMENT BAG MOVING AFT AFTER BEING ACCELERATED BY CONTAINER THROUGH BRIDLE LINES. RISER LINES SLIGHTLY EXTENDED; ONE RISER LINE HAS METAL CUTTER NEAR DEPLOYMENT BAG WITH NYLON CORD LACED THROUGH IT AND DEPLOYMENT-BAG BRIDLE LOOPS. CORD IS USED TO TIE ENDS OF BRIDLE TOGETHER TO TO RETAIN RISER LINES AND BALLUTE ENVELOPE IN DEPLOYMENT BAG WHEN LOADS ARE APPLIED TO BAG BY CONTAINER.

3 DEPLOYMENT-BAG BRIDLE FULLY EXTENDED. CONTAINER AND DEPLOYMENT BAG AT LOWER VELOCITY AND DECELERATING MORE THAN MISSILE; BALLUTE RISER LINES EXTRACTED AFTER CUTTER CUTS NYLON CORD.

4 SECOND SET OF FOUR LOOPS INSIDE BAG, TIED TOGETHER BY CORD TO HOLD BALLUTE ENVELOPE IN PLACE WHILE RISER LINES ARE BEING PULLED OUT.

5 CORD BROKEN BY BREAK LOOP; FOUR LOOPS FREE, WITH DEPLOYMENT BAG PEELED INSIDE-OUT AND OFF BALLUTE. AFT SECTION OF BALLUTE STILL ATTACHED TO DEPLOYMENT BAG WITH NYLON CORD TO ENSURE EXTENSION AND TO POSITION RAM-AIR INLETS IN AIRSTREAM FOR BALLUTE INFLATION AND PRESSURIZATION

6 CORD BROKEN; BALLUTE FULLY INFLATED; CONTAINER AND DEPLOYMENT BAG ENTIRELY SEPARATED FROM BALLUTE.

Figure 80 - Details of BALLUTE Deployment Sequence

2

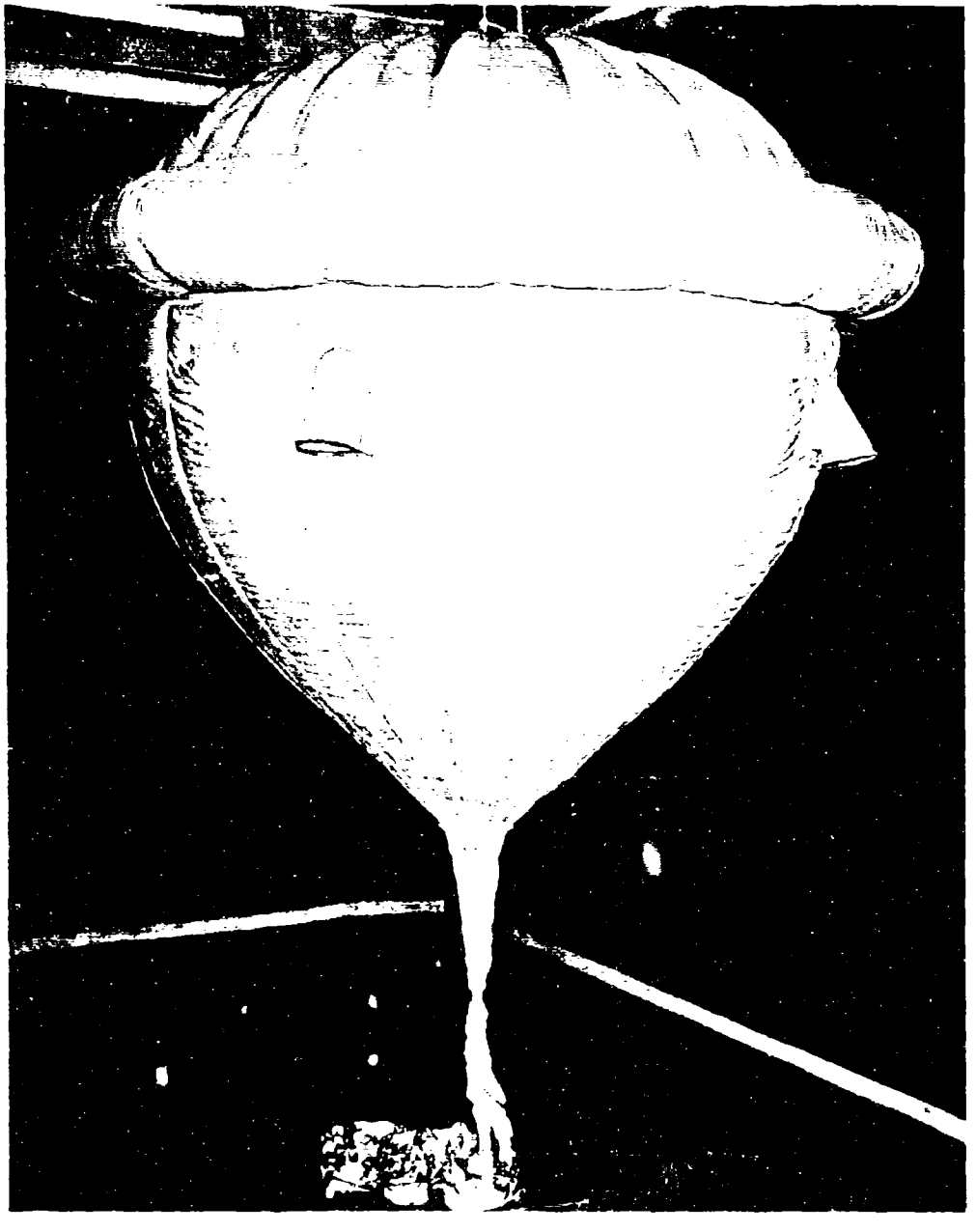

Figure 81 - TB-1 BALLUTE

The four inflation inlets are equally spaced around the BALLUTE and located forward of the burble fence. Each inlet has its leading edge canted back 15 deg from the vertical to increase structural stability.

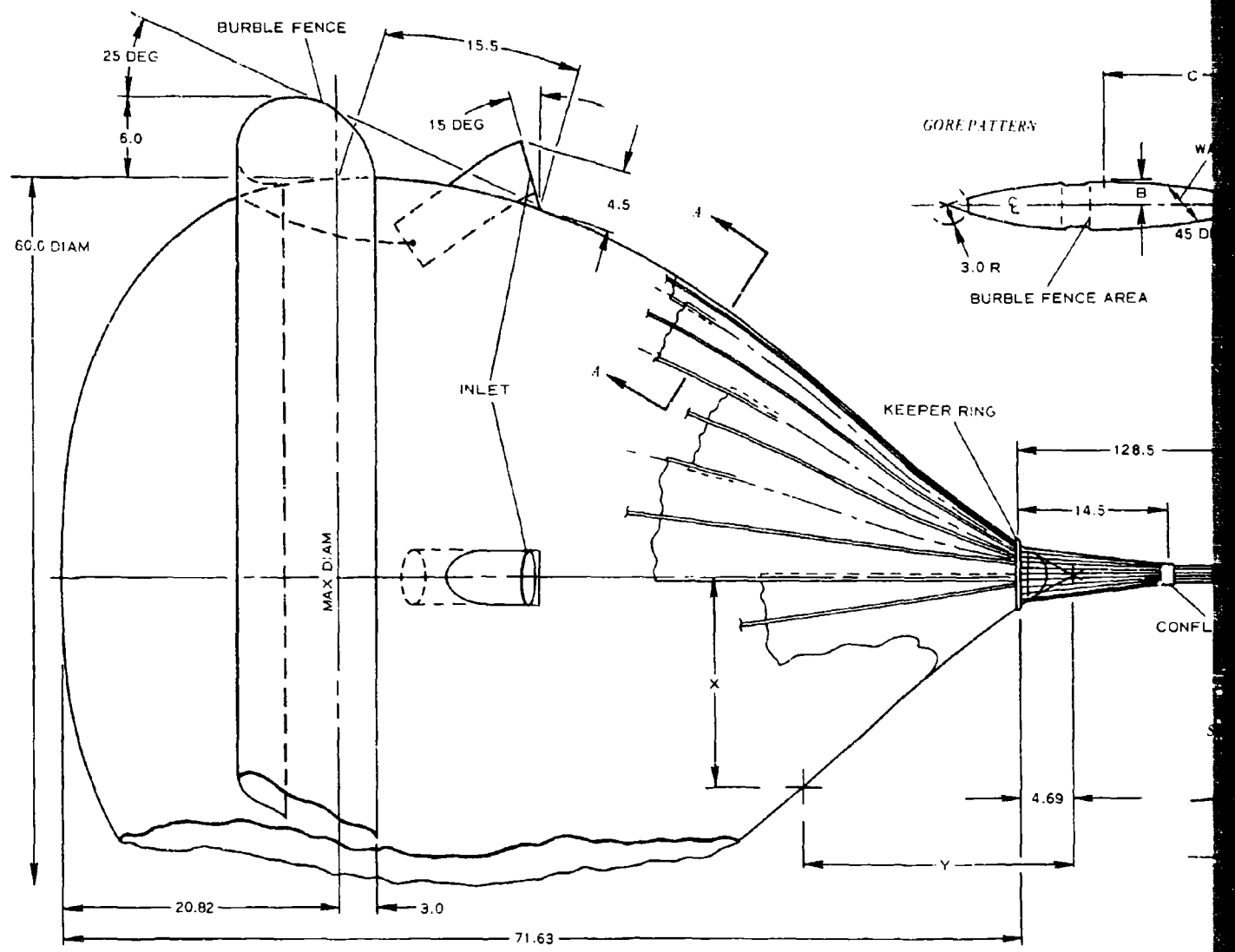
BURBLE FENCE
25 DEG
6.0
15.5
15 DEG
4.5
60.0 DIAM
INLET
MAX DIAM
KEEPER RING
128.5
14.5
X
Y
4.69
20.82
3.0
71.63
GORE PATTERN
C
B
3.0 R
BURBLE FENCE AREA
45 D

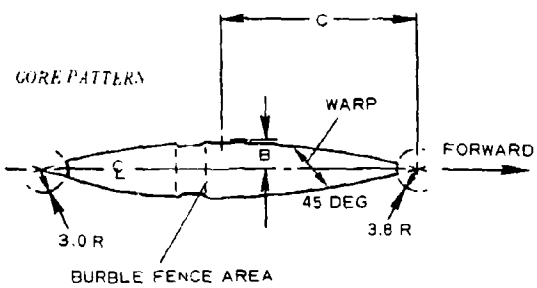

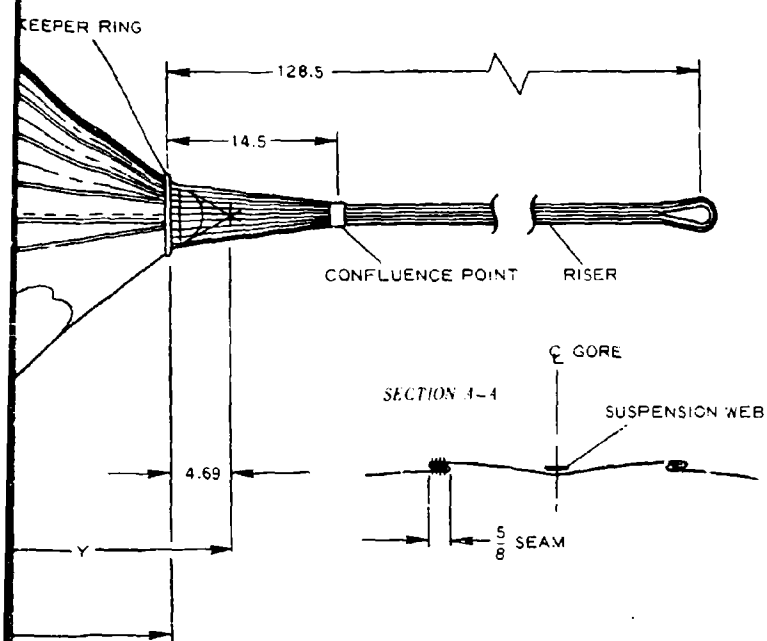

GORE COORDINATES				PROFILE COORDINATES	
C	B	C	B	X	Y
6.00	0.63	61.63	5.95	3.0	4.69
12.00	1.34	63.00	5.84	9.0	12.44
24.00	2.88	68.00	5.75	15.0	19.54
30.00	3.65	69.20	5.84	21.0	27.23
36.00	4.33	72.00	5.69	27.0	38.22
42.00	4.95	78.00	5.05	30.0	55.50
48.00	5.43	84.00	4.15	27.0	65.73
54.00	5.77	90.00	3.10	18.0	73.50
60.00	5.94	102.00	0.76	12.0	75.50
				0	76.32

NOTE: ALL DIMENSIONS ARE IN INCHES.

Figure 82 - Schematic of TB-1 and TB-1a BALLUTE

2

SECTION V - LARGE SUPERSONIC (HIGH-Q) PARACHUTE

1. GENERAL

a. History

Deceleration and safe recovery of heavy equipment at supersonic speeds and medium altitudes require large-diameter parachutes capable of withstanding high deployment loads and operating under optimum inflation conditions. It became apparent that only gradual inflation and loading will provide an acceptable solution at this time.

Basically, two concepts emerged - the hemisflo and the conical parachutes. Development work on these types used wind-tunnel tests conducted at $1.5 \leq M \leq 3.0$ range, as described in References 3, 10, 11, and 13. During later phases, full-scale, free-flight data will be provided by the LP-1 and LP-2 designs, deploying from the "A" payload vehicle when airdropped or ballistically boosted to predetermined test points.

b. Conditions

The conditions for test points of the LP-1 and LP-2 designs of Project 8151, Task 01 (large supersonic parachutes), were established by trajectory analysis and concurrence by the Flight Dynamics Laboratory. The following parameters express the test conditions:

1. Aircraft drop altitude - 50,000 ft
2. Aircraft drop speed - Mach 0.78
3. Test-item deployment altitude - 14,000 ft
4. Test-item deployment Mach number - 1.25
5. Test-item deployment dynamic pressure (q) - 1350 psf

The trajectory study is summarized in Figure 83. The test-point selection is justified for the following reasons:

1. To meet contract Mach 1.2 requirement
2. To have sufficient altitude after test-item deployment for data acquisition and second-stage landing-parachute deployment
3. To have sufficient altitude for second-stage parachute deployment after possible test-item malfunction

c. Configuration Selection

The approach to advance the state of the art of large supersonic parachutes and achieve high-drag and stability objectives while maintaining structural integrity, thermal protection, and shape stability would be:

1. To evaluate the performance of specific configurations (canopy shape and geometric porosity) of previous wind-tunnel, sled, and flight tests
2. To select configurations that will be based on the ultimate objective to extend the parachute performance to Mach 3 and dynamic pressure of approximately 5000 psf

The LP-1 and LP-2 designs were selected in accordance with the requirements of the contracting agency and the following specific parameters:

1. Type of canopy - 20-deg conical ribbon, 16-ft diam (D_o)
2. Large parachute LP-1, geometric porosity - 29 percent
3. Large parachute LP-2, geometric porosity - 15 percent
4. Detail design per Air Force drawing No. 59K6273

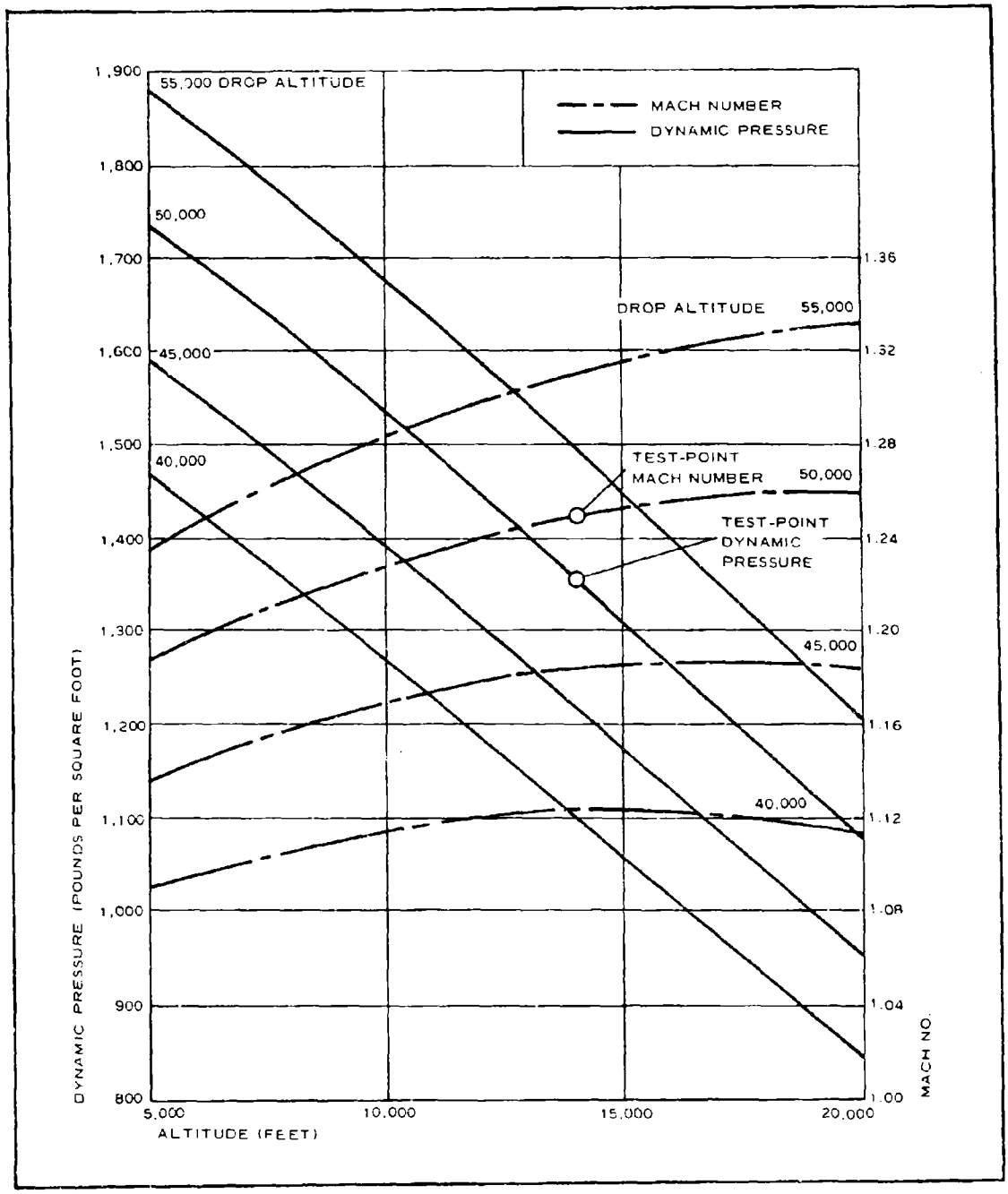

Figure 83 - Drop-Test Trajectory Study (High-Q)

5. Exceptions to Air Force drawing No. 59K6273

   a. Ribbon spacing - as required

   b. Vertical ribbons - as required

   c. Latest fabrication methods required (e.g., continuous ribbons will be used)

6. Canopy reefing - none

2. AERODYNAMICS AND STRESS

a. General

The aerodynamic requirements consist of defining the environment for a given configuration and determining how it performs because of that environment. The environment is defined by the test conditions listed above and influences due to the configuration of the payload and possible local perturbations. For Vehicle A and the relative position of the parachute behind it, although the wake of the payload has a small-scale effect, the wake can become an important factor in shaping the local-flow environment.

The performance of the large supersonic parachute is yet to be determined. Present predictions are based mostly upon empirical observations. The following can be stated, based on these observations.[44]

1. There is hyperbolic decrease in the mean shock factor as the mean time to inflate increases.
2. Steady drag is proportional to the dynamic pressure.
3. Stability is judged by the coning angle.
4. Porosity and canopy shape influence parachute performance

The structural-load requirements are based on the aerodynamic opening-shock load. Once the opening shock load is established, the required strength

of the suspension lines is determined based on a given safety factor and sewing efficiency. From experience, the canopy fabric is selected based on a given line strength.

b. Empirical

In preparation for the feasibility of the free-flight development of specific configurations, wind-tunnel tests had been conducted with various ribbon parachute configurations at Arnold Air Force Station, (see References 3, 11, 12, and 13). References 3 and 13, which are the most recent tests for ADDPEP requirements, present the results for reefed ribbon parachutes. Applicable test results[13] are given in Table 37 for the following configuration:

Type	Hemisflo or 20 deg conical
Diameter	19.3 in. (D_o)
Geometric porosity	14 percent
Suspension-line length	38.6 in. ($2D_o$)
Reefed diameter	4 and 4.5 in. (D_{r_1})
Riser line	None (confluence point located at payload aft bulkhead)
Reefed to (percent)	20.7 and 23.3 ($D_{r_1}/D_o \times 100$)

The following comments describe the parachute performance throughout the Mach range of 1.5 to 3.0:

1. Absence of coning (stability about confluence point) and rotation
2. Absence of canopy and suspension-line flutter, except for some flutter of ribbons near canopy lip
3. Absence of canopy buzzing (inflation instability)
4. Inflation of canopy crown to a near-rigid condition

It is important to note that the resulting reefed shape performed in a similar

TABLE 37 - VON KARMAN TUNNEL A DATA

Run no.	Type of parachute	Reefed to (percent)	Mach no.	q (psf)	Drag (lb)	C_DA (sq ft)	16-ft-diam C_DA equivalent (sq ft)
19	Hemisflo	20.7	1.5	177	25.0	0.141	13.8
			2.0	183	29.5	0.161	15.8
			2.5	150	23.5	0.157	15.4
			3.0	112	16.0	0.205	20.1
20	Conical		1.5	179	34.5	0.193	18.9
			2.0	183	39.5	0.213	20.9
			2.5	150	32.5	0.217	21.3
			3.0	112	22.5	0.201	19.7
21	Hemisflo	23.3	1.5	184	. . .	. . .	. . .
			2.0	181	47.0	0.259	25.4
			2.5	150	40.5	0.270	26.5
			3.0	114	26.0	0.229	22.5

manner whether the bow shock was detached (below Mach 2) or attached (above Mach 2).

In all tests, the parachute canopies were packed in a deployment bag in a line-stretched condition behind a 2-in.-diameter ADDPEP missile "C" configuration. When the tunnel was at test point (Mach 3 for Run 19 and Mach 1.5 for Runs 20 and 21), the bag was withdrawn manually from the canopy allowing canopy inflation.

Table 38 presents applicable test results[3] for the following test configuration:

Type	20-deg conical ribbon
Diameter	10 ft (D_o)
Geometric porosity	15 percent
Suspension-line length	20 ft ($2D_o$)
Reefed diameter	1.5 ft (D_{r_1})

Reefed to 15 percent ($D_{r_1}/D_o \times 100$)

TABLE 38 - PROPULSION WIND-TUNNEL DATA

Run no.	Type of parachute	Reefed to (percent)	Mach no.	q (psf)	Drag (lb)	C_DA (sq ft)	16-ft-diam C_DA equivalent (sq ft)
8	Conical	15	2.59	122	412	3.39	8.63
8	Conical	15	2.79	120	417	3.07	7.81

The 10-ft-diameter parachute performed in a manner similar to the 19.3-in. chutes. Figure 84 shows the test setup. The test parachute and bag assembly were forcibly deployed aft with an initial spring force of 75 lb at Mach 2.59. The payload diameter was 17.6 in.; the shape of the payload was similar to that of ADDPEP Vehicle C, although the length was somewhat shortened.

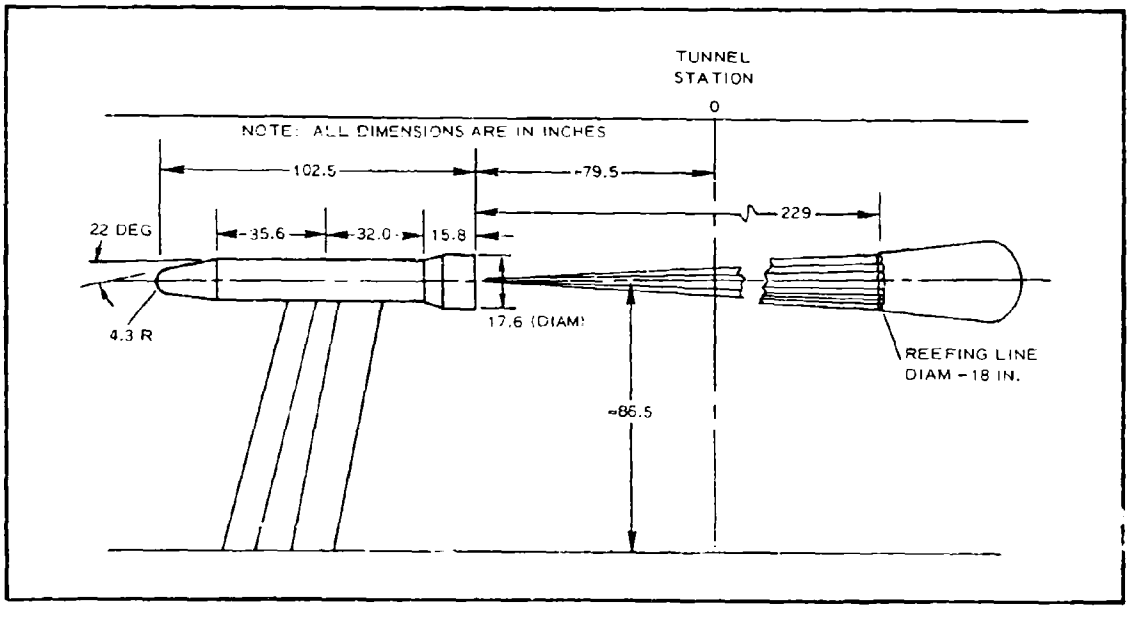

Figure 84 - Test Setup, 10-Ft-Diameter Conical Ribbon Parachute

c. Correlation

Since most previous and current investigations to extend the operating range (higher Mach number and dynamic pressure) of large parachutes have been empirical, data comparison and significant observations were limited to the results of wind-tunnel tests of various test configurations.

Conical and hemisflo ribbon-parachute configurations with geometric porosities greater than 20 percent were tested with various amounts of reefing;[11, 12] there was some evidence of satisfactory performance at isolated Mach-number test points. It was not until later tests[3, 13] that both conical and hemisflo ribbon parachutes with geometric porosities of 14 percent performed satisfactorily in a reefed condition at all Mach numbers 1.5 and 3.

A lower geometric porosity when the fully inflated canopy is disreefed may lead to stability deterioration and a higher opening-shock factor. Further tests are required to investigate opening-shock values and coning amplitude to evaluate the acceptability of this configuration.

According to the results described in Reference 12, the hemisflo configuration indicates stable position only when it is located in the wake of the forebody.

Based on the present state of the art, a large high-q parachute for high-g deceleratio can be designed to perform up to Mach 2 at a dynamic pressure as high as 1500 psf. The aerodynamic performance would be affected by the following system parameters:

1. Size of parachute
2. Weight of parachute
3. Ratio of chute size to payload size
4. Location of chute aft of payload
5. Deployment techniques

To select a configuration and deployment system that have been proved by tests to minimize adverse dynamic loadings, canopy-inflation instability

(breathing), and canopy flutter (buzzing), the structural integrity of the parachute (design load) will be based on the peak predicted opening load that will occur during deployment and canopy inflation. Either of two approaches can be used to determine the opening-shock design load. The conservative and simple approach is to use the handbook[45] infinite-mass opening-shock factor. However, if the weight and packaging-space requirements demand a less conservative shock factor, available flight-test data should be evaluated. To use a lower shock value obtained in flight (lower because the payload slows down during inflation), the system parameters must be similar to the above design factors. A drop-test has been conducted under the following conditions, which are very similar to this contract requirement:

1. Type of trajectory - vertical descent
2. Mach number - 1.12
3. Dynamic pressure - 1402 psf
4. Payload weight - 2118 lb
5. Parachute - 16-ft-diameter (D_o) conical ribbon (geometric porosity, 27 percent)
6. Type of deployment - line first from bag
7. Reefing - none

With the above conditions, the canopy-filling time was 0.156 sec, and the opening shock load was 104,000 lb. Based on a parachute drag area of 100 sq ft, the shock factor is

$$X = \frac{F_o}{C_D A q}$$

$$= \frac{104,000}{140,000}$$

$$= 0.743 .$$

With this shock factor, the peak load for this contract test point (Mach 1.25, q = 1350 psf) would be

$$F_o = XC_D Aq$$

$$= 0.74 \times 100 \times 1350$$

$$= 100,000 \text{ lb}.$$

Both LP-1 (29-percent porosity) and LP-2 (15-percent porosity) were designed and built to a design load of 150,000-lb.

It is evident that LP-1 has sufficient strength. However, since no performance data were available for a 15-percent-porosity parachute, an increased opening-shock value of 1 was estimated. This value corresponds to the infinite-mass conditions for higher porosity (i.e., greater than 20 percent) conical parachutes below speeds of Mach 1.[45] This should be a conservative estimate based on the 0.743 calculated for the 29-percent-porosity parachute and the reduction in the X factor associated with operation above Mach 1. Using X = 1,

$$F_o = XC_D Aq$$

$$= 1 \times 100 \times 1350$$

$$= 135,000 \text{ lb},$$

and the 150,000-lb strength for LP-2 is adequate.

Once the design load is established, the component design can be made based on the parachute handbook[45] and military design specifications for ribbon parachutes.

Figure 85 presents design data to show the feasibility of a candidate configuration to meet a requirement for Mach 3 high-dynamic deployment. These data were derived from the previously mentioned wind-tunnel tests at Arnold Air Force Station. The dashed curve indicates drag area ($C_D A$) capabilities of a reefed 16-ft-diameter ribbon parachute at various Mach numbers, although not at a high dynamic pressure. The test values of drag area were obtained by dividing the developed drag by the test dynamic pressuring using 1-, 1.61-, and 10-ft-diameter parachutes. Values shown in the figure were obtained by multiplying by a factor equal to the ratio of the area of a 16-ft-diameter chute

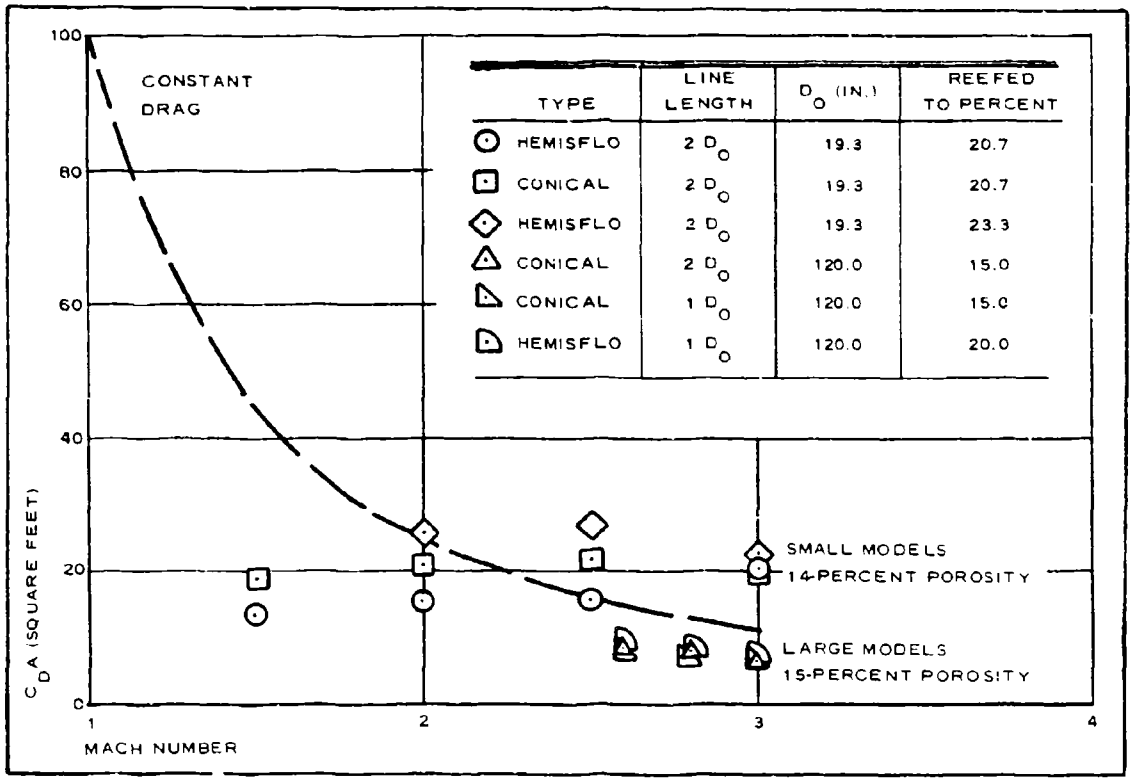

Figure 85 - Drag Area versus Mach Number (Equivalent to 16-Ft D_o Parachute)

to the area of the diameters of the wind-tunnel test parachutes. The dotted curve shows the theoretical drag area of a parachute at a sea-level aerodynamic decelerating force of 148,000 lb. This curve indicates an optimum design where there would be an infinite number of reefing stages and maximum deceleration, in minimum time and distance. Therefore, the technique to initiate the design of an efficient Mach 3 large-parachute-decelerating system would be to use a known canopy configuration plus portions of proven system designs. The following are a proven combination of sizing conditions that are recommended for future designs:

1. Type of canopy - ribbon
2. Canopy geometric porosity - 14 percent (evenly distributed)

3. Size - 16-ft diameter (D_o)
4. Payload weight - 2000 lb
5. Canopy reefing - two stages, reefed and disreefed
6. Suspension-line strength - 32 ft ($2D_o$)
7. Reefed to 20 percent - 3.2-ft reefing-line diameter

Figures 86 and 87 show deployment characteristics of the three different models (10-ft D_o) deployed at Mach 2.59 in a wind tunnel (infinite-mass condition). These figures show that drag area values are twice the average values over a one-second period at this Mach number; they indicate also that the $2D_o$ lines reduce the C_DA oscillations compared with the $1D_o$ lines.

3. DESIGN AND FABRICATION

a. General

Test items LP-1 and LP-2 were designed and built in accordance with the configuration requirements given in Item 1c, above.

b. Approach

(1) Parachute Test Unit

The test unit is designed to incorporate the following requirements.

1. The parachute deployment loads will be less than 100 g.
2. The large-parachute test-unit system will consist of
   a. Test-unit canopy and suspension lines
   b. Test-unit deployment bag and bridle
   c. Four-foot-diameter (D_c) guide-surface-type pilot parachute, bag, and bridle assembly
3. Minimum-weight component design must be considered.

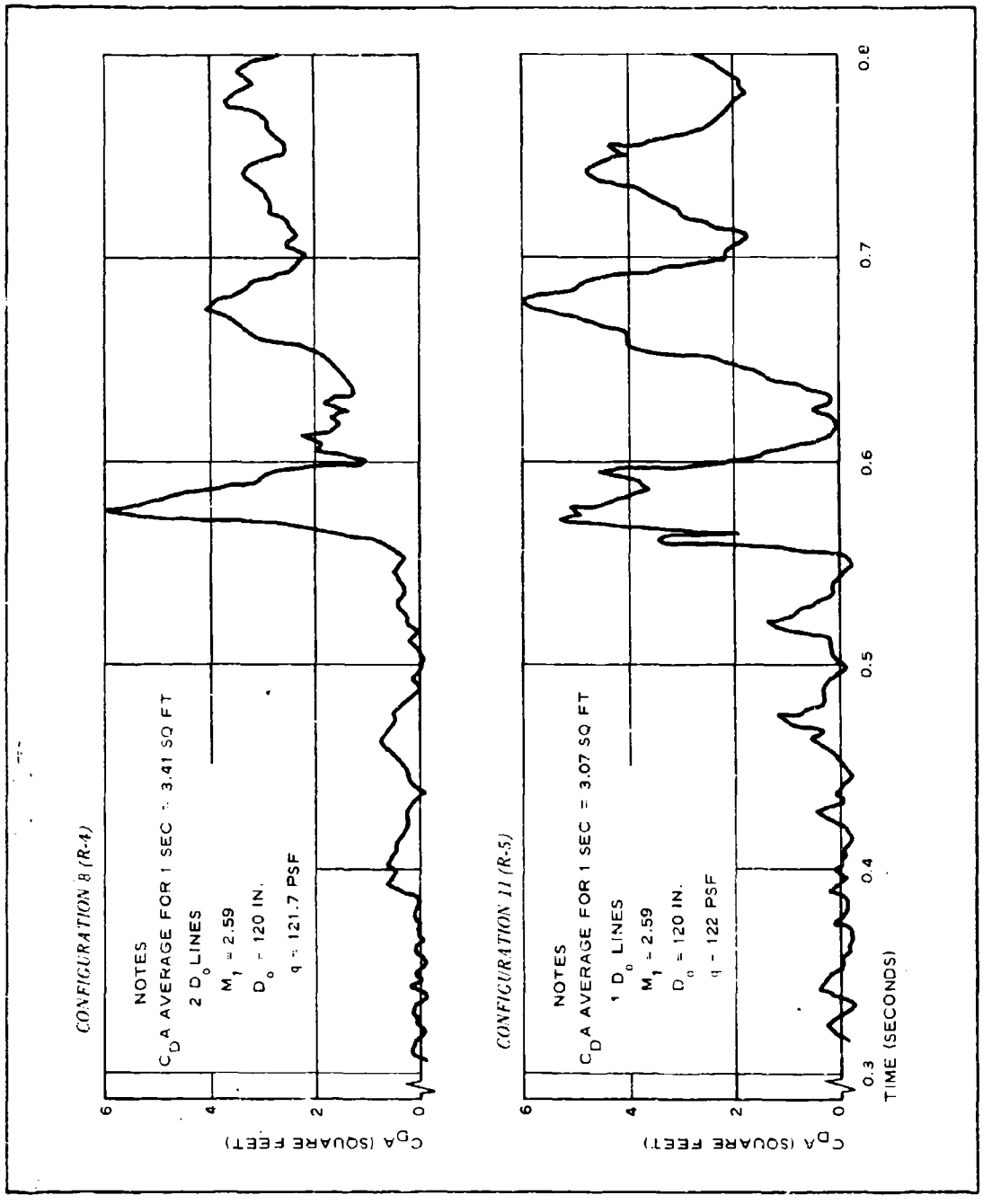

Figure 86 - Deployment Characteristics - 10-Ft D_o Reefed Conical Parachute

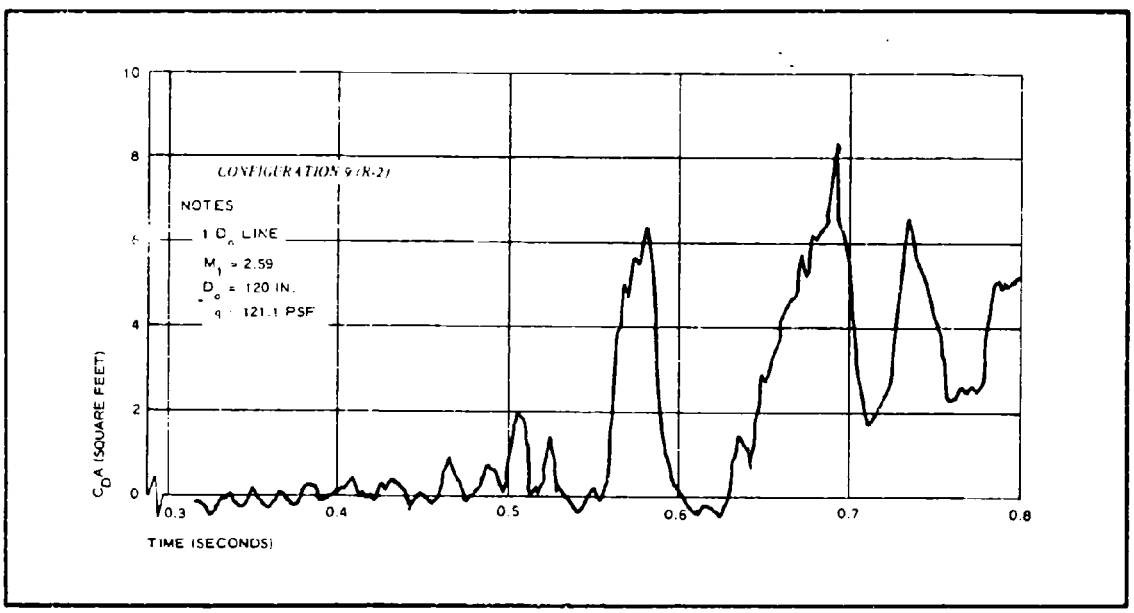

Figure 87 - Deployment Characteristics - 10-Ft-D_o Reefed Hemisflo Parachute

4. The parachute system will be compatible with Missile A canister installation.

5. The test-unit deployment bag will have a system to cut lacing.

6. The test unit will be packed with a system of break cords on the parachute lines to absorb energy during line stretch; this system will be made by sewing the lines to themselves and to the deployment bag.

7. The porosity of the test-unit canopy will be distributed evenly throughout the canopy gores.

8. The test-unit suspension lines will terminate with eight attachment-point loops.

9. Each suspension line will be wrapped with leather buffers; the midpoint of each buffer will be located on each suspension approximately 20.75 in. from the center line of the terminal-loop attachments.

10. The test-unit deployment bag will be approximately 15 in. in diameter and not longer than 42 in.

Based on the design load of 150,000 lb, the required strength of both LP-1 and LP-2 suspension lines is as follows:

$$F_{(\text{suspension line})} = \frac{F_o J}{c \times u \times n}$$

$$= \frac{150,000 \times 1.5}{0.95 \times 0.90 \times 32}$$

$$= 8250 \text{ lb (use 9000-lb line)},$$

where:

F_o = maximum opening force,

c = factor related to suspension-line convergence angle,

u = factor involving the strength loss at the connection of suspension-line and drag-producing surface or riser, respectively,

n = number of suspension lines, and

J = safety factor.

The results of the design of LP-1 are shown in Figures 88 and 89; those for LP-2 are shown in Figures 90 and 91. The results of ribbon-spacing calculations are given in Table 39. The canopy horizontal-ribbon strength was based on previous high-q parachute designs that withstand similar high-dynamic-pressure flight-test loads.

The design was made using Air Force drawing 59K6273 as a guide. The design agrees with the drawing for the following items:

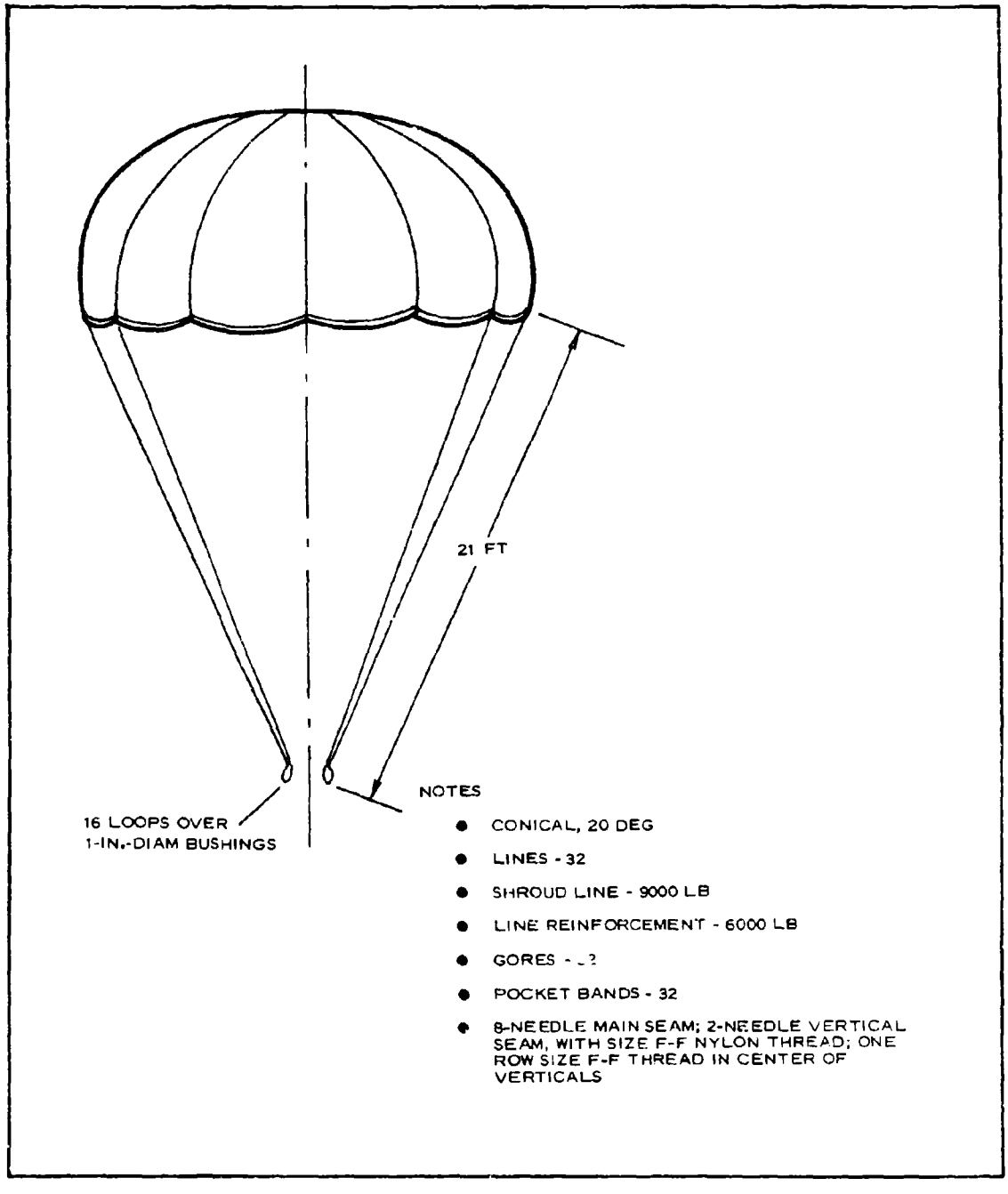

Figure 88 - Ribbon Parachute - 16-Ft-Diameter Fist Type, LP-1

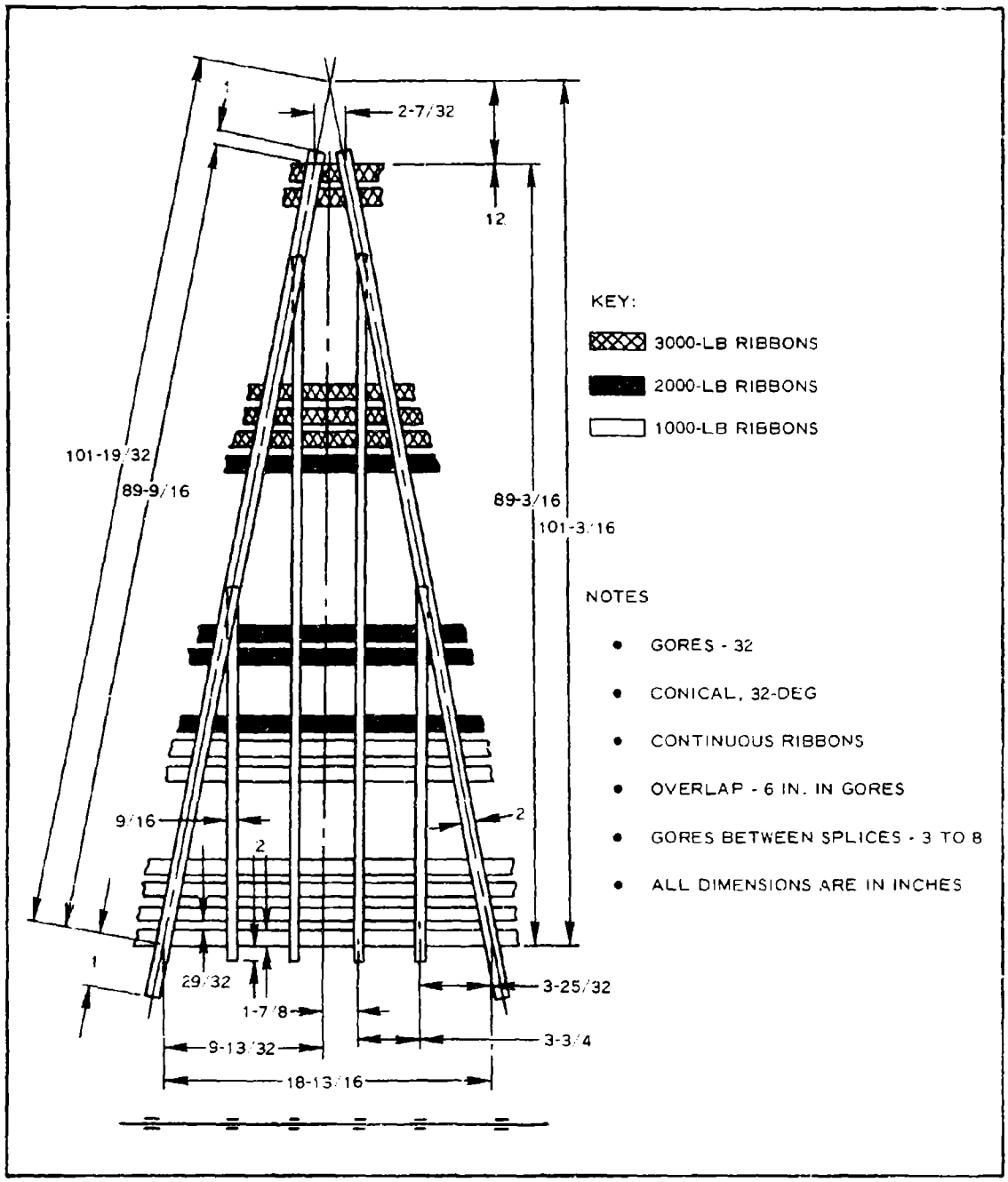

Figure 89 - Ribbon Canopy - 16-Ft LP-1

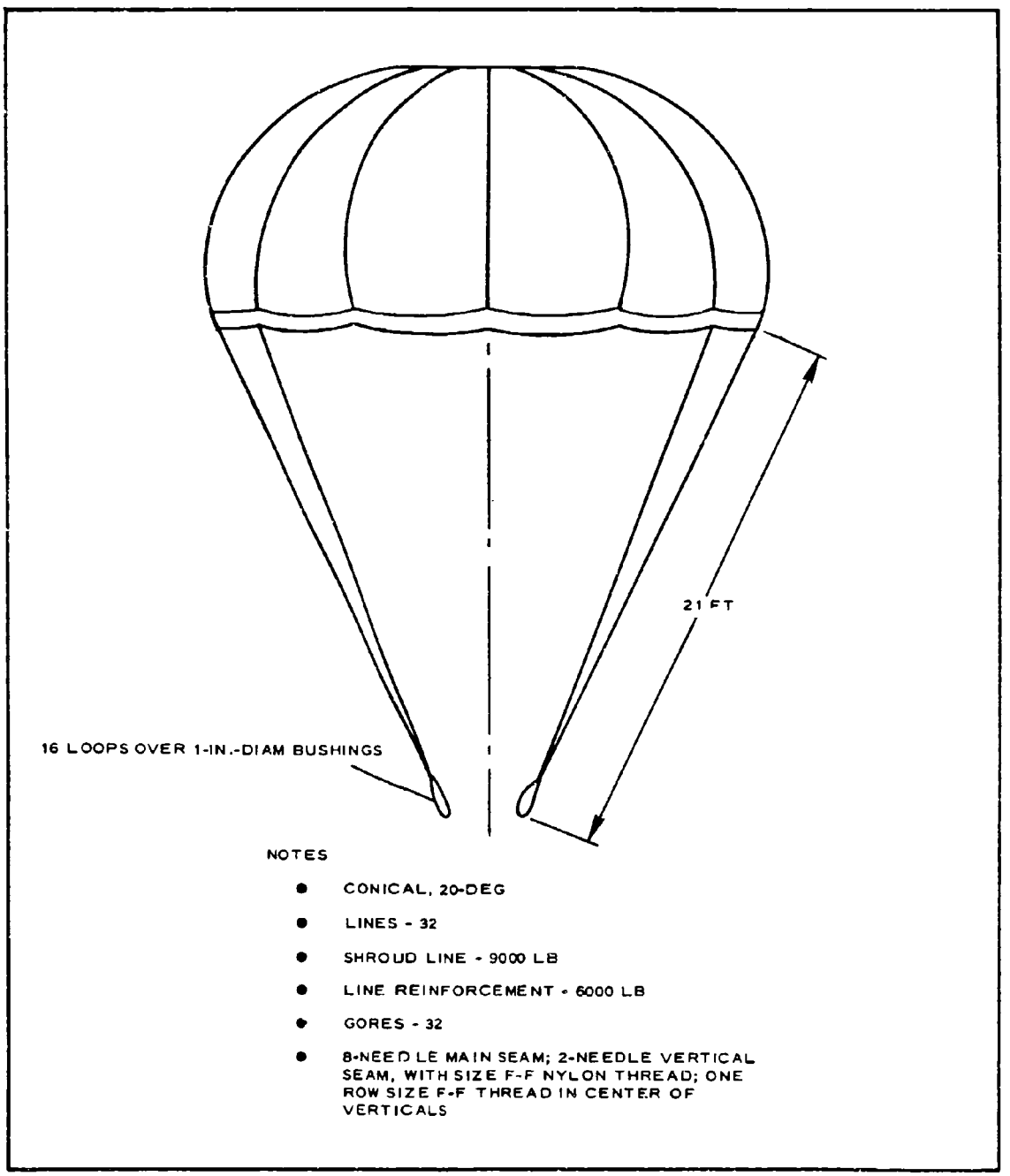

Figure 90 - Ribbon Parachute - 16-Ft-Diameter Fist Type, LP-2

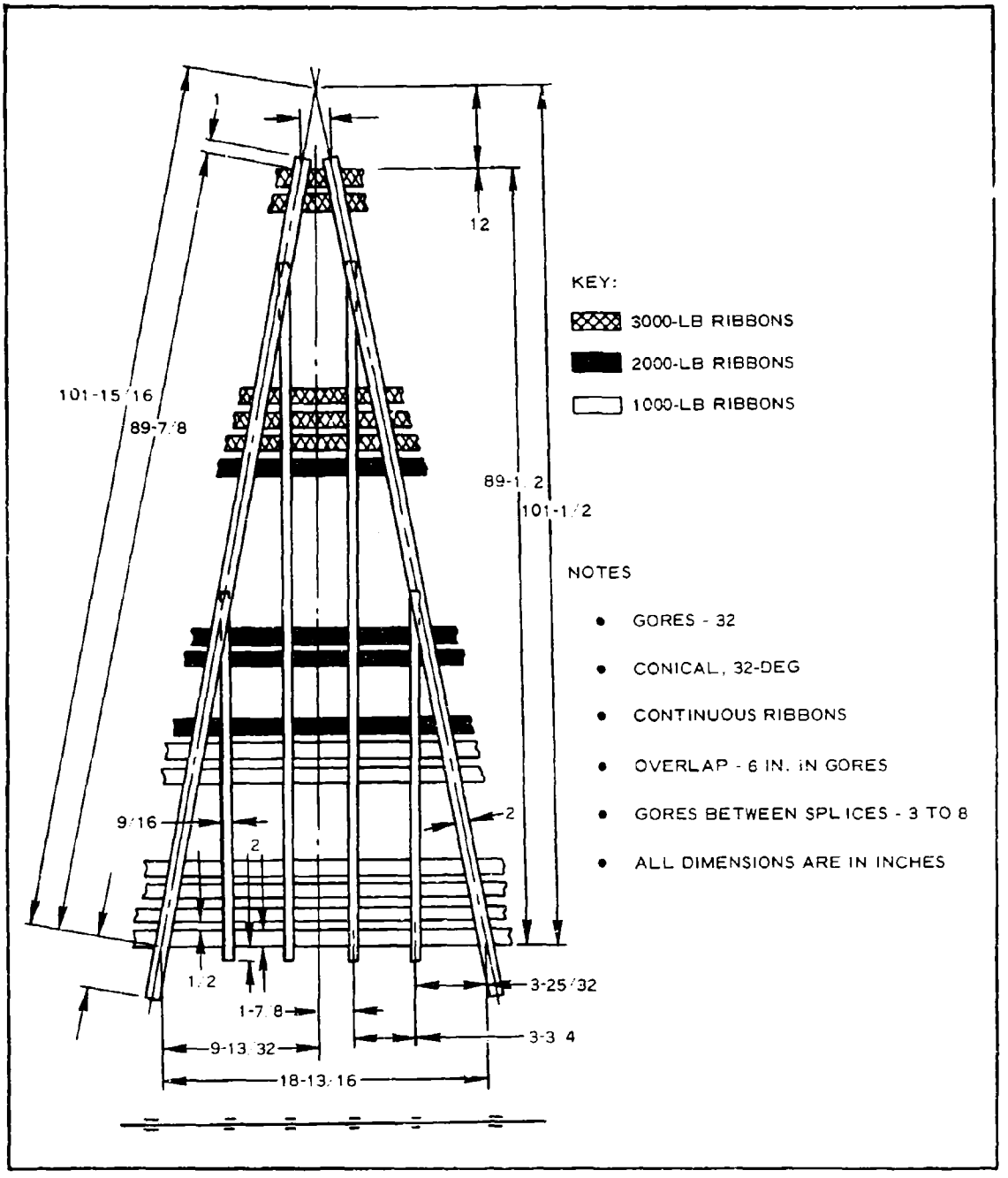

Figure 91 - Ribbon Canopy, 16-Ft LP-2

TABLE 39 - RESULTS OF RIBBON-SPACING CALCULATIONS

Type of ribbon	Spacing (in.)	Geometric porosity (percent)
LP-1	0.906	29.6
LP-2	0.500	16.4

1. Number of gores and lines
2. Strength of lines
3. Strength of vent and skirt hems
4. Strength of vertical ribbons

The significant differences are:

1. Porosity
2. Ribbon spacing
3. Use of continuous horizontal ribbons
4. Omission of intermediate reinforcing band
5. Use of twice-as-strong ribbons in the intermediate section
6. Pocket bands omitted on LP-2
7. Greater number of ribbons adding to ultimate strength

(2) Deployment Sequence

Figure 92 depicts the system deployment sequence; Figures 93 and 94 show the actual test item, LP-1. Packaged dimensions of the large parachutes are 15-in. in diameter and 35.6 in. long; the packaged volume is 5850 cu in. System weights are as follows:

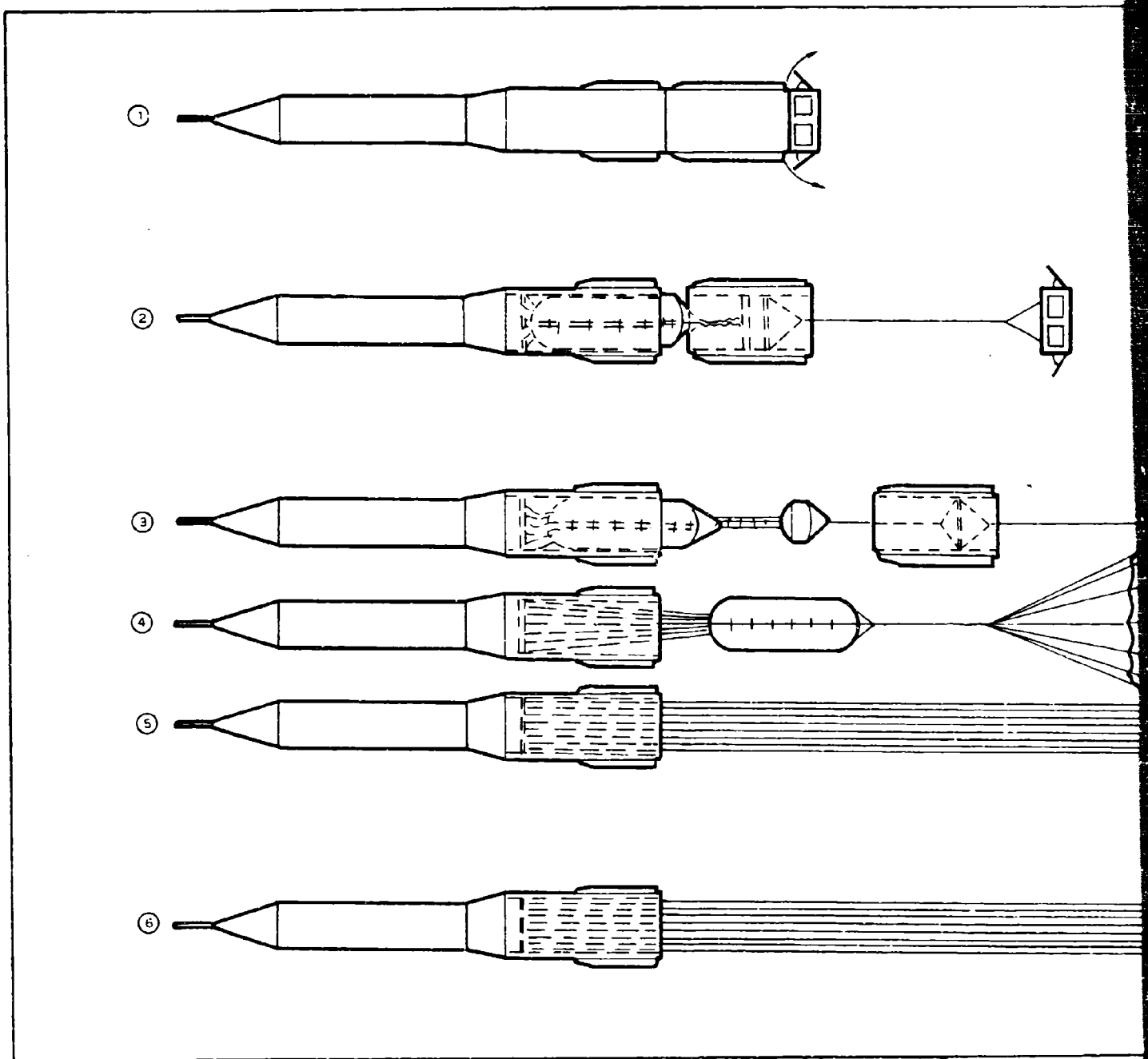
①
②
③
④
⑤
⑥

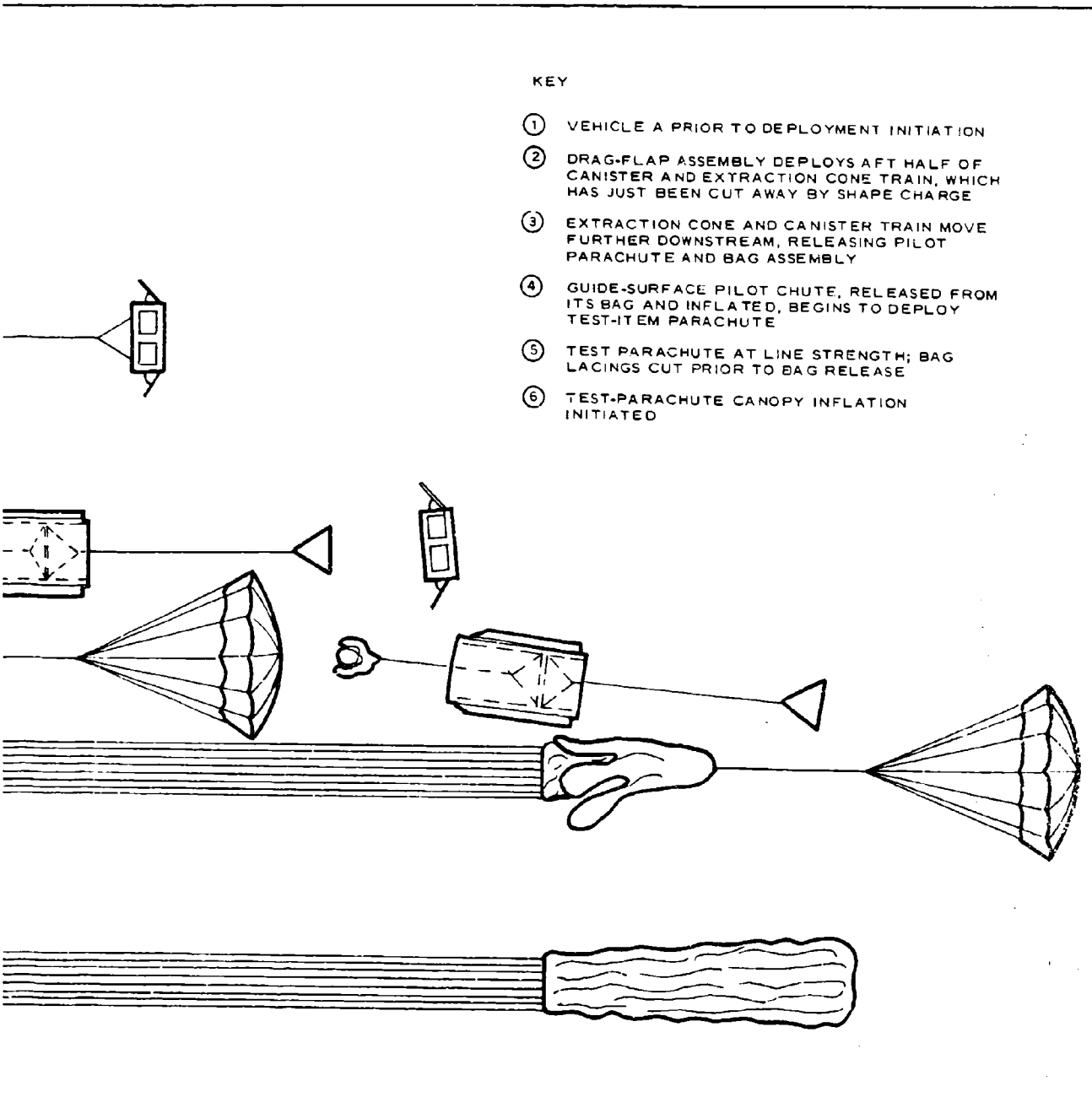

Figure 92 - Details of Deployment Sequence for 16-Ft-High-Q Test Parachute

2

Figure 93 - Test Item LP-1 Being Packaged

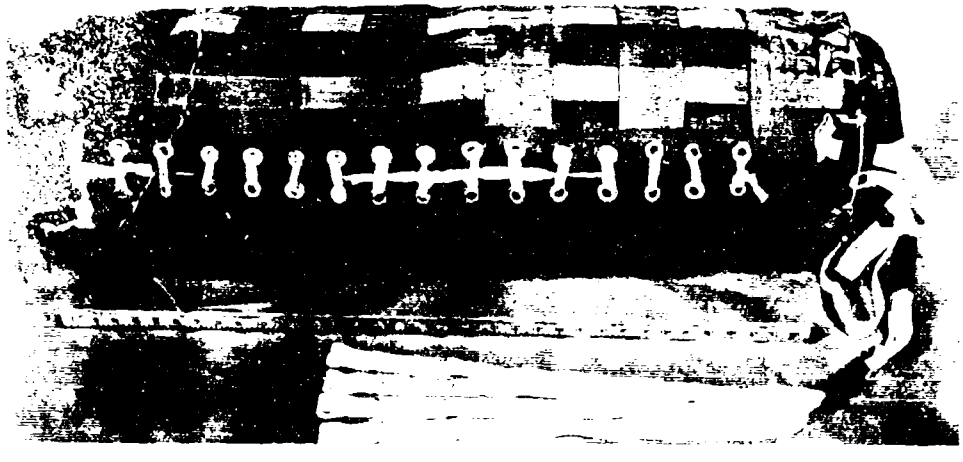

Figure 94 - Test Item LP-1 Packaged

LP-1 test item - 107.4 lb
LP-2 test item - 110.0 lb

The above weights include the following for accessory components:

1. Parachute bag - 8.06 lb
2. Pilot parachute - 6.37 lb
3. Pilot parachute bag - 1.0 lb
4. Miscellaneous - 1.44 lb

The 48-in. (D_c) guide-surface pilot parachute was built similar to Air Force drawing 58K6095.

SECTION VI - PROGRAM CONCLUSIONS

1. DECELERATORS

a. BALLUTE

The following conclusions are based on (1) the state of the art of analytical techniques and (2) empirical knowledge from wind-tunnel and free-flight tests:

1. The pressure distribution and the internal pressure can be predicted by analytical methods. The effect of the wake on the distribution can be estimated from available data.
2. The technique for combined analysis of aerodynamic-pressure distribution and isotensoid structure provides a means for designing a structurally stable, lightweight BALLUTE.
3. The high degree of stability observed during wind-tunnel tests also occurred during the flight test.
4. The drag coefficients correlate between small- and full-scale tests.
5. Future analytical techniques should be evaluated at high free-flight velocities and under severe heating conditions.
6. High-temperature materials, fabrication techniques, and coatings should be evaluated under the dynamic, static, and heating loads associated with high-speed deployable decelerators at high free-flight velocities.

b. Small Supersonic Parachute

The following conclusions are based on the full-scale wind-tunnel tests and laboratory tests:

1. For full canopy inflation, the ratio of the inlet area and

the roof open area should exceed isentropic requirements (i.e., $A_i/A_e > A/A^*$).

2. Coatings effectively reduce the roof porosity.

3. Canopy performance decreases with time in the wind tunnel, indicating continual structural degradation of the basic materials under the high-frequency pulsing. Additional wind-tunnel tests of full-scale models should be conducted to determine the porosity requirement for full inflation and to reduce canopy pulsing for a range of supersonic Mach numbers from 1.8 to 4.0.

4. Additional wind-tunnel tests of full-scale models should be conducted to determine techniques for reducing skirt flutter.

5. The parachute drag coefficient at the tested geometric relationships (diameter ratios and diameters aft of the missile) is approximately one-half of that predicted for no wake; this can be proved by either the simple analysis or a numerical integration of the variable pressure over the surface of the parachute.

6. Analytical techniques are available to predict the thickness of the coating and the diameter of mesh elements required for the test environment when the effective heat absorption of the materials is known.

7. Additional laboratory tests should be conducted to establish more completely the coating requirements for Nomex mesh at the higher supersonic velocities.

8. Fabrication techniques are available to attach the mesh roof material structurally.

c. Large High-Q Parachute

The following conclusions are based on wind-tunnel tests using large models (D_o = 10 ft):

1. Large parachutes with low porosity can have structurally stable inflated shapes when reefed to small sizes. However, tests were not sufficient to determine acceptable porosity-to-reefing ratios for the range of Mach numbers tested. Additional wind-tunnel tests should be conducted with large models to determine the ratios that will result in structurally stable configurations.
2. Flight tests should be conducted to evaluate the suitability of the static results (wind-tunnel data) for the design of a large parachute operating in a rapidly-decaying-q environment.
3. Material tests should be conducted to establish the heat-protection requirements for typical environments to Mach 3.

2. FREE-FLIGHT TEST CAPABILITY

a. ADDPEP Test Missile System B/C

The following conclusions are based on the free flight tests:

1. Satisfactory engineering design modifications and development led to an accurate free-flight-test system that uses standard hardware without a sophisticated guidance system. The design-improvement work should be continued.
2. Air Force/contractor coordination led to this test capability without prior system development.

3. Future test points can be achieved with confidence because of the close correlation between calculated and actual trajectories.
4. Data acquisition has been greatly improved over that of past test vehicles.
5. Retrorockets should be considered for final-stage separation in future high-altitude tests.
6. The size of the test-item container should be increased.
7. A second flotation system should be considered for the missile.

b. ADDPEP Test Missile System A

The following conclusions are based on design analysis, in-plant tests, and the subsystems' being in common with the B/C test missile:

1. The test capability can be developed further during testing.
2. The data acquisition, event programming, and pyrotechnic subsystems are well developed.
3. The future test points are attainable with the system.
4. To prove reliability, the vehicle should undergo a static functional check before flight.
5. The vehicle should undergo a vibration test before boost flight.

LIST OF REFERENCES

1. Design and Instrumentation Testing for a Hypersonic Parachute Free Flight Test Capability. ASD-TR-63-64, January 1963.

2. Aerodynamic Deployable Decelerator Performance Evaluation Program (ADDPEP) Test Vehicles. GER-11765, Final Report, Design and Development Phase, Goodyear Aerospace Corporation, October 1964.

3. Lowry, J.: Aerodynamic Characteristics of Various Types of Full-Scale Parachutes at Mach Numbers from 1.8 to 3.0. AEDC-TDR-64-120, Arnold Air Force Station, 1964.

4. Sims, L. W.: Analytical and Experimental Investigation of Supersonic Airfoils. NACA TN 1678, 1948.

5. Study and Exploratory Free-Flight Investigation on Deployable Aerodynamic Decelerators Operating at High Altitudes and at High Mach Numbers. RTD-TDR-64-35, July 1964.

6. Serbin, H.: Supersonic Flow around Blunt Bodies. IAS Volume 25, No. 1, January 1958.

7. Laidlaw, W. R.: "Lecture Notes on Aircraft Dynamics." Ohio State University, Columbus, Ohio, October 1958.

8. Mirels, H : Theoretical Wave Drag and Lift of Thin Supersonic Ring Airfoils. NACA TN 1768, 1948.

9. Pankhurst, R. C.; and Holder, D. W.: Wind Tunnel Technique. Pitman and Sons, Ltd., London, 1952.

10. Deitering, J. S.: Investigation of Flexible Parachute Model Characteristics at Mach Numbers from 1.5 to 6. AEDC-TDR-62-185, October 1962. (Confidential)

11. Deitering, J. S.: Performance of Flexible Aerodynamic Decelerators at Mach Numbers from 1.5 to 4. AEDC-TDR-62-234, December 1962. (Confidential)

12. Deitering, J. S.: Performance of Flexible Aerodynamic Decelerators at Mach Numbers from 1.5 to 6. AEDC-TDR-63-119, July 1963. (Confidential)

13. Deitering, J. S.: The Wind Tunnel Investigation of Flexible Parachute Model Characteristics at Mach Numbers 1.5 to 5. AEDC-TDR-63-263, January 1963.

14. Equations, Tables, and Charts for Compressible Flow. Ames Research Staff, NACA Report 1135, 1953.

15. Boren, T. C.; and Hatalsky, W.: Jet Effects upon Base Drag. General Dynamics, Pomona, Calif.

16. Bartz, D. R.: "A Simple Equation for Rapid Estimation of Rocket-Nozzle Convective Heat Transfer Coefficients." Jet Propulsion, Vol. 27, No. 1, pp 49-51, January 1957.

17. Schneider, P. J.: Temperature Response Charts. John Wiley and Sons, Inc., New York, 1963.

18. Air Flow Characteristics of Parachute Fabrics at Simulated High Altitudes. Massachusetts Institute of Technology, WADC-TR-59-374, March 1960.

19. Metal Filaments for High Temperature Fabrics. A. D. Little Company, ASD TR 62-180, February 1962.

20. Instantaneous Local Temperatures of Aerodynamic Decelerators, Part II - Thermal Properties. American Machine and Foundry Company, Mechanics Research Division, WADD-TR-60-670, February 1961.

21. Thermal Transport and Radiative Properties of Fibrous Structural Materials. General American Transportation Corporation, MRD Division, ASD-TR-62-810, November 1962.

22. Timoshenko, S.; and Woinowsky-Krieger, S.: Theory of Plates and Shells. Second Edition, McGraw-Hill, New York, 1959.

23. Investigation to Determine the Feasibility of Using Inflatable Balloon Type Drag Devices for Recovery Applications in the Transonic, Supersonic and Hypersonic Flight Regime, Part II - Mach 4 to 10 Feasibility Investigation. ASD-TDR-62-702, Goodyear Aerospace Corporation, Akron, Ohio, October 1962.

24. Rosko, A.: On the Development of Turbulent Wakes from Vortex Sheets. NACA Report 1191, 1959.

25. Gold, H.: Stability of Laminar Wakes. Calcit, 1963, Ph. D. Thesis.

26. Lin, C. C.: On the Stability of the Laminar Mixing Region between Two Parallel Streams in a Gas. NACA TN 2887, January 1953.

27. Chapman, B. R.; Kuehn, D. M.; and Larson, H. K.: Investigation of Separated Flows in Supersonic and Subsonic Streams with Emphasis on the Effect of Transition. NACA Report 1356, 1958.

28. Shapiro, A. H.: The Dynamics and Thermodynamics of Compressible Fluid Flow. Vol. I, The Ronald Press Company, New York, 1953.

29. Lighthill, M. J.: Higher Approximations in Aerodynamic Theory No. 5. Princeton University Press, 1960.

30. Eggers, A. J.; and Savin, R. C.: Approximate Methods for Calculating the Flow About Non-Lifting Bodies of Revolution at High Supersonic Air Speeds. NACA TN-2579, December 1951.

31. Ehert, D. M.: Accuracy of Approximate Methods for Predicting Pressures on Pointed Non-Lifting Bodies of Revolution in Supersonic Flow. NACA TN-2769, August 1952.

32. Charczenko, N.: Aerodynamic Characteristics of Towed Spheres, Conical Rings and Cones Used as Decelerators at Mach Numbers from 1.57 to 9.65. NASA TN-1789, April 1963.

33. Bell, D. R.: Pressure Measurements on the Rigid Model of a Balloon Decelerator in the Wake of a Simulated Missile Payload at Mach Numbers 1.5 to 6.0. AEDC-TDR-64-65, April 1964.

34. McShera, J. T.: Prospective NASA Technical Note. 1964.

35. Lees, L.; and Hromas, L.: Turbulent Diffusion in the Wake of a Blunt-Nosed Body at Hypersonic Speeds. IAS Paper No. 62-71, IAS 30th Annual Meeting, New York, January 22-24, 1962.

36. Liepmann, H. W.; and Roshko, A.: Elements of Gas Dynamics. John Wiley and Sons, Inc., New York, 1957.

37. Hoerner, S. F.: Aerodynamic Drag. 1961.

38. A Manual for Determining Aerodynamic Heating of High-Speed Aircraft. Volume I, Report No. 7006-3352-001, Bell Aircraft Corporation, July 1959.

39. Hutchinson, F. W.: Industrial Heat Transfer. Industrial Press, 1952.

40. A Method of Predicting Skin, Compartment, and Equipment Temperatures for Aircraft. WADC-TR-53-119, July 1953.

41. Nebiker, F. R.: Feasibility Study of an Inflatable Type Stabilization and Deceleration System for High Altitude and High Speed Recovery. WADD-TR-60-182, December 1961.

42. Clay, W. R.; and Long, W. C.: Physical and Chemical Properties of HT-1. E. I. DuPont de Nemours Company, Inc., Textile Fibers Department, Textile Research Laboratory, Wilmington, Delaware, May 1961.

43. Neff, R. J.: Development of HT-1 Materials for Decelerators. ASD-TDR-63-248, March 1963.

44. Marsden, A. T.: The Drag and Opening Characteristics of Parachutes of Several Designs When Towed behind an Aircraft - Their Consistency and Comparison with Previous Data. RAE, Technical Note, Mechanical Engineering 390, 1963.

45. Performance of and Design Criteria for Deployable Aerodynamic Decelerators. ASD-TR-61-579, December 1963.

APPENDIX I - EXPERIMENTAL AND ANALYTICAL INVESTIGATION OF PROTECTIVE COATINGS FOR TEXTILE MATERIALS AT VERY LOW HEAT-FLUX RATES

The critical-temperature environment of the SP-5 flight required development of a suitable coating material and validation of that selection to provide thermal protection of the Nomex mesh. A temperature limit of approximately 650 F for retaining 25 percent of its quick-break strength was required. Accordingly, a test method was developed to compare different sizes of Nomex cords and the effectiveness of various coating materials. A radiant-heat source of known output was prepared for time-testing each sample to tensile separation. Samples were prepared in sufficient categories of variables for meaningful analysis of the resultant data. Possible variables considered for the comparison study included the following:

1. Nomex cord size - 200 denier, 800 denier, E, F, FF, 3, and 6
2. Coating specification - Dow-Corning - Q9-0090; Dow-Corning - Q-93-002; Dyna-Therm Chemical, Dyna-Therm D-65; Emerson Electric, Thermo-Lag T-500; General Dispersions, Inc., Gental 101; and General Electric - RTV-511
3. Coating thickness - uncoated, 0.002 in., 0.005 in., and 0.007 in.
4. Heat flux - 1 and 3.5 Btu per square foot per second

Nomex cord of 200 and 800 denier was carefully prepared by twisting separate lengths of raw yarn under tension to 14 twists per inch. This operation was mechanized by a pneumatic drill and an electrically operated counter. Each

50-ft length of yarn was weighted where the opposite end ran over a pulley, which provided uniform tautness and additional length during twist shrinkage. Despite these careful efforts, subsequent testing experience dictated the use of available commercial cord because of its uniformity of twist and consistent construction among sizes. Commercial sizes E and No. 3 were chosen for the application, heat testing, and analysis of coatings; other sizes of uncoated cord were chosen for heat testing and comparison.

The coating materials were applied to the cords by spraying, and by extruding to it with the cord passing through an orifice. The degree of affinity with the nylon and viscosity of each sample were the principal characteristics that determined the necessary techniques to ensure relatively uniform and predictable thicknesses of coating. The spraying and extruding were facilitated by simultaneously rotating the cord with the twisting mechanism. These operations were further facilitated by application while the cord was suspended vertically.

An electric furnace of vertically placed quartz tubes was rigged to heat-test weighted cords suspended at the exact center within a tube cluster. The clustered-tube design for the furnace was chosen to obtain a distribution of the heat-flux rate on the entire circumferential area of the test pieces. The furnace was calibrated by a thin tube calorimeter for the two heat fluxes. Weight equal to 25 percent of the quick-break strength of the particular size cord at room temperature was used to suspend each cord during test. Care was taken to blacken each cord to the same value as that of the calibrating calorimeter to ensure equivalent radiant-heat absorption.

On a separate graph for each candidate coating and heat rate, test data of time to tensile separation were plotted against the diameter of coated cord. An intersecting plot for the similar testing of uncoated commercial cords was also shown on each graph for immediate comparison. The findings are plotted in Figures I-1 through I-12.

A comparison of the graphs showed (1) that the thermodynamic capability of coated yarns will be equal or superior to that of uncoated yarns of the same

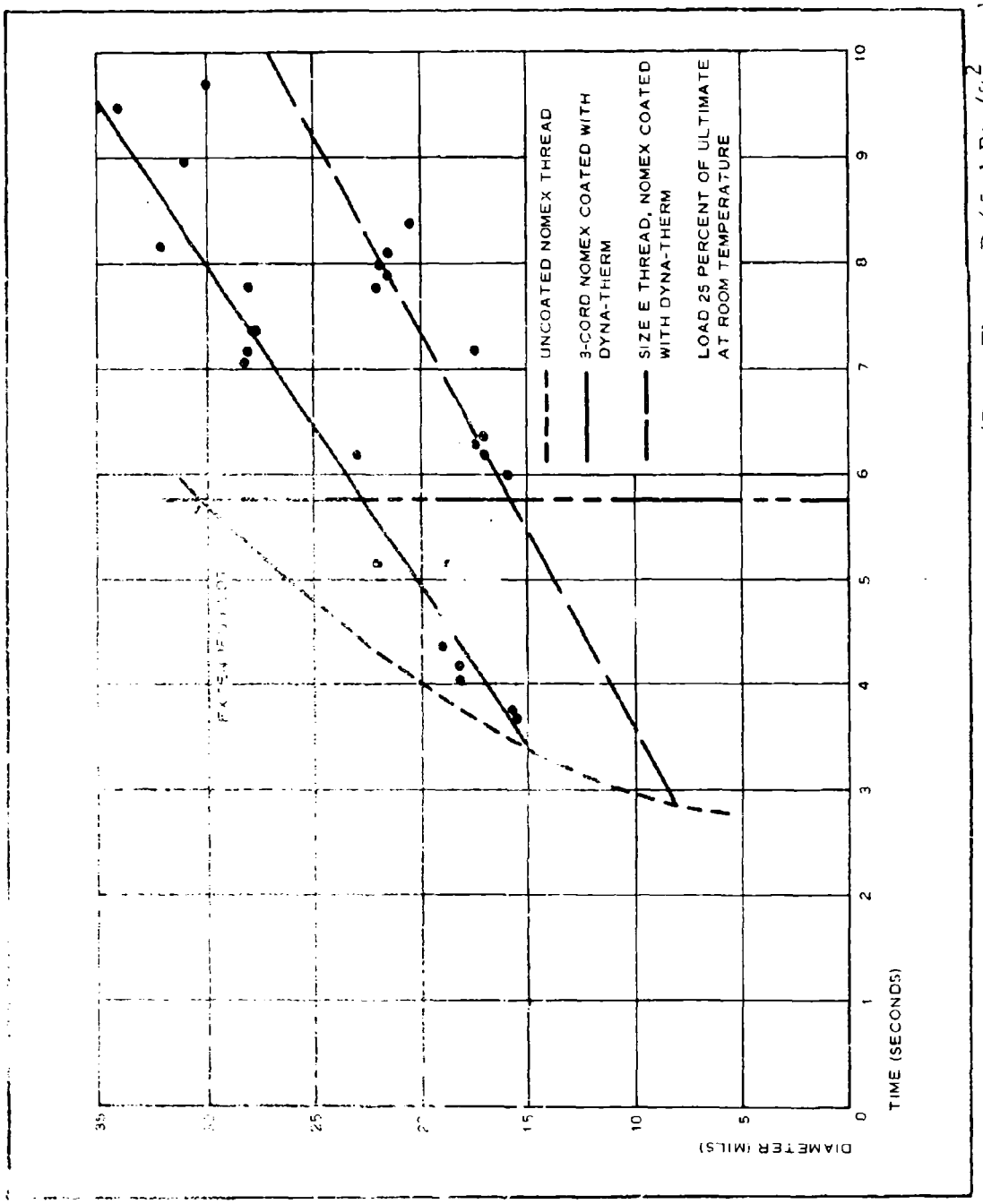

Figure I-1 - Time to Failure versus Coated-Yarn Diameter (Dyna-Therm D-65, 1 Btu/ft^2-sec)

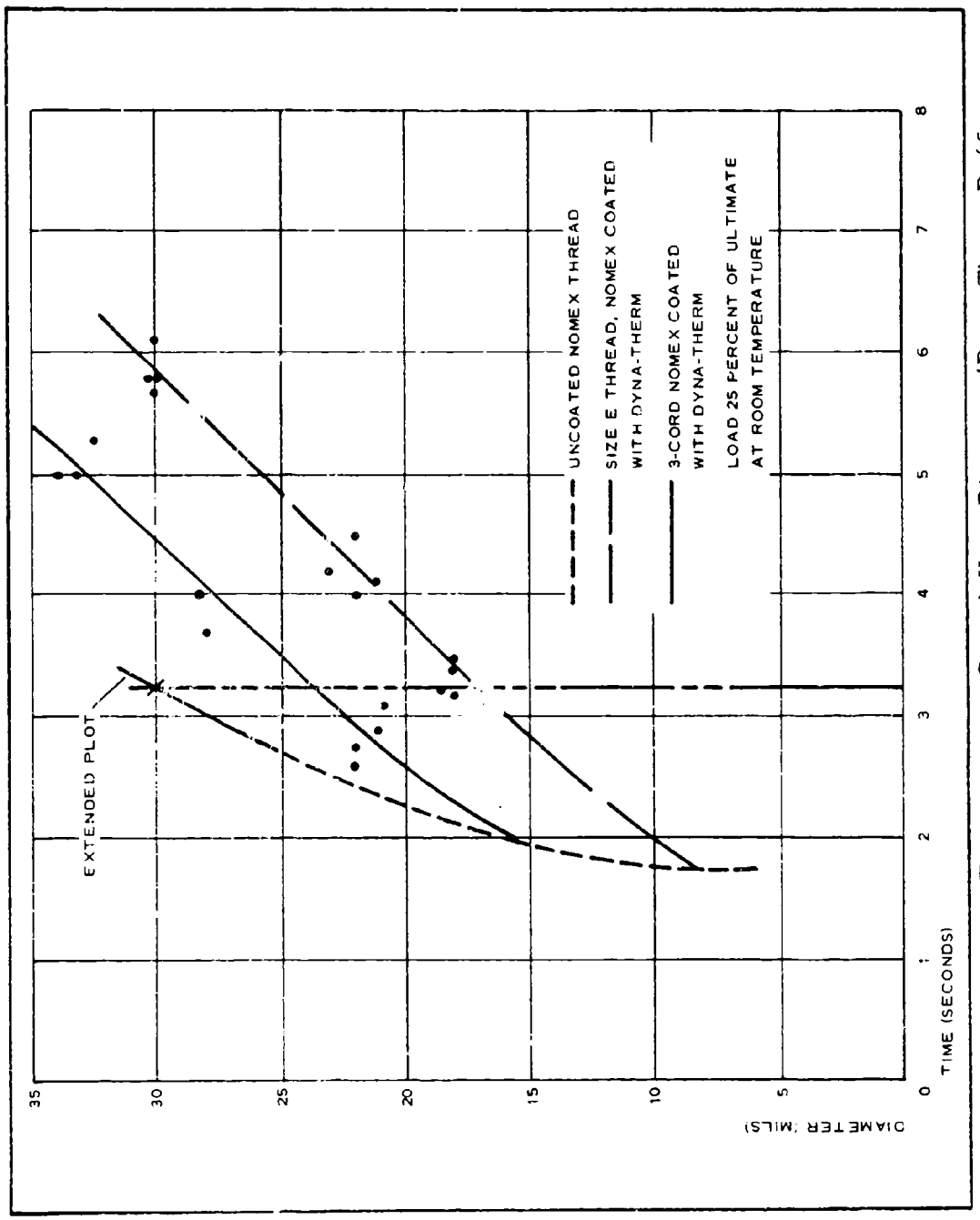

Figure I-2 - Time to Failure versus Coated-Yarn Diameter (Dyna-Therm D-65, 3.5 Btu/ft^2-sec)

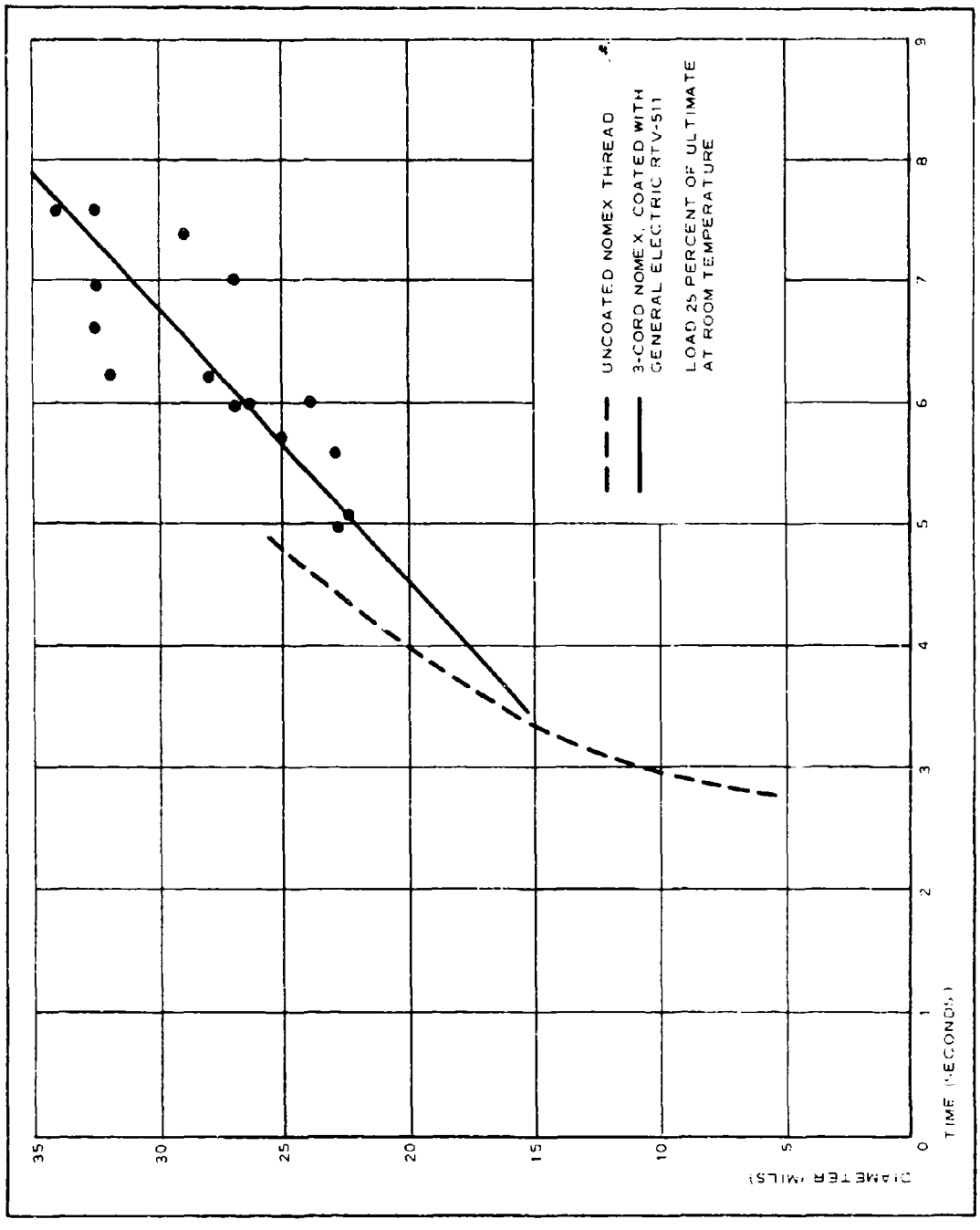

Figure I-3 - Time to Failure versus Coated-Yarn Diameter (General Electric RTV-511, 1 Btu/ft^2-sec)

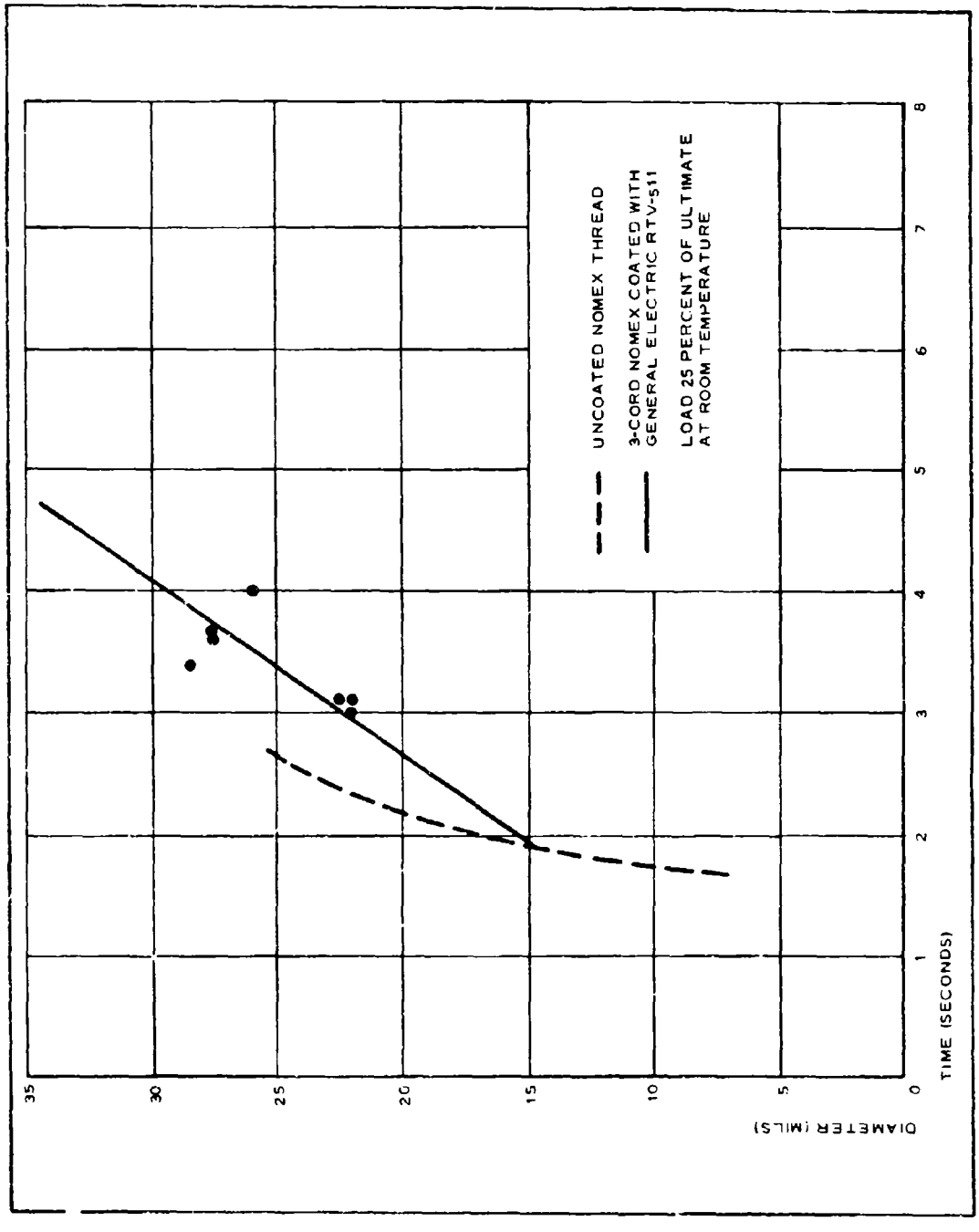

Figure I-4 - Time to Failure versus Coated-Yarn Diameter (General Electric RTV 511, 3.5 Btu/ft2-sec)

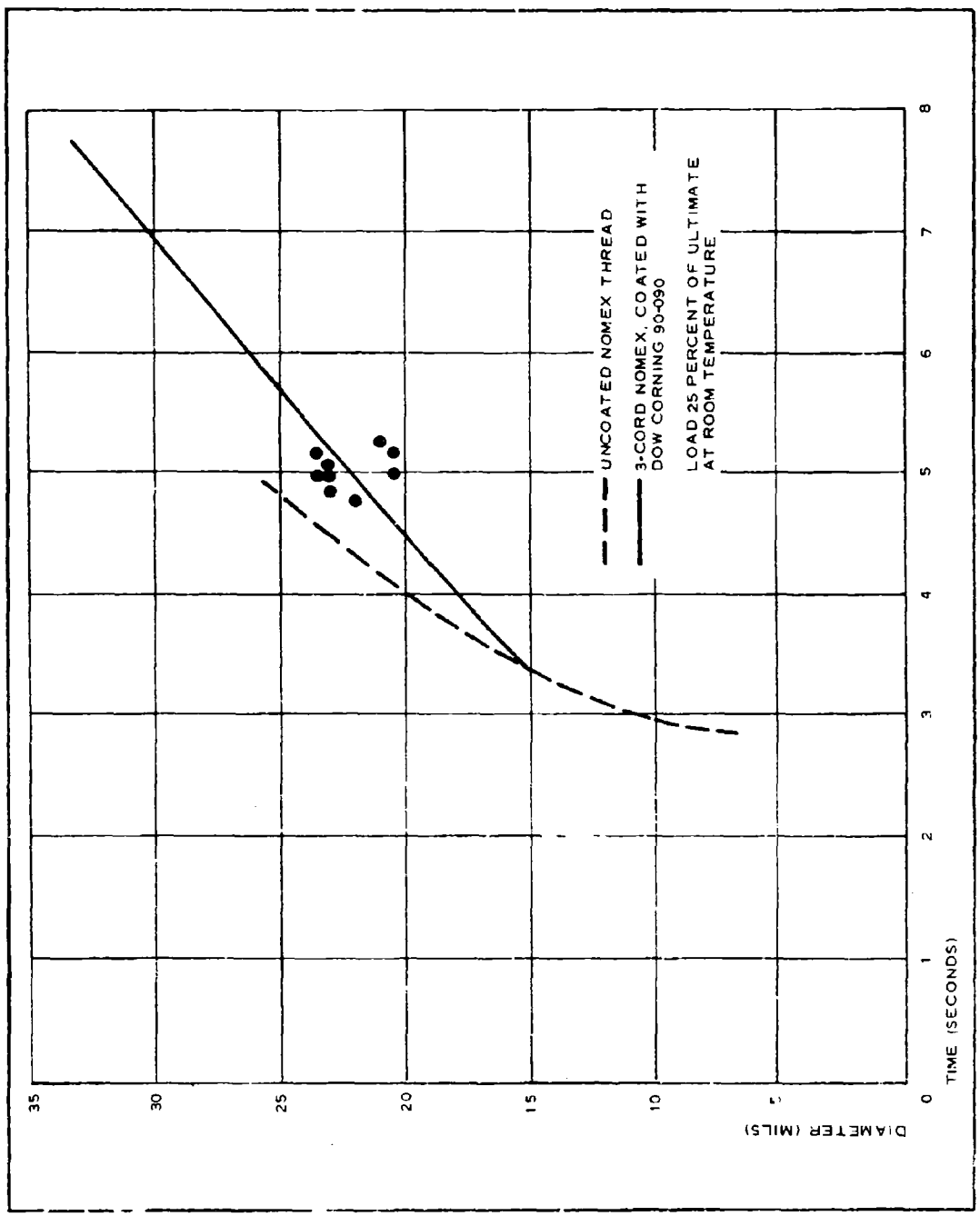

Figure I-5 - Time to Failure versus Coated-Yarn Diameter (Dow Corning 90-090, 1 Btu/ft^2-sec)

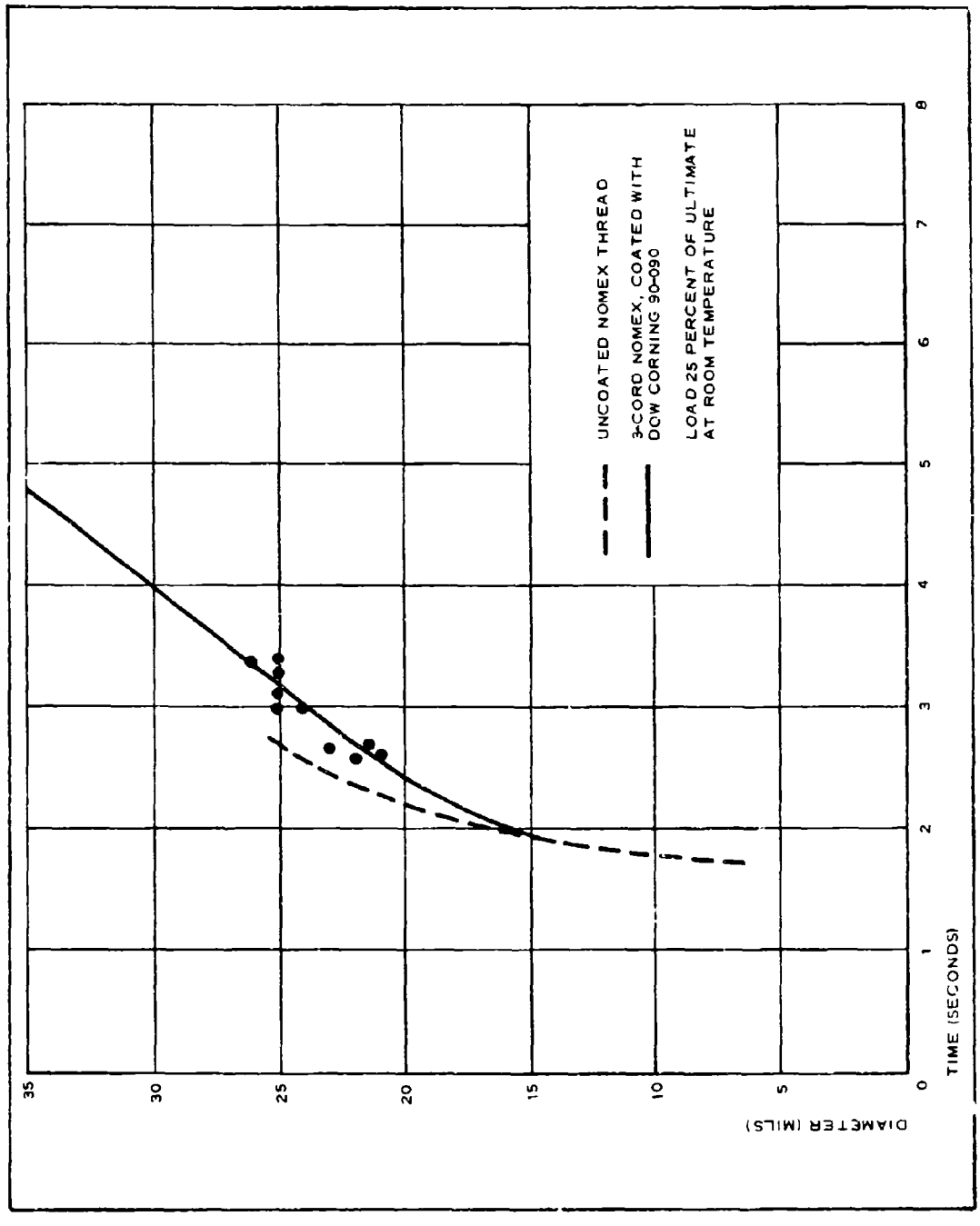

Figure I-6 - Time to Failure versus Coated-Yarn Diameter (Dow Corning 90-090, 3.5 Btu/ft^2-sec)

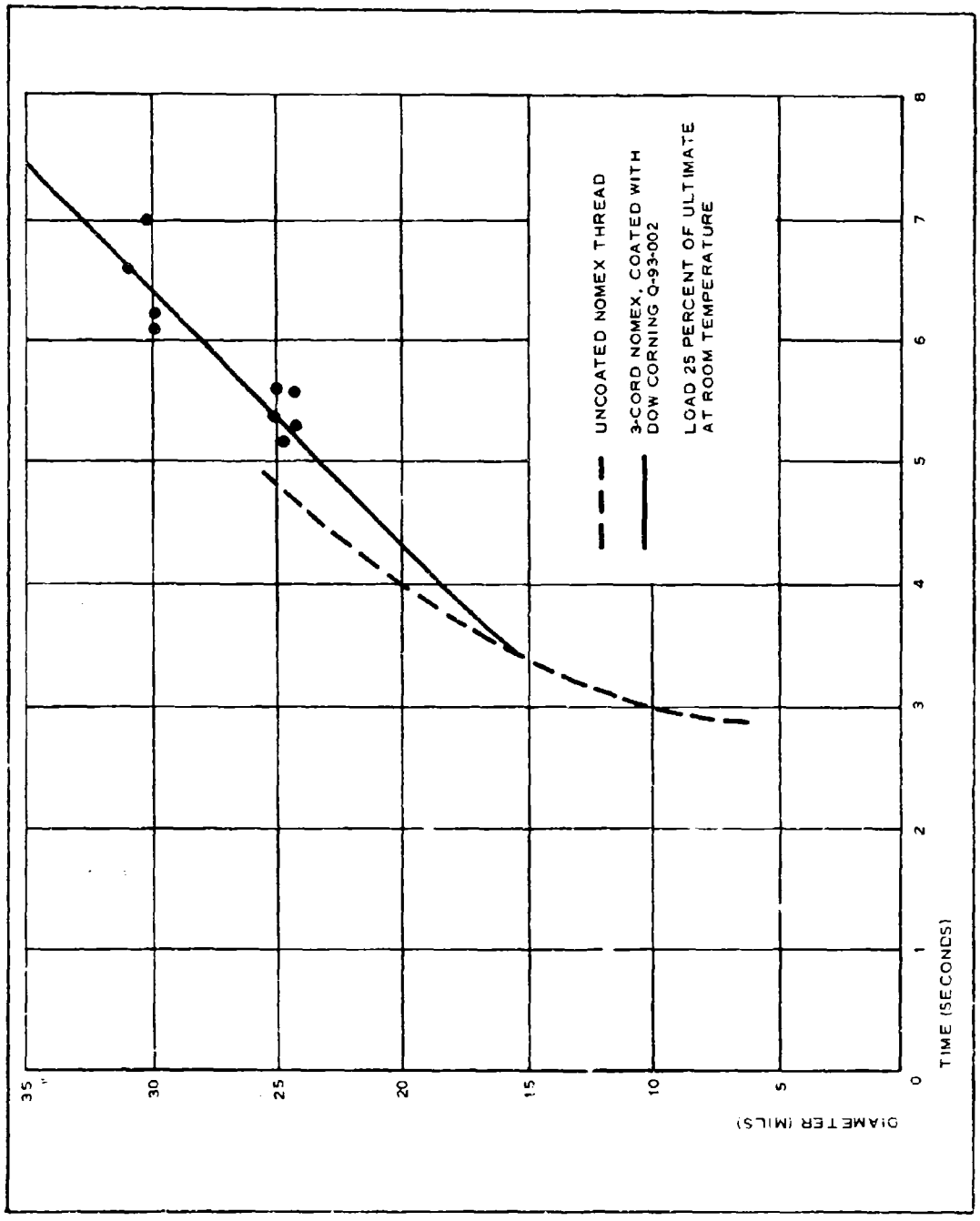

Figure I-7 - Time to Failure versus Coated-Yarn Diameter (Dow Corning - Q-93-002, 1 Btu/ft^2-sec)

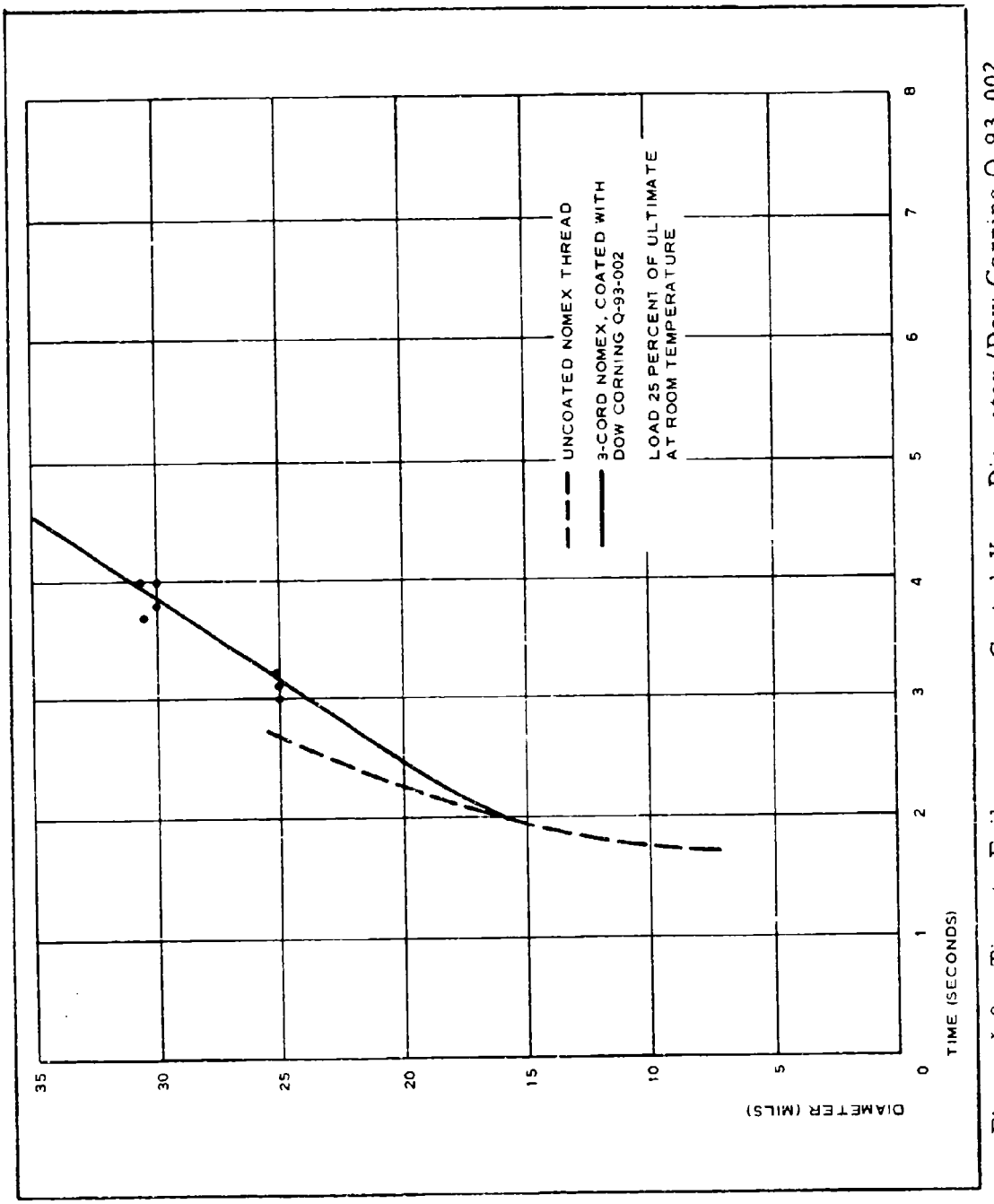

Figure I-8 - Time to Failure versus Coated-Yarn Diameter (Dow Corning Q-93-002, 3.5 Btu/ft^2-sec)

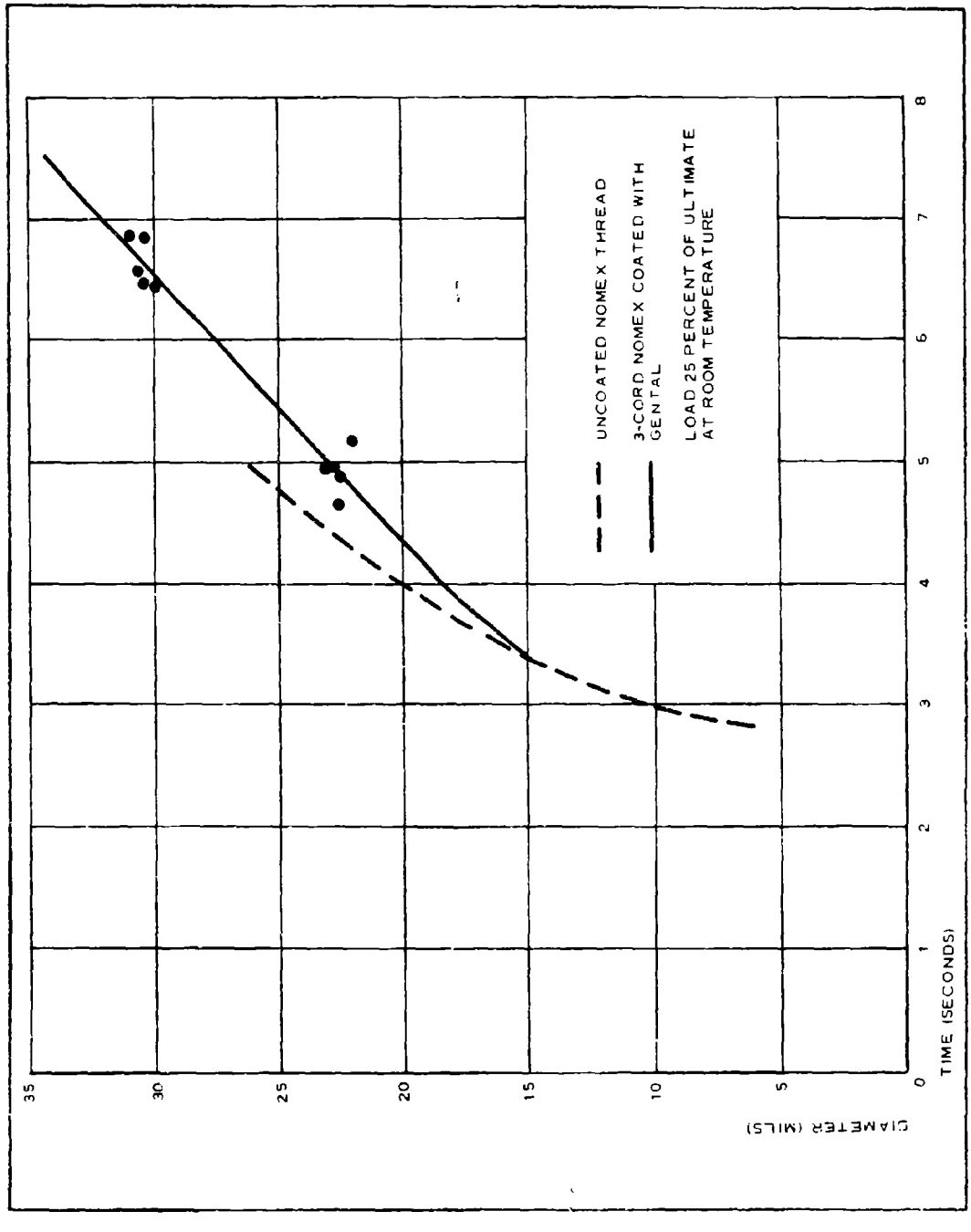

Figure I-9 - Time to Failure versus Coated-Yarn Diameter (Gental 101, 1 Btu/ft^2-sec)

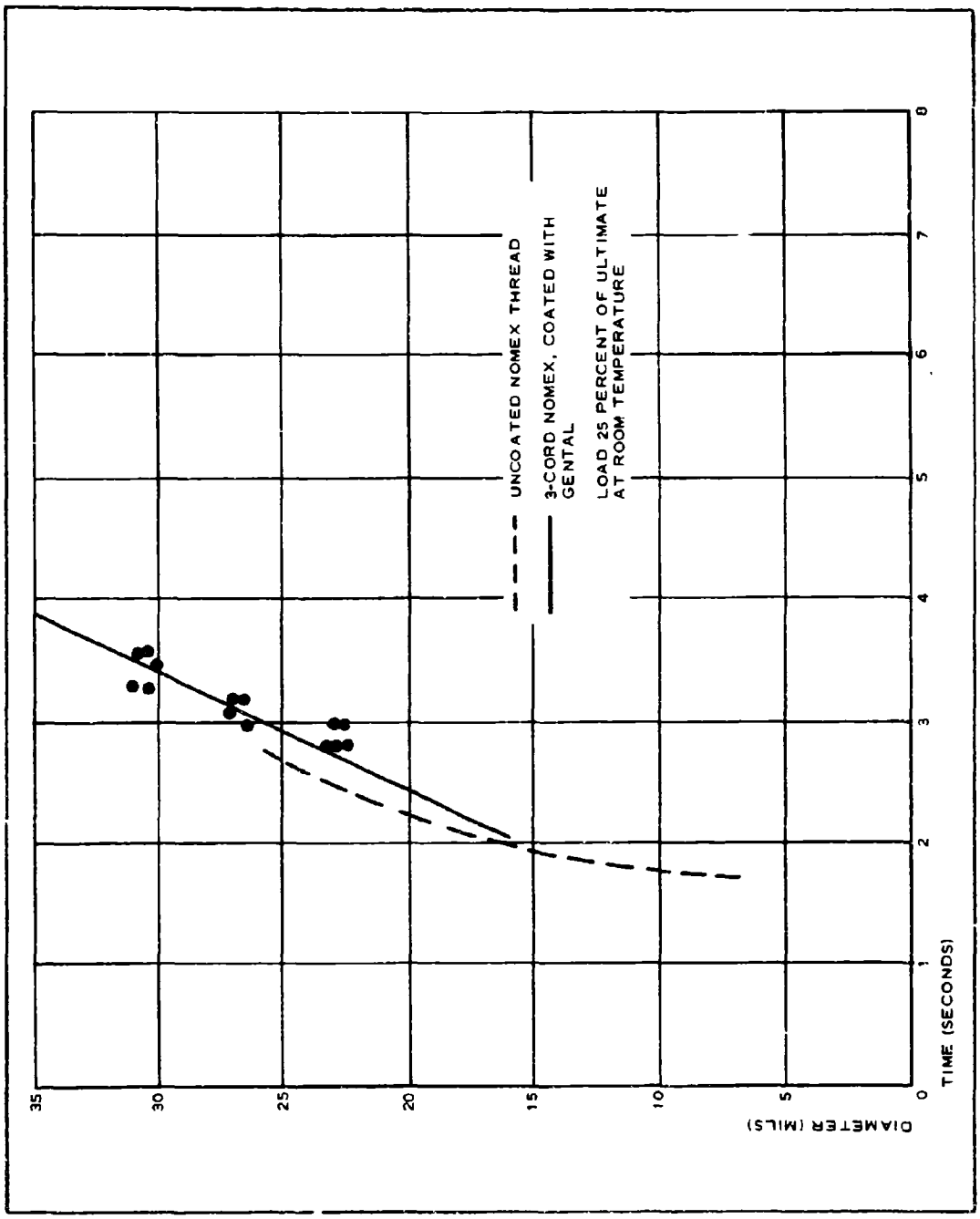

Figure I-10 - Time to Failure versus Coated-Yarn Diameter (Gental 101, 3.5 Btu/ft^2-sec)

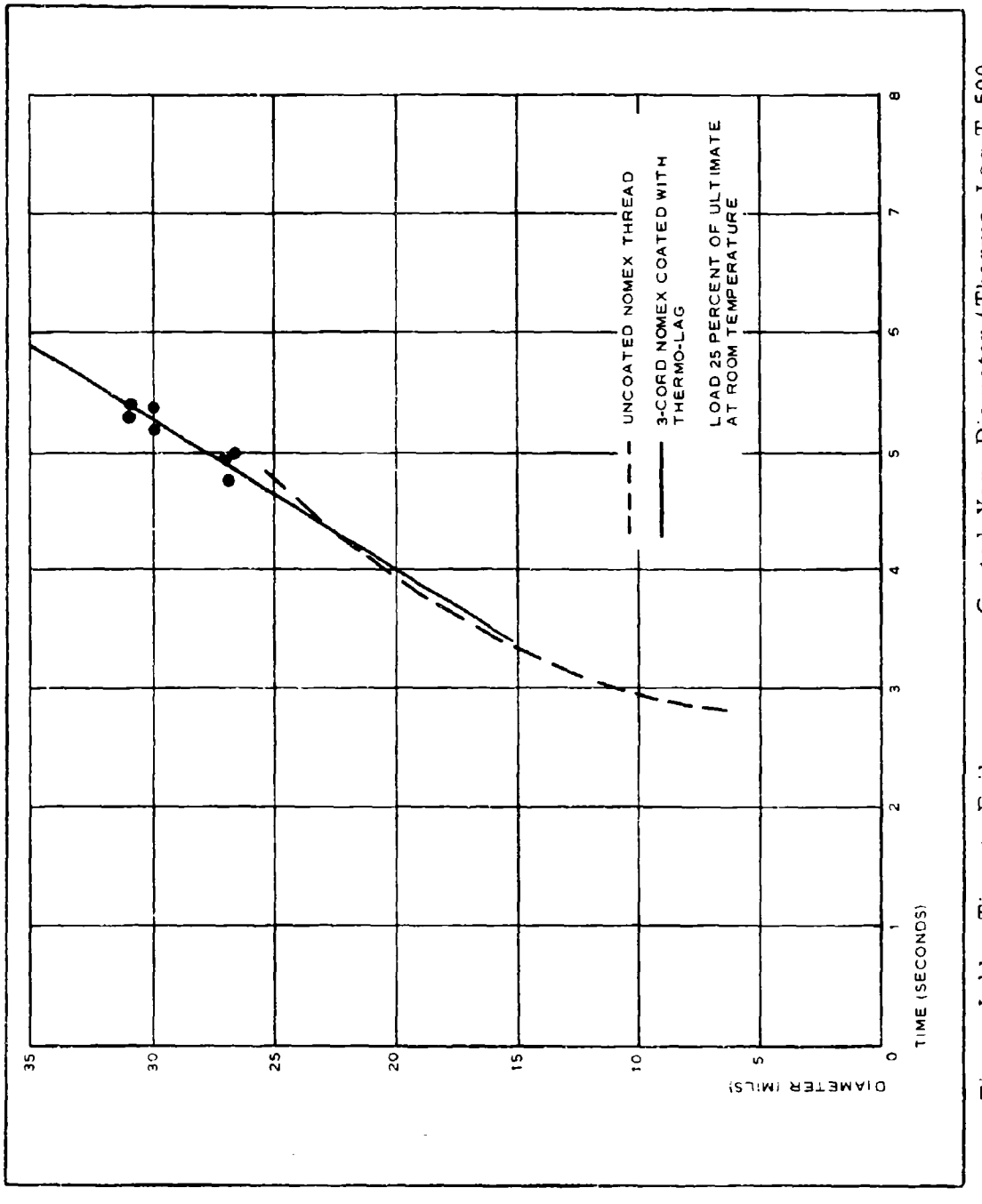

Figure I-11 - Time to Failure versus Coated-Yarn Diameter (Thermo-Lag T-500, 1 Btu/ft^2-sec)

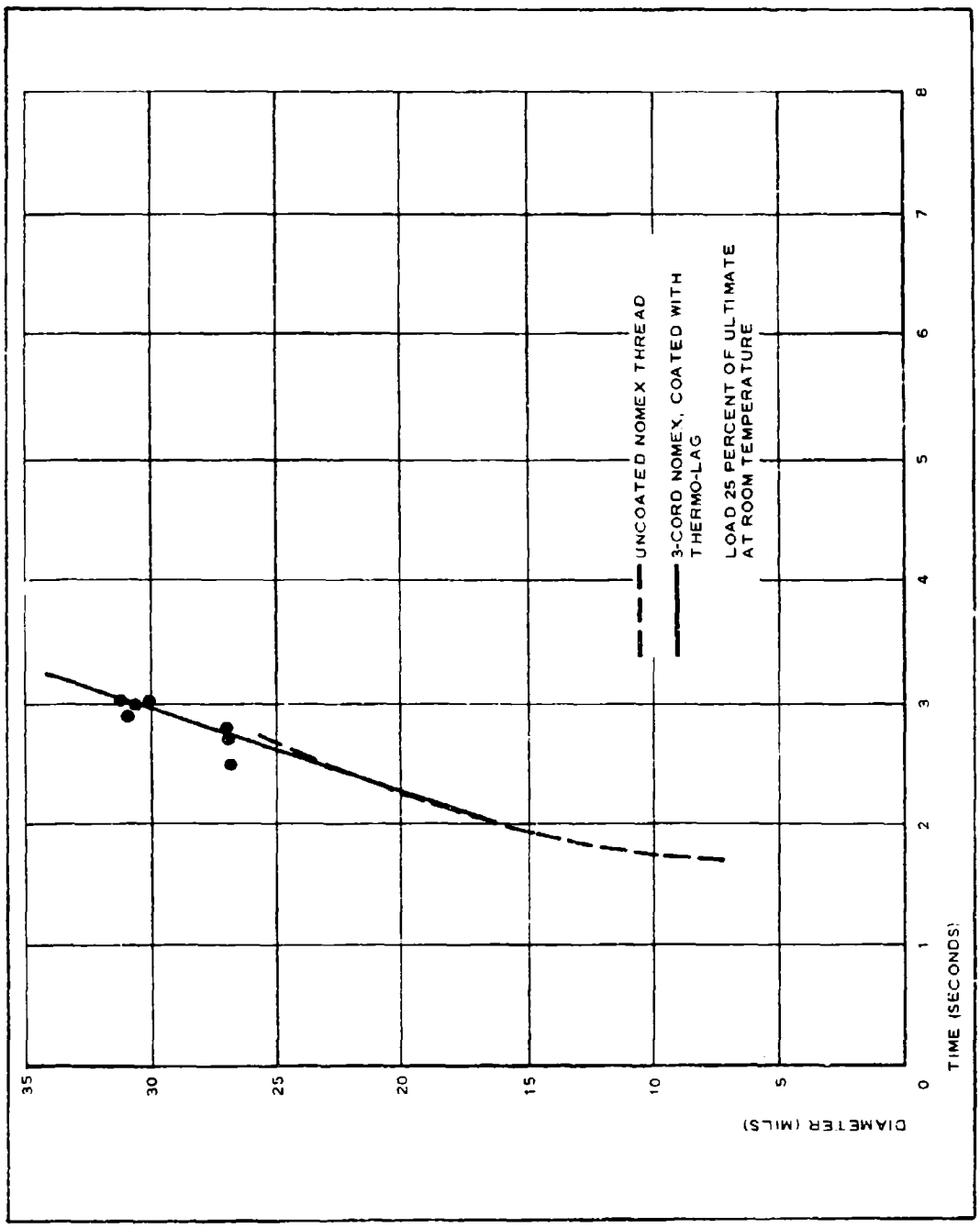

Figure I-12 - Time to Failure versus Coated-Yarn Diameter (Thermo-Lag T-500, 3.5 Btu/ft^2-sec)

diameter and (2) that the thermal-resistance coating known as Dyna-Therm D-65 is unquestionably better than the other five candidates, as evidenced by the shallower slope of the plot (Figures I-1 and I-2).

Elements of 0.030-in.-diameter uncoated Nomex would be required to withstand the temperature for the test-point conditions of SP-5. An examination of Figures I-1 and I-2 shows that choices of smaller size Dyna-Therm-coated cords can be found, equivalent to the size of analyzed uncoated cord, that will be sufficiently heat resistant for load carrying. Specifically, it is seen from the equivalent flux plots of Figure I-1 that Dyna-Therm-coated Size E Nomex with an 0.016-in. total diameter has thermal resistance equal to that of the required 0.030-in.-diameter uncoated Nomex. An analytical correlation of the experimental test results is described in the following paragraphs.

The experimental data shown in Figures I-1 and I-2 was obtained in an electric furnace as described previously. However, the test specimens were exposed to a uniform radiant-heat input, which was calibrated to be 1 and 3.5 Btu/ft^2-sec when the specimen surface temperature approached 600 to 700 F. As a result, the initial heat-flux rates were considerably higher during the initial exposure time when specimen temperature is low and then decays to the calibrated levels. This test heat-flux-rate variation is shown in Figure I-13 as a function of time. The peak rates were reconstructed from calibration measurements at lower temperatures (approximately 200 F) and from the recorded power input to the electric furnace. These initial heat-flux rates, then, are only estimated values for the initial transient period of the testing time.

Analytically, it can be postulated that the energy absorbed by the specimen must equal the energy reaching the outer surface of the specimen from the quartz lamps. This is a fairly good assumption since the initial specimen temperatures are low, and therefore the outward radiation is negligible. At 600 F, the outward radiation approaches 0.5 Btu/ft^2-sec; however, the net radiation into the specimen was fixed intentionally at 1 or 3.5 Btu/ft^2-sec by

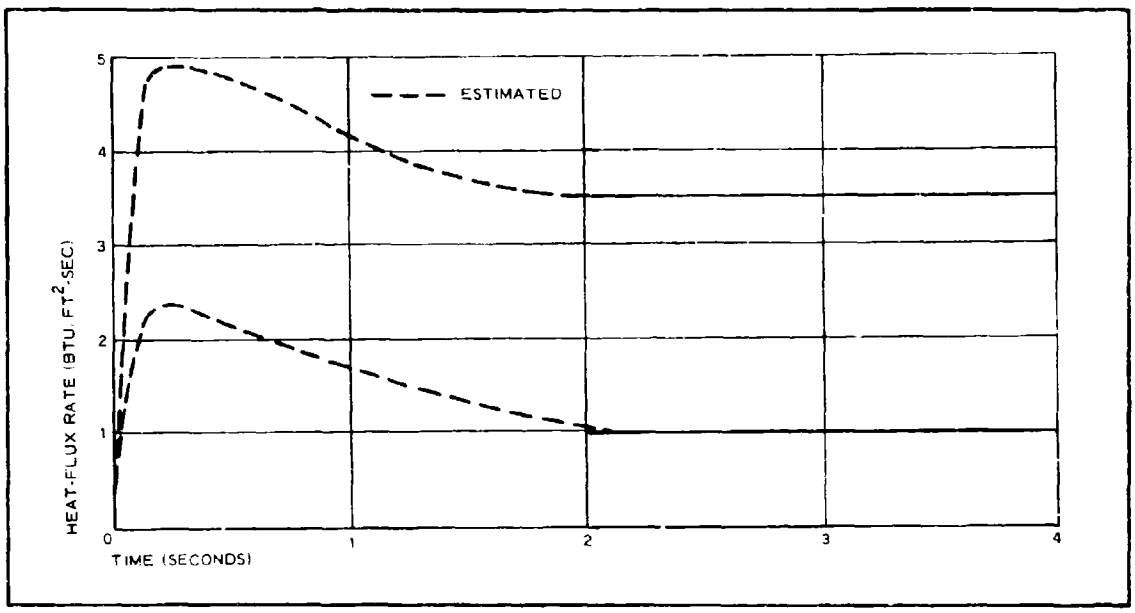

Figure I-13 - Experimental Heat-Flux Rate

calibration. Furthermore, the specimens were blackened carefully to ensure this prospect. The following heat balance, then, can be written for the specimen:

$$Q_{in} = Q_{abs} \tag{I-1}$$

or

$$A_S \int q d\tau = WC\Delta T$$
$$= \rho V Q_{eff} . \tag{I-2}$$

From Equation I-2 and the experimental heat-flux rate shown in Figure I-13, the effective heat absorbed by the Nomex filaments alone were calculated from the results presented in Figures I-1 through I-12. The results are given in Table I-1.

If these experimentally obtained values are compared with the heat capacity of Nomex using a specific heat value (c) of 0.29 Btu/lb-deg F and a temperature rise from room temperature to 650 F, the resulting heat capacity of

TABLE I-1 - EFFECTIVE HEAT ABSORBED (NOMEX)

Diameter (in.)	q = 1 Btu/ft^2-sec Q_{eff} (Btu/lb)	q = 3.5 Btu/ft^2-sec Q_{eff} (Btu/lb)
0.072	193	312
0.020	168	257
0.030	147	244

168 Btu/lb compares favorably with the results obtained experimentally at a q of 1 Btu/ft^2-sec. The effective heat absorbed by the Nomex at a q of 3.5 Btu/ft^2-sec is increased over the heat capacity of Nomex and is probably an indication of the heat absorbed by the surface layers as they degrade and regress.

Once the effective heat absorbed by the Nomex material has been established, a comparative index figure for the composite effective heat absorbed can be calculated with the test data of Figures I-1 through I-12. Using Equation I-2 and comparing a Nomex specimen with a composite specimen that failed at the same time increment, the following equation for the index figure can be established:

$$\frac{Q_{eff_{comp}}}{Q_{eff_{Nomex}}} = \frac{\frac{D_o}{D_{N_1}}}{\frac{\rho_C}{\rho_N}\frac{D_o^2}{D_{N_1}^2} + \frac{D_{N_2}^2}{D_{N_1}^2}\left(1 - \frac{\rho_C}{\rho_N}\right)} \qquad (I\text{-}3)$$

Where equal diameters of both a Nomex specimen and a composite specimen are compared, the following equation, derived from Equation I-2, can be established:

$$\frac{Q_{eff_{comp}}}{Q_{eff_{Nomex}}} = \frac{q_C}{q_{N_1}}$$

$$= \frac{\frac{D_o}{D_{N_1}}}{\frac{\rho_C}{\rho_N}\frac{D_o^2}{D_{N_1}^2} + \frac{D_{N_2}}{D_{N_1}}\left(1 - \frac{\rho_C}{\rho_N}\right)}, \qquad \text{(I-4)}$$

where

$q_C = \int \dot{q}\, dt$ = test heat flux to failure of composite and

$q_N = \int \dot{q}\, dt$ = test heat flux to failure of Nomex.

The results of using these equations and the test data of Figures I-1 and I-2 are shown in Figure I-14; Figure I-15 depicts the geometry of the test specimens that were compared.

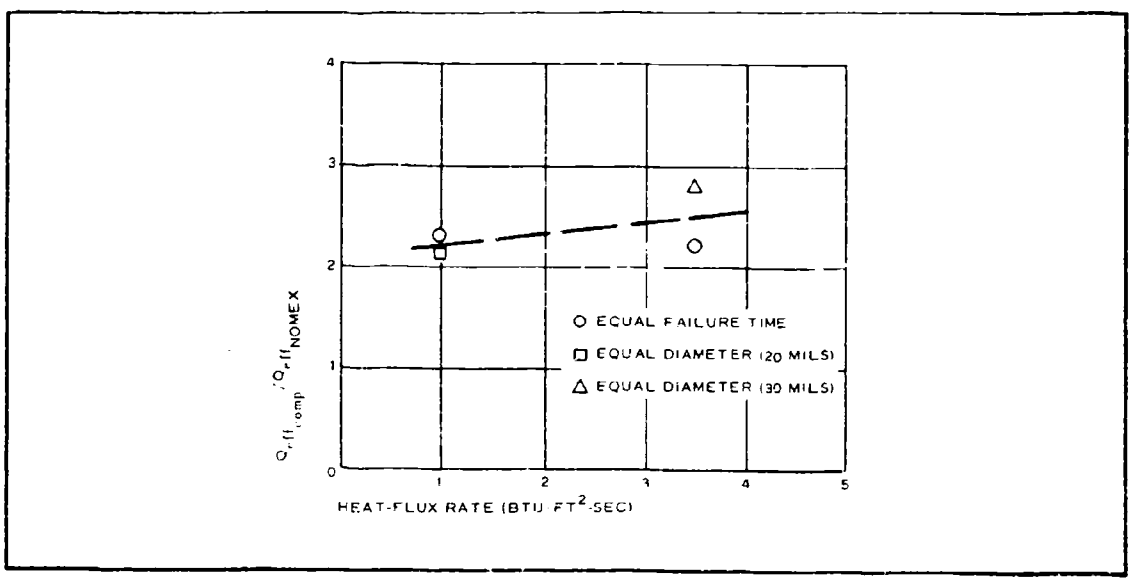

Figure I-14 - Comparative Heat Absorption

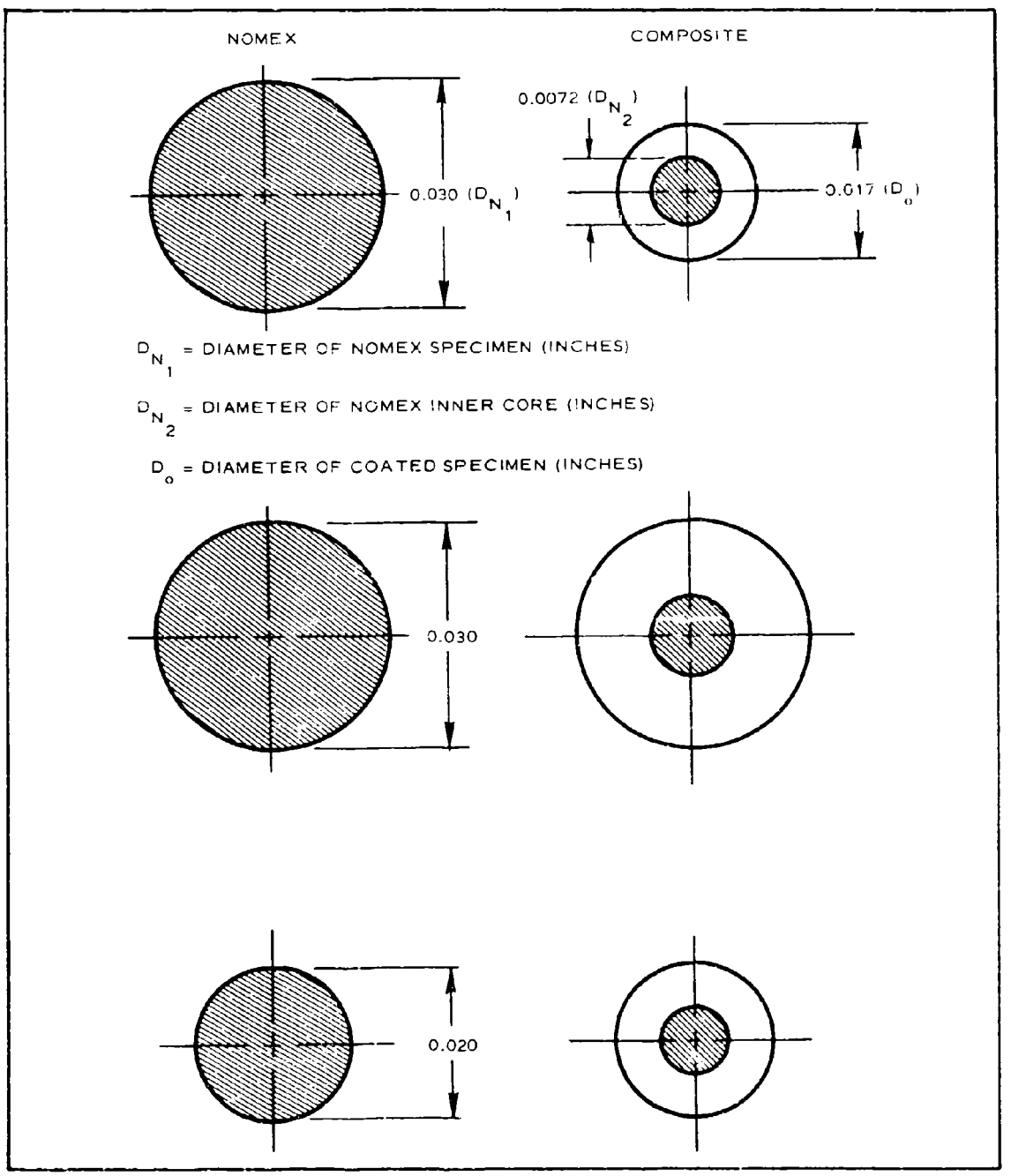

Figure I-15 - Comparative Specimens

After the effective heat absorbed by the Nomex specimen and the comparative effectiveness of the composite specimen with respect to the Nomex specimen have been established, the effective heat absorbed by a composite specimen can be evaluated. This is summarized in Figure I-16, using the data of Table 27 (see page 172) and the comparative heat-absorption-capability data shown in Figure I-14.

At a heat-flux rate of 1 Btu/ft^2-sec, the composite specimen absorbs about 350 Btu/lb; at a heat-flux rate of 3.5 Btu/ft^2-sec, the composites evidently can absorb about 600 Btu/lb. In each case, the effective heat absorbed by the composites offers a considerable increase over the uncoated Nomex specimen.

The results obtained above then were applied to the SP-5 roof panel. The heat-flux rate as a function of time from deployment for the SP-5 flight-test item is shown in Figure I-17. An element of the roof of this test item must absorb a heat flux equal to that area under this curve, if it is assumed that this heat-flux rate has a constant value around the periphery of the element. Analytical results presented previously showed that the heat-flux rate is a variable around this peripheral length and actually could be significantly less. However, it will be assumed constant and equal to that shown in Figure I-17 for estimated diameter requirements. Again, if Equation I-2 is used in a form suitable for a composite element, then the effective heat absorbed by a composite element can be written as

$$Q_{eff} = \frac{A_S \int \dot{q}\, dt}{\rho_C \left(V_o - V_{N_2} \right) + \rho_N V_{N_2}} . \qquad (I\text{-}5)$$

When Equation I-5 is solved for the outside diameter of a composite roof element required to absorb the heat flux generated during the deceleration of the SP-5 flight vehicles, the following equation results:

$$D_o^2 = \frac{4 \int \dot{q}\, dt}{\rho_C Q_{eff}} D_o + \left(\frac{\rho_N}{\rho_C} - 1 \right) D_N^2$$

$$= 0 \qquad (I\text{-}6)$$

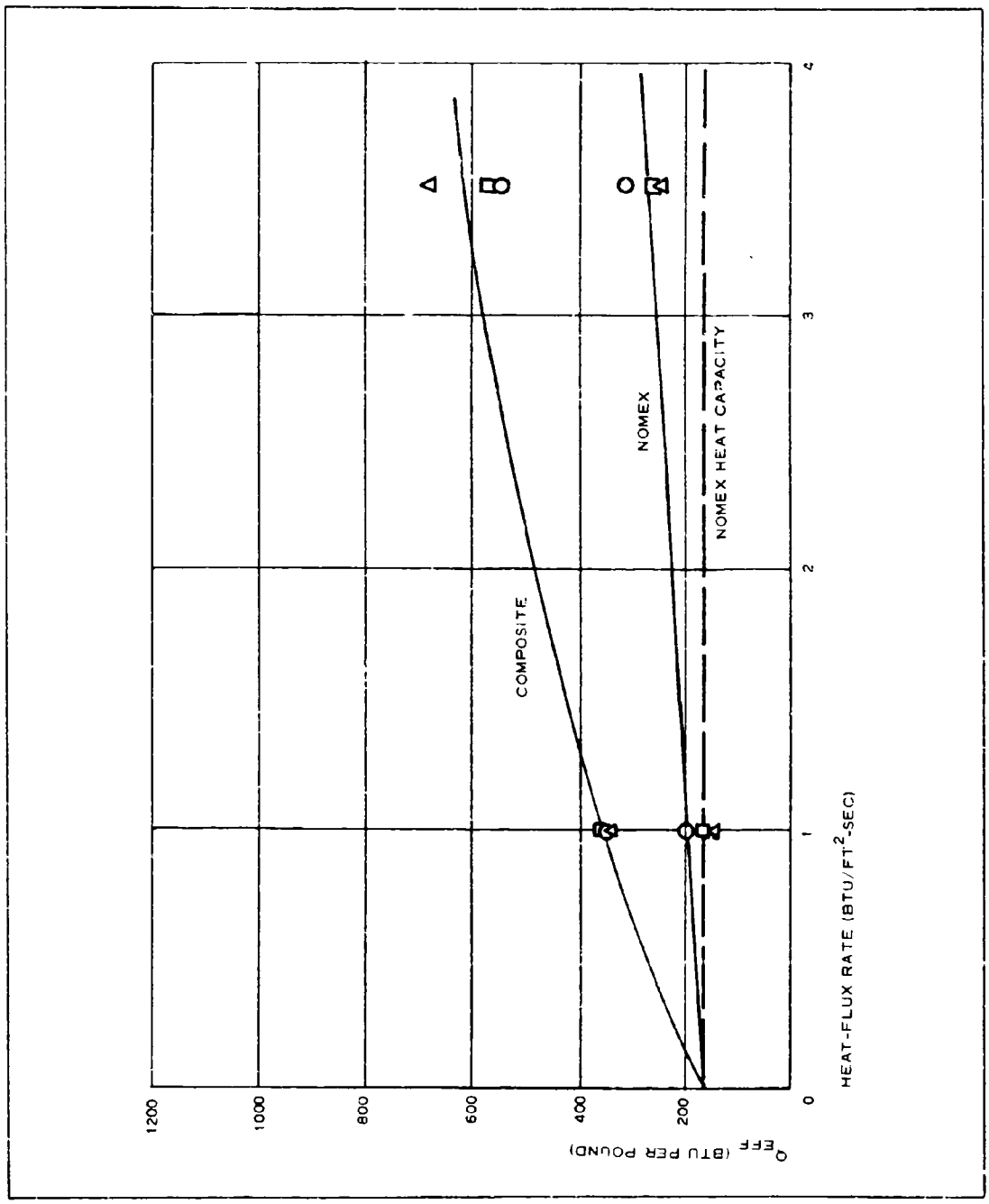

Figure I-16 - Effective Heat Absorbed

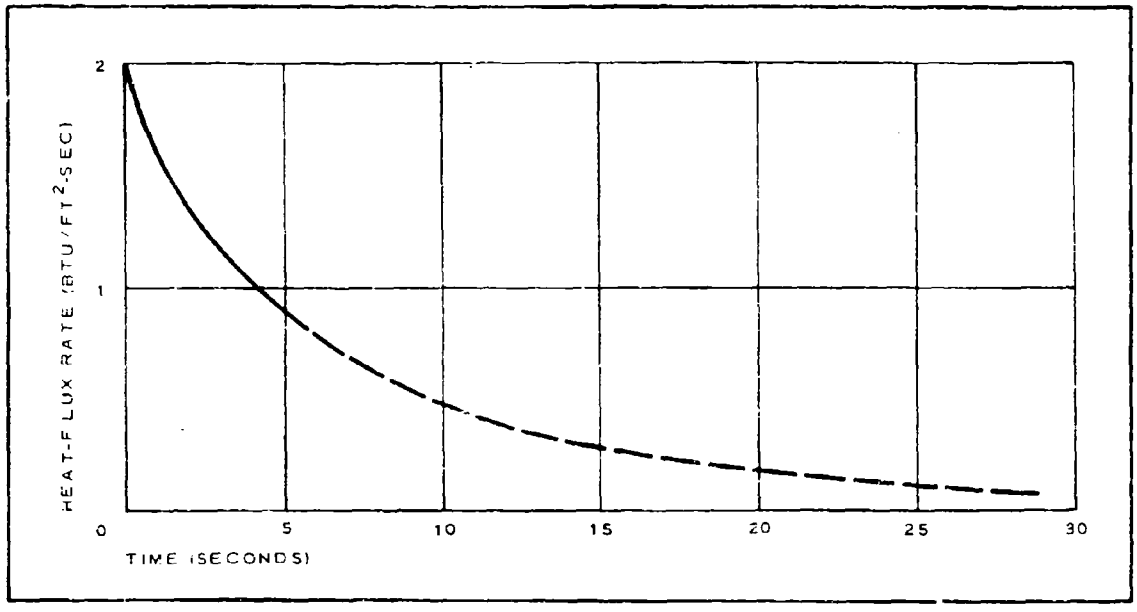

Figure I-17 - Heat Flux versus Time

This is a quadratic equation that can be solved if (1) the coating material is specified for which an effective heat absorption is known at the expected heat-flux rates and (2) the diameter of the inner core is specified. For the SP-5 hyperflo test item, a Nomex roof element with a diameter of approximately 0.0072 in. is to be used for the inner core, and the coating material was chosen to be Dyna-Term D-65. Vendor data show that the Dyna-Therm coating material has a specific gravity of about 1.1; the material specific gravity of Nomex is about 1.38. Based on the experimental data shown in Figure I-16, the composite element can absorb about 480 Btu/lb at the initial heat-flux rate of about 2 Btu/ft^2-sec, with decreasing capability as the heat-flux rate decreases as encountered during the test flight of the SP-5 vehicles. Therefore, it will be assumed for purposes of this calculation that the effective heat absorption of the composite element is 350 Btu/lb. When these values are inserted into Equation I-5, the resulting diameter required for a roof element is calculated to be about 18 mils.

As a result of the analysis of the experimental test data of coatings for the

SP-5 flight, the Dyna-Therm D-65 coating was determined to be the most efficient thermal coating tested. Additional analysis of this material established an effective heat-absorption capability for this material when it is used in combination with a specified diameter of the inner-core material, Nomex. From data obtained during experimental testing of the Dyna-Therm material, it was found that a total roof-element diameter of 0.018 in. should be sufficient to absorb the heat flux generated during deceleration of the SP-5 flight.

APPENDIX II - OPTIMIZATION OF INFLATABLE DRAG DEVICES BY ISOTENSOID DESIGN

1. INTRODUCTION

The advent of the missile age has caused a great deal of attention to be focused in recent years on the problem of recovering objects traveling at high speeds and at high altitudes. The inflatable drag device, which can be stowed in a small fraction of its inflated volume until it is needed, is one of the recovery devices under consideration.

Inflatable drag devices thus far have been divided into two major categories - parachutes and Goodyear Aerospace BALLUTEs.[a] The parachute is well known; the BALLUTE is a newer concept designed to overcome the flutter and stability problems often encountered with supersonic parachutes. In its typical form it is a pear-shaped body, approximating a cone with an 80-deg apex angle at the front.

A recurring problem in the design of inflatable drag devices is the method by which concentrated loads can be applied to the structure without causing locally high stresses. If the drag device is towed some distance behind the payload, the two bodies usually are connected by a single riser line attached to the nose of the drag device, causing a concentrated load at this point. If the payload is enclosed in the front of the drag device, the concentration is not so severe, but in general the diameter of the payload is still small compared with that of the drag device. In either case concentrated forces are required in the meridian direction in the region of the nose of the drag device. These forces are carried most efficiently by tension-carrying elements, such as cords or cables, which lie along the meridians of the drag device. If the

[a] TM, Goodyear Aerospace Corporation, Akron, Ohio.

meridian elements are cemented to the fabric, it is not necessary for them to extend all the way to the rear of the drag device, but there are several reasons why it is desirable for them to do so. First, the meridian cords carry part of the internal pressure load, allowing a smaller fabric stress than would otherwise exist. Second, the rear pole provides a second point on the drag device at which a concentrated load can be applied, a feature that is useful in cases in which the payload is a cylindrical body enclosed within the drag device. Third, it has been found that if the meridians run from front to rear, it is possible to generate curves of the drag device.

In this type of isotensoid surface the meridian cable tensions are constant and the fabric stress is uniform in all directions throughout the surface. The isotensoid design has two very desirable characteristics, which are discussed below.

First, the isotensoid surface provides a uniform factor of safety throughout the drag device (neglecting the effect of variations of temperature on the strength of the material), allowing a minimum weight with a constant thickness fabric.

Second, wind-tunnel tests have demonstrated that in supersonic flow the presence of wrinkles in the fabric causes flutter and rapid failure, leading to deflation and eventual loss of the entire drag device. The uniform fabric stress prevents local wrinkles.

The primary objective of this analysis is to derive the equations for the profile shapes of these surfaces of revolution, for both constant and variable pressure and to show briefly how they are used in the design of BALLUTEs and parachutes. In the analysis only static loads (which come from aerodynamic pressures) are considered; snatch loads, opening shock, and vibration problems are beyond the scope of this work.

2. BEHAVIOR OF THREE THREAD-SET MATRIX UNDER SYMMETRICAL LOADING

Figure II-1 shows an element of a matrix composed of one straight-thread

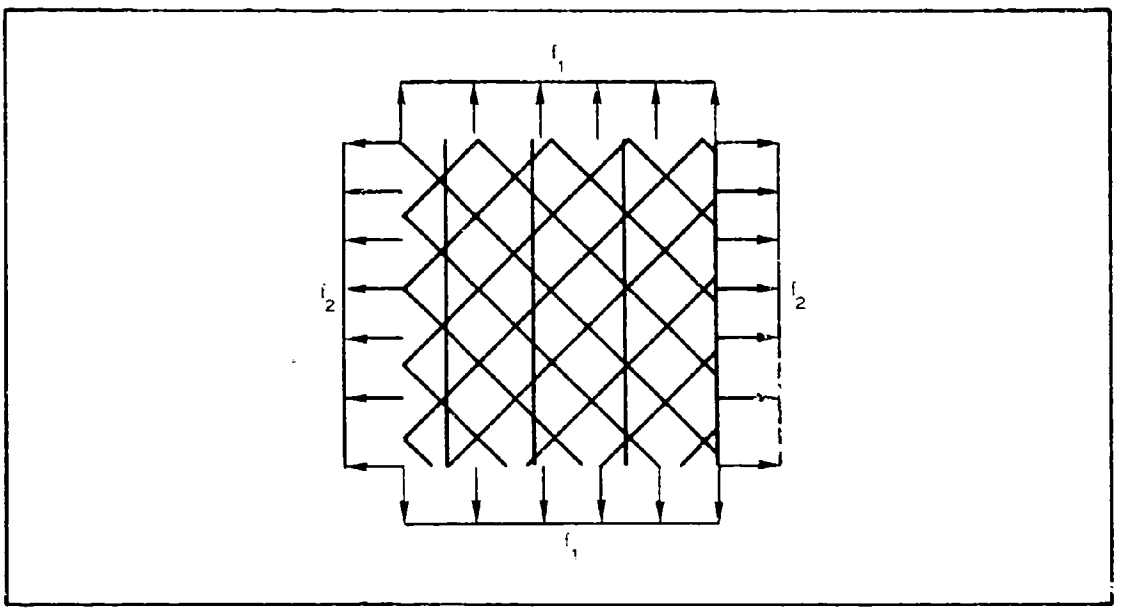

Figure II-1 - Equilibrium of an Element of a Three-Thread Set Matrix

set and two identical bias-thread sets. (The straight-thread set is parallel to the larger of the two principal stresses[a] (f_1) and the bias-thread sets are at 45 deg to it.) It is assumed that the threads of the straight-thread set are bonded to the bias threads at the intersections. It is also assumed that elongations in the threads are small. By symmetry the stresses in the bias-thread sets are equal. Because small strains are assumed, the bias-thread sets must remain at approximately 45 deg to the straight set under load and at 90 deg to each other. Therefore, the two bias-thread sets together form a matrix, whixh has a uniform stress (f) in all directions. From Figure II-1, it is clear that this stress must be equal to f_2. Thus,

$$f_2 = f \tag{II-1}$$

and

$$f_1 = f_s + f \, . \tag{II-2a}$$

[a] "Stress" is defined as force per unit of length.

where f_s is the stress in the straight-thread set. Equations II-1 and II-2 give the stresses f and f_s in terms of the principal stresses, f_1 and f_2, demonstrating that the stresses in the individual thread sets of the matrix of Figure II-1 are statically determinate under the given loading. Because the present construction of many drag devices (all BALLUTEs and some types of parachutes) conforms to the geometry and loading of Figure II-1, Equations II-1 and II-2 allow the stresses in all the components to be determined from equations of statics alone.

3. DERIVATION OF ISOTENSOID SURFACE

With Equations II-1 and II-2, it is now possible to derive the coordinates of the meridian curve of a surface of revolution in which the forces in the straight and bias threads do not vary with x; such a surface is one form of an isotensoid. The two bias-thread sets appear in the structure in the form of an envelope, seamed together from bias-cut gores, of a single ply of woven fabric, in which ideally the two thread sets are identical. The thread spacing in each thread set is constant, giving a constant stress, f, in the fabric. The straight threads appear in the structure in the form of cords, which lie along the meridians of the surface. These meridian cords vary in spacing, depending on their distance from the axis of revolution. The stress in the straight-thread set therefore varies with x according to the relation $f_s = nT_m/2\pi x$, where n is number of cords on the surface and T_m is the tension in each an. Equation II-2a becomes

$$f_1 = f + \frac{nT_m}{2\pi x} . \qquad \text{(II-2b)}$$

At x = 0, f_1 goes to infinity even though f and T_m remain constant, because the meridian cords converge and produce a concentrated load. If the slope of the membrane is not zero at x = 0, an axial load, F, is required to maintain equilibrium, as shown in Figure II-2.

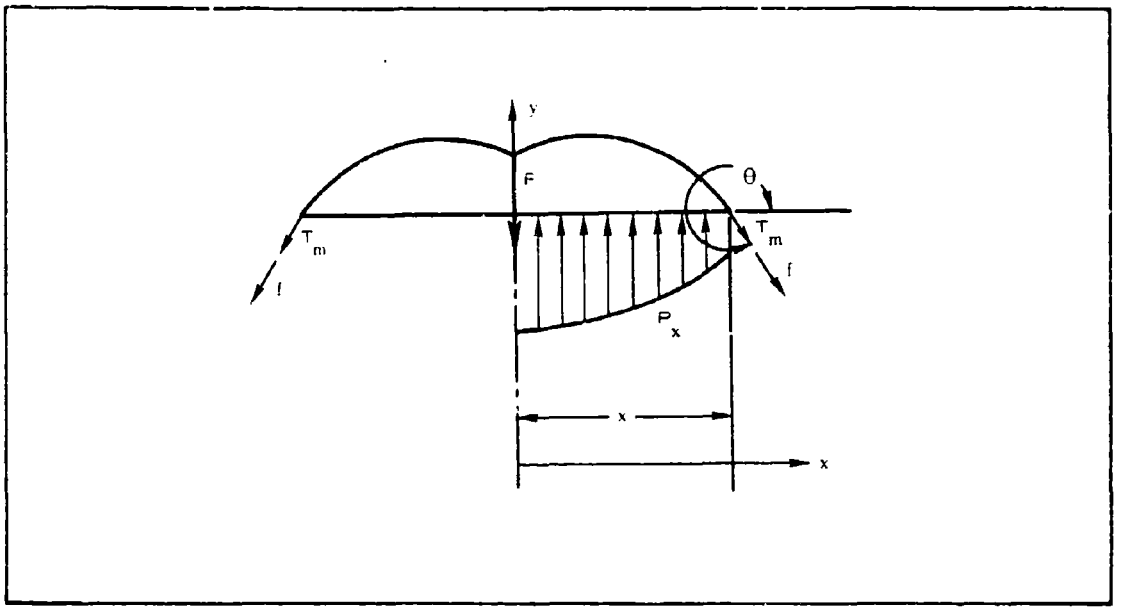

Figure II-2 - Vertical Equilibrium of the Plane of a Parallel Circle of Radius X

The remainder of the loading is a normal pressure distribution that has rotational symmetry but varies with x. The axial force on an annular ring of radius, x, and width, dx, is $2\pi x P_x dx$ and the total axial load on the surface up to a radius, x, is $\int_0^x 2\pi x P_x dx$. Figure II-2 shows the portion of the membrane above a parallel circle of radius, x.

Summing forces vertically uields

$$\int_0^x 2\pi x P_x dx + (nT_m + 2\pi xf) \sin\theta = F . \qquad (II-3)$$

Equation II-3 can be made nondimensional by dividing by $P\pi R^2$:

$$2\int_0^{x/R} \frac{x}{R}\frac{P_x}{P}\frac{dx}{R} + \left(\frac{nT_m}{P\pi R^2} + \frac{x}{R}\frac{2f}{PR}\right)\sin\theta = \frac{F}{P\pi R^2} . \qquad (II-4)$$

For convenience, the following definitions are made:

$$2\int_0^{x/R} \frac{x}{R}\frac{P_x}{P}\frac{dx}{R} = I_x$$

$$\frac{nT_m}{P\pi R^2} = k \qquad \text{(meridian cord factor)}$$

$$\frac{F}{P\pi R^2} = \rho \qquad \text{(axial load factor)}$$

Substituting the above definitions into Equation II-4 gives

$$I_x + \left(k + \frac{x}{R}\frac{2f}{PR}\right)\sin\theta = \rho \,. \tag{II-5}$$

Substituting

$$\sin\theta = \frac{\frac{dy}{dx}}{\left[1 + \left(\frac{dy}{dx}\right)^2\right]^{1/2}}$$

and solving for dy/dx gives

$$\frac{dy}{dx} = \frac{\pm 1}{\left[\left(\frac{k + \frac{x}{R}\frac{2f}{PR}}{\rho - I_x}\right)^2 - 1\right]^{1/2}} \tag{II-6}$$

When x/R = 1, sin θ = -1, and Equation II-5 becomes

$$\frac{2f}{PR} = I_R - k - \rho \,. \tag{II-7}$$

Substituting Equation II-7 into Equation II-6 gives

$$\frac{dy}{dx} = \frac{\pm 1}{\left[\left(\frac{k + \frac{x}{R}(I_R - k - \rho)}{\rho - I_x}\right)^2 - 1\right]^{1/2}} \,. \tag{II-8}$$

Given an external pressure distribution, Equation II-8 defines a family of surfaces with a constant meridian stress (f) in the fabric envelope and

constant loads (T_m) in the meridian cords. Nothing has been said yet, however, about the hoop stress in the membrane. The membrane equation (from Reference II-1) becomes

$$\frac{f + \frac{nT_m}{2\pi x}}{r_1} + \frac{f_2}{r_2} = P_x , \tag{II-9}$$

where

$$r_1 = \frac{-\left[1 + \left(\frac{dy}{dx}\right)^2\right]^{3/2}}{\frac{d^2y}{dx^2}} \tag{II-10}$$

and

$$r_2 = \frac{-x}{\sin\theta} = \frac{-x\left[1 + \left(\frac{dy}{dx}\right)^2\right]^{1/2}}{\frac{dy}{dx}} . \tag{II-11}$$

Differentiating Equation II-8 and writing the results in terms of dy/dx gives

$$\frac{d^2y}{dx^2} = \frac{k\left(\frac{dy}{dx}\right)^2\left[1 + \left(\frac{dy}{dx}\right)^2\right]^{1/2}}{\rho - I_x} - \frac{\frac{dy}{dx}\left[1 - \left(\frac{dy}{dx}\right)^2\right]\left(\rho + \frac{2x^2}{R^2}\frac{P_x}{P} - I_x\right)}{x(\rho - I_x)} . \tag{II-12}$$

After substitution for r_1 and r_2, Equation II-9

$$\frac{2f_2}{RP} = \frac{\frac{-2x}{R}\frac{P_x}{P}\left[1 + \left(\frac{dy}{dx}\right)^2\right]^{1/2}}{\frac{dy}{dx}} - \frac{\left(\frac{2f}{PR} + \frac{Rk}{x}\right)x\frac{d^2y}{dx^2}}{\frac{dy}{dx}\left[1 + \left(\frac{dy}{dx}\right)^2\right]} . \tag{II-13}$$

After substitution for dy/dx and d^2y/dx^2 from Equations II-8 and II-12, respectively, Equation II-13 becomes

$$f_2 = f ,$$

or the same as Equation II-1, which satisfies the analysis in Part 2, above.

Equation II-8 has not yet been integrated in terms of known functions. In practice, however, either a numerical or graphical integration has given satisfactory results. For the constant-pressure case $I_R = 1$ and $I_x = x^2/R^2$, Equation II-8 gives

$$\frac{dy}{dx} = \frac{\pm 1}{\left\{\left[\frac{k + \frac{x}{R}(1 - k - \rho)}{\rho - \frac{x^2}{R^2}}\right]^2 - 1\right\}^{1/2}} \qquad \text{(II-14)}$$

Equation II-14 has been plotted for various values of k and ρ for use as rear halves of BALLUTEs, which in some cases have nearly uniform pressure loading. Figure II-3 shows a family of curves for which $\rho = 0$. For the case in which k is also zero, the meridian cords disappear and the membrane becomes a constant-pressure surface with uniform stress throughout and no axial load. Such a surface must be a sphere, as is indicated by the upper (circular) curve. At the other extreme in Figure II-3 is the case in which all the membrane stress is in the meridian direction (f = 0). This shape is often observed in parachutes with a large number of gores and a small gore radius in the fabric, resulting in a very small fabric stress. This curve for $k = 1$, $\rho = 0$ is known as Taylor's curve (Reference II-2). The curves between the two extremes have both fabric stress and meridian-cable tension in varying combinations; the range from k = 0.4 to k = 0.6 has been found most useful in BALLUTE design. Figures II-4 and II-5 show similar families of curves for positive values of ρ, and Figure II-6 shows a family for negative values of ρ. All the curves of Figures II-3 through II-6 are for the absolute value of ρ less than k. If $|\rho| > k$, the curve does not pass through the axis of revolution. By joining two identical surfaces of this type at their equators, a toroidal surface is obtained, as exemplified by the family of curves in Figure 7. At the inner diameter of these toroidal surfaces, a compression ring is required to maintain equilibrium of the fabric stresses at the intersection of the two surfaces. The curves of Figure II-6

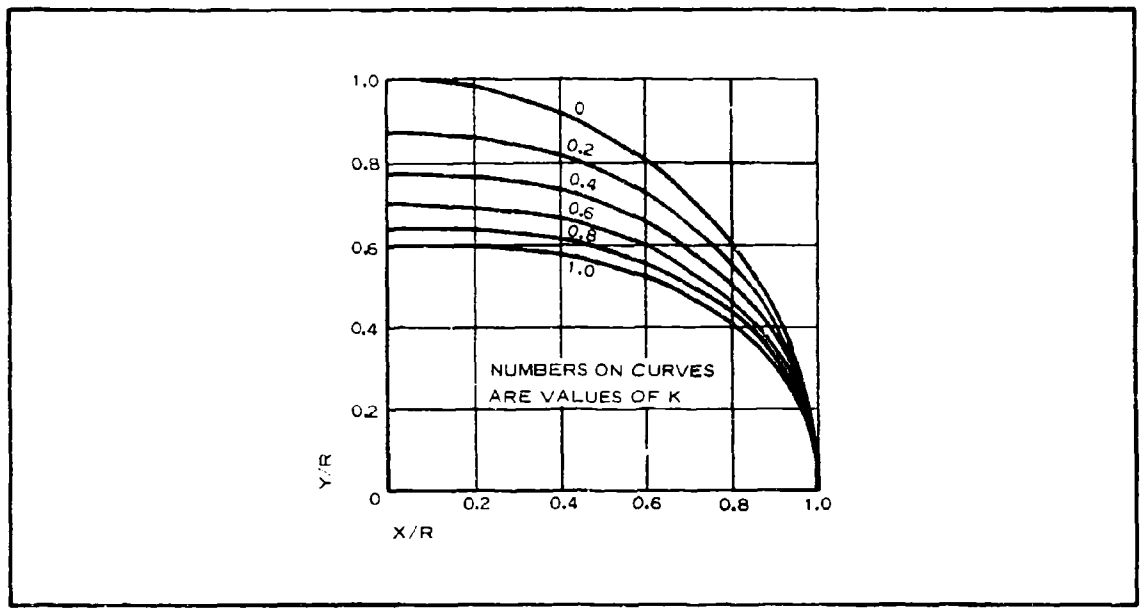

Figure II-3 - Profile Curves for ρ = 0 and Values of k

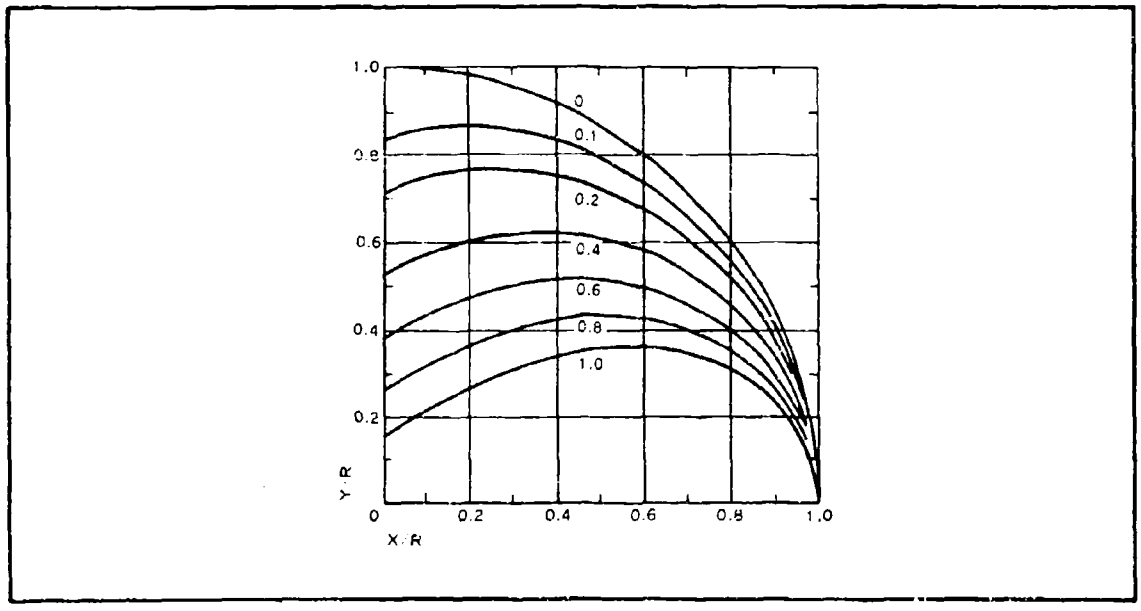

Figure II-4 - Profile Curves for ρ/k = 0.5 and Values of k + ρ

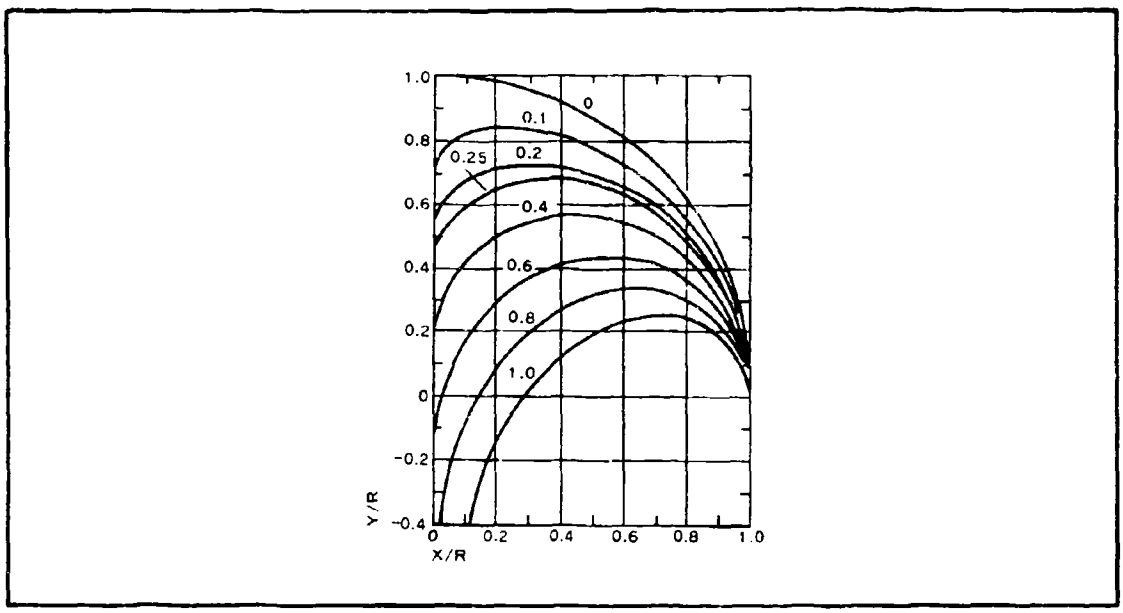

Figure II-5 - Profile Curves for $\rho/k = 1$ and Values of $k + \rho$

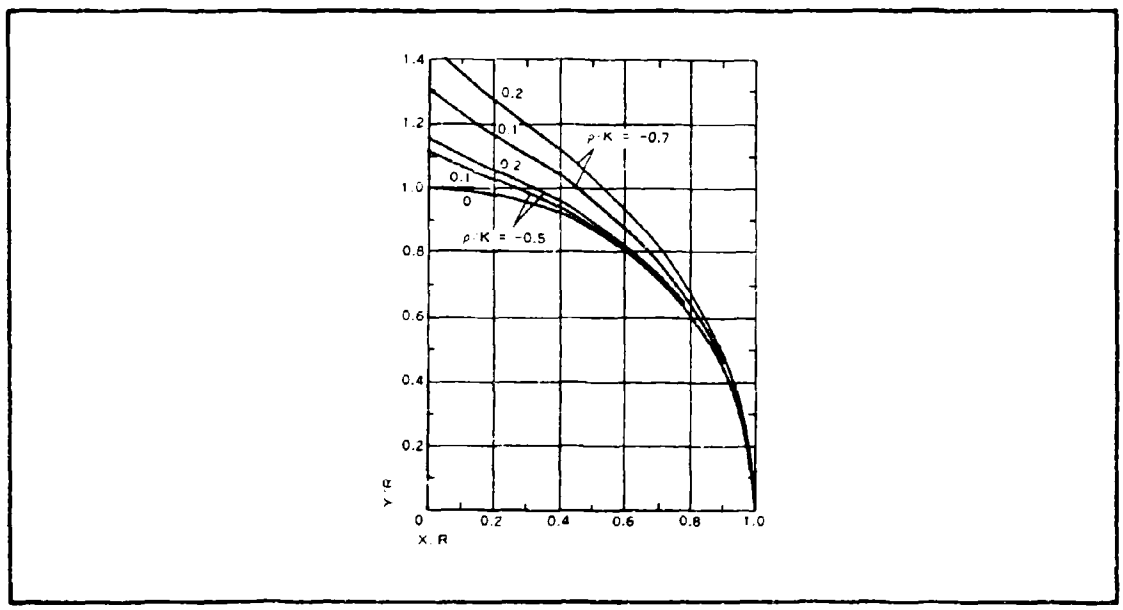

Figure II-6 - Profile Curves for $\rho/k = -0.5$, $\rho/k = -0.7$, and Values of $k + \rho$

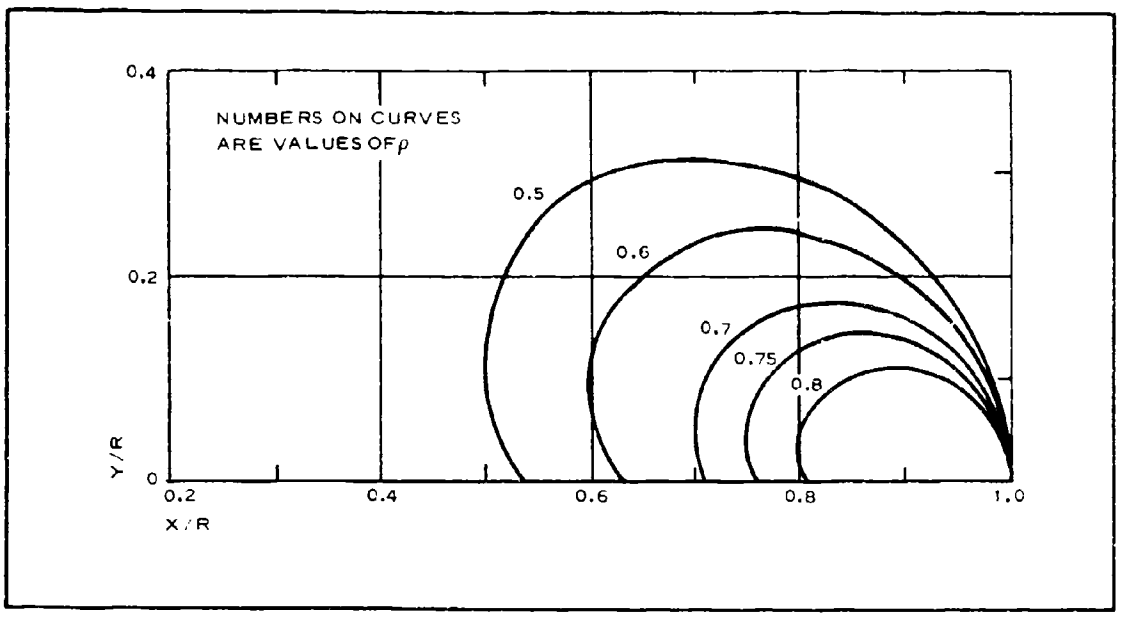

Figure II-7 - Profile Curves for k = 0 and Values of ρ

and II-7 do not apply directly to the simplified drag devices of Figure II-8, but are included to show the range of shapes obtainable with Equation II-14.

4. STRESS ANALYSIS FOR GENERAL SYMMETRICAL LOADINGS

Equations II-3, II-4, and II-5 apply as before, except that T_m and f are now functions of x instead of constants. If the quantities that apply to a general loading condition (as opposed to the loading used to derive the isotensoid surface) are denoted by primes, Equation II-5 becomes

$$I_x' + \left(k' + \frac{x}{R}\frac{2f'}{PR}\right)\sin\theta = \rho' \,. \qquad \text{(II-15)}$$

Because the fabric envelope is seamed together from bias-cut gores of a single-ply (two-thread set) fabric, the thread angle is maintained at 45 deg to the meridian cords. The stress ratio in the fabric must therefore be equal to unity under any loading condition. Substituting Equation II-1, Equation II-13 becomes

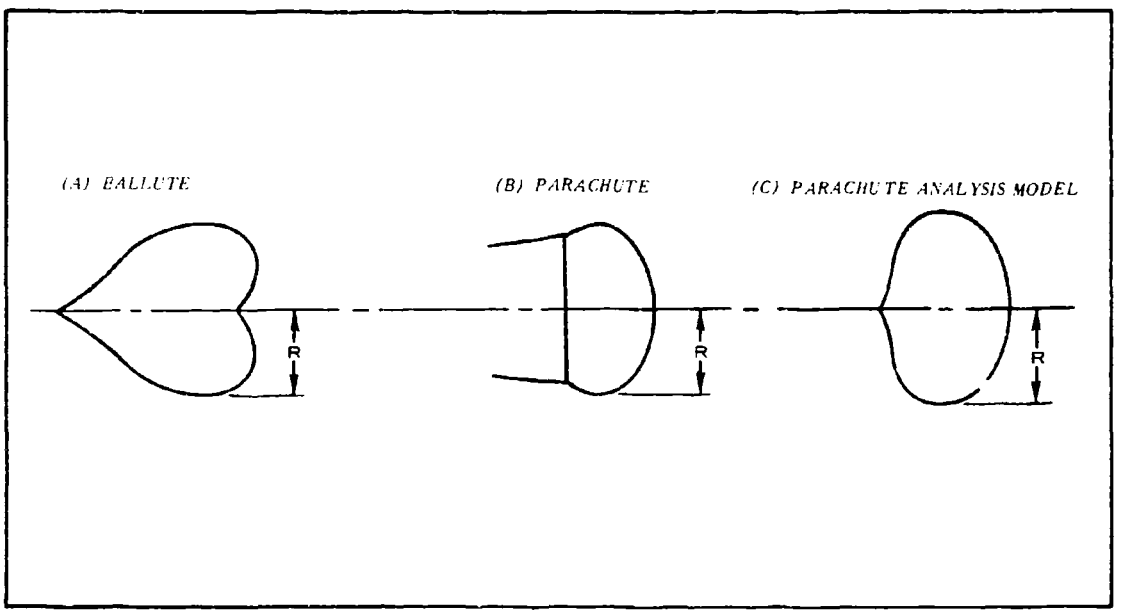

Figure II-8 - Typical Drag-Device Configurations

$$\frac{2f'}{P'R} = \frac{\frac{-2x}{R}\frac{P'_x}{P'}\left[1+\left(\frac{dy}{dx}\right)\right]^{3/2} - \frac{Rk'}{x}\frac{xd^2y}{dx^2}}{\frac{xd^2y}{dx^2}+\frac{dy}{dx}\left[1+\left(\frac{dy}{dx}\right)^2\right]} \qquad \text{(II-16)}$$

After substituting for d^2y/dx^2, dy/dx, and $2f'/P'R$ from Equation II-12, II-8, and II-16, respectively, Equation II-15 becomes

$$k' = \left[\frac{k+\frac{x}{R}(I_R - k - \rho)}{\rho - I_x}\right]\left\{\frac{\rho' - I_x'}{\rho}\left[\frac{k(\rho - I_x)}{k+\frac{x}{R}(I_R - k - \rho)} - \frac{2x^2}{R^2}\frac{P_x}{P}\right] + \frac{2x^2}{R^2}\frac{P_x'}{P'}\right\} . \qquad \text{(II-17)}$$

After k' is obtained from Equation II-17, Equation II-15 can be rearranged to give $2f'/P'R$:

$$\frac{2f'}{P'R} = \left\{ \frac{(\rho' - I_x')\left[k + \frac{x}{R}(I_R - k - \rho)\right]}{\rho - I_x} - k' \right\} \frac{R}{x} . \qquad \text{(II-18)}$$

5. COMPATIBILITY REQUIREMENTS FOR DRAG DEVICES (ISOTENSOID CONDITION)

The analysis in Parts 3 and 4, above, applies to a membrane in the form of a surface of revolution that satisfies the boundary condition of Equation II-7. To obtain a complete drag device, two such membranes must be joined at their boundaries (x = R), resulting in a configuration typified by Figure II-8.

For the BALLUTE, the two membranes are complete; for the parachute, however, the front membrane is truncated. For purposes of analysis it can be extended to the axis, and any desired pressure can be assumed to act on the extended portion, as shown in Figure II-8. The relationship of the drag force on the resulting structure to the drag force on the actual parachute is discussed later.

When the two membranes are joined, their mutual boundary becomes the maximum diameter (equator) of the resulting drag device. At the equator the meridian-cable tensions and the fabric stresses must be respectively equal so that the two membranes will be compatible. Using the subscripts f for front and r for rear,

$$f_f = f_r \qquad \text{(II-19)}$$

and

$$T_{mf} = T_{mr} \qquad \text{(II-20)}$$

where

$$x = R;$$

and

$$n_f = n_r . \qquad \text{(II-21)}$$

In the optimum case, f and T_m are constant throughout the surface of the drag device. Although it is not always possible to obtain this condition, it is assumed to be possible in the first attempt to obtain a profile shape. Equation II-3 therefore applies to any cross section of the drag device with constant values of f and T_m. For convenience, the same value of P is used in obtaining Equation II-4 for front and rear halves. Therefore, the quantities k and 2f/PR are equal for both halves of the drag device. Rewriting Equation II-7 for both front and rear gives

$$\frac{2f}{PR} = I_{Rf} - k - \rho_f \tag{II-22}$$

and

$$\frac{2f}{PR} = I_{Rr} - k - \rho_r , \tag{II-23}$$

or

$$I_{Rf} - \rho_f = I_{Rr} - \rho_r . \tag{II-24}$$

Equations II-22 through II-25 are the compatibility relationships for isotensoid drag devices. Generally, the internal and external pressures are given (obtained from aerodynamic analysis), allowing I_{Rf}, I_{Rr}, and P to be determined. When these are known, it is still necessary to make arbitrary choices for two other values to solve the system of Equations II-22 through II-24. The number of arbitrary choices is reduced to one if another boundary condition is introduced. From wind-tunnel tests, it has been found that a conical drag body must have an included angle of 80 deg or less to be aerodynamically stable. Tests on BALLUTEs have shown that a similar limitation applies. Experience in deriving BALLUTE front-profile shapes has shown that there is usually a nearly conical portion in the region of x/R = 0.5. For BALLUTEs, therefore, stability is ensured by introducing the condition that θ = -50 deg at x/R = 0.5. Equation II-5 becomes

$$I_{xf_{(x/R\ =\ 0.5)}} - \left[k + (0.5)\frac{2f}{PR} \right] (0.766) = \rho_f . \tag{II-25}$$

Equation II-25 applies to BALLUTEs only. For parachutes, no additional boundary condition is specified here. Eliminating 2f/PR and o_f from the system of Equations II-22 through II-25 yields

$$k = 1.61(I_{Rr} - \rho_r) - 2.61\left[I_{Rf} - I_{xf_{(x/R\,=\,0.5)}}\right]. \qquad \text{(II-26a)}$$

By assuming a value for ρ_r, k can be obtained from Equation II-26a, ρ_f from Equation II-24, and 2f/PR from II-22 or II-23. The front and rear profile shapes are then obtained by a numerical integration of Equation II-6.

Sometimes the value of k so obtained is not compatible with the desired number of gores, as discussed in Part 6, below. In this case, it may not be possible to obtain an isotensoid structure for the given internal pressure, and it may be necessary to choose a value of k arbitrarily and solve for the value of P that would be required to obtain the isotensoid condition. The resulting structure can then be analyzed for the actual internal pressure as discussed in Part 6. Substituting the definitions of the I terms in Equation II-26a and solving for P/q yields

$$\frac{P}{q} = \frac{1.61\int_0^1 (C_R - C_{xr})\frac{x}{R}\frac{2dx}{R} - 2.61\int_{0.5}^1 (C_R - C_{xf})\frac{2x}{R}\frac{dx}{R}}{k + 1.61\,\rho_r + 0.35}. \qquad \text{(II-26b)}$$

If Equation II-26b is used, the integrals of Equation II-26a and Equation II-6 must be re-evaluated for the value of P/q so obtained. ρ_f, 2f/PR, and the front- and rear-profile shapes are then obtained as described above.

If the inertia of the drag device is small compared with that of the payload to which it is attached, the riser-line load is equal to the aerodynamic drag, D, of the drag device. For equilibrium, then, the riser-line load must be equal to

$$\int_o^R 2\pi x P_{xr}\,dx - \int_o^R 2x P_{xf}\,dx,$$

or

$$D = P\pi R^2(I_{Rr} - I_{Rf}) ; \tag{II-27}$$

and it follows that

$$C_D = \frac{P}{q}(I_{Rr} - I_{Rf}) . \tag{II-28}$$

Equations II-27 and II-28 apply directly to BALLUTEs and to the parachute analysis model of Figure II-8. They apply to the actual parachute if the pressure P_x is taken to be zero from $x = 0$ to x equals the inlet radius for the front of the parachute.

5. COMPATIBILITY UNDER GENERAL SYMMETRICAL LOADING

In order that all structural members will be in tension, ρ_r must be positive or zero. The rear membrane therefore must always have a value of x at which $dy/dx = 0$. If the strains are small, the point of zero slope does not change under various loading conditions. At the point of zero slope, Equation II-15 gives

$$\rho'_r = I'_{x_o} \tag{II-29}$$

Substituting Equation II-29 into Equation II-17 and II-18 and adding the subscript r gives

$$k'_r = \left[\frac{k + \frac{x}{R}(I_{Rr} - k - \rho)}{\rho_r - I_{xr}}\right]\left\{\frac{I'_{x_o} - I'_{xr}}{\rho_r - I_{xr}}\left[\frac{k(\rho_r - I_{xr})}{k + \frac{x}{R}(I_{Rr} - k - \rho_r)} - \frac{2x^2}{R^2}\frac{P_{xr}}{P}\right] + \frac{2x^2}{R^2}\frac{P'_{xr}}{P'}\right\} \tag{II-30}$$

and

$$\frac{2f'_r}{P'R} = \left\{\frac{\left(I'_{x_o} - I'_{xr}\right)\left[k + \frac{x}{R}(I_{Rr} - k - \rho)\right]}{\rho_r - I_{xr}} - k'_r\right\}\frac{R}{x} . \tag{II-31}$$

Equations II-30 and II-31 give the stress parameters for the rear of a BALLUTE or a parachute. To obtain the values for the front, ρ_f' must be determined. By adding primes, Equation II-24 applies to any symmetrical loading condition. Substituting for ρ_r' from Equation II-29 gives

$$\rho'_f = I'_{Rf} - I'_{Rr} + I'_{x_o} . \tag{II-32}$$

Substituting for ρ_f' into Equation II-17 and II-18 and adding the subscript f gives

$$k'_f = \left[\frac{k + \frac{x}{R}(I_{Rf} - k - \rho_f)}{\rho_f - I_{xf}}\right]\left\{\frac{I'_{Rf} - I'_{Rr} + I'_{x_o} - I'_{xf}}{\rho_f - I_{xf}}\left[\frac{k(\rho_f - I_{xf})}{k + \frac{x}{R}(I_{Rf} - k - \rho_f)} - \frac{2x^2}{R^2}\frac{P_{xf}}{P}\right] + \frac{2x^2}{R^2}\frac{P'_{xf}}{P'}\right\}, \tag{II-33}$$

and

$$\frac{2f'_1}{PR} = \left\{\frac{I'_{Rf} - I'_{Rr} + I'_{x_o} - I'_{xf}}{\rho - I_{xf}}\left[k + \frac{x}{R}(I_{Rf} - k - \rho_f)\right] - k'_f\right\}\frac{R}{x}. \tag{II-34}$$

All the previous analysis is based on the assumption that the drag device is a surface of revolution, a configuration that can be obtained only if there are many closely spaced meridian cords. However, present construction methods place limits on the number of meridian cords; a typical value for n is 16. The resulting structure has the scalloped effect often observed in parachutes instead of the circular cross sections of a perfect surface of revolution. For the fabric stress to have the values of f' calculated by Equation II-31 and II-34, the radius of the scallop (gore radius), r_g, must have a specific value at every cross section. This value is obtained from the membrane equation (Reference II-1, page 435) by substituting f' for each of the principal stresses. In using the membrane equation, it is assumed that the meridian of the gore fabric is the same as the radius, r_1, of the nominal surface of revolution. Thus,

$$\frac{f'}{r_1} + \frac{f'}{r_g} = P_x ,$$

or

$$r_g = \frac{f'}{P_x - \frac{f'}{r_1}} . \qquad \text{(II-35)}$$

Radius r_1 is obtained in terms of dy/dx by substituting Equation II-12 into Equation II-10:

$$r_1 = \frac{-\left[1 + \left(\frac{dy}{dx}\right)^2\right] (\rho - I_x)}{k\left(\frac{dy}{dx}\right)^2 - \frac{dy}{dx}\left[1 + \left(\frac{dy}{dx}\right)^2\right]^{1/2}\left(\rho + \frac{2x^2}{R^2}\frac{P_x}{P} - I_x\right)} \qquad \text{(II-36)}$$

Once a given shape has been derived, numerical values of f' from Equation II-31 or II-34 and r_1 from Equation II-36 are substituted into Equation II-35 to obtain values of r_g. These r_g values should then be laid out for various cross sections (taken normal to the nominal surface) of the drag device to determine the amount of fabric distortion required to obtain the calculated curvature. Because the bias-cut fabric has the ability to rack (change the angle between the thread sets) between the meridian cords, moderate amounts of distortion can be obtained without any thread elongation. However, in some cases the gore radius might not be big enough to span the distance between cords; in such cases changes would be required in the design (such as an increase in the number of gores) before proceeding further.

The following example is presented as an illustration of the type of results obtained from the preceding analysis.

PROBLEM: Design an 80-deg BALLUTE without center cable ($\rho_r = 0$).

GIVEN: C_{xr} values are constant at -0.18. C_{xi} values are given in Table II-1.

The quantity $(C_R - C_{xr})$ is equal to zero for all values of x. The quantity $x/R(C_R - C_{xf})$ is given in Table II-1. By graphical integration, the quantity

TABLE II-1 - TERM COMPUTATIONS

$\frac{x}{R}$	C_{xf}	Calculated	
		$C_R - C_{xf}$	$\frac{x}{R}(C_R - C_{xf})$
0	0.6	-0.78	0
0.05	0.63	-0.81	-0.0405
0.1	0.66	-0.84	-0.084
0.15	0.685	-0.865	-0.130
0.2	0.715	-0.895	-0.179
0.25	0.745	-0.925	-0.231
0.3	0.775	-0.955	-0.286
0.35	0.81	-0.99	-0.346
0.4	0.84	-1.02	-0.408
0.45	0.88	-1.06	-0.477
0.5	0.925	-1.105	-0.553
0.55	0.975	-1.155	-0.635
0.6	1.03	-1.21	-0.725
0.65	1.085	-1.265	-0.822
0.7	1.115	-1.295	-0.906
0.75	1.13	-1.31	-0.982
0.8	1.13	-1.31	-1.049
0.85	1.115	-1.295	-1.10
0.9	0.95	-1.13	-1.026
0.95	0.27	-0.45	-0.428
0.98	-0.14	-0.40	-0.0392
0.995	-0.18	0	0
1.0	-0.18	0	0

$$\int_{0.5}^{1} (C_R - C_{xf}) \frac{2x}{R} \frac{dx}{R}$$

is found to be -0.794. The value of k is arbitrarily chosen as 0.5; substituting into Equation II-26b gives P/q = 2.44. The pressure difference, P_x, is equal to P + q (C_R - C_{xf}) and

$$\frac{P_x}{P} = 1 + \frac{C_R - C_{xf}}{2.44} . \qquad \text{(II-37)}$$

Substituting into the definition of I_x gives

$$I_{Rf} = \int_{0}^{1} \frac{2x}{R} \left(1 + \frac{C_R - C_{xf}}{2.44}\right) \frac{dx}{R}$$

$$= 1 + \frac{\int_0^1 \frac{2x}{R} (C_R - C_{xf}) \frac{dx}{R}}{2.44} . \qquad \text{(II-38)}$$

By graphical integration, I_{Rf} is found to be 0.543 and similarly, I_{Rr} = 1.0. Equation II-24 gives ρ_f = 0.457. Substituting the above values into Equation II-8 gives the derivative of the front-profile curve at various values of x/R. A numerical integration gives the front-profile curve, and the rear-profile curve is the curve for k = 0.5 in Figure II-3. The resulting BALLUTE profile is shown in Figure II-9.

7. NOMENCLATURE

a. Primary

c_D = aerodynamic-drag coefficient

c_x = external-pressure coefficient

D = drag force

f = fabric stress

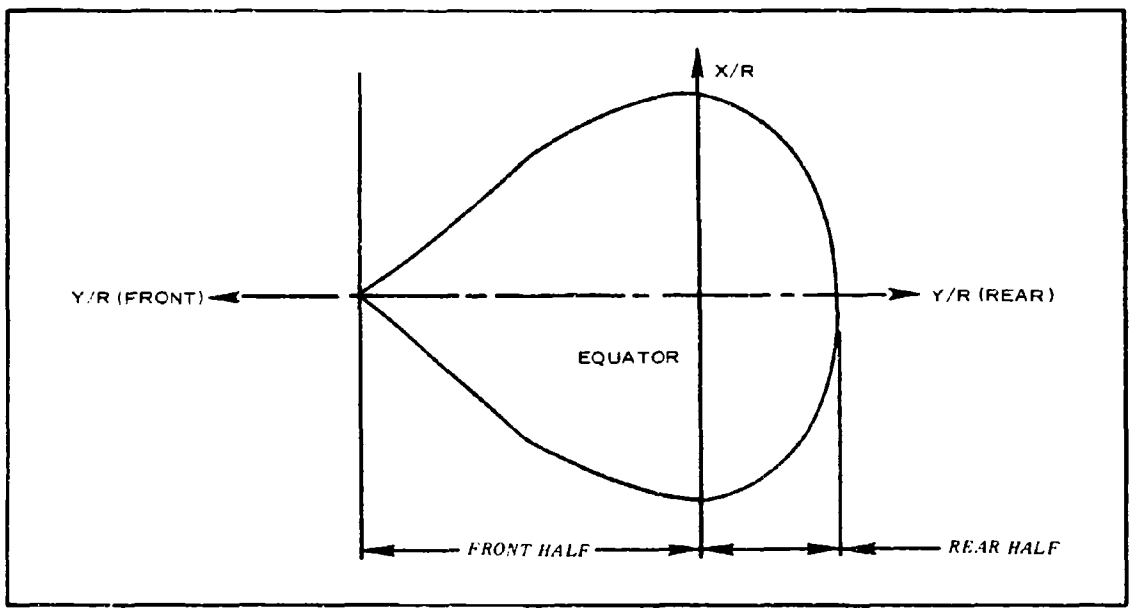

Figure II-9 - Profile of Example BALLUTE

f_s = stress in straight-thread set

f_1 = principal stress in membrane (meridian direction)

f_2 = principal stress in membrane (hoop direction)

F = axial load on membrane (see Figure II-2)

$$I_x = 2\int_0^{x/R} \frac{x}{R}\frac{P_x}{P}\frac{dx}{R}$$

$$k = nT_m/P\pi R^2$$

n = number of gores = number of meridian cords

P = value of P_x at x = R

P_x = pressure difference on membrane at any point, x

q = dynamic pressure

r_1, r_2 = principal radii of curvature

r_g = gore radius

R = equatorial radius

T_m = tension in each meridian cord

x = radial coordinate axis

x_o = value of x at $dy/dx = 0$

y = axial coordinate

$\rho = F/P\pi R^2$

θ = angle between tangent to a meridian and radial line (see Figure II-2)

b. Subscripts

f = value of quantity on the front of a drag device

r = value of a quantity on the rear of a drag device

R = value of a quantity at the equator ($x = R$)

x = value of a quantity at any point, x

x_o = value of a quantity at x_o

8. REFERENCES

1. Timoshenko, S., and Woinowsky-Krieger, S.; Theory of Plates and Shells. 2nd ed., McGraw-Hill, N. Y., 1959, p. 435.

2. Jones, R., "On the Aerodynamic Characteristics of Parachutes." R and M No. 862, June, 1923.

APPENDIX III - GORE-PATTERN DETERMINATION

BALLUTEs and parachutes, when inflated, usually have a scalloped appearance because of the small radius of curvature of the gore fabric between the meridian cords. This radius, known as the gore radius, requires that the fabric have rather severe compound curvature. Before inflation, however, the fabric is a flat sheet, and the cross section of a tailored BALLUTE or parachute is a regular polygon. It is clear, therefore, that the fabric must distort considerably under load. If the gores are cut from a single ply of fabric with the warp and fill threads at 45 deg to the gore center lines, this distortion is accomplished easily by thread racking, in which the angle between the thread sets varies across the gore. If the meridian cords are placed along the gore seams, the mechanism can be approximated by the model shown in Figure III-1.

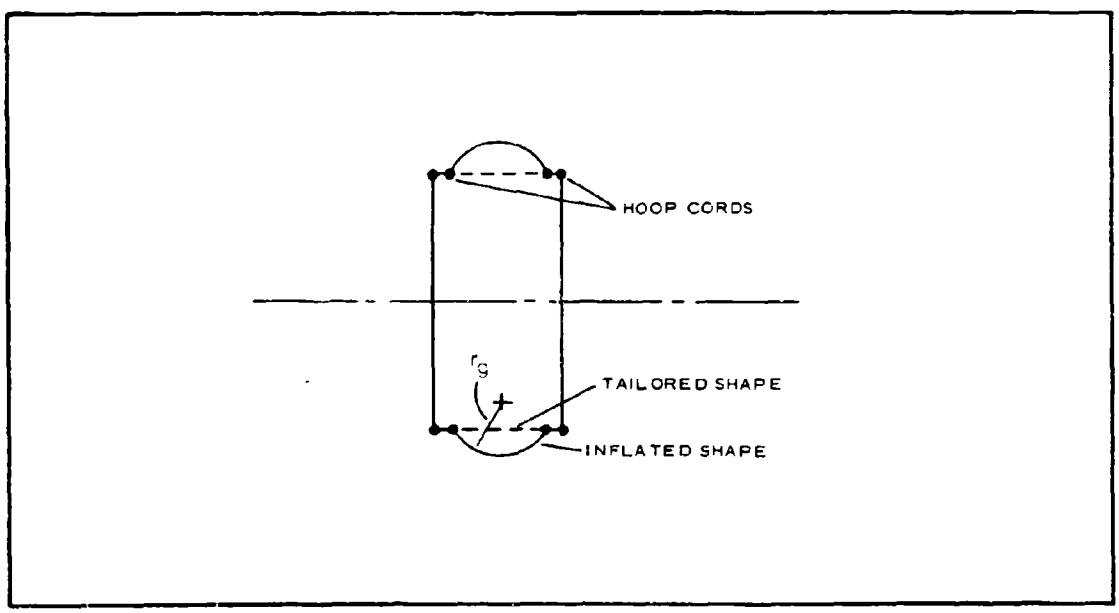

Figure III-1 - Fabric-Distortion Model

The tailored structure in Figure III-1 is a short, bias-cut cylinder with a hoop on each end. For this analysis, it is assumed that the end hoops and the fabric threads are nonextensible. Under some combination of internal pressure and axial load (the means of end closure is not specified), the cylinder will take a gore radius, r_g, as shown in Figure III-1.

It is clear that every circular cross section except the end hoops must be larger than tailored, requiring fabric distortion as shown in Figure III-2.

From Figure III-2

$$(d\ell)^2 = (ds)^2 + (dh)^2 \qquad \text{(III-1)}$$

The inflated geometry is shown in more detail in Figure III-3. From the geometry of Figures III-2 and III-3,

$$\frac{\sqrt{2}\, dh}{d\ell} = \frac{r}{r_o}, \qquad \text{(III-2)}$$

$$ds = r_g\, d\beta, \qquad \text{(III-3)}$$

and

$$r = r_o + r_g (\sin\beta - \sin\beta_o). \qquad \text{(III-4)}$$

Substituting for ds and dh into Equation III-1 gives

$$d\ell = \frac{r_g\, d\beta}{\sqrt{1 - \frac{1}{2}\left(\frac{r}{r_o}\right)^2}}. \qquad \text{(III-5)}$$

Substituting for r from Equation III-4 gives

$$d\ell = \frac{r_g\, d\beta}{\sqrt{1 - \frac{1}{2}\left[1 + \frac{r_g}{r_o}(\sin\beta - \sin\beta_o)\right]^2}}. \qquad \text{(III-6)}$$

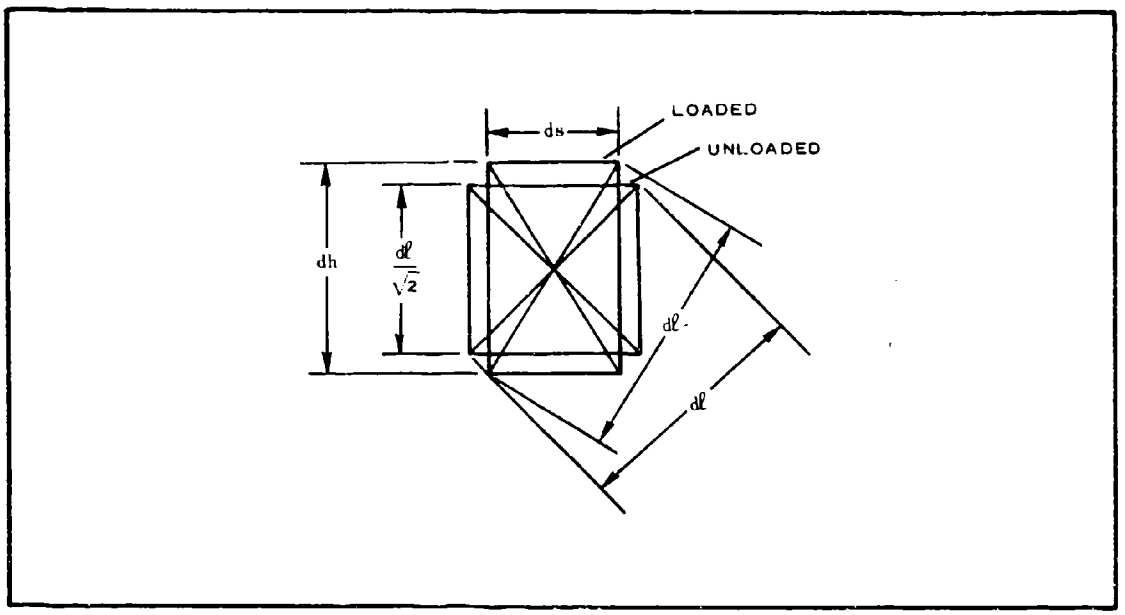

Figure III-2 - Distortion of Fabric Element under Load

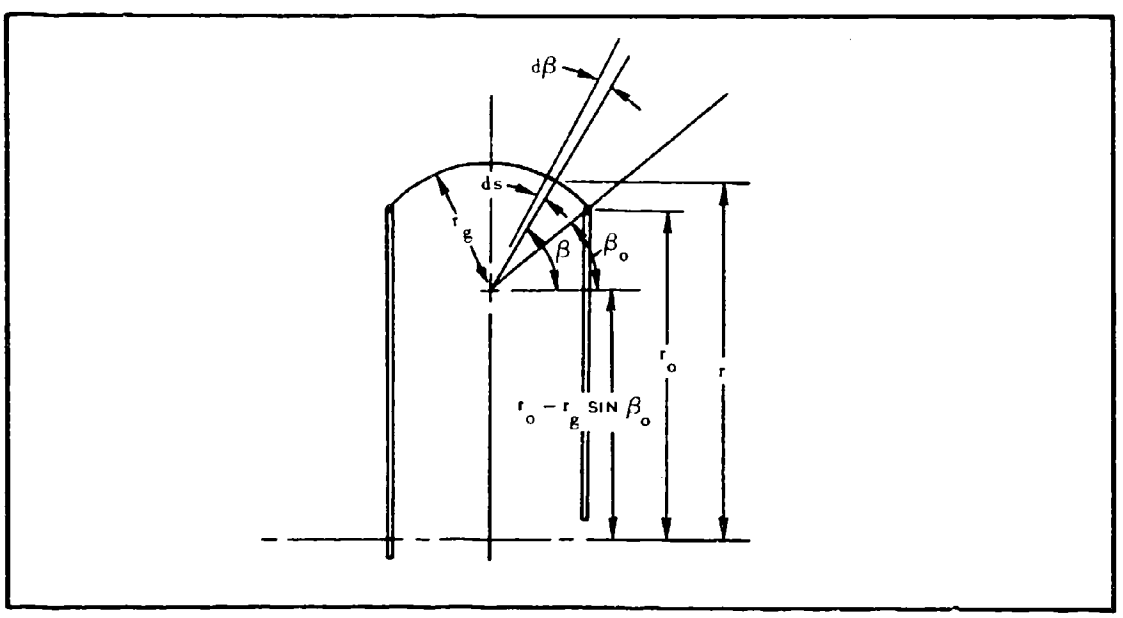

Figure III-3 - Inflated Geometry Detail

From Figure III-3, it is clear that the tailored width that corresponds to ds is $d\ell/\sqrt{2}$, or

$$\frac{r_g \, d\beta}{\sqrt{2 - \left[1 + \frac{r_g}{r_o}(\sin\beta - \sin\beta_o)\right]^2}} . \qquad \text{(III-7)}$$

The total tailored width is then

$$w = 2r_g \int_{\beta_o}^{\frac{\pi}{2}} \frac{d\beta}{\sqrt{2 - \left[1 + \frac{r_g}{r_o}(\sin\beta - \sin\beta_o)\right]^2}} \qquad \text{(III-7)}$$

The integral in Equation III-7 is best evaluated graphically. However, values of r_g and r_o must be known for each station at which the gore width is to be determined. The value for r_g is found from Equation II-35 of Appendix II for a constant-pressure membrane; r_1 is from Equation II-36 of Appendix II; and r_2 is from Equation II-11 of Appendix II. The values of r_o and β_o are obtained graphically by making a layout similar to Figure III-4.

The value of e is laid out normal to the computed profile curve at every point, x. Then these points are connected by a smooth curve that represents each meridian cord, as shown in Figure III-5.

The arc length, s, can be obtained graphically from Figure III-5. Because the meridian cords lie along the gore seams, s is also equal to the arc length of the edge of the gore pattern. The gore width is then obtained from Equation III-7, in which r_o is given by

$$r_o = r_1 - e .$$

The gore pattern can now be laid out by trial, giving a curve as shown in Figure III-6.

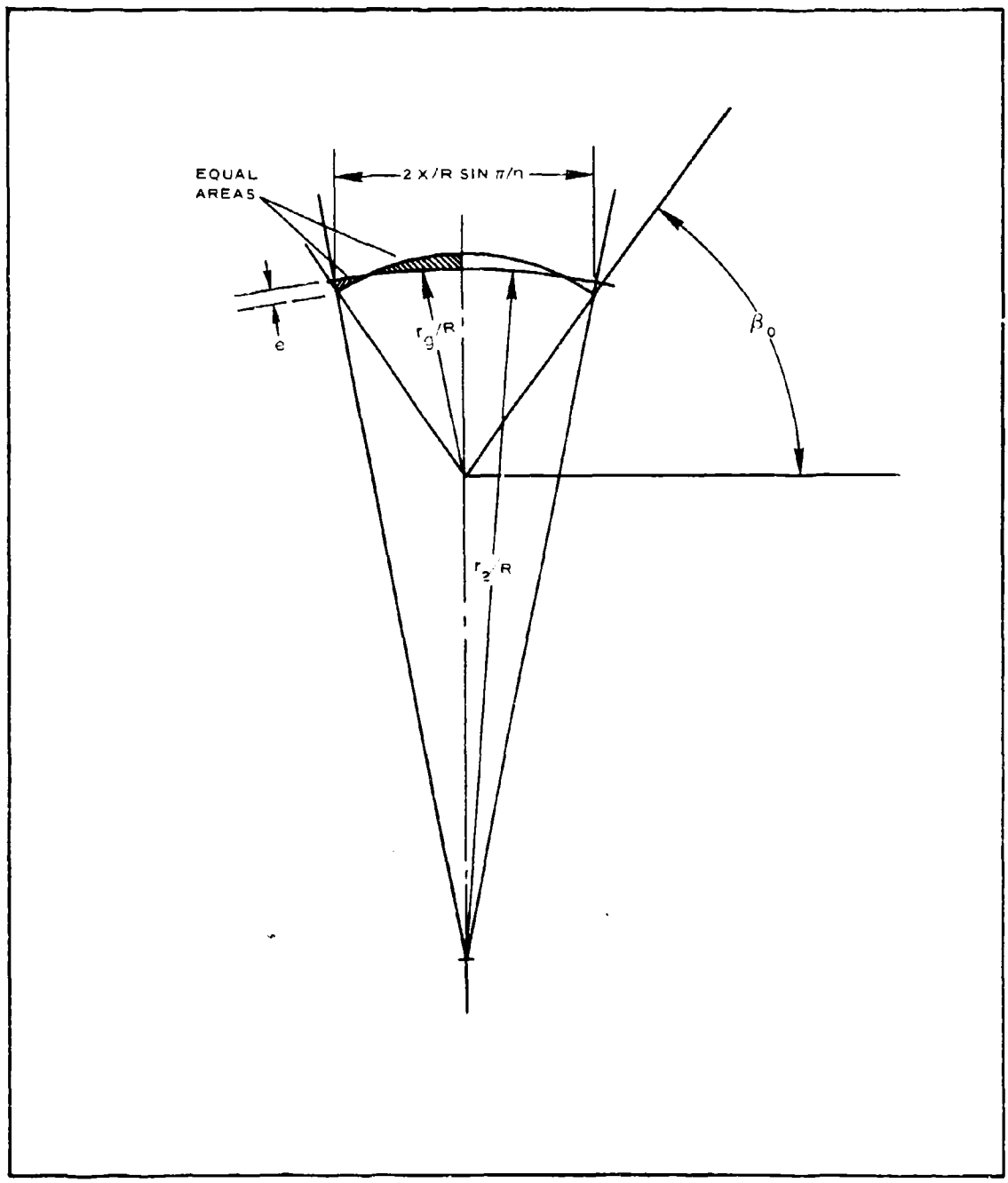

Figure III-4 - Gore Cross Section at Any Point, x

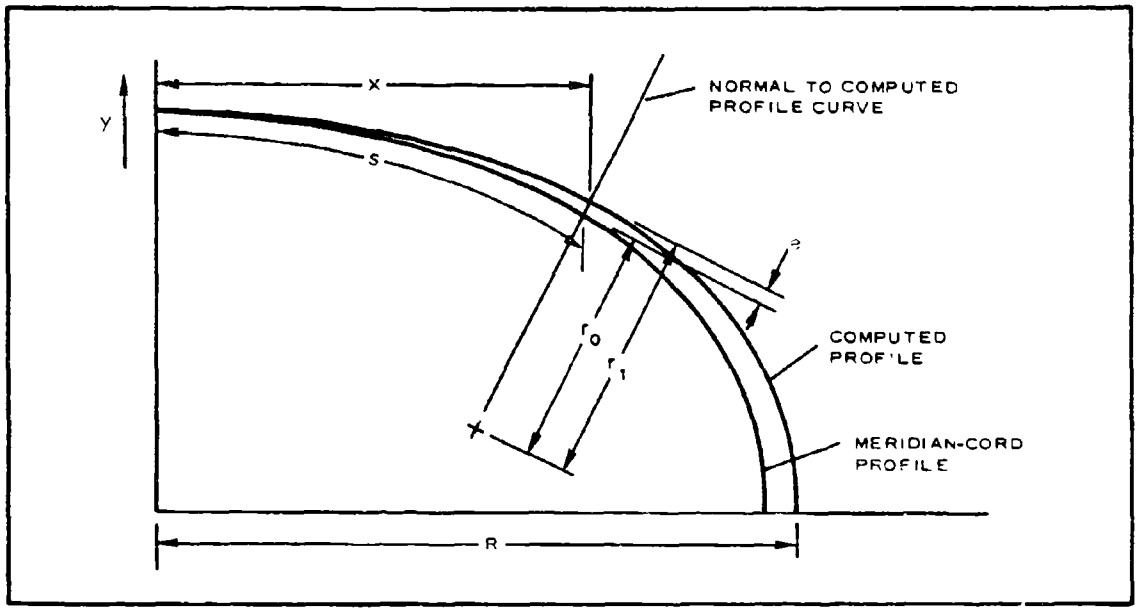

Figure III-5 - Determination of Meridian-Cord Profile

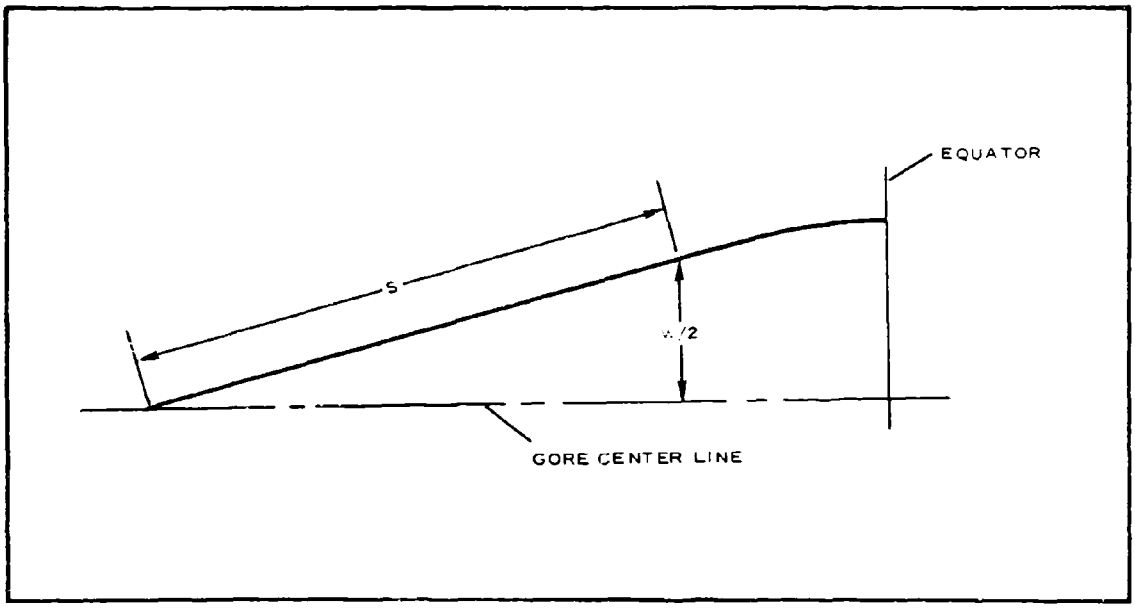

Figure III-6 - Gore-Pattern Layout

APPENDIX IV - DEPLOYMENT ANALYSIS

During the boost phase of the trajectory, the BALLUTE or parachute is packaged inside a deployment bag, which is inside a cylindrical canister. The canister, which is part of the primary structure of the missile, is reduced on the inside to bring its inside diameter to the same size as the outside diameter of the deployment bag. The rear of the deployment bag is connected to the back wall of the canister by a nylon line of length ℓ. The packaged configuration is shown in Figure IV-1.

After the boost phase, the booster is discarded. At the beginning of the recovery phase the canister is ejected rearward with an initial velocity, V_o, causing the package to come out of the canister. Assuming no friction between the deployment bag and the canister, the package remains stationary with

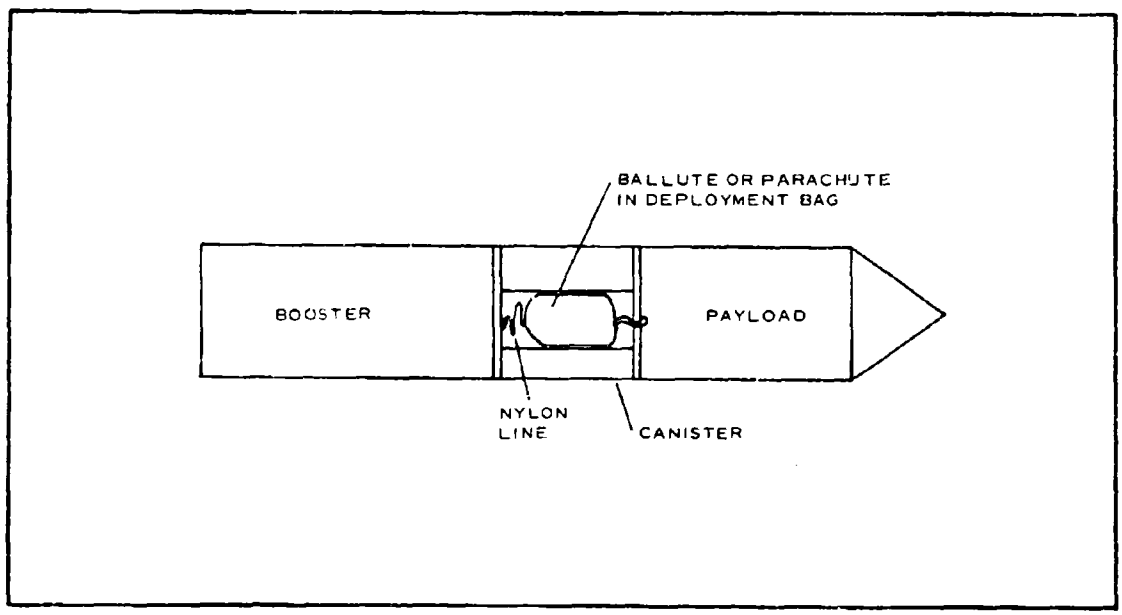

Figure IV-1 - Missile Configuration

respect to the payload until the canister has traveled a distance (ℓ) with respect to the package. (Aerodynamic forces also are neglected in this first phase of deployment.) The configuration at this point is shown in Figure IV-2.

The canister and the package now are represented by a system of two masses, m_1 and m_2, connected by a spring. The motion of this system is a simple harmonic vibration. It is shown schematically in Figure IV-3.

The load in the spring (deployment-bag line) is given by

$$P_\ell = \frac{E_\ell}{\ell} \Delta \ell, \tag{IV-1}$$

where

$$\Delta \ell = x_1 - x_2 . \tag{IV-2}$$

Equilibrium of mass m_1 yields

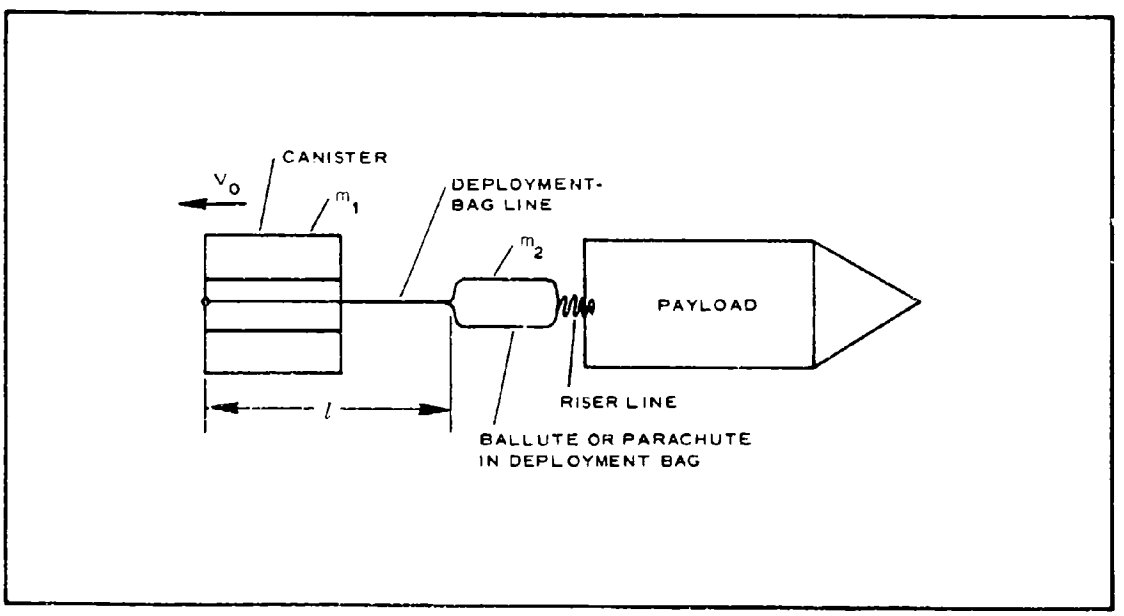

Figure IV-2 - Configuration at Instant of Deployment-Bag Line Stretch

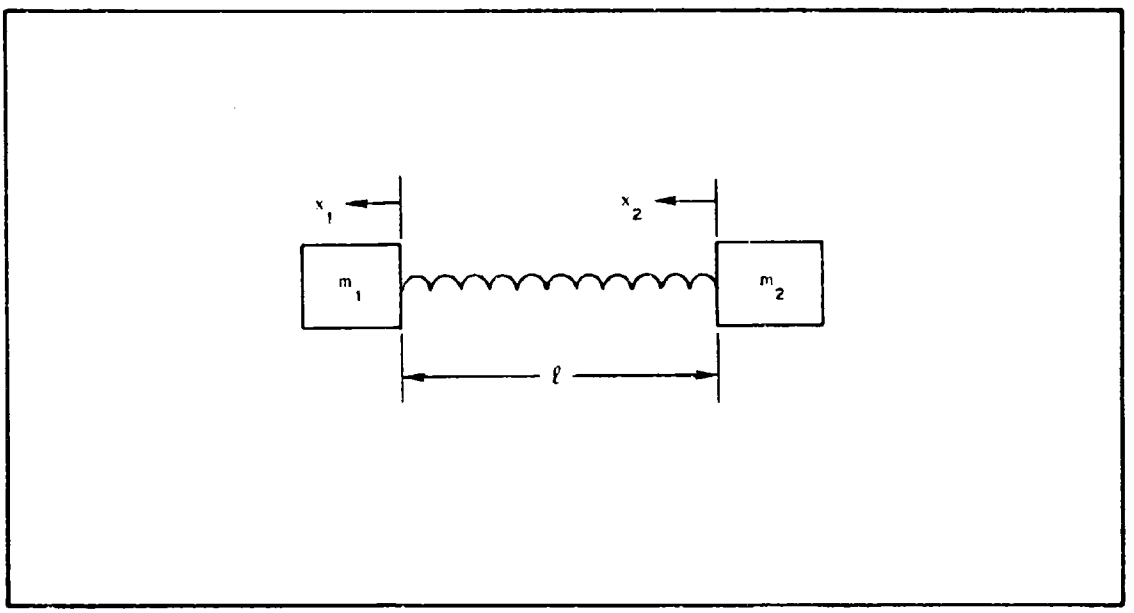

Figure IV-3 - Canister and Deployment-Bag Motion

$$P_\ell = -m_1 \frac{d^2 x_1}{d t^2} . \qquad \text{(IV-3)}$$

Similarly for mass m_2,

$$P_\ell = m_2 \frac{d^2 x_2}{d t^2} . \qquad \text{(IV-4)}$$

Equations IV-1 and IV-4 give

$$\frac{E_\ell \Delta \ell}{\ell} = m_2 \frac{d^2 x_2}{d t^2} . \qquad \text{(IV-5)}$$

Equations IV-2 and IV-5 give

$$\frac{E_\ell \Delta \ell}{\ell} = m_2 \left(\frac{-d^2 \Delta \ell}{d t^2} + \frac{d^2 x_1}{d t^2} \right) . \qquad \text{(IV-6)}$$

Equations IV-1 and IV-3 give

$$\frac{E\ell\Delta\ell}{\ell} = -m_1 \frac{d^2x_1}{dt^2} . \qquad \text{(IV-7)}$$

Equations IV-6 and IV-7 give

$$\frac{d^2\Delta\ell}{dt^2} + \frac{E\ell}{\ell}\left(\frac{1}{m_1} + \frac{1}{m_2}\right)\Delta\ell = 0 . \qquad \text{(IV-8)}$$

Equation IV-8 is a simple harmonic equation whose solution is

$$\Delta\ell = A_1 \sin \omega t + A_2 \cos \omega t , \qquad \text{(IV-9)}$$

where A_1 and A_2 are arbitrary constants,

$$\omega = \sqrt{\frac{E\ell}{\ell}\left(\frac{1}{m_1} + \frac{1}{m_2}\right)}, \qquad \text{(IV-10)}$$

and

$$t = 0 \quad \text{and}$$

$$\Delta\ell = 0,$$

which gives

$$A_2 = 0 . \qquad \text{(IV-11)}$$

Differentiating Equation IV-9,

$$\frac{d\Delta\ell}{dt} = \omega A_1 \cos \omega t \qquad \text{(IV-12)}$$

when

$$t = 0$$

and

$$\frac{d\Delta\ell}{dt} = V_o ,$$

which gives

$$A_1 = \frac{V_o}{\omega} . \qquad \text{(IV-13)}$$

Equation IV-9 thus becomes

$$\Delta \ell = \frac{V_o}{\omega} \sin \omega t . \qquad \text{(IV-14)}$$

The maximum value of $\Delta \ell$ occurs when $\sin \omega t = 1$, which gives

$$\Delta \ell_{max} = \frac{V_o}{\sqrt{\frac{E_\ell}{\ell}\left(\frac{1}{m_1} + \frac{1}{m_2}\right)}} . \qquad \text{(IV-15)}$$

Substituting for $\Delta \ell_{max}$ in Equation IV-1 gives

$$P_{\ell_{max}} = \frac{E_\ell V_o}{\ell \sqrt{\frac{E_\ell}{\ell}\left(\frac{1}{m_1} + \frac{1}{m_2}\right)}} . \qquad \text{(IV-16)}$$

Equation IV-16 gives the force the deployment bag must be able to carry without allowing the BALLUTE to break out. At the instant of maximum line stretch, the canister and deployment bag have a common velocity, V_1. The momentum of the system must be the same as the initial momentum of the canister.

Thus

$$V_1(m_1 + m_2) = m_1 V_o ,$$

or

$$V_1 = \frac{m_1 V_o}{m_1 + m_2} . \qquad \text{(IV-17)}$$

This is the velocity the canister and BALLUTE or parachute have at the end of the first phase of deployment as they begin to accelerate rearward under the action of the aerodynamic drag. The acceleration is given by

$$a = \frac{D}{m_1 + m_2}; \qquad \text{(IV-18)}$$

and the kinetic energy at the instant of line stretch is

$$KE = \frac{(m_1 + m_2)V_1^2}{2} + \int_0^L D dx . \qquad \text{(IV-19)}$$

If V_2 is the velocity of the BALLUTE or parachute and canister at the instant of line stretch,

$$\frac{(m_1 + m_2)V_2^2}{2} = \frac{(m_1 + m_2)V_1^2}{2} + \int_0^L D dx ,$$

or

$$V_2 = \sqrt{\left(\frac{2}{m_1 + m_2}\right)\left[\left(\frac{m_1 + m_2}{2}\right)V_1^2 + \int_0^L D dx\right]} . \qquad \text{(IV-20)}$$

In Equation IV-20, the quantity D is the drag on both the package and the canister during the second phase of deployment.

V_2 is the initial condition for snatching the BALLUTE or parachute alone, which is shown in Figure IV-4.

The load in the riser is given by

$$P_L = \frac{E_L x_2}{L} . \qquad \text{(IV-21)}$$

Equilibrium of mass m_2 yields

$$D_2 - P_L = m_2 \frac{d^2 x_2}{dt^2} . \qquad \text{(IV-22)}$$

Eliminating P_L gives

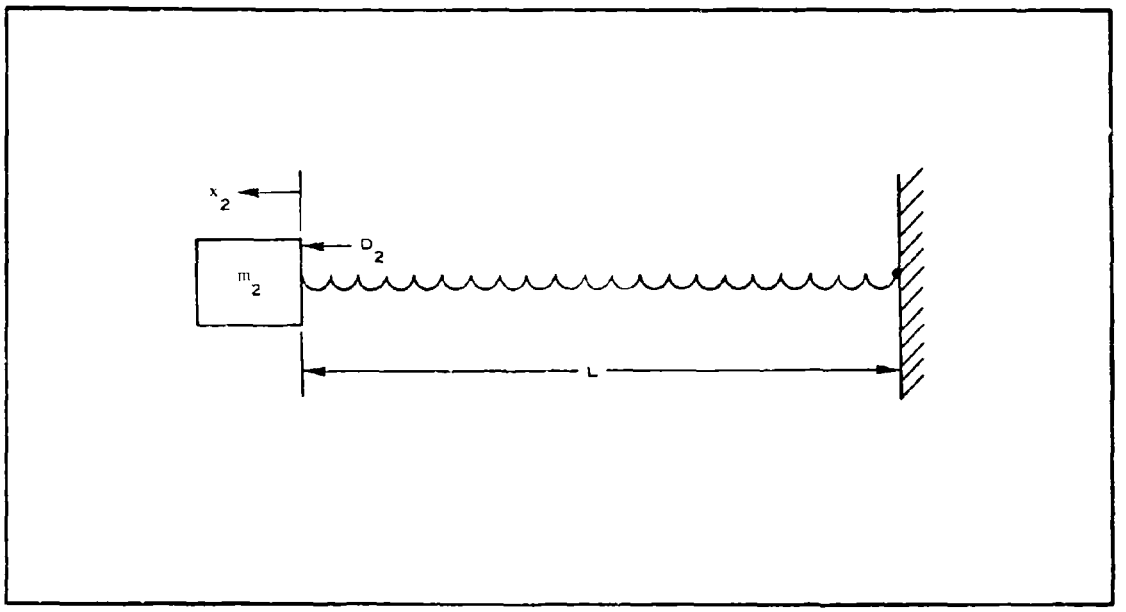

Figure IV-4 - Snatching BALLUTE or Parachute Alone

$$D_2 - \frac{E_L}{L} x_2 = m_2 \frac{d^2 x_2}{dt^2} ,$$

or

$$\frac{d^2 x_2}{dt^2} + \frac{E_L}{m_2 L} x_2 - \frac{D_2}{m_2} = 0 . \qquad \text{(IV-23)}$$

The particular solution is

$$x_2 = \frac{D_2 L}{E_L} . \qquad \text{(IV-24)}$$

The auxiliary equation is

$$u^2 + k = 0 , \qquad \text{(IV-25)}$$

and the roots are

$$u = \pm \sqrt{-k} . \qquad \text{(IV-26)}$$

The total solution is then

$$x_2 = \frac{D_2 L}{E_L} + C_1 e^{i\sqrt{k}\,t} + C_2 e^{-i\sqrt{k}\,t} \qquad \text{(IV-27)}$$

where

$$k = \frac{E_L}{m_2 L}, \qquad \text{(IV-28)}$$

when $t = 0$, $x_2 = 0$, which gives

$$C_1 + C_2 = -\frac{D_2 L}{E_L}. \qquad \text{(IV-29)}$$

Differentiating Equation IV-27 gives

$$\frac{d x_2}{d t} = i\sqrt{k}\left(C_1 e^{i\sqrt{k}\,t} - C_2 e^{-i\sqrt{k}\,t}\right) \qquad \text{(IV-30)}$$

when

$$t = 0$$

and

$$\frac{d x_2}{d t} = V_2,$$

which gives

$$V_2 = \sqrt{k}(C_1 - C_2)\, i. \qquad \text{(IV-31)}$$

Solving Equations IV-29 and IV-31 for C_1 and C_2,

$$C_1 = \frac{-\frac{D_2 L}{E_L} + \frac{V_2}{i\sqrt{k}}}{2} \qquad \text{(IV-32)}$$

and

$$C_2 = \frac{-\frac{D_2 L}{E_L} - \frac{V_2}{i\sqrt{k}}}{2} \qquad \text{(IV-33)}$$

The maximum value of P_L occurs when $d x_2/d t = 0$. Equation IV-30 gives

$$C_1 e^{i\sqrt{k}\, t_{max}} = C_2 e^{-i\sqrt{k}\, t_{max}},$$

or

$$t_{max} = \frac{\ln\left(\frac{C_2}{C_1}\right)}{2\, i\sqrt{k}}. \qquad \text{(IV-34)}$$

Equation IV-27 then gives

$$x_{2_{max}} = \frac{D_2 L}{E_L} + 2\sqrt{C_1 C_2}, \qquad \text{(IV-35)}$$

and Equation IV-21 gives

$$P_{L_{max}} = D_2 + 2\frac{E_L}{L}\sqrt{C_1 C_2}. \qquad \text{(IV-36)}$$

LIST OF SYMBOLS

a = Acceleration of canister and package

A_1, A_2, C_1, C_2 = Constants of integration (defined in text)

$D = D_1 + D_2$

D_1 = Drag on canister during second and third phases of deployment

D_2 = Drag on deployment bag during second and third phases of deployment

E = Modulus of deployment-bag line

E_L = Modulus of riser lines

$i = \sqrt{-1}$

$k = \dfrac{E_L}{m_2 L}$

ℓ = Length of deployment-bag line

L = Length of riser line

$\Delta\ell$ = Elongation of deployment-bag line

m_1 = Mass of canister

m_2 = Mass of BALLUTE or parachute

P_ℓ = Load in deployment-bag line

P_L = Load in riser line

q = Dynamic pressure

t = Time

u = Roots of auxiliary equation (defined in text)

V_o = Canister ejection velocity

V_1 = Velocity of canister and BALLUTE or parachute after first phase of deployment

V_2 = Velocity of canister and BALLUTE or parachute after second phase of deployment

x_1 = Displacement of canister at time, t

x_2 = Displacement of BALLUTE or parachute at time, t

$$\omega = \frac{E_\ell}{\ell}\left(\frac{1}{m_1} + \frac{1}{m_2}\right)$$

APPENDIX V - BALLUTE INTERNAL PRESSURE AND INLET LOCATION REQUIREMENTS

To satisfy inflation requirements, the location of an inlet along the BALLUTE surface is important. Since the inlet is fixed, its location or configuration is a compromise between the extremes of an intended operational range. The most important parameter is the pressure recovery. The most important variation is the relationship between the available pressure recovery and that which is required.

The available pressure is determined by the free-stream Mach number and the system of shocks generated by the BALLUTE. The required pressure (internal) is governed by the requirement to preserve shape and structural integrity.

If a reversible isentropic process for an ideal gas is assumed, the pressure recovery (ideal) is defined by the static-to-total-pressure ratio (or its inverse). For higher Mach numbers, the kinetic-energy efficiency can be used. Figure V-1 presents recovery efficiency versus Mach number for various shock systems.

Previous experience indicates that inflatable decelerators operate from the point of deployment to a point where conventional (low-speed) parachutes initiate the final stage of recovery. At present, the following operational modes are set up for testing:

$$2.4 \leqq M \leqq 10$$

$$80 \times 10^{3} \leqq h \leqq 225 \times 10^{3} \text{ ft}$$

$$0.684 \times 10^{-1} \leqq p/p_t \leqq 0.2356 \times 10^{-4}$$

$$0.2758 \leqq q/p_t \leqq 0.1649 \times 10^{-2}$$

$$0.4647 \leqq T/T_t \leqq 0.4762 \times 10^{-1}$$

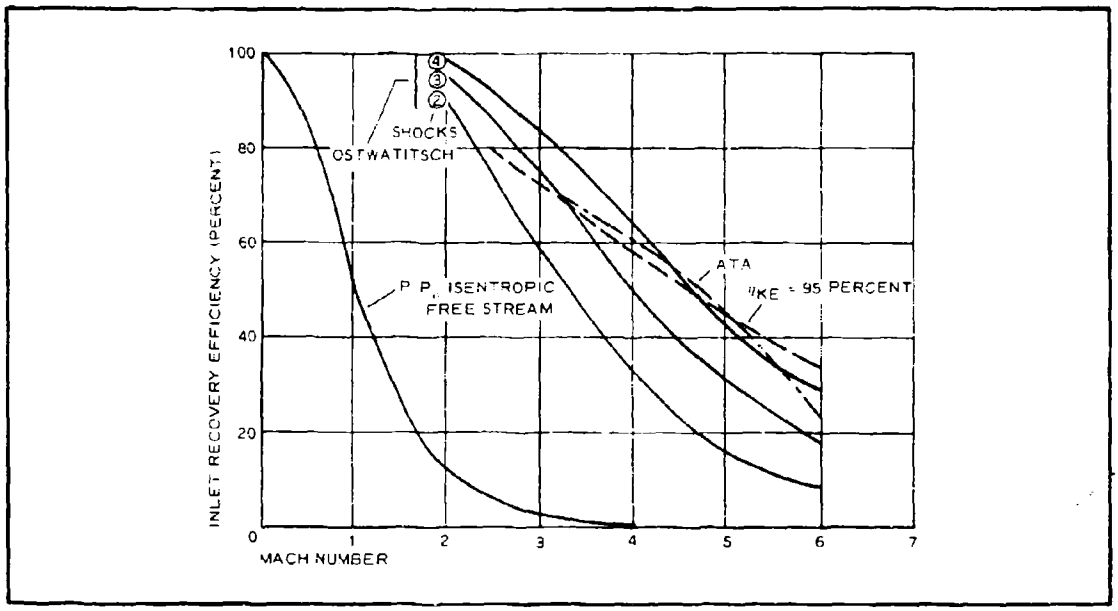

Figure V-1 - Typical Pressure Recovery for Supersonic Ducts

The external loading of a decelerator (defined as a spheroidal body with a maximum conical angle of 80 deg) operating throughout the modes shown, is indicated by the values of surface-pressure coefficients. Since the main shock generated by this body is oblique (at the Mach numbers shown) the following maximum surface-pressure coefficients apply:[a]

$$0.88 \leqq C_p \leqq 1.0$$

The wind-tunnel tests indicate the following range:

$$0.75 \leqq C \leqq 1.09$$

at

$$\frac{X}{D} = 7.11$$

Figure V-2 shows the variation in plotted form.

[a]Ames Research Staff: Equations, Tables and Charts for Compressible Flow. NACA Report 1135, 1953.

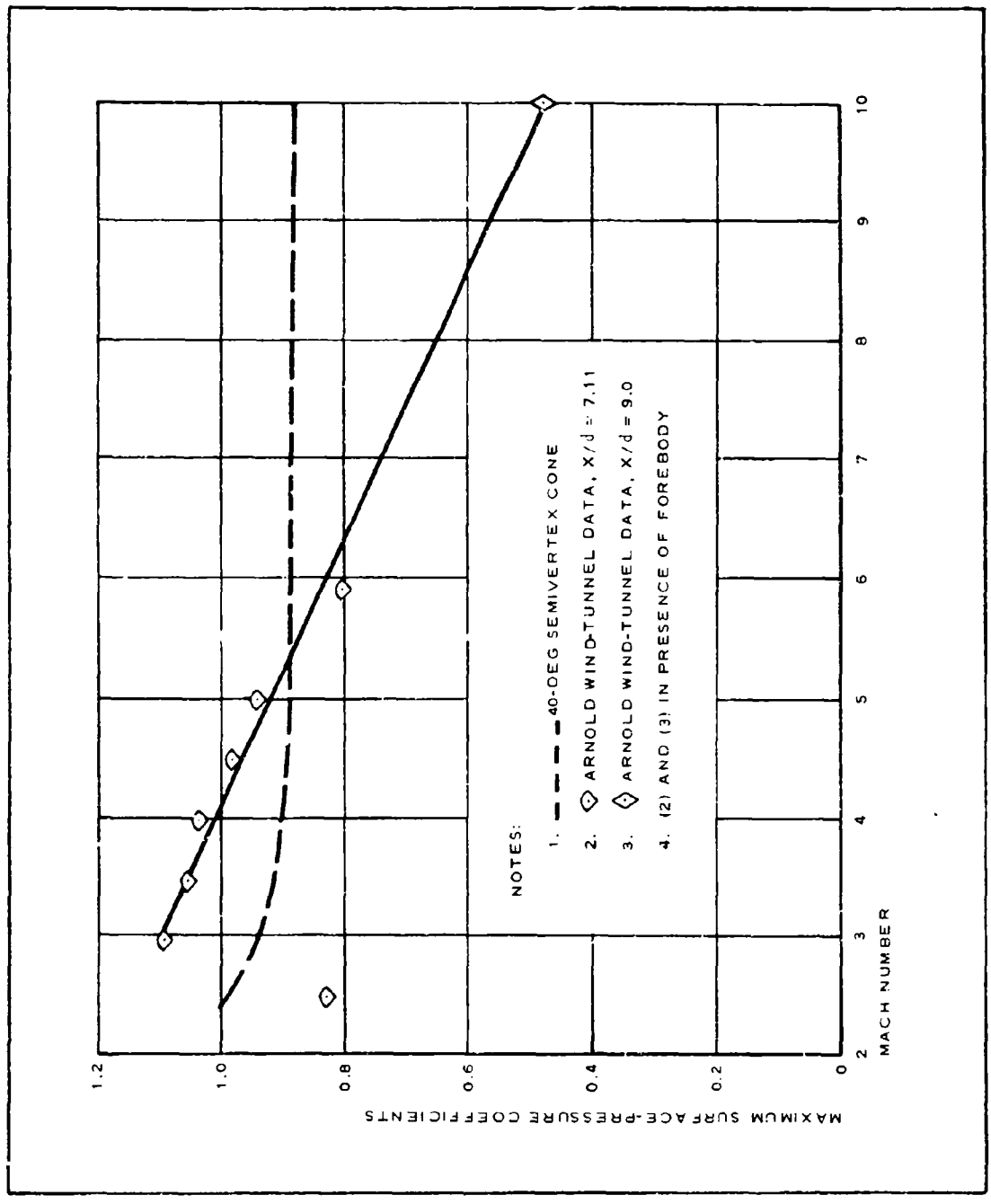

Figure V-2 - BALLUTE Surface Maximum Pressure Coefficients

NOTE

Maximum C_p does not imply C_p stagnation but one along the surface downstream.

To ensure proper inflation at all modal points and at the same time to comply with strength and material-property requirements, the inside pressure at all points must be greater than the maximum external value at the same point.

With dynamic pressure as a criterion for inside loading and considering the plot of Figure V-2, it is concluded that inflation pressure equivalent to $p_i = 2\,q$ is sufficient to satisfy the requirements stated above.

To express it in a coefficient form, the following procedure is developed: If

$$C_{p_i} = \frac{p_L - p_\infty}{q_\infty},$$

where

$$q_\infty = 0.7\, p_\infty\, M_\infty^{\,2},$$

then

$$p_\infty = \frac{q_\infty}{0.7\, M_\infty^{\,2}}$$

The inside pressure (local in this case) is

$$p_L = 2\, q_\infty .$$

Hence,

$$C_{p_i}\, q_\infty = 2\, q_\infty - \frac{q_\infty}{0.7\, M_\infty^{\,2}} .$$

Dividing by q_∞ gives

$$C_{p_i} = 2 - \frac{1}{0.7\ M_\infty^2}.$$

The coefficients, for Mach numbers under consideration, are given in Table V-1.

TABLE V-1 - COEFFICIENTS

M	$0.7\ M^2$	$1/0.7\ M^2$	C_p
2.5	4.38	0.228	1.772
3.0	6.30	0.159	1.841
3.5	8.58	0.117	1.883
4.0	11.20	0.088	1.912
4.5	14.29	0.071	1.929
5.0	17.50	0.057	1.943
6.0	25.2	0.039	1.961
8.0	44.8	0.022	1.978
10.0	70.0	0.014	1.986

PREVIOUS PAGE WAS BLANK, THEREFORE NOT FILMED.

APPENDIX VI - BALLUTE INFLATION PROCESS

Inflation of a BALLUTE that leaks because of material and fabrication porosity is analogous to filling a vessel with a gas and emptying it at the same time.

Consider the system shown in Figure VI-1, where

V = BALLUTE volume,

A_i = inlet area,

X_i = initial duct length,

A_e = exit area, f (porosity),

P_{10}, ρ_{10}, and T_{10} = initial parameters at inlet,

P_{20}, ρ_{20}, and T_{20} = initial parameters in BALLUTE,

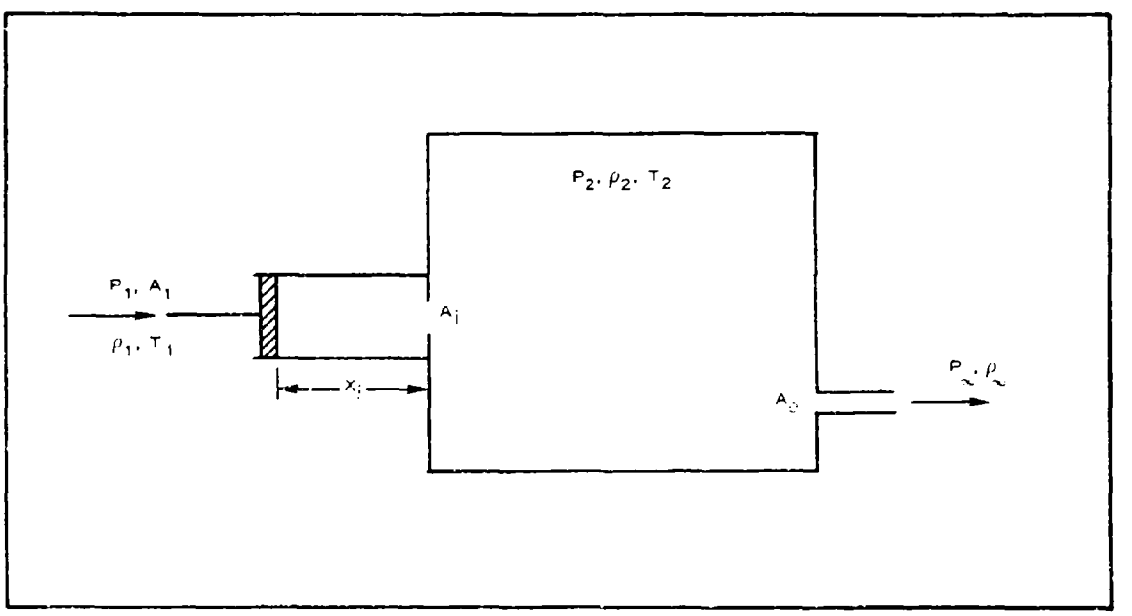

Figure VI-1 - Schematic of Inflation System

P_1, ρ_1, and T_1 = current values at inlet, and

P_2, ρ_2, and T_2 = current values in BALLUTE.

The gas is assumed to be ideal. Then, the rate of flow is

$$W_1 = \bar{q}_1 A_e \rho_2 \sqrt{\frac{2K}{K-1} gRT_2} \qquad \text{(flow from BALLUTE)} \qquad \text{(VI-1)}$$

and

$$W_2 = \bar{q}_2 A_i \rho_1 \sqrt{\frac{2K}{K-1} gRT_1} \qquad \text{(flow into BALLUTE)} \qquad \text{(VI-2)}$$

where

$$\bar{q}_1 = \bar{q}_1 \left(f_1, \frac{P_\infty}{P_2} \right),$$

$$\bar{q}_2 = \bar{q}_2 \left(f_2, \frac{P_2}{P_1} \right),$$

and

$$f_1 = \text{local resistance}.$$

By introducing the discharge coefficient,

$$C_W = \frac{\text{actual flow}}{\text{insentropic flow rate}},$$

the q can be defined by

$$\bar{q}_1 = \bar{q}_{10}$$

$$= C_{W_1} \left(\frac{2}{K+1} \right)^{\frac{1}{K-1}} \sqrt{\frac{K-1}{K+1}} \qquad \text{(VI-3)}$$

when

$$\frac{P_\infty}{P_2} \leq \left(\frac{2}{K+1}\right)^{\frac{K}{K-1}} ;$$

by

$$\bar{q}_1 = C_{W_1}\left(\frac{P_\infty}{P_2}\right)^{\frac{1}{K}} \sqrt{1 - \left(\frac{P_\infty}{P_1}\right)^{\frac{K-1}{K}}} \qquad \text{(VI-4)}$$

when

$$\frac{P_\infty}{P_2} \geq \left(\frac{2}{K+1}\right)^{\frac{K}{K-1}} ;$$

by

$$\bar{q}_2 = \bar{q}_{20}$$

$$= C_{W_2}\left(\frac{2}{K+1}\right)^{\frac{1}{K-1}} \sqrt{\frac{K-1}{K+1}} \qquad \text{(VI-5)}$$

when

$$\frac{P_2}{P_1} \leq \left(\frac{2}{K+1}\right)^{\frac{K}{K-1}} ;$$

and by

$$\bar{q}_2 = C_{W_2}\left(\frac{P_2}{P_1}\right)^{\frac{1}{K}} \sqrt{1 - \left(\frac{P_2}{P_1}\right)^{\frac{K-1}{K}}} \qquad \text{(VI-6)}$$

when

$$\frac{P_2}{P_1} \geqq \left(\frac{2}{K+1}\right)^{\frac{K}{K-1}} .$$

The enthalpy of the gas (assuming insulated inlets) is

$$h_1 = C_P T_2$$

and

$$h_2 = C_P T_1 .$$

The solution for the rates of flow is divided into two cases, depending on pressure ratios:

For Case 1, if

$$\frac{P_\infty}{P_2} \leqq \left(\frac{2}{K+1}\right)^{\frac{K}{K-1}}$$

and

$$\frac{P_2}{P_1} \leqq \left(\frac{2}{K+1}\right)^{\frac{K}{K-1}} ,$$

then q_1 and q_2 are determined by Equations VI-3 and VI-5.

For Case 2, if

$$\frac{P_\infty}{P_2} \geqq \left(\frac{2}{K+1}\right)^{\frac{K}{K-1}}$$

and

$$\frac{P_2}{P_1} \geqq \left(\frac{2}{K+1}\right)^{\frac{K}{K-1}} ,$$

then q_1 and q_2 are determined by Equations VI-4 and VI-6.

The next task is to determine flow-discharge coefficients, C_{W_1} and C_{W_2}. The discharge coefficient is determined experimentally; it depends on the shape of the opening and the local RN. According to References VI-1 and VI-2, the discharge coefficient with straight axes is $C_W \approx 0.99 \rightarrow 0.92$; or by Reference VI-3 for a nozzle with $\ell > 3d$, where ℓ is length and d is diameter, $C_W = 0.62$, and with a rounded opening, $C_W = 0.97$. The C_W for a sharp-edged opening (orifice) can be found from Figure 4.17 of Reference VI-1 or from Reference VI-3; for bent ducts, see Reference VI-3.

REFERENCES

VI-1. Shapiro, A. H.: The Dynamics and Thermodynamics of Compressible Flow. The Ronald Press Company, 1953.

VI-2. Eshbach, O. W.: Handbook of Engineering Fundamentals. T. Wiley and Sons, Inc., 1952.

VI-3. Ginzburg, I. P.: Applied Hydrogasdynamics. Leningrad State University, 1958.

PREVIOUS PAGE WAS BLANK, THEREFORE NOT FILMED.

APPENDIX VII - INFLATION TIME FOR A BALLUTE

e time to fill to the critical pressure ratio was used to determine the approxi-
te time to reach maximum drag for trajectory considerations. Consider the
lowing problem of a vessel being filled by a gas. The vessel volume can be a
iable or a constant.

s assumed that pressure and temperature of an environment in which the ves-
is placed are constant (see Figure VII-1).

om Figure VII-1,

ρ_i, P_i, T_i = initial values in BALLUTE,

A_i = inlet area,

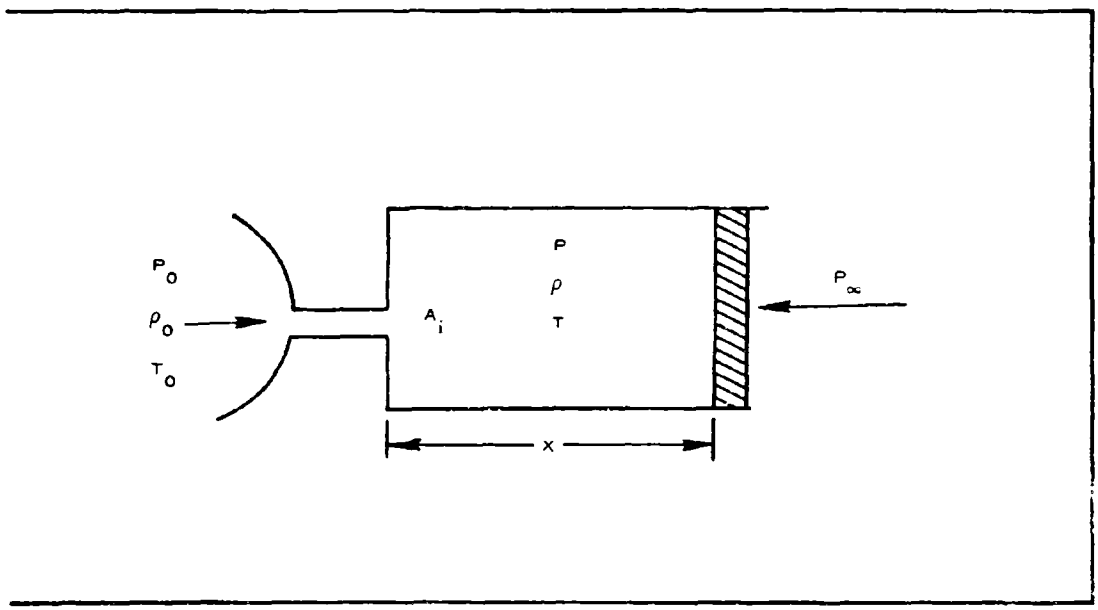

Figure VII-1 - Inflation Schematic

ρ, P, T = current values in BALLUTE,

and

ρ_o, P_o, T_o = stream-tube values in front of BALLUTE.

A quasi-steady process for an ideal gas is assumed. The conservation of mass, then, can be written as:

$$\frac{d\,A\,x\rho}{d\,t} = W \qquad \text{(VII-1)}$$

and the conservation of energy is

$$\frac{d\rho A\,x\,U}{d\,t} + JP\frac{dAx}{d\,t} = \frac{d\,Q}{d\,t}\,, \qquad \text{(VII-2)}$$

where

U = internal energy of unit of gas mass

= $C_v T$,

J = 778 Btu/ft-lb,

$\frac{d\,Q}{d\,t}$ = amount of heat transferred to a mass of gas in vessel in unit of time,

W = rate of flow, and

A = cross-sectional area of an equivalent cylinder.

The momentum equation is

$$m\frac{d^2x}{d\,t^2} = A\,(P - P_\infty) - P_f\,, \qquad \text{(VII-3)}$$

where

m = mass of a piston

≡ BALLUTE mass, and

P_f = friction force of a piston

≡ fabric friction force.

Assuming no heat transfer for ideal gas,

$$h = C_P T_o . \qquad \text{(VII-4)}$$

The rate flow of gas flowing into a vessel, being quasi-steady, is

$$W = \bar{q}\left(f, \frac{P}{P_o}\right) A_i \sqrt{\frac{2K}{k-1} g R T} , \qquad \text{(VII-5)}$$

where

$$\bar{q} = \bar{q} \text{ (friction coefficient and pressure ratio).}$$

and the rate can be determined from Ginsburg.[a]

If the inlet is small, ther flow process is assumed to be adiabatic and,

$$\bar{q} = C_W \left(\frac{P}{P_o}\right)^{\frac{1}{K}} \sqrt{1 - \left(\frac{P}{P_o}\right)^{\frac{K-1}{K}}} ,$$

when

$$\frac{P}{P_o} \geq \left(\frac{2}{K+1}\right)^{\frac{K}{K-1}} ;$$

the flow is subcritical.

And

$$\bar{q} = \bar{q}_o$$

$$= C_W \left(\frac{2}{K+1}\right)^{\frac{1}{K-1}} \sqrt{\frac{K-1}{K+1}} ,$$

when

$$\frac{P}{P_o} \leq \left(\frac{2}{K+1}\right)^{\frac{K}{K-1}} ;$$

[a] Ginsburg, I. P.: Applied Hydrogasdynamics. Leningrad State University 1958.

the flow is supercritical. For supercritical flow where W is constant, integrating Equation VII-1 gives

$$\frac{d\,A\,x\rho}{d\,t} = W$$

$$\int d\,A\,x\rho = \int W\,d\,t$$

$$A \quad \rho = Wt + A\,x_i\rho_i \qquad \text{(VII-6)}$$

where

$$x_i \text{ is at } t = 0.$$

The time of inflation is

$$A\,x\rho - A\,x_i\,\rho_i = Wt$$

$$t = \frac{A\,x \;- A x_i \rho_i}{W} \qquad \text{(VII-7)}$$

Variation of T, ρ, and P versus time can be obtained by solving Equations VII-2 and VII-3 with the help of VII-6.

If the vessel is insulated and of constant volume with no heat transfer, then

$$x = x_i .$$

The following equations define the values for flow parameters:

$$\rho = \rho_i + \frac{Wt}{V}, \qquad \text{(VII-8)}$$

where

$$V = \text{vessel volume}$$

and

$$T = \frac{T_i + K\,T_o^{\frac{W\,t}{F_i}}}{1 + \frac{Wt}{F_i}}, \qquad \text{(VII-9)}$$

and where

$$F_i = A\, x_i\, \rho_i$$

= initial mass, and

$$P = P_i + K \frac{\rho_i}{\rho_o} P_o \frac{Wt}{F_i} . \qquad \text{(VII-10)}$$

The time at which the pressure in a vessel becomes critical (P_{cr}) is defined by the following equation:

$$P_{cr} = P_i + K \frac{\rho_i}{\rho_o} P_o \frac{Wt_{cr}}{F_i} \qquad \text{(VII-11)}$$

If

$$P_{cr} = P_o \left(\frac{2}{K+1}\right)^{\frac{K}{K-1}} , \qquad \text{(VII-12)}$$

then

$$\frac{W\, t_{cr}}{F_i} = \frac{1}{K} \frac{\rho_o}{\rho_i} \left[\left(\frac{2}{K+1}\right)^{\frac{K}{K-1}} - \frac{P_i}{P_o} \right]$$

and

$$t_{cr} = \frac{\frac{F_i}{K} \frac{\rho_o}{\rho_i} \left[\left(\frac{2}{K+1}\right)^{\frac{K}{K-1}} - \frac{P_i}{P_o} \right]}{W} . \qquad \text{(VII-13)}$$

UNCLASSIFIED

Security Classification

DOCUMENT CONTROL DATA - R&D

(Security classification of title, body of abstract and indexing annotation must be entered when the overall report is classified)

1. ORIGINATING ACTIVITY (Corporate author)
Goodyear Aerospace Corporation
1210 Massillon Road
Akron 15, Ohio

2a. REPORT SECURITY CLASSIFICATION
UNCLASSIFIED

2b. GROUP

3. REPORT TITLE
Aerodynamic Deployable Decelerator Performance - Evaluation Program

4. DESCRIPTIVE NOTES (Type of report and inclusive dates)
Final Report April 1963 - June 1964

5. AUTHOR(S) (Last name, first name, initial)
F. R. Nebiker, A. C. Aebischer, J. J. Dean, F. Floetscher, W. W. Sowa, I. M. Jaremenko, J. Schlemmer, W. A. Barr, N. E. Houtz and R. G. Slaymann

6. REPORT DATE	7a. TOTAL NO. OF PAGES	7b. NO. OF REFS
August 1965	305	45

8a. CONTRACT OR GRANT NO.	9a. ORIGINATOR'S REPORT NUMBER(S)
AF 33(657)-10955	AFFDL-TR-65-27
b. PROJECT NO. 6065 and 8151	
c. Tasks: 606505, 606506	9b. OTHER REPORT NO(S) (Any other numbers that may be assigned this report)
d.	

10. AVAILABILITY/LIMITATION NOTICES
Qualified requesters may obtain copies of this report from DDC. Foreign announcement and dissemination of this report is not authorized. DDC release to CFSTI is not authorized.

11. SUPPLEMENTARY NOTES

12. SPONSORING MILITARY ACTIVITY
Air Force Flight Dynamics Laboratory
Research and Technology Division
Air Force Systems Command
Wright-Patterson AFB, Ohio

13. ABSTRACT

The objective of this program is to advance the state of the art by using analytical and engineering techniques for designing aerodynamic deployable decelerators. Three classes of decelerators - small supersonic parachutes, ram-air-inflated BALLUTEs, and large high-dynamic-pressure parachutes were investigated. Free-flight tests using a newly developed GAC missile system and wind-tunnel tests in the full-scale propulsion wind-tunnel facility at Arnold Research Center were conducted. The results indicated that the engineering techniques that were developed led to improved decelerators and that an improved free-flight test capability was established.

DD FORM 1 JAN 64 1473

UNCLASSIFIED

Security Classification

UNCLASSIFIED

Security Classification

14. KEY WORDS	LINK A		LINK B		LINK C	
	ROLE	WT	ROLE	WT	ROLE	WT
Free flight performance tests Supersonic parachutes Wind tunnel tests Recovery Rockets Telemetry Supersonic drag Floatation						

INSTRUCTIONS

1. ORIGINATING ACTIVITY: Enter the name and address of the contractor, subcontractor, grantee, Department of Defense activity or other organization *(corporate author)* issuing the report.

2*a*. REPORT SECURITY CLASSIFICATION: Enter the overall security classification of the report. Indicate whether "Restricted Data" is included. Marking is to be in accordance with appropriate security regulations.

2*b*. GROUP: Automatic downgrading is specified in DoD Directive 5200.10 and Armed Forces Industrial Manual. Enter the group number. Also, when applicable, show that optional markings have been used for Group 3 and Group 4 as authorized.

3. REPORT TITLE: Enter the complete report title in all capital letters. Titles in all cases should be unclassified. If a meaningful title cannot be selected without classification, show title classification in all capitals in parenthesis immediately following the title.

4. DESCRIPTIVE NOTES: If appropriate, enter the type of report, e.g., interim, progress, summary, annual, or final. Give the inclusive dates when a specific reporting period is covered.

5. AUTHOR(S): Enter the name(s) of author(s) as shown on or in the report. Enter last name, first name, middle initial. If military, show rank and branch of service. The name of the principal author is an absolute minimum requirement.

6. REPORT DATE: Enter the date of the report as day, month, year, or month, year. If more than one date appears on the report, use date of publication.

7*a*. TOTAL NUMBER OF PAGES: The total page count should follow normal pagination procedures, i.e., enter the number of pages containing information.

7*b*. NUMBER OF REFERENCES: Enter the total number of references cited in the report.

8*a*. CONTRACT OR GRANT NUMBER: If appropriate, enter the applicable number of the contract or grant under which the report was written.

8*b*, 8*c*, & 8*d*. PROJECT NUMBER: Enter the appropriate military department identification, such as project number, subproject number, system numbers, task number, etc.

9*a*. ORIGINATOR'S REPORT NUMBER(S): Enter the official report number by which the document will be identified and controlled by the originating activity. This number must be unique to this report.

9*b*. OTHER REPORT NUMBER(S): If the report has been assigned any other report numbers *(either by the originator or by the sponsor)*, also enter this number(s).

10. AVAILABILITY/LIMITATION NOTICES: Enter any limitations on further dissemination of the report, other than those imposed by security classification, using standard statements such as:

(1) "Qualified requesters may obtain copies of this report from DDC."

(2) "Foreign announcement and dissemination of this report by DDC is not authorized."

(3) "U. S. Government agencies may obtain copies of this report directly from DDC. Other qualified DDC users shall request through

_____."

(4) "U. S. military agencies may obtain copies of this report directly from DDC. Other qualified users shall request through

_____."

(5) "All distribution of this report is controlled. Qualified DDC users shall request through

_____."

If the report has been furnished to the Office of Technical Services, Department of Commerce, for sale to the public, indicate this fact and enter the price, if known.

11. SUPPLEMENTARY NOTES: Use for additional explanatory notes.

12. SPONSORING MILITARY ACTIVITY: Enter the name of the departmental project office or laboratory sponsoring *(paying for)* the research and development. Include address.

13. ABSTRACT: Enter an abstract giving a brief and factual summary of the document indicative of the report, even though it may also appear elsewhere in the body of the technical report. If additional space is required, a continuation sheet shall be attached.

It is highly desirable that the abstract of classified reports be unclassified. Each paragraph of the abstract shall end with an indication of the military security classification of the information in the paragraph, represented as *(TS)*, *(S)*, *(C)*, or *(U)*.

There is no limitation on the length of the abstract. However, the suggested length is from 150 to 225 words.

14. KEY WORDS: Key words are technically meaningful terms or short phrases that characterize a report and may be used as index entries for cataloging the report. Key words must be selected so that no security classification is required. Identifiers, such as equipment model designation, trade name, military project code name, geographic location, may be used as key words but will be followed by an indication of technical context. The assignment of links, rules, and weights is optional.

UNCLASSIFIED

Security Classification